Georgia Institute of Technology

School of Civil and Environmental Engineering

Structural Engineering, Mechanics and Materials
Research Report

Durability of Precast Prestressed Concrete Piles in Marine Environment, Part 2
Volume 1: Concrete

Final Report

Prepared for

Office of Materials and Research
Georgia Department of Transportation

GDOT Research Project No. 10-26
Task Order No. 02-78

by

R. Brett Holland, Robert Moser, Lawrence Kahn,
Preet Singh, and Kimberly Kurtis

June 2012

Contract Research

GDOT Research Project No. 10-26
Task Order No. 02-78

Durability of Precast Prestressed Concrete Piles in Marine Environment, Part 2
Volume 1: Concrete

Final Report

Prepared for

Office of Materials and Research
Georgia Department of Transportation

By

R. Brett Holland, Robert Moser, Lawrence Kahn,
Preet Singh, and Kimberly Kurtis

June 2012

(This page intentionally left blank.)

1.Report No.: FHWA-GA-12-1026	2. Government Accession No.:	3. Recipient's Catalog No.:

4. Title and Subtitle: Durability of Precast Prestressed Concrete Piles in Marine Environment: Reinforcement Corrosion and Mitigation, Part 2	5. Report Date: June 2012
	6. Performing Organization Code:
7. Author(s): R.B.Holland, R. Moser, L. Kahn, P. Singh, and K. Kurtis	8. Performing Organ. Report No.: 10-26
9. Performing Organization Name and Address: School of Civil & Env. Engineering Georgia Institute of Technology Atlanta, Georgia 30332-0355	10. Work Unit No.:
	11. Contract or Grant No.: SPR00-0008-00853 (RP 10-26)
12. Sponsoring Agency Name and Address: Georgia Department of Transportation Office of Materials & Research 15 Kennedy Drive Forest Park, GA 30297-2534	13. Type of Report and Period Covered: Final; Dec. 2010 – June 2012
	14. Sponsoring Agency Code:

15. Supplementary Notes:
Prepared in cooperation with the U.S. Department of Transportation, Federal Highway Administration.

16. Abstract:

The overall purpose of this research was to determine methods which may be applied economically to mitigate corrosion of reinforcement in precast prestressed concrete piles in Georgia's marine environments. The research was divided into two parts, reported in volumes 1 and 2: (1) to develop and evaluate concrete mix designs to prolong service lives of precast prestressed concrete piles in aggressive marine environments, and (2) to assess the potential of using stainless steel for prestressing reinforcement and to compare the strength and corrosion resistance of stainless steel strand to conventional prestressing strand.

Studies of piles from Georgia's coastal environment showed that the brackish waters caused both sulfate attack of the cement paste and biological attack to limestone aggregate. Use of granite aggregate, Type II cement, class F fly ash and slag are recommended. For corrosion resistance and high strength, the best, readily accessible stainless steel alloys were 2205 and 2304. Actual production of stainless steel wire and strand showed that induction heating, while the strand was under tension, increased the strand strength and lowered the relaxation from about 8% to about 2.5% for both 2205 and 2304. The presence of crevices in normal A416 prestressing strand geometry significantly increased and accelerated corrosion as compared with plain wires. Strands made with Grades 2205 and 2304 developed ultimate tensile strengths of 242 ksi and 261 ksi, respectively; but the 2304 exhibited notch sensitivity at the prestressing grips, and its use is not recommended in production at this time.

17. Key Words: Piles, corrosion, concrete durability, marine environment, stainless steel		18. Distribution Statement:	
19. Security Classification (of this report): Unclassified	20.Security Classification(of this page): Unclassified	21. Number of Pages: Volume 1: 336	22. Price:

(This page intentionally left blank.)

Executive Summary

The overall purpose of this research was to determine methods which may be applied economically to mitigate corrosion of reinforcement in precast prestressed concrete piles in Georgia's marine environments. The research was divided into two parts, reported here in volumes 1 and 2: (1) to develop and evaluate concrete mix designs to prolong service lives of precast prestressed concrete piles in aggressive marine environments, and (2) to assess the potential of using stainless steel for prestressing reinforcement and to compare the strength and corrosion resistance of stainless steel strand to conventional prestressing strand. The research presented in Volume 1 was focused on increasing the resistance of concrete mix designs to the various deterioration mechanisms present in coastal exposures to create a High Performance Marine Concrete (HPMC). While it was known that chloride intrusion into concrete piles caused corrosion of the prestressed and non-prestressed reinforcement, studies of piles from the coastal environment showed that the brackish waters caused sulfate attack of the concrete and that long-term exposure resulted in decreased pH due to carbonation. The decreased pH lead to more rapid corrosion of reinforcement.

Studies into chloride ingress resistance demonstrated that slag mix designs containing metakaolin provided superior resistance compared to other mix designs; rapid chloride permeability was less than 500 coulombs. Sulfate resistance testing demonstrated that the performance characteristic measured during sulfate exposure had significant effect on the apparent resistance of mix designs. Compression degradation and expansion testing both showed that slag mix designs with metakaolin performed well, regardless of the testing method for sulfate resistance. Concretes made with Type III

cement were found much more susceptible to sulfate attack than those made with Type II and Type V cement. Carbonation testing of mix designs showed that mixes with a water-to-cementitious materials ratio (w/cm) of 0.3 are capable of providing service lives in excess of 200 years, and that fly ash mix designs with silica fume performed the best.

Cracks were formed in concrete prisms to mimic cracking in pretensioned concrete piles. Mix designs with fly ash and those with slag self-healed so that the cracks resisted further chloride penetration. Yet, in the several weeks during which self-healing occurred, sufficient chlorides penetrated to the depth of reinforcement to initiate corrosion.

The following two mix designs are proposed for construction of test piles; both were found to have excellent resistance to chloride ingress, carbonation, and sulfate attack.

Mix F25-S5		Mix S50-MK5	
Material	Weight (lb/yd^3)	Material	Weight (lb/yd^3)
Water	285	Water	285
Type I/II cement	665	Type I/II cement	428
Class F Fly Ash	238	Slag	475
Silica Fume	48	Metakaolin	48
Natural Sand	866	Natural Sand	866
#67 Stone	1,905	#67 Stone	1,905
Admixture	oz./yd^3	Admixture	oz./yd^3
AEA 14	9.5	AEA 14	9.5
V2100	54.0	V2100	52.2

The research presented in Volume 2 on corrosion resistance and mechanical properties of six grades of high-strength stainless steel showed that grade 2205 stainless steel wire and strand showed excellent promise to mitigate corrosion; it is recommended

for trial use as reinforcement in prestressed concrete bridge substructures exposed to marine environments. The combination of high-performance marine concrete and stainless steel reinforcement is expected to provide piles with well over a 100-year life.

(This page intentionally left blank.)

Acknowledgements

The research reported herein was sponsored by the Georgia Department of Transportation through Research Project Number 10-26, Task Order Number 02-78. Mr. Paul Liles, Assistant Division Director of Engineering, Mr. Myron Banks, Concrete Engineer, Mr. Mike Clements, Bridge Maintenance Engineer, and Ms. Supriya Kamatkar, Research Engineer, of GDOT provided many valuable suggestions throughout the study. The opinions and conclusions expressed herein are those of the authors and do not represent the opinions, conclusions, policies, standards or specifications of the Georgia Department of Transportation, the Federal Highway Administration, or of other cooperating organizations.

Mr. Daniel Schuetz assisted with the production of the corrosion test specimens and materials testing.

(This page intentionally left blank.)

Table of Contents

Executive Summary ii

Acknowledgments iii

Table of Contents iv

Chapter

1. Introduction 1-1

2. Background – Concrete 2-1

3. Forensic Investigation 3-1

4. Mix Design Development and Mechanical Properties 4-1

5. Chloride Ingress Resistance 5-1

6. Sulfate Resistance 6-1

7. Carbonation Resistance 7-1

8. Conclusions and Recommendations 8-1

Appendices

A: Georgia Coastal Bridge Inspection A-1

B: Interview Summaries B-1

C: Chloride Ingress Results C-1

D: Carbonation Testing Results D-1

E: Sulfate Attack Resistance Testing E-1

F: Self-Healing Investigation Results F-1

G: High Performance Marine Concrete For Coastal Georgia: Usage Conditions G-1

References R-1

(This page intentionally left blank)

CHAPTER 1

Introduction

1.1 Purpose and Objectives

The overall purpose of this research was to determine methods which may be applied economically to mitigate corrosion of reinforcement in precast prestressed concrete piles in Georgia's marine environments. The overall goal is to improve the durability of bridge piles so that a design life of 100 years may be achieved. The research was divided into two parts, reported here in volumes 1 and 2: (1) to develop and evaluate concrete mix designs to prolong service lives of precast prestressed concrete piles in aggressive marine environments, and (2) to assess the potential of using stainless steel for prestressing reinforcement and to compare the strength and corrosion resistance of stainless steel strand to conventional prestressing strand.

The research presented in Volume 1 was focused on increasing the resistance of high performance concrete (HPC) mix designs to the various deterioration mechanisms present in coastal exposures. HPC differs from high strength concrete (HSC), in that high performance concrete encompasses any concrete meeting particular performance requirements (strength, durability, workability), where as HSC is purely based upon a strength requirement. In particular, the research focused on five primary objectives:

1. Determine and quantify environmental conditions in marine environments in Georgia, as well as design details and construction practices, which may limit service life of reinforced concrete elements

2. Establish properties of current HPC mix designs in use as a basis for comparison with proposed designs
3. Investigate the resistance of new high performance marine concrete (HPMC) mix designs to chloride ingress, sulfate attack, and carbonation resistance
4. Investigate the potential for the self-healing of cracks in HPMC and the effect on chloride ingress in cracked sections under prestressing forces
5. Provide recommendations and draft design standards for HPMC mix designs for concrete piling

1.2 Need for Research

Nearly 53% of the United States population lives in coastal counties and the growth rate is increasing (Crossett, et al., 2004). The increase in population has led to an increased demand for infrastructure in coastal counties. Additionally, there is an increase in the relative frequency of natural hazard occurrences, including hurricanes and flooding, that leads to an increased likelihood of infrastructure interacting with water or seawater during its service life (UNEP, 2005).

Over 13% of the 595,000 bridges in the United States are classified as structurally deficient according to the Federal Highway Administration (FHWA). Studies have indicated that 15% of the structural deficiencies reported are the results of corrosion. An estimated amount of $4 billion is spent annually to maintain and replace corroded bridge structures (Koch, et al., 2008). The indirect costs of corrosion are estimated to be an additional $50 to $200 billion annually, due to increased traffic, bridge closures, and affected businesses. The FHWA is proposing to require all new construction be designed

for a 75 to 100 year lifespan (Koch, et al., 2008); however, current design methods and construction practices are proving unable to meet this requirement.

The deterioration of concrete structures in marine environments has become an area of concern after several Georgia Department of Transportation structures in coastal environments have shown extensive deterioration after only 30 years of service. Figure 1.1 presents the substructure status of concrete bridge substructures over bodies of water in Georgia, where it was found that 29.3% of the bridges showed damage to the substructure. The concrete bridges can experience damage due to multiple deterioration mechanisms, including chemical, physical, and biological attack. This deterioration leads to reductions in mechanical properties, serviceability, and aesthetics of the structure.

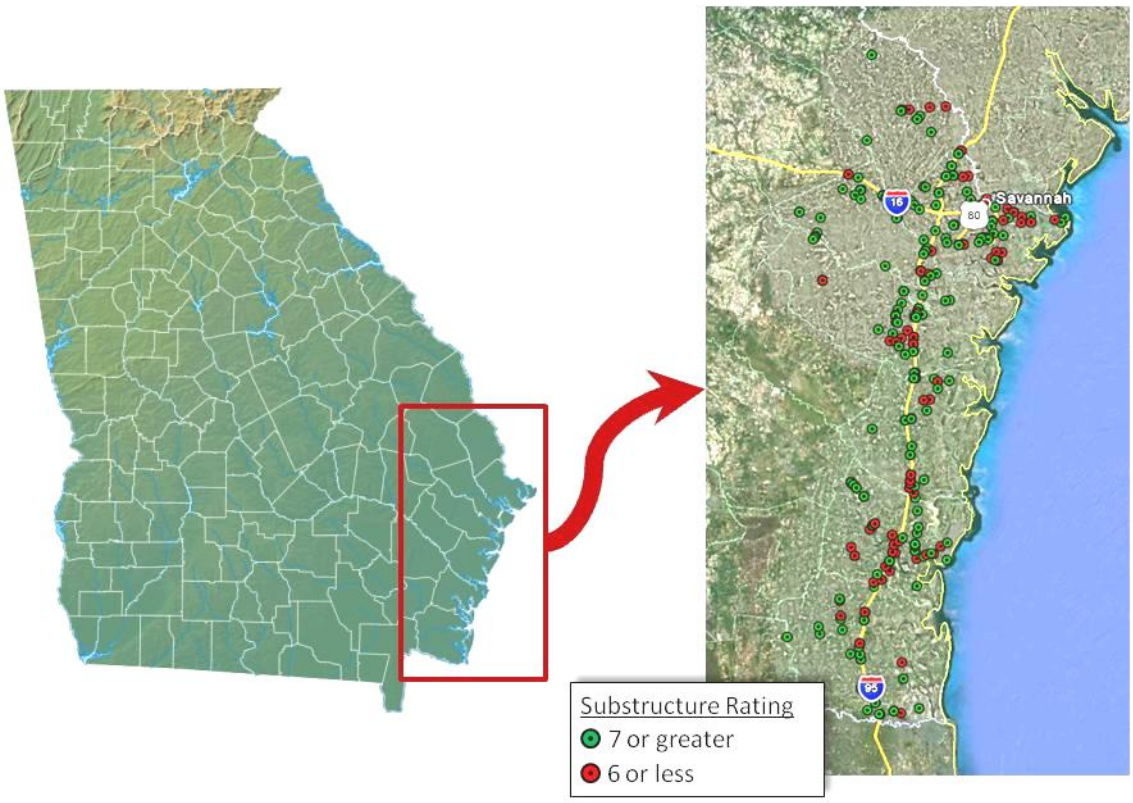

Figure 1.1: Deterioration of bridge substructures in Georgia's coastal counties

In order to develop and construct durable bridge structures capable of providing a 100+ year lifespan, it is critical to fully understand the degradation mechanisms present in Georgia's marine environment. After the durability concerns were identified, mix designs were developed and tested for their performance when subjected to a marine environment and life cycle modeling performed to ensure a 100+ year lifespan.

1.3 Scope

The scope of the experimental program is presented in the flowchart in Figure 1.2. Two phases of work were conducted. First, a series of tasks was conducted to characterize the durability concerns for prestressed precast concrete piles exposed to marine environments. This objective was completed by performing a thorough literature review (Chapter 2), reviewing bridge inspection reports and visiting bridge sites (Appendix A), and performing a forensic investigation of piles from a decommissioned bridge substructure (Chapter 3).

Based upon the findings, a second series of experiments was performed to develop and evaluate the durability characteristics of mix designs exposed to a marine environment. The research investigated the use of binary and ternary blend cements utilizing supplementary cementitious materials (SCM's) to accomplish adequate chloride, sulfate, and carbonation resistance. Coatings, corrosion inhibitors, and other admixture mitigation techniques were not considered. Ten potential HPMC mix designs were cast in addition to two control mix designs representing the current GDOT high performance concrete mix design and one Portland cement concrete mix without SCM's.

Mechanical property testing was performed on the mix designs for compressive strength gain behavior and elastic modulus to determine their suitability with current strength requirements and service life estimator equations. Durability testing was performed for carbonation using an accelerated test method and existing modeling techniques utilized for predicting corrosion initiation due to decreased pH. Chloride ingress resistance was characterized on samples using accelerated and long-term exposure techniques, and the results were used for predicting usable service lives of structures.

The results of the durability assessment were used to develop service life estimates using existing modeling techniques. For service life modeling, only single contaminate ingress due to diffusion was considered. Additionally, for research conducted on self-healing of cracks, only autogenous healing due to continued hydration of cementitious phases and calcium carbonate formation were investigated. The use of encapsulated materials and biological self-healing was not included in this investigation. Biological attack was not considered in the development of HPMC mix designs.

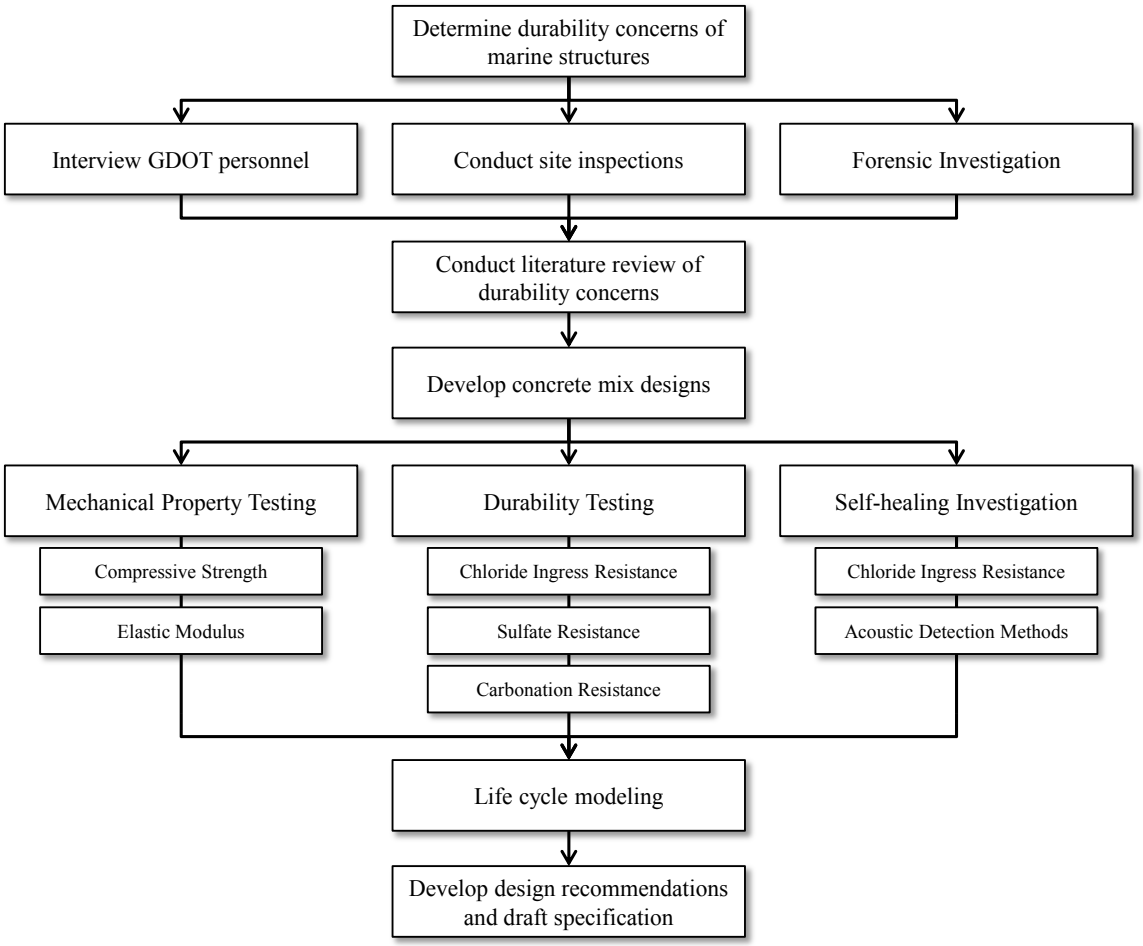

Figure 1.2: Scope of experimental program

1.4 Organization of Dissertation

Chapter 2 presents the results of a literature review into the degradation mechanisms of chloride induced corrosion, carbonation, sulfate attack and biological attack which are present in marine structures, as well as the influence of cracks and self-healing on durability. Areas where additional research is necessary are identified.

Chapter 3 presents the results of a forensic investigation into the degradation mechanisms present in the decommissioned piles from the I-95 at Turtle River Bridge.

Chapter 4 introduces the development of potential HPMC mix designs, the mixing procedure and raw material properties, and mechanical properties of each mix design, including compressive strength gain and elastic modulus.

Chapter 5 presents the results of chloride ingress resistance testing of potential HPMC mix designs utilizing accelerated and long-term ponding procedures and service life modeling based upon the experimental findings.

Chapter 6 presents the findings of studies into the sulfate resistance of potential HPMC mix designs utilizing expansion and strength degradation measurements and investigates changes to composition of each mix design when subjected to a sulfate rich environment.

Chapter 7 presents the results of carbonation resistance testing of the potential HPMC mix designs and service life modeling based upon the experimental findings utilizing existing techniques.

Chapter 8 provides a summary of the research performed and its primary conclusions. Recommendations for the implementation of HPMC for the production of durable prestressed concrete piles and areas requiring future research are given.

Appendices include the results of coastal bridge inspections, GDOT personnel interviews, proposed HPMC usage conditions, and a list of references for all chapters.

(This page intentionally left blank.)

CHAPTER 2

Background Information

2.1 Deterioration Mechanisms of Concrete Piles in Marine Environments

Concrete structures exposed to marine environments are subjected to multiple deterioration mechanisms. The reinforcing steel, aggregate, and paste all have the potential for degradation under the environmental conditions present. Figure 2.1 shows the typical degradation mechanisms that occur in marine environments.

Prestressed concrete piling in coastal exposures is subjected to biological, physical, and chemical attack. From the forensic investigation (Chapter 3), the durability concerns identified included chloride ingress and chloride induced corrosion (Section 2.2), carbonation of concrete and carbonation induced corrosion (Section 2.3), sulfate attack of concrete (Section 2.4), biological attack of concrete (Section 2.5), and the self-healing of cracked concrete (Section 2.6). Reinforcement corrosion is amplified in Chapter 2 of Volume 2 of this report.

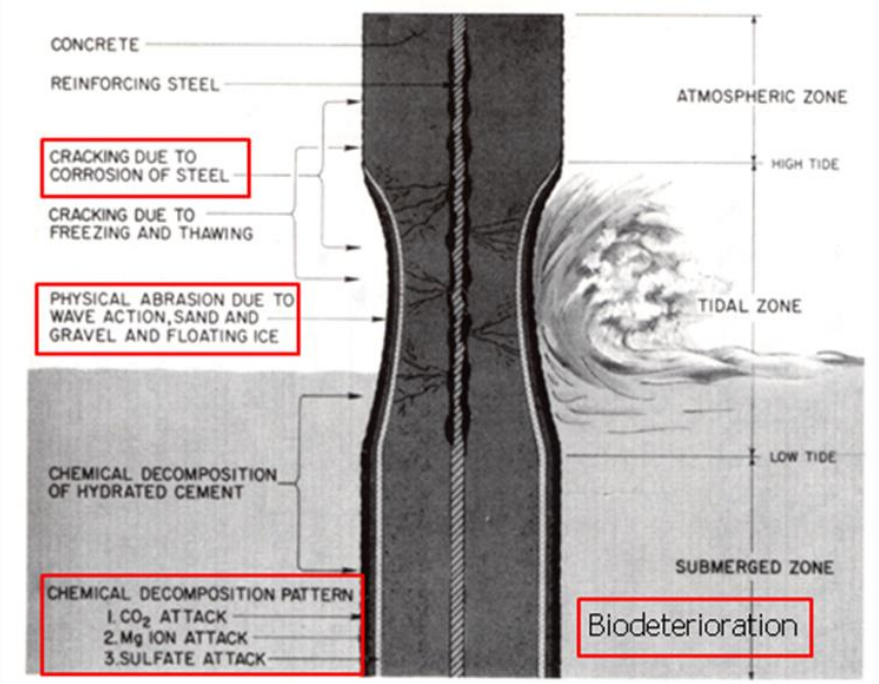

Figure 2.1: Typical degradation mechanisms in coastal concrete piling (Mehta, 1991)

2.2 Chlorides in Concrete

The ingress of chlorides into reinforced concrete is an important concern for the durability of prestressed concrete piles. The rate of ingress and concentration of chlorides at the steel reinforcement depth can dictate the usable service lives of structures by inducing damage by the corrosion of prestressing steel (ACI 222, 2001). Figure 2.2 demonstrates life cycle model for estimating the service life of a structure, where the initiation period is the length of time for chlorides to ingress to the reinforcement and initiate corrosion, and the propagation period is the length of time after initiation before the structure must be replaced.

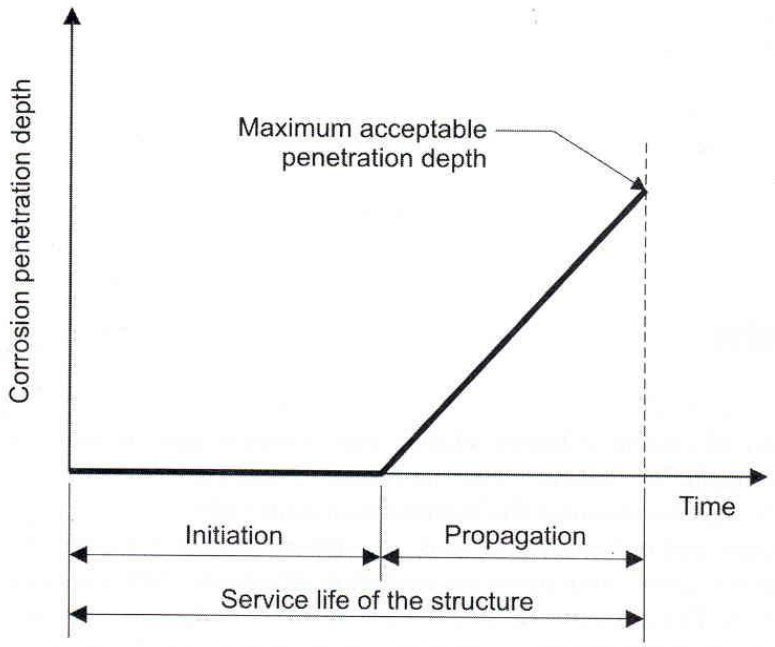

Figure 2.2: Service life model for corrosion induced damage (Bertolini, et al., 2004)

2.2.1 Sources of Chlorides

Chlorides can be introduced into concrete from either internal or external sources. Internal sources of chlorides could include the use of sea water for mixing water, dredged aggregate, aggregate washed with sea water, and chloride containing admixtures (Bertolini, et al., 2004). External chlorides typically occur from environmental factors. Typical external sources are from the ingress of seawater in marine environments, and from the use of deicing salts containing chlorides in colder climates (Bertolini, et al., 2004). Additionally, concrete may be exposed to chlorides if used in industrial applications where chemicals may contain chlorides, like dry-cleaning facilities, paper mills, and aquariums (Bertolini, et al., 2004).

2.2.2 Transport Mechanisms

External chlorides ingress into concrete occurs through several transport mechanisms. Three primary forms of transport occur in concrete: diffusion, permeation, and absorption (Stanish, et al, 1997). Additionally, the binding of chlorides can affect these transport mechanisms (Bertolini, et al., 2004). For life cycle modeling, typically only diffusion-based transport is considered (Rodriguez, 2001). Additionally, the models to be used do not account for the presence of other ions on the ingress of chlorides.

2.2.2.1 Chloride Diffusion

The primary form of ingress through the bulk of the concrete is through diffusion, often modeled to Fick's second law (Bertolini, et al., 2004). Diffusion occurs due to the presence of a concentration gradient, where ions flow from areas of high concentration to low concentration (Stanish, et al., 1997). Fick's second law is given in Eq. 2.1 for non-steady state conditions.

$$\frac{\partial C}{\partial t} = D_{eff} \frac{\partial^2 C}{\partial x^2} \qquad \text{(Eq. 2.1)}$$

Solving this equation using the boundary conditions that the surface concentration is constant, initial concentration is zero, and that infinite points are zero, yields Eq. 2.2. This solution to Fick's second law is often used to model the ingress of chlorides into concrete, and neglects other transport mechanisms present (Rodriguez, 2001). The diffusion coefficient is a material property, and can be determined using several methods (Section 2.2.4). The water to cement ratio, cement chemistry, and age of the structure

have large effects on the diffusion coefficient, and are discussed in Section 2.2.5 (Suryavanshi, et al., 2002).

$$\frac{C(x,t)}{C_o} = 1 - \text{erf}\left(\frac{x}{\sqrt{4 * D_{eff} * t}}\right) \qquad \text{(Eq. 2.2)}$$

Where,

$C(x,t)$ = chloride concentration, measured at depth x and exposure time t, mass %

C_o = initial chloride-ion concentration of the cementitious mixture prior to submersion in the exposure solution, mass %

x = depth below the exposed surface (to the middle of a layer), m

D_{eff} = effective chloride diffusion coefficient, m^2/s

t = the exposure time, s

erf = error function

$$= \frac{2}{\sqrt{}} * \int_0^z \exp(-u^2)\, du$$

u^2 = $\frac{x^2}{2\sigma^2}$ *where x = datum, σ = standard deviation*

This interpretation of diffusion data is not representative of the exact behavior occurring due to the chlorides ingressing through a non-homogeneous solution, effects of the capillary pore structure (which is prevalent in near-surface concrete) and absorption (section 2.2.2.4), and the effects of chloride binding (section 2.2.2.2).

2.2.2.2 Chloride Binding

Within the concrete, chlorides exist in a free or uncombined form and in bound forms, where they may combine with existing hydration products or unhydrated

cementitious and supplementary cementitious material phases. The bound chlorides do not contribute to corrosion initiation in concrete (Mohammed and Hamada, 2003). In the bound form, the most common product formed is Friedel's salt [$Ca_2Al(OH)_6Cl \cdot 2H_2O$]. The extent of chloride binding that can occur in a mix depends upon the cementitious materials contained in the mix (Mohammed and Hamada, 2003).

2.2.2.3 Chloride Permeation

Permeation occurs due to the presence of a pressure gradient. If an applied hydraulic head exists on one face of the concrete and chlorides are present, they may permeate into the concrete under the pressure gradient. This mechanism requires a large pressure head to cause the flow of chlorides to the depth of reinforcement (Stanish, et al., 1997), which may be present in concrete piping or pressurized containment vessels. The pressure head present on marine bridge structures is rarely large enough to cause any significant chloride transport through permeation.

2.2.2.4 Chloride Absorption

As a concrete surface is exposed to the environment, it will undergo wetting and drying cycles. When water, potentially containing chlorides, encounters a dry surface, it will be drawn into the pore structure through absorption, which is a capillary suction due to surface tension in the capillaries. Absorption is a physical process driven by moisture gradients, and for wetting and drying cycles, the depth of drying is small in high quality concretes. Therefore, absorption is not able to bring chlorides to the depth of reinforcement for a good quality concrete (Stanish, et al., 1997). Absorption differs from

adsorption, which is the adhesion of ions to a surface, and is not a significant cause of chloride ingress in concrete.

2.2.3 Chloride-Induced Corrosion

Concrete's highly alkaline environment (pH >11) allows for the formation of a thin oxide layer on the surface of reinforcing steel. The thin passive film protects the steel from corrosion in alkaline environments. If the passive layer is destroyed, active corrosion will initiate. The passive film can be broken down by decreasing the pH to less than approximately 10 of the surrounding environment, localized attack of the passive film by aggressive ions, or a concurrence of both (Bertolini, et al., 2004). The initiation of general corrosion resulting from a decreased pH is addressed in section 2.3.

Chlorides from the surrounding marine environment are able to ingress into the concrete over time through various transport mechanisms. The protective oxide film that forms on the surface of the steel in the alkaline concrete environment is broken down locally by the presence of a sufficient local chloride concentration, and pitting corrosion can result. Pitting is a localized form of corrosion which initiates when chlorides attack defective sites in the passive film. Two reactions that occur in breaking down the passive film due to chloride ion presence are given below in Eq. 2.3 and Eq. 2.4 (Bertolini, et al., 2004).

$$Fe^{3+} + 6Cl^{-} \rightarrow FeCl_6^{-3} \qquad \text{(Eq. 2.3)}$$

$$FeCl_6^{-3} + 2OH^{-} \rightarrow Fe(OH)_2 + 6Cl^{-} \qquad \text{(Eq. 2.4)}$$

The reactions do not consume the chlorides, and they lower the pH at the pitting site by depleting the OH^- ions in the formation of the relatively less soluble iron oxides. In concrete, the surrounding regions remain alkaline, and hydroxide ions are available in the pore solution which causes the surrounding regions to act as cathodes for the corrosion reactions. As the pit grows, it gains a net positive charge from the hydrogen and metal ions which attract more chlorides into the pit, causing an autocatalytic reaction. At the surface, a porous cap can form from the corrosion products that further allows the pit to grow.

The corrosion of the prestressing steels leads to a loss of steel section. Additionally, the corrosion of steel leads to the formation of iron oxides which are less dense than the original steel and occupy up to 6.5 times more volume. The formation of oxides causes tensile forces in the surrounding concrete which can lead to cracking and delamination of the cover concrete as well as rust staining on the surface of the piles. The cracking and delamination lead to reduced strength of the structural element, as well as greatly lower the resistance of the concrete to further ingress of chlorides and other deleterious substances and lead to accelerated corrosion.

2.2.4 Test Methods for Chloride Durability

Several methods exist for the determination of chloride transport properties in concrete. This section introduces the most common methods and investigates the advantages and drawbacks of each.

2.2.4.1 AASHTO T259: Salt Ponding Test

The AASHTO T259 (1980) test is a long-term test that measures the penetration of chloride into concrete. The experimental set-up consists of three slabs at least 3 in. thick and a having a surface are of 46.5 in^2. The slabs are moist cured for 14 days, and then stored at 50% relative humidity for 28 days. All sides of the specimen are sealed except for the top and bottom face; then the specimen has a 3% NaCl solution ponded on the top surface for 90 days. After the exposure period, the chloride concentrations of 0.5 in. thick sections are determined.

The AASHTO T259 test provides a crude one-dimensional chloride ingress profile; however, the profile attained is the result of multiple transport phenomenon, including sorption, wicking, and diffusion (Stanish, et al., 1997). These transport mechanisms may be present in structures, but the impact of wicking and sorption are amplified in this test method due to its relatively short duration where diffusion may not be the primary transport mechanism (Stanish, et al., 1997). The wicking and sorption can mask the diffusion process, especially in low permeability concretes where the total chloride levels over 90 days can be very small.

2.2.4.2 Bulk Diffusion Test

The bulk diffusion test (ASTM C 1556, 2004) was developed to overcome some of the deficiencies of the salt ponding test for measuring diffusion. Specimens are fully saturated with limewater and sealed on all but one surface at the time of exposure. This helps to prevent initial sorption effects and wicking action during the test (Stanish, et al.,1997). The specimens are exposed to a 2.8 M NaCl solution for a minimum of 35

days. (Note that in the current research, bulk diffusion tests were carried out for 180 days because the permeability of the concrete was very low.)

Profile grinding is performed on the sample after the exposure period. The total chloride concentration of each increment is determined in accordance with ASTM C 1152 (2004). A regression analysis of the results to Fick's Second Law (Eq. 2.2) allows for the determination of an apparent diffusion coefficient. The bulk diffusion test yields a better estimate of the diffusion behavior of a concrete mix; however, the exposure period must be extended to 90 days or more for HPC (ASTM C 1556, 2004).

2.2.4.3 Rapid Chloride Permeability Test

The ASTM C 1202 (2007) Rapid Chloride Permeability Test (RCPT) is an electrical migration test. The test is performed on a 2 in. thick piece of a 4 in. diameter cylinder. The specimen is fully saturated, and subjected to a 60 V DC voltage for 6 hours with one face exposed to a 3% NaCl solution and the other to a 0.3 M NaOH solution. The total charge passed is monitored and used to rate the concrete according to the criterion in Table 2.1. GDOT currently uses the RCPT test as a durability requirement for HPC mix designs with a maximum charge passed of 2,000 coulombs (GDOT, 2004).

Table 2.1: Chloride ion penetrability based on charge passed (ASTM C 1202, 2007)

Charge Passed (coulombs)	Chloride Ion Penetrability
> 4,000	High
2,000-4,000	Moderate
1,000-2,000	Low
100-1,000	Very Low
<100	Negligible

The RCPT measures both permeability and ionic movement. Additionally, the movement of all ions present are measured, not just chloride ions, and can affect the test result (Stanish, et al.,1997). Andrade (1993), Zhang and Gjorv (1991), Roy (1989), and Geiker, et al. (1990) have criticized that high voltage applied leads to an increase in temperature, which increases the charge passed. Additionally, the inclusion of conductive materials like steel fibers and calcium nitrate inhibitors will cause a higher charge to be measured (Stanish, et al.,1997).

The RCPT provides a short-term rating of the permeability of concrete, but the precision of the results can have a coefficient of variation on a single test up to 12.3% (Mobasher and Mitchell, 1988). Despite the drawbacks and limitations, attempts have been made to correlate RCPT results to apparent diffusion coefficients by Thomas and Jones (1996) and Berke and Hicks (1992).

2.2.4.4 Electrical Migration Techniques

The movement of chloride ions can be accelerated through the use of an electrical field. The intensity of this field is often lower than that used by the RCPT to decrease heating of the sample. The movement of ions in a solution subjected to an electrical field is governed by the Nernst-Planck equation (Andrade, 1993) and a simplified version can be used to determine the diffusion coefficient.

Electrical migration tests are typically performed in a two-chamber cell with the concrete sample dividing the two cells, as shown in Figure 2.3. The size of the specimen, applied voltage, and initial concentration of chlorides present in the cathode chamber vary from the multiple versions of this test that have been developed by Streicher and

Alexander (1995), Zhang and Gjorv (1991), Andrade and Sanjuan (1994), McGrath and Hooten (1996) and many others.

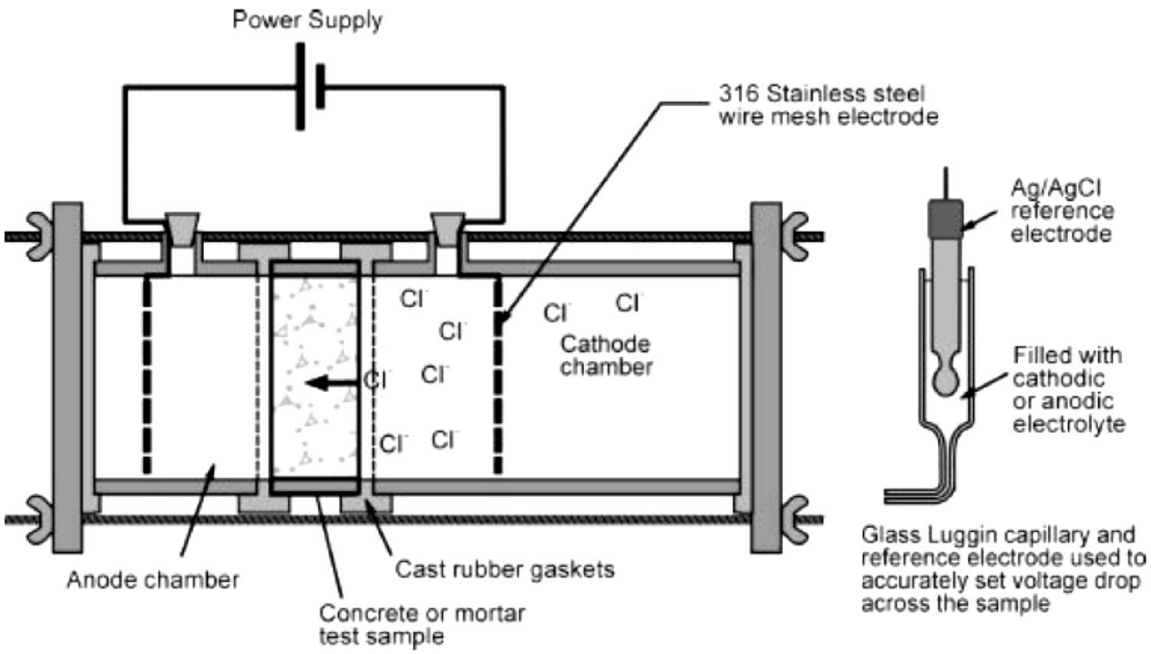

Figure 2.3: Typical chloride migration cell (Stanish, et al., 1997)

The interpretation of the electrical migration tests is different from the RCPT test in that the downstream chloride content in the anode chamber is measured periodically. This ensures that only the movement of chloride ions is considered in determination of the diffusion coefficient. Electrical migration techniques have the same drawback as the RCPT test in that conductive materials will affect the results.

2.2.4.5 Resistivity Techniques

Resistivity measurements are another method for assessing the chloride penetration resistance of concrete. Two methods of resistivity testing are to apply a voltage to a specimen and measuring the current, or the Wenner array probe technique with applies a current and measures the potential.

Resistivity techniques can be rapidly performed and avoid heating of the concrete due to the use of lower voltages (Streicher and Alexander, 1995). However, the conductivity of the pore solution has a large effect on the measured resistance and the methods of accounting for it or standardizing the pore solution during testing are difficult (Stanish, et al.,1997). Resistivity techniques, RCPT and electrical migration tests, are sensitive to the use of conductive materials in the concrete mix design, such as silica fume and certain fibers.

2.2.4.6 Summary

Table 2.2 provides a summary of the test methods described in the previous sections. Each test has strengths and weaknesses in its ability to determine the chloride resistance properties of concrete. For long term tests, the bulk diffusion test appears to be the best technique for accurate determination of diffusion coefficients. For short term, the RCPT and Wenner array probe are the only techniques that have standard versions of the procedure.

Table 2.2: Summary of chloride resistance test procedures

Test Method		Chloride Ion Movement	At a Constant Temperature	Affected by Conductors in Concrete	Approximate Duration
Long Term	Salt Ponding	Yes	Yes	Yes	90 days
	Bulk Diffusion	Yes	Yes	Yes	40-120 days
Short Term	RCPT	No	No	No	6 hours
	Electrical Migration	Yes	Yes	No	Varies
	Resistivity	Yes	Yes	No	30 minutes

2.2.5 Effects of Mix Design on Chloride Durability

Alterations to concrete mix design can drastically affect the chloride ingress properties. The primary parameters with large effects on the diffusion coefficient of concrete are the water to cementitious materials ratio, age at exposure, and the addition of supplementary cementitious materials (SCMs).

2.2.5.1 Water-to-cementitious materials ratio

Polder (1995), Luping and Nilsson (1992), Luping (1995), Bamforth (1993), Collepardi (1972), Diab (1988), Dhir (1990), and Johnson (1996) each investigated the effect of varying water-to-cement ratios on the diffusion coefficient of concrete. The results of these investigations are shown in Figure 2.4. The data show that the diffusion coefficient increases with the water-to-cement ratio. The large spread of values on the graph for the same water-to-cement ratio is due to differences in the mix designs, including aggregate type and content, type of cement used, and maturity before exposure.

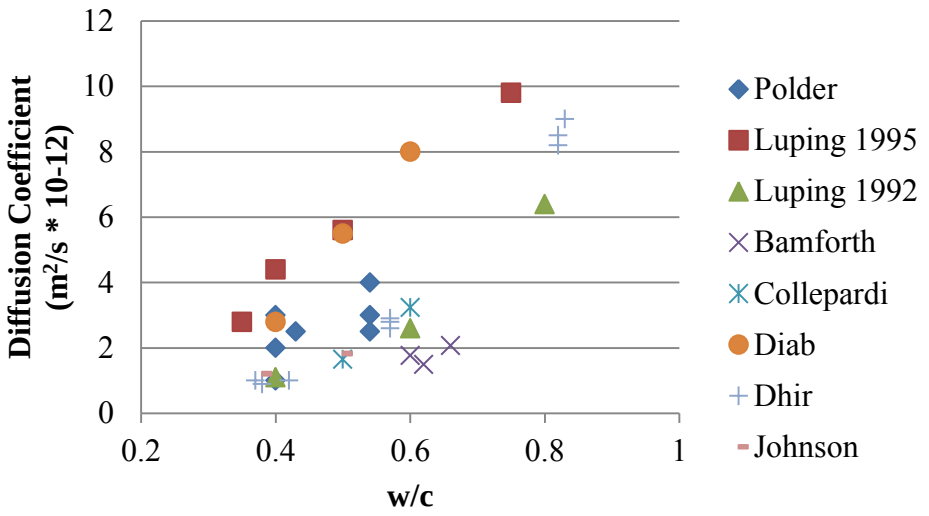

Figure 2.4: Effect of water-to-cement ratio on diffusion coefficient in plain portland cement concrete

2.2.5.2 Age at exposure

The effect of age of exposure on the diffusion coefficient was investigated by Polder (1995), Luping and Nilsson (1992), Kanaya (1998), Pedersen and Arntsen (1998), and Mangat and Molloy (1994), and the results of their studies are shown in Figure 2.5. The data suggest that the diffusion coefficient decreases as the chloride exposure is initiated at later concrete ages. Stanish and Thomas (2003) developed Eq. 2.5 to predict the diffusion coefficient of concrete at any age given that it is known through testing for at least one age. The coefficient, m, for mix designs can be determined experimentally using the procedure developed by Stanish and Thomas (2003) using bulk diffusion tests.

$$D_{avg} = D_{ref}\left(\frac{t_{ref}}{t_{eff}}\right)^{m} \quad \text{(Eq. 2.5)}$$

Where,

D_{avg}	=	average diffusion coefficient at t_{eff}
D_{ref}	=	diffusion coefficient at reference age
t_{ref}	=	reference age of concrete
t_{eff}	=	effective age of concrete
m	=	coefficient based upon mix parameters
	=	0.32 for portland cement, 0.66 for 25% fly ash replacement

Figure 2.6 shows Stanish's estimator equation plotted with the experimental results for diffusion coefficients of plain portland cement concrete mixes. The data suggest the estimator equation provides an accurate estimate of how the diffusion coefficient varies with time. The decreased diffusion coefficient with time suggests that longer curing periods would lead to decreased rates of chloride ingress.

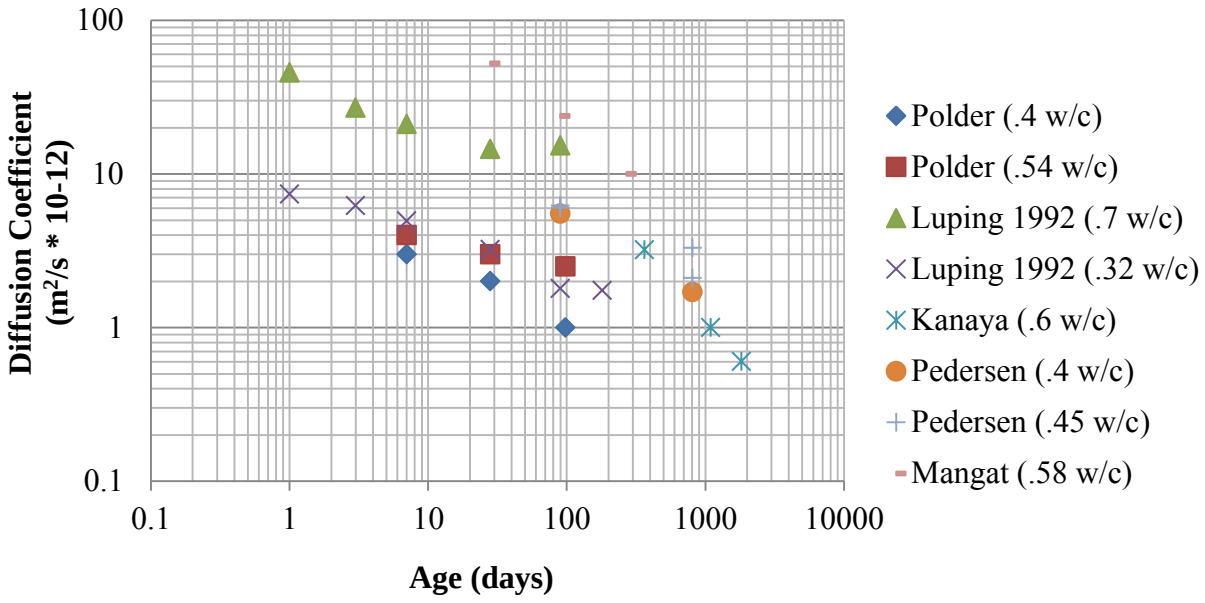

Figure 2.5: Effect of age of exposure on diffusion coefficient in plain portland cement concrete

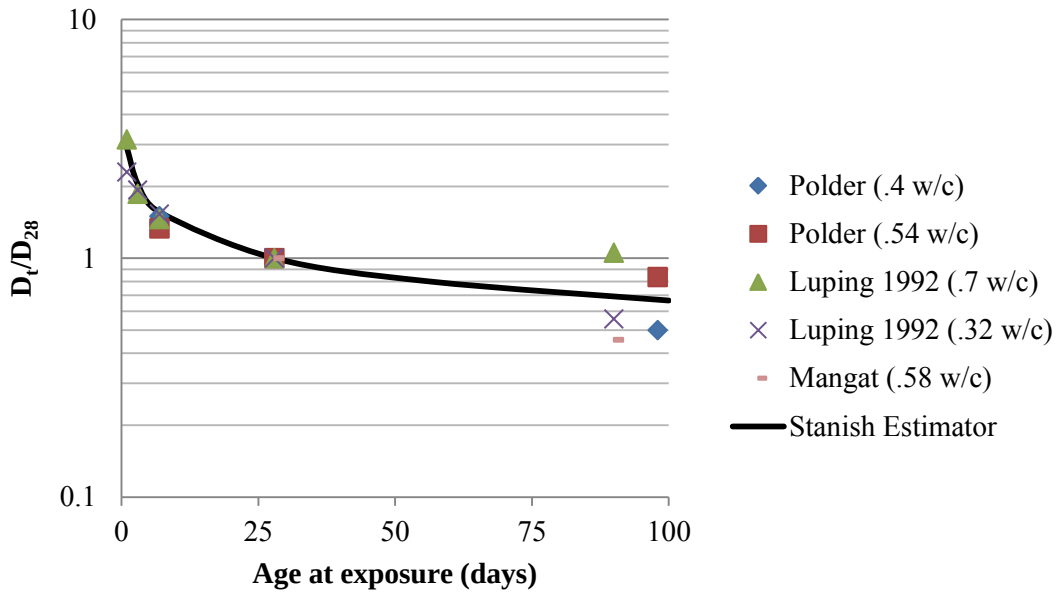

Figure 2.6: Comparison of time dependent diffusion coefficients with estimator equation

2.2.5.3 Supplementary Cementitious Materials

The effect of using SCMs on the diffusion coefficient has been widely studied. The four primary types of SCMs utilized are slag, fly ash, silica fume, and metakaolin. Basheer, et al. (2002), Bleszynski, et al. (2002), Luo, et al. (2003), Mangat and Molloy (1994), Saleem, et al. (2010), Thomas and Bamforth (1999), Thomas, et al. (2008), and Thomas, et al. (1999) investigated the use of slag replacement of cement on the chloride resistance of concrete. It was found that replacement levels over 50% resulted in large reductions in the diffusion coefficient. Thomas, et al. (2008) found that the best performance occurred with a combination of a low w/cm (water-to-cementitious materials ratio) and replacement levels above 40%. It was found that for high w/cm (>0.5) in slag replacement mix designs, salt scaling of samples exposed to wetting and drying cycles was an issue. It was found by Thomas, et al. (2008) that slag causes larger

decreases in the apparent diffusion coefficient over time than a plain portland cement concrete.

Fly ash has been shown to drastically improve chloride ingress resistance by Basheer, et al. (2002), Mangat and Molloy (1994), Papadakis (2000), Thomas and Bamforth (1999), Thomas and Matthews (2004), and Thomas, et al. (1999). Thomas and Matthews (2004) found that like slag, fly ash causes a larger decrease in the apparent diffusion coefficient over time than a plain portland cement concrete. Papadakis (2000) investigated the effect of using a Class F fly ash (low CaO) versus a Class C fly ash (high CaO) and found that both have similar effects, but that a low CaO content leads to a marginally lower diffusion coefficient.

Silica fume has been shown capable of decreasing the diffusion coefficient by orders of magnitude by Bentz (2000), Bleszynski, et al. (2002), Mangat and Molloy (1994), Papadakis (2000), Saleem, et al. (2010), Smith (2001), and Thomas, et al. (1999). Figure 2.7 shows the results of studies performed by Bentz (2000), where the decrease in diffusion coefficient is plotted for various replacement levels of silica fume. This result is in contradiction to the findings of Basheer, et al. (2002), who found that silica fume resulted in an approximately 30% decrease in the diffusion coefficient from a plain portland cement concrete.

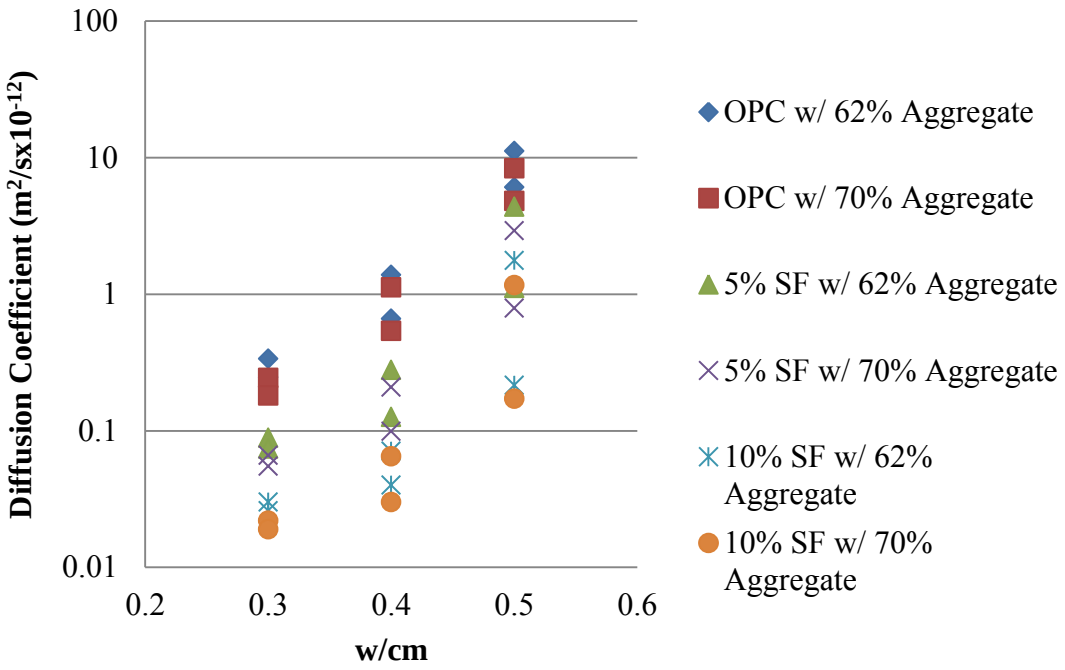

Figure 2.7: Effect of silica fume content on diffusion coefficient

The replacement of cement with metakaolin has been shown to dramatically lower the diffusion coefficient of concrete by Basheer, et al. (2002), Batis, et al. (2005), Gruber, et al. (2001), and Saleem, et al. (2010). Many of the studies compared equivalent replacement levels of silica fume and metakaolin and the results varied on which provided the largest improvement for the same replacement level. Batis, et al. (2005) found that metakaolin replacement levels over 20% will begin to increase the diffusion coefficient, and that the optimum replacement levels are between 8-12%, which was in agreement with the findings of Gruber, et al. (2001).

Saleem, et al. (2010) investigated the use of ternary blends of slag, silica fume, and metakaolin with portland cement with 20% replacement levels of each. The results

showed that ternary blends containing metakaolin and silica fume provided the largest decrease in the diffusion coefficient from control samples.

Thomas, et al. (1999) investigated the use of silica fume and fly ash ternary blend cements and found that the ternary blends provided superior chloride ingress resistance to binary blends. The fly ash provided a long-term decrease in the diffusion coefficient, while silica fume increased early age resistance.

Basheer, et al. (2002) investigated the use of ternary blends containing fly ash or slag with metakaolin or silica fume. The results of the investigation are shown in Figure 2.8. Basheer et al. (2002) concluded that the use of ternary blends resulted in lower diffusion coefficients than binary blends.

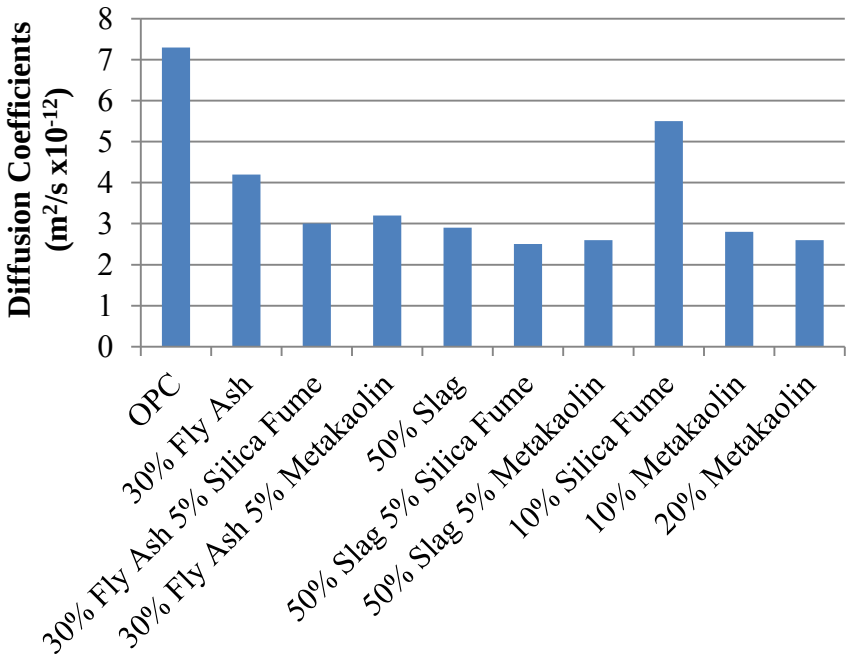

Figure 2.8: Effect of SCMs on diffusion coefficient (Basheer, et al., 2002)

2.3 Carbonation of Concrete

Carbonation of concrete can occur due to the diffusion of carbon dioxide from the atmosphere through the pores of concrete. Carbonation of concrete leads to the depletion of calcium hydroxide, which causes the decrease in pH, and can lead to a loss of calcium silicate hydrate (C-S-H), which is the primary strength giving component of hydrated cement paste (Neville, 1997). Carbonation of concrete can cause strength loss of the concrete and initiate corrosion of reinforcing steel due to the decreased pH (Papadakis, et al, 1991). Additionally, carbonation shrinkage can occur and alter the surface properties and cause cracking near the exposed surface of a structural element (Mindess, et al., 2003).

Eqs. 2.6 to 2.8 show the reactions that occur in the pore solution to cause the decrease in pH (Bohni, 2005). Water has been included as both a reactant and product due to the intermediate step in each reaction where carbonic acid is formed when carbon dioxide and water are together.

$$2NaOH+H_2O+CO_2 \rightarrow Na_2CO_3 + 2H_2O \quad \text{(Eq. 2.6)}$$

$$2KOH+H_2O+CO_2 \rightarrow K_2CO_3 + 2H_2O \quad \text{(Eq. 2.7)}$$

$$Ca(OH)_2+H_2O+CO_2 \rightarrow CaCO_3 + 2H_2O \quad \text{(Eq. 2.8)}$$

The sodium and potassium carbonates formed have a high solubility and remain in solution, but the calcium carbonate has a low solubility and precipitates out of the solution, often filling the pore structure and causing a denser microstructure. The consumption of alkali hydroxyls and dissolution of solid $Ca(OH)_2$ leads to a reduction in

the pH to approximately 8 to 9 (Broomfield, 2007). Once the pH drops to this range at the depth of reinforcing, carbonation induced corrosion will occur as the passive film on the surface of the steel becomes unstable (Broomfield, 2007). Figure 2.9 illustrates a typical distribution of pH with carbonation depth.

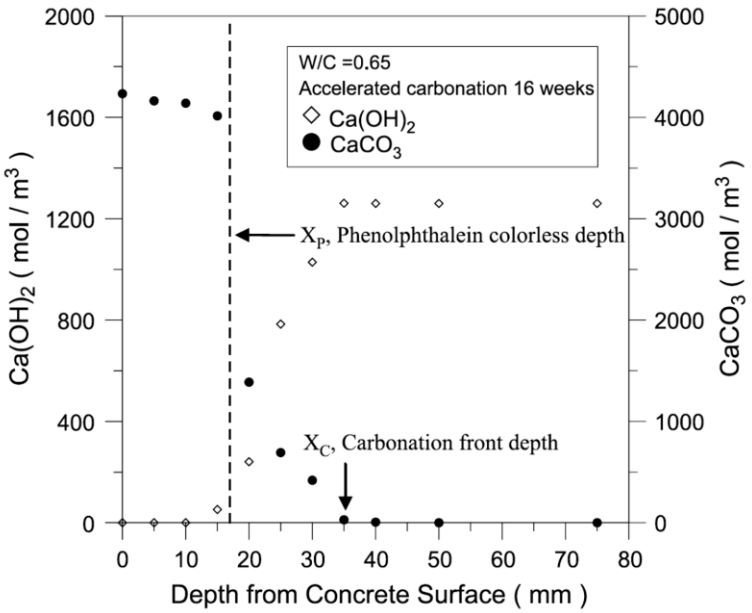

Figure 2.9: $Ca(OH)_2$ concentration as an indicator of carbonation depth measured using thermogravimetric analysis (Chang and Chen, 2006)

With an understanding of the rate of corrosion and how carbonation occurs over time (Section 2.3.1), the time to onset of corrosion can be estimated. The rate of carbonation is greatly affected by environmental factors such as humidity, temperature, CO_2 concentration (Section 2.3.2), and concrete properties (Section 2.3.3).

2.3.1 Carbonation Modeling

Carbonation has been shown to be a diffusion based phenomenon by Papadakis, et al. (1991). A simple model for carbonation is that the depth of ingress is proportional to the n^{th} root of time, as given in Eq. 2.9 (Bertolini, et al., 2004).

$$d = Kt^{1/n} \quad \text{(Eq. 2.9)}$$

Where,

d = depth of carbonation

K = constant

t = time

n = curve fitting factor

Research by Papadakis, et al. (1991) and Papadakis (2000) formed a more sophisticated model that gives a mathematical and physical meaning to the constant, K. A generic form of the Papadakis (2000) model is given in Eq. 2.10.

$$x_c = \sqrt{\frac{2\, D_{e,CO_2}\left(\frac{CO_2}{100}\right)t}{0.33CH + 0.214CSH}} \quad \text{(Eq. 2.10)}$$

Where,

x_c = depth of carbonation

$D_{e,CO2}$ = diffusivity of CO_2 in carbonated concrete, m^2/s

CO_2 = carbon dioxide content of ambient air at concrete surface

t = time, s

CH = estimated calcium hydroxide content

CSH = estimated calcium-silicate-hydrate content

2.3.2 Environmental Conditions

The effect of humidity on carbonation rate is shown in Figure 2.10. The maximum carbonation rate has been shown by Papadakis, et al. (1991) and Bertolini, et al. (2004) to occur at approximately 55-65% relative humidity. At high levels of relative humidity, the void space present in the hydrated cement paste (HCP) is largely filled with water, limiting the transport of carbon dioxide into the concrete. Additionally, at low levels of relative humidity, insufficient water is available in the pores to solubilize CO_2 and $Ca(OH)_2$ which are required for carbonation to occur.

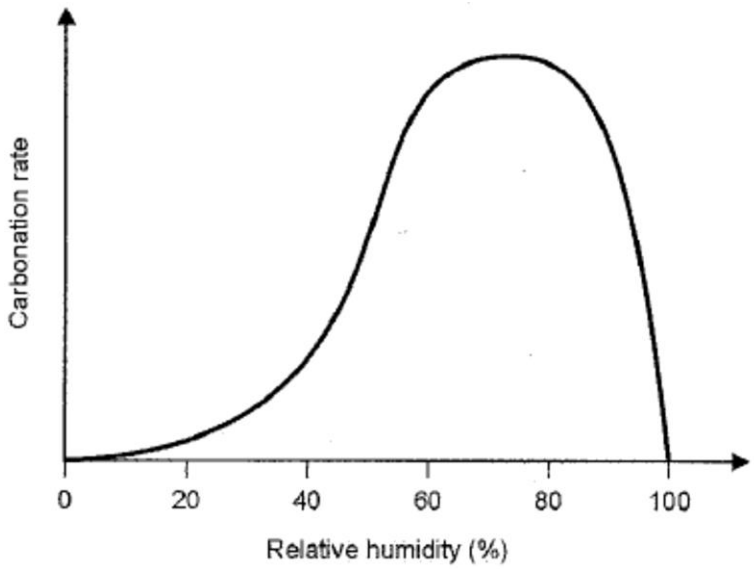

Figure 2.10: Effect of relative humidity on carbonation rate (Bertolini, et al., 2004)

An increase in temperature will cause the carbonation rate to increase (Bertolini, et al., 2004). The CO_2 concentration can have a large impact on carbonation rates. Atmospheric CO_2 levels vary from 0.03% in rural areas, up to 0.3% in industrial and urban areas, and up to 3% in areas such as highway tunnels or power plants (ACI 222, 2001). The concentration of dissolved carbon dioxide in seawater can be up to 15%, and CO_2 reacts with the water to form carbonic acid (Bertolini, et al., 2004).

2.3.3 Concrete Mix Design Effects on Carbonation

The permeability of concrete has a large influence on the rate of carbonation. Decreasing the water-to-cement ratio (w/c) can vary the permeability by orders of magnitude (Papadakis, et al., 1991). Figure 2.11 shows the effect of water-to-cement ratio on depth of carbonation. Research by Bertolini, et al. (2004) and Sulapha, et al. (2003) showed that increased wet curing lengths led to reductions in the rate and depth of carbonation, as shown in Figures 2.11 and 2.12.

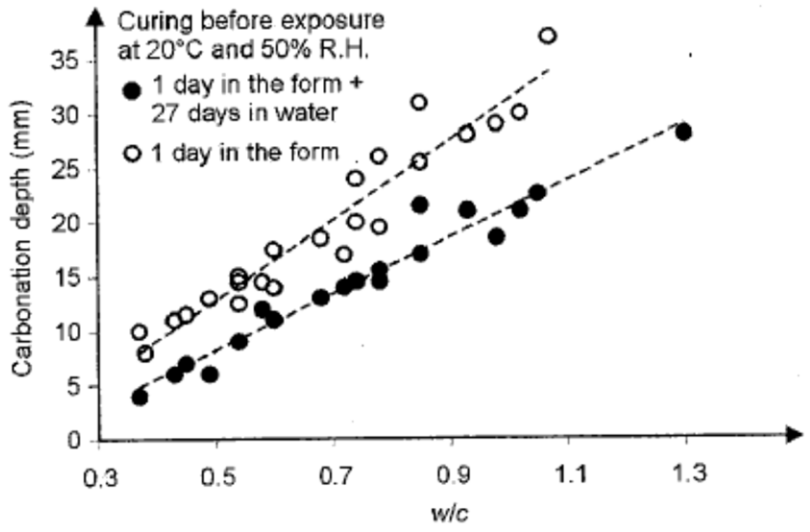

Figure 2.11: Effect of water-to-cement ratio on carbonation depth (Bertolini, et al., 2004)

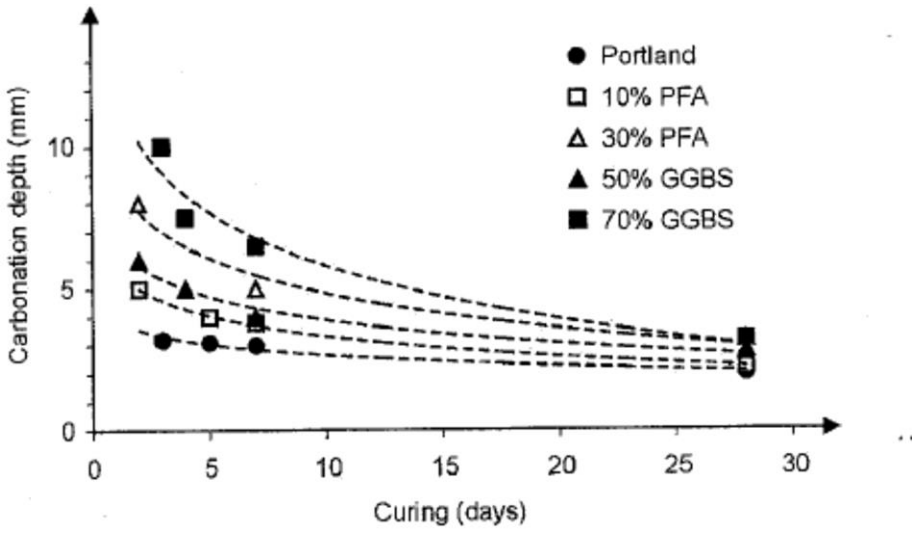

Figure 2.12: Effect of binder composition on carbonation depth (PFA=pozzanlic fly ash, GGBS= ground granulated blast-furnace slag)(Bertolini, et al., 2004)

Also, the binder composition has a large influence on the carbonation resistance. The use of SCMs may decrease the initial pH of the concrete through consumption of calcium hydroxide (CH), but also decreases the permeability by refinement of the pore structure and the creation of secondary calcium silicate hydrate (C-S-H) (Bertolini, et al.,

2004). Research by Atis (2003), Maslehuddin, et al. (1996), Papadakis (2000), Sideris, et al. (2006), and Sulapha, et al. (2003) on concretes utilizing fly ash replacement for cement showed that the carbonation depth increased with increasing the replacement levels. Additionally, Papadakis (2000) demonstrated that the CaO content of fly ash had a negligible effect on the carbonation rate. Slag replacement of cement was shown to increase the carbonation depth by Maslehuddin, et al. (1996) and Sulapha, et al. (2003).

The replacement of cement with silica fume was shown to increase the carbonation depth (as defined by the color change of a phenolphthalein solution) at all ages by Papadakis (2000) and Sulapha, et al. (2003). The results of Maslehuddin, et al. (1996) contradict this finding, and showed that a 10% replacement with silica fume led to a decrease in carbonation rate compared to a plain portland cement concrete. Sulapha, et al. (2003) found that 10% silica fume replacement performed better than fly ash replacement (20-50%) and slag replacement (65%). Additionally, Sulapha, et al. (2003) found that a ternary blend of 10% silica fume and 55% slag replacement performed better than a 55% slag only mixture.

The research performed on carbonation has shown that the addition of slag or fly ash leads to an increase in carbonation depth. However, Sideris, et al. (2006) found that the carbonation rate was lower at later ages for mix designs containing SCMs. This suggests that the decreased pH initially due to CH consumption in the formation of secondary C-S-H may be offset in the long-term by the decreased rate of ingress due to the formation of a more dense matrix with smaller pores in the presence of SCMs.

The research by Sulapha, et al. (2003) on ternary blended cement suggests that ternary blends may offer lower rates of carbonation than binary mix designs. No research on the carbonation resistance of mix designs containing metakaolin cements was found.

2.4 Sulfate Attack

2.4.1 Degradation Mechanisms

Concrete piling in seawater and brackish water can be exposed to high concentrations of sulfates. The primary forms of sulfates present are $NaSO_4$, $MgSO_4$, and $CaSO_4$ (Skalny, et al., 2002). Damage to the concrete due to various reactions between the ingressing sulfate ions and hydration products and anhydrous cement phases in the cement paste is termed "sulfate attack". Two primary mechanisms are associated with sulfate attack. First, sulfate ions can react with monosulfo- aluminate or available tricalcium aluminate (C_3A) to form ettringite. The formation of ettringite can be expansive and lead to cracking and spalling. In addition, sulfate ions may react with available calcium hydroxide to form gypsum. If there is no portlandite present, then the calcium comes from the decomposition of the calcium silicate hydrate phase (C-S-H). The loss of calcium from the C-S-H leads to a reduction in strength (Skalny, et al., 2002).

In the case of magnesium sulfate attack, additional reaction mechanisms are possible. Magnesium sulfate reacts with portlandite to form brucite, in addition to gypsum. Simultaneously, C-S-H is decomposed and converted to an amorphous hydrous silica or magnesium silicate hydrate phase. The decomposition of C-S-H is significantly

faster with exposure to magnesium sulfate compared to sodium sulfate (Skalny, et al., 2002).

The concentration of sulfates has a large effect on the extent and rate of sulfate attack. ACI 201 (2010) provides guidelines for four exposure classes and requirements to protect against each level of exposure. Table 2.3 shows the requirements proposed by ACI 201 for a given sulfate exposure in water. The recommended cement type is based upon an ASTM C 150 (2009) cement designation. Alternatively, the ASTM C 1157 (2011) performance based specification for cements can be used. For the S3 exposure class, ASTM C 1012 (2009) expansion tests must be performed to classify a blended cement or the use of SCMs sufficient for this exposure condition. ACI 201 (2010) does not provide design guidelines based upon the source of sulfates or the cation present, but only on the concentration of sulfate ions.

Table 2.3: Exposure Classes as specified by ACI 201 (2010)

Exposure Class		**Cement Type**	**Exposure (%)**	**w/cm**
S0	Not Applicable	No Restriction	$SO_4 < 0.10$	None
S1	Moderate	Type II	$0.10 \leq SO_4 < 0.20$	w/cm < 0.5
S2	Severe	Type V	$0.20 \leq SO_4 < 2.0$	w/cm < 0.45
S3	Very Severe	Type V + Pozzolan or Slag	$SO_4 > 2.0$	w/cm < 0.40

2.4.2 Test Methods for Sulfate Attack Durability

2.4.2.1 ASTM C 1012 Expansion Tests

The ASTM C 1012 (2009) test is performed on 1 in. x 1 in. x 11.25 in. mortar bars exposed to a 5% Na_2SO_4 solution. Samples are moist cured until the time of exposure, which begins once a minimum strength of 2,850 psi is achieved. The expansion of the bars is measured periodically, typically for 12-18 months. The results are compared with the expansion limits given by ACI 201 (2010) as shown in Table 2.4, which correspond to the equivalent binder compositions recommended for the exposure classes outlined in Table 2.3.

Table 2.4: Maximum expansion percentages specified by ACI 201 (2010)

Exposure Class	**Expansion Percent**		
	6 Months	12 Months	18 Months
S1	0.10%	-	-
S2	0.50%	0.10%	-
S3	-	-	0.10%

The test measures expansion due to ettringite formation, but does not account for strength loss. Additionally, the age at exposure can cause a large variation in the initial expansion. This effect is amplified when comparing portland cement with SCM containing mixtures since the strength gain behavior is altered, and therefore so is the age when the strength criterion is met (Thomas, et al., 1999).

2.4.2.2 Compression Strength Degradation Testing

Mehta (1975), Mehta and Gjorv (1974), Kurtis, et al. (2001), Brown (1981), and Lee, et al. (2005) performed compressive strength testing of paste cubes exposed to sulfate solutions. The tests performed by Mehta (1975), Kurtis, et al. (2001), and Brown (1981) utilized a pH controlled test in a 4% Na_2SO_4 solution that was circulated. Lee, et al. (2005) tested the strength degradation of samples exposed to a 5% Na_2SO_4 solution and a 5% $MgSO_4$ solution.

The test methodology utilized varied; however, the results measured were directly comparable to a material property. Research is necessary to determine if there is a correlation between the strength loss and expansion of samples.

2.4.3 Effect of Binder Composition

Alterations to the binder composition have been shown to improve sulfate resistance of concretes. It has been shown that decreasing the C_3A content will increase sulfate resistance (Mindess, 2003). Additionally, lowering the water-to-cementitious materials ratio will lead to a more resistant mixture (Kurtis, et al., 200) by slowing the rate of sulfate ingress.

For severe exposures including seawater, it has been shown (Mindess, et al., 2003) that the use of a sulfate resistant cement (ASTM C 150 (2009) Type II or V) alone is not sufficient to prevent damage. In a severe environment, a low C_3A content helps to eliminate damage due to ettringite formation and a low water-to-cement ratio helps decrease the rate of ingress, but the CH and potentially C-S-H are vulnerable to attack

(Mindess, et al., 2003). Additionally, Kurtis, et al. (2000) showed that a low C_3S content helps improve sulfate durability.

The use of SCMs as a partial replacement of cement has been shown to produce large improvements in the resistance of binder compositions to sulfate attack. There are two primary causes for the improvement of sulfate resistance by the use of SCMs. First, the "dilution effect" occurs since the addition of SCMs generally reduces the amount of C_3A present in the binder, which leads to less susceptibility to ettringite formation (Sideris, 2006). Second, the "pozzolanic effect" occurs when pozzolanic SCMs react with calcium hydroxide (CH) and water to produce secondary calcium-silicate-hydrate (C-S-H). The formation of secondary C-S-H increases the density of the hydrated cement paste by filling capillary pores, which improves the strength and transport properties (Sideris, 2006). The "pozzolanic effect" occurs slowly and the improvement in durability properties will only occur after adequate time has passed for the materials to react (Odler, 1997).

2.4.3.1 Fly ash

The use of fly ash replacement has been shown to have positive or negative effects on the sulfate resistance, depending on the CaO content. Research by Tikalsky and Carrasquillo (1992) showed that fly ash with high CaO contents increased the risk of sulfate attack compared to a plain ASTM C 150 (2009) Type II cement. Additionally, it was found that the replacement of cement with a low CaO fly ash increased the sulfate resistance. The research of Bonakdar and Mobasher (2010) found that the use of high

CaO content fly ash lead to improved sulfate resistance over portland cement, but that low CaO content fly ashes led to superior resistance.

The research of Mangat and El-Khatib (1995) demonstrated similar findings, and that replacement levels of 0% and 22% with a low CaO fly ash led to dramatic improvement in sulfate resistance, as shown in Figure 2.13. It was found that an 11% replacement level had deleterious effects to the sulfate resistance. Monteiro and Kurtis (2003) demonstrated similarly that replacement levels between 25% and 45% with a low CaO fly ash led to improved sulfate resistance.

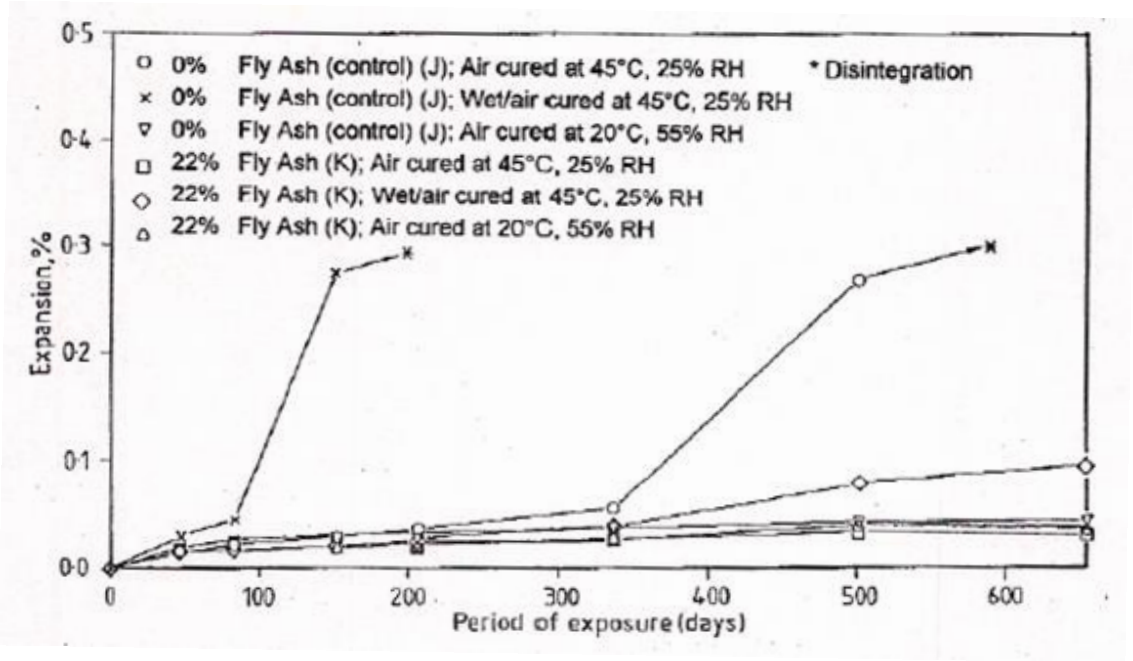

Figure 2.13: Expansion results for cements replaced with fly ash (Mangat and Khatib, 1995)

2.4.3.2 Slag

Research by Mangat and Khatib (1995), Hooten and Emery (1990), and Rozeire, et al. (2009) showed that slag replacement levels above 40% led to dramatic improvement in the sulfate resistance of binders. The results of Hooten and Emery (1990), shown in Figure 2.14, demonstrated that with increasing replacement, the resistance to sulfates increased. The results showed that any replacement level above 40% resulted in samples meeting the 18 month expansion limit given by ACI 201 (2010).

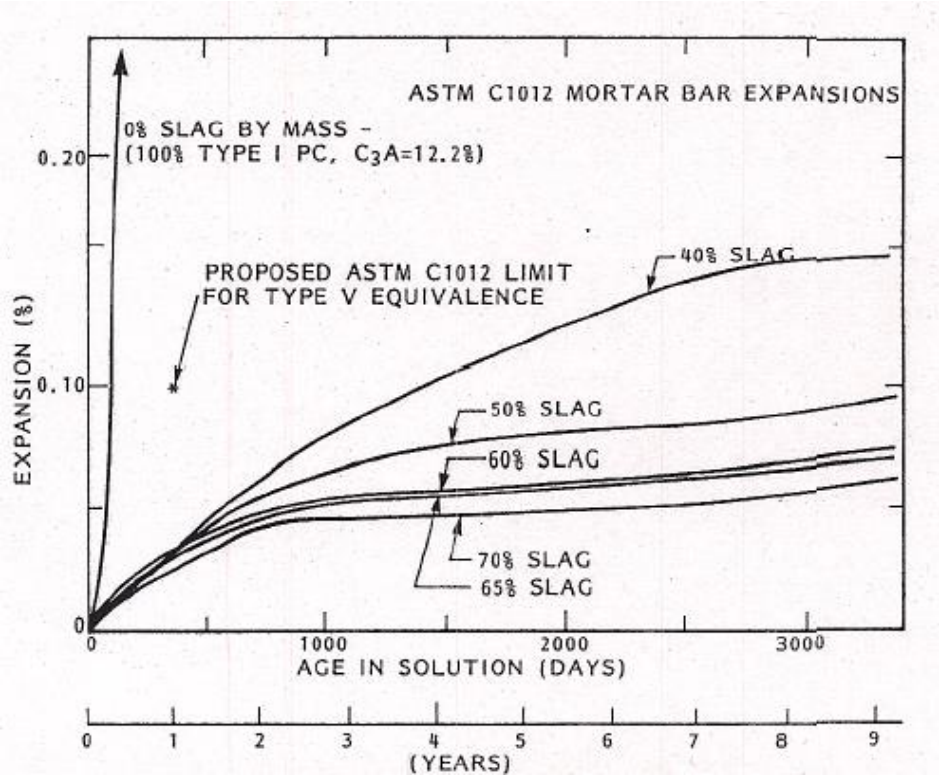

Figure 2.14: Expansion of slag cements exposed to 50,000mg/l Na_2SO_4 solution (Hooten and Emery, 1990)

2.4.3.3 Silica Fume

The expansion of silica fume blended cements was studied by Torii and Mitsunori (1994) and Akoz, et al. (1995) and found that replacement levels between 5% and 10% led to increased sulfate resistance. Torii and Mitsunori (1994) found that replacement levels above 10% led to decreasing sulfate resistance.

The strength degradation behavior of silica fume blended cements was studied by Lee, et al. (2005), Al-Amoudi (2002), and Bonen (1993). It was found that silica fume replacement levels of 5% to 10% lead to increased resistance to strength loss to samples exposed to Na_2SO_4 over portland cement, as shown in Figure 2.15. However, silica fume showed increased strength loss compared to portland cement when exposed to $MgSO_4$, as shown in Figure 2.16. Figure 2.17 shows samples after 180 days of exposure. The increased damage observed is attributed to the easier attack of C-S-H due to the decreased CH content of silica fume containing blended cements.

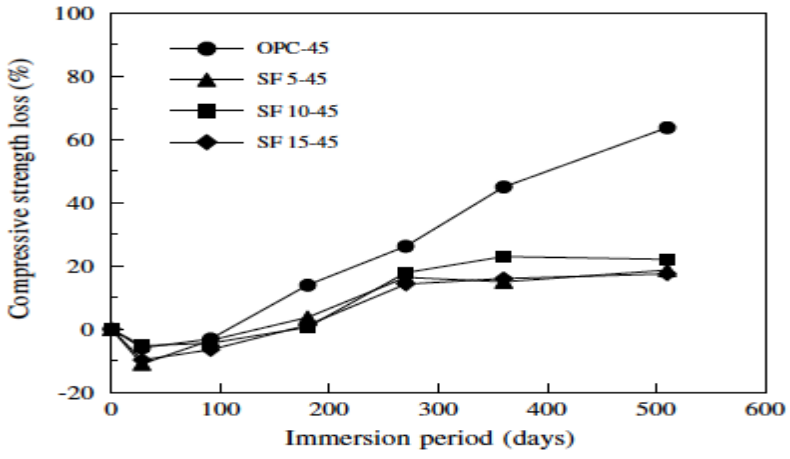

Figure 2.15: Compressive strength loss of silica fume mortars in sodium sulfate (Lee, et al., 2005)

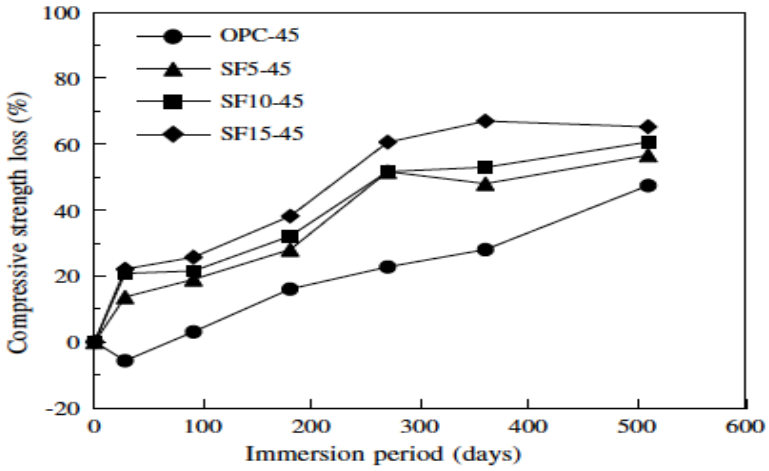

Figure 2.16: Compressive strength loss of silica fume mortars in magnesium sulfate (Lee, et al., 2005)

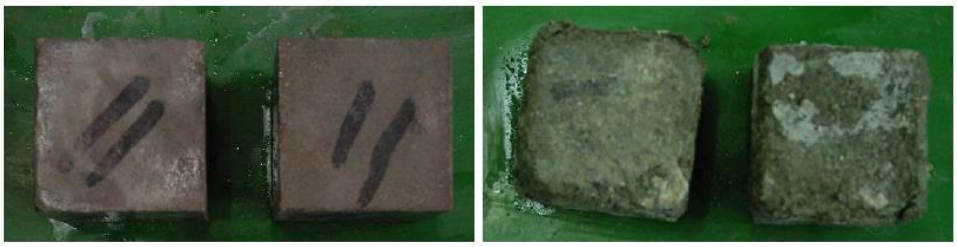

Figure 2.17: 10% silica fume mortars exposed to 5% sodium sulfate (left) and 5% magnesium sulfate (right) (Lee, et al., 2005)

2.4.3.4 Metakaolin

The expansion of blended cements containing metakaolin was investigated by Courard, et al. (2003) and Khatib and Wild (1998) and found that replacement levels above 10% led to improvement of the sulfate resistance. However, a replacement level of 5% led to lowered resistance.

The compressive strength degradation of metakaolin blended cements was studied by Khatib and Wild (1998) and Guneyisi, et al. (2010) and found that replacement levels

above 10% led to increased resistance to strength loss in a Na_2SO_4 solution compared to portland cement. The results of Guneyisi, et al. (2010) are shown in Figure 2.18, where increasing metakaolin content led to increasing sulfate resistance.

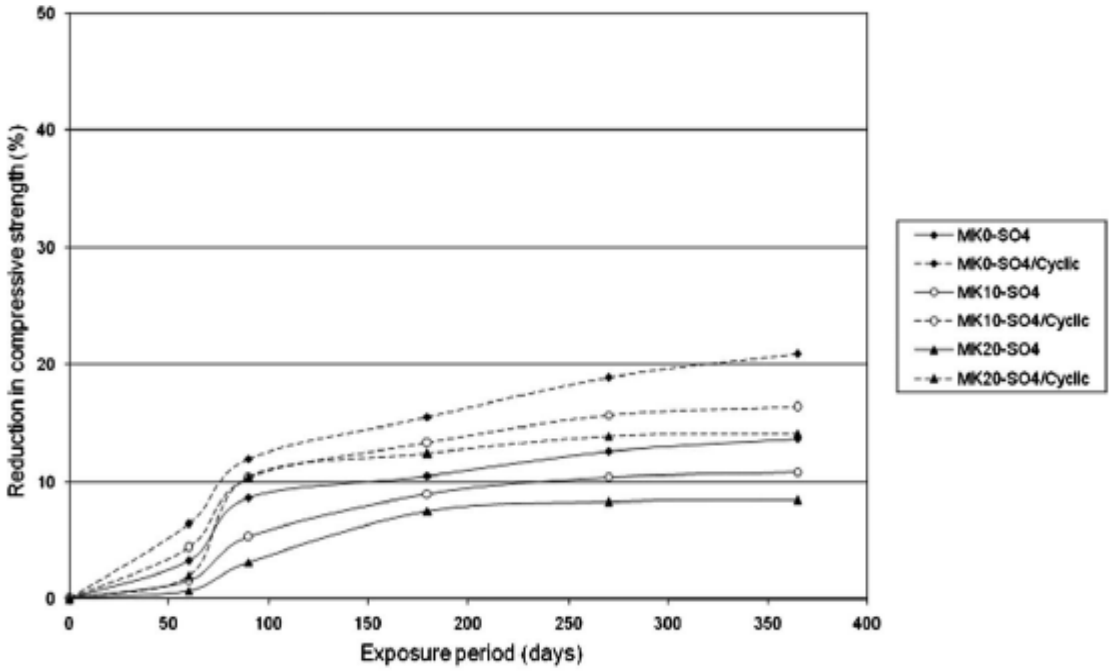

Figure 2.18: Compression strength reduction of metakaolin cements that were water cured (Guneyisi, et al., 2010)

2.4.3.5 Ternary Blends

Thomas, et al. (1999) investigated the use of ternary blended cements containing fly ash and silica fume. The study compared the ternary mix to binary mix designs containing low and high CaO content fly ashes. The expansion results are shown in Figure 2.19, which show that the addition of 3% silica fume to a sulfate susceptible mix (high CaO content fly ash) led to dramatic improvement of sulfate resistance.

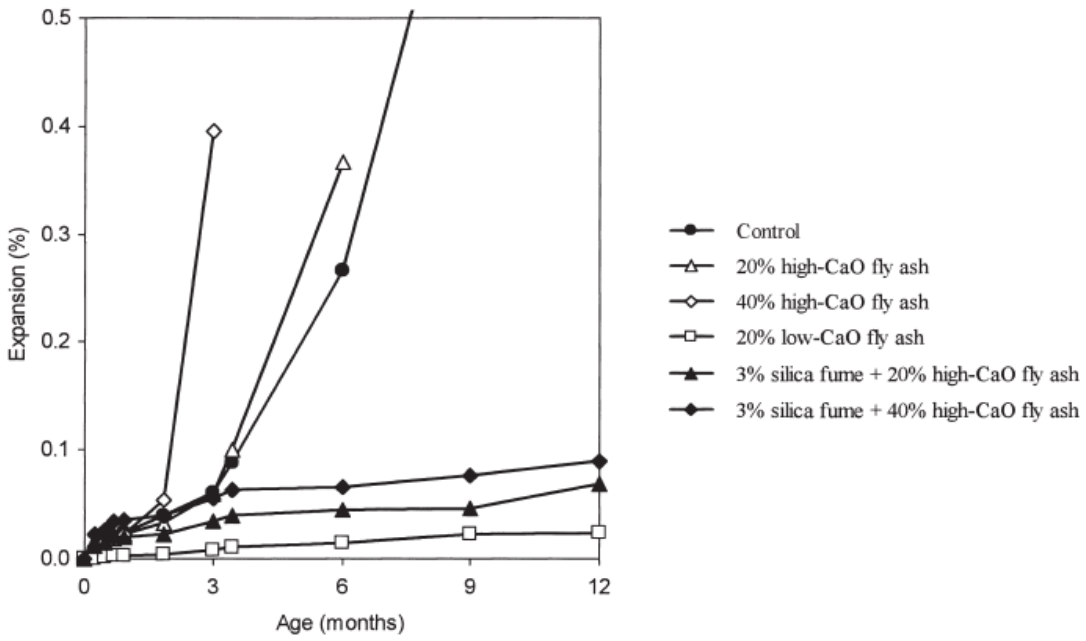

Figure 2.19: Effect of fly ash and silica fume cements when exposed to sodium sulfate (Thomas, et al., 1999)

2.4.3.6 SCMs Summary

Previous research has shown that the replacement levels given in Table 2.5 of SCMs will lead to improved sulfate resistance from a plain portland cement. The research by Thomas, et al. (1999) suggests that the combination of SCMs in ternary mix designs may lead to further improvement of sulfate resistance and needs to be investigated.

Table 2.5: Recommended replacement percentages of SCMs

Material	Class F - Fly Ash	Slag	Metakaolin	Silica Fume
% Replacement	25-35	50-80	5-20	5-10

2.5 Biological Attack

The biological attack on marine structures occurs due to several different organisms and damage mechanisms. Barnacles, mollusks, and sea urchins are known to secrete acids which can deteriorate the concrete and lead to the presence of boreholes (Mehta, 1991). Additionally, Lea (1971) reports mollusks that produce ammonium carbonate, which causes significant damage to concrete. Bacterial degradation of concrete marine structures has been reported due to the presence of anaerobic bacteria, *Thiobacilli*, that produce sulfuric acid which is highly corrosive to concrete and reinforcing steel (Mehta, 1991). Additionally, from the results in Chapter 5 and Scott, et al., (1988), it was identified that the boring sponge, *Cliona*, will attack limestone aggregate in marine structures.

Biological attack may be a concern in prestressed concrete piles, specifically the effect of the boring sponge, *Cliona.* There have been reports of *Cliona* sponges at Gardiner's Island, New York (Nicol and Reisman, 1976), along the coast of Virginia (Hopkins, 1962), Corpus Christi, Texas (Miller, et al., 2010), and off the coast of Jamaica (Scott, et al., 1988).

A reported case of boring sponge attack was reported in Jamaica due to *Cliona lampa* (Scott, et al., 1988). The sponges burrowed through the limestone aggregate of concrete masonry blocks. The damage was primarily at the corners, and irregular shaped bore holes occurred in the aggregate. The sponges use etching secretions to penetrate calcium carbonate and form the boreholes (Nicol and Reisman, 1976). The genus *Cliona* sponges leave silicate spicules near the surface of their borings. The length of the spicules varies by species but is typically between 200 μm to 400 μm (Zea and Weil, 2003). Studies on

the erosion rate of the sponge show that the rate may exceed 1 mm (0.04 in.) per year of ingress in solid limestone (Neumann, 1966). Further research is needed on biological attack of concrete piles including a foundation of knowledge on the species causing attack, the rate and effects of their ingress, as well as methods of preventing and mitigating damage to existing piles need to be assessed.

2.6 Self-healing of Cracked Concrete

The cracking of concrete can have a large influence on the transport and durability behavior of structures. Cracks increase the penetrability of concrete, reduce concrete strength, decrease aesthetics of structures, and may indicate deterioration of the structure (Rodriguez, 2001). As discussed in Chapter 5, piles in marine environments are primarily susceptible to reflective tensile cracking due to driving and to flexure cracking during handling and placement.

Corrosion in cracked concrete starts either in the crack zone or in the area adjacent to the crack. Figure 2.20 from Rodriguez (2001) demonstrates the two following corrosion mechanisms that can be observed:

- The anodic and cathodic reactions take place in the crack. The anodic and cathodic areas are small and located close to each other and cause microcell corrosion where the oxygen required is provided by the crack.
- The reinforcement in the crack zone is anodic, and the passive steel surface adjacent to the crack acts as the cathode, forming a macro corrosion cell. The

steel surface involved in the cathode reaction is typically larger, causing a higher corrosion rate.

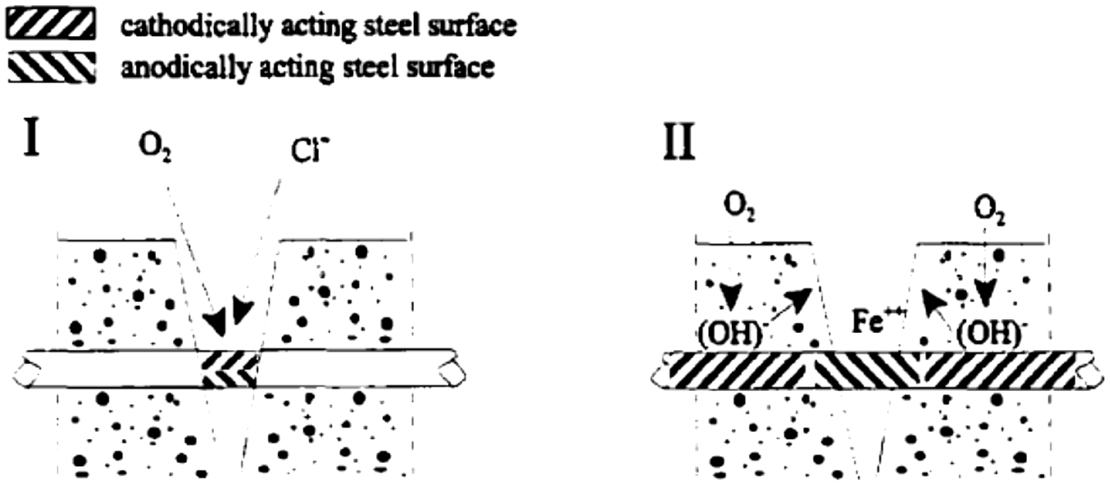

Figure 2.20: Two types of corrosion processes in the region of cracks (Rodriguez, 2001)

It has been reported by many authors that corrosion in cracked concrete typically occurs as a direct result of cracking and the initiation time is reduced compared to uncracked concrete in similar conditions (Suzuki, et al., 1989; Suzuki, et al., 1990; Borgard, et al., 1991; Bentur, et al., 1997; Thursesson, et al., 1997) and the rate of corrosion is typically higher in cracked concrete due to increased availability of oxygen and water (Otsuki, et al., 2000). Additionally, it has been shown that increasing crack width decreased the initiation time for corrosion (Suzuki, et al., 1990). The influence of crack size is presented in section 2.6.3.

2.6.1 Crack Healing Mechanisms

It has been shown that cracks in concrete can self-heal and reduce the penetrability of chlorides into the section (Jacobsen, et al., 1998). Autogenous healing of cracked concrete can occur due to the cementitious material's capability to heal and fill cracks in fractured concrete by (1) the formation of calcium carbonate or calcium hydroxide (Neville, 1997), (2) sedimentation of particles (Edvardsen, 1999), and (3) continuing hydration and swelling of the cement matrix (Neville, 1997). Additionally, research has shown that microbial self-healing (Van Tittelboom, et al., 2010; Biswas, et al., 2010; Jonkers, et al., 2010; De Muynck, et al., 2008; Patil, et al., 2008; Bang, et al., 2001) and encapsulation aided self-healing (Yang, 2009) can occur.

Previous research by Lauer and Slate (1955) and Heide (2005) has shown that the following environmental conditions must be present for self-healing to occur: the presence of water, stability of the crack, and that the liquid may not lead to a leaching or dissolution reaction. Prestressed concrete piles in marine environments provide each of these environmental conditions necessary for self-healing to occur.

2.6.2 Permissible Crack Widths

Of course, the effects of cracking on concrete depend on the crack width and depth. Many existing specifications set recommended values for the maximum chloride content, minimum cover thickness, and maximum tolerable crack width. Crack widths are often limited based upon the exposure environment, and Table 2.6 gives the recommended values by ACI 224 (1998).

Table 2.6: Permissible crack widths for exposure conditions (ACI 224, 1990)

	Tolerable Crack Width	
Exposure Condition	**in.**	**mm**
Dry air, protective membrane	0.016	0.41
Humidity, moist air, soil	0.012	0.30
De-icing chemicals	0.007	0.18
Seawater and seawater spray; wetting and drying	0.006	0.15
Water-retaining structures	0.004	0.10

The recommended values do not form a design guideline that ensures adequate protection for any desired service life. Edvardsen (1999) made recommendations for permissible crack widths ranging from 0.004 to 0.01 in. (0.1 to 0.25 mm) where the results showed that cracks could be expected to almost completely self-heal and have similar flow rates under a pressure head to virgin concrete.

2.6.3 Chloride Ingress into Cracked Concrete

The influence of flexure cracking on chloride ingress has been widely studied. Mangat and Gurusamy (1987) studied chloride diffusion into cracked steel fiber reinforced concrete. Crack widths of between 0.0027 in. (0.069 mm) and .0425 in. (1.08 mm) were produced and samples were subjected to cyclic wetting and drying to represent splash and tidal zone marine exposure. The results showed that the chloride concentration near the cracks increased as the crack width increased. The chloride concentration increase was most pronounced for crack widths 0.02 in. (0.51 mm) and wider.

Raharinaivo, et al. (1986) performed a similar study investigating the influence of crack width on chloride diffusivity in samples submerged in a salt solution. The results

showed that the diffusion coefficient of cracked concrete was one or two orders of magnitude larger than uncracked concrete, and wider cracks resulted in higher diffusion coefficients. Their results contradicted Mangat and Gurusamy (1987) in that even small cracks (approximately 0.004 in. (0.1 mm)) were found to be significant. Rodriguez (2001) asserts that the noticed differences are most likely due to differences in the concrete types utilized.

Francois and Maso (1988) performed a long-term study on concrete beams that were loaded in three-point bending and were exposed to a salt-fog while loaded. Crack widths between 0.002 to 0.02 in. (0.05 to 0.5 mm) were studied. The authors found that chlorides quickly penetrated in the tension zone. It was found that chlorides penetrated through the crack and diffused through the walls of the crack into the surrounding concrete. As part of the same study, Francois and Arliguie (1999) reported that the apparent chloride diffusion coefficient was related to the tensile stress in the reinforcing bar, and could be used as a guideline for evaluation of chloride ingress into concrete subjected to a tensile stress. Konin, et al. (1998) investigated chloride ingress with microcracking due to flexural loads and also found a linear relationship between the chloride apparent diffusion coefficient and the applied tensile stress in the rebar for tensile stresses between 0 to 32 ksi, which agreed with the findings of Francois and Arliguie (1999).

Chloride diffusivity of concrete cracked in flexure was also studied by Gowripalan, et al. (2000). Concrete prisms were cracked in flexure and stressed with bolts to maintain a crack width of 0.0118 in. (0.3 mm) and were ponded in a salt solution for 300 days. Their results found that the apparent chloride diffusion coefficient is larger

in the tensile than in the compression zone. This finding was consistent with the findings of Francois and Maso (1988). The authors proposed that the crack width-to-cover ratio should be used as a performance parameter instead of the crack width alone since the crack width at the surface is not the same as the crack width at the steel with flexure induced cracks.

Edvardsen (1995) investigated the relationship between crack width and water permeability since chloride ions are transported with water. The results of the study showed that the flow of water through cracks is proportional to the cube of the crack width. Additionally, it was found that crack healing significantly reduced the flow of water through the sample. This suggests that self-healing would also limit the flow of chlorides into the section through a crack.

Sahmaran (2007) investigated the chloride diffusivity of cracked concrete with varying crack widths. Specimens were precracked to various widths and subjected to ponding of a salt water solution. The chloride profiles for various crack widths were determined and are shown in Figure 2.21. The relationship between the crack width and diffusion coefficient was found to be a power relation. Additionally, for cracks less than 0.005 in. (0.13 mm), the effect of crack widths on the effective diffusion coefficient was found to be marginal. Cracks with a width less than 0.002 in. (0.05 mm) experienced significant self-healing which further reduced the effective diffusion coefficient.

The research findings on cracked concrete behavior identified that self-healing is a viable mechanism for limiting the ingress of chloride ions into a cracked concrete section.

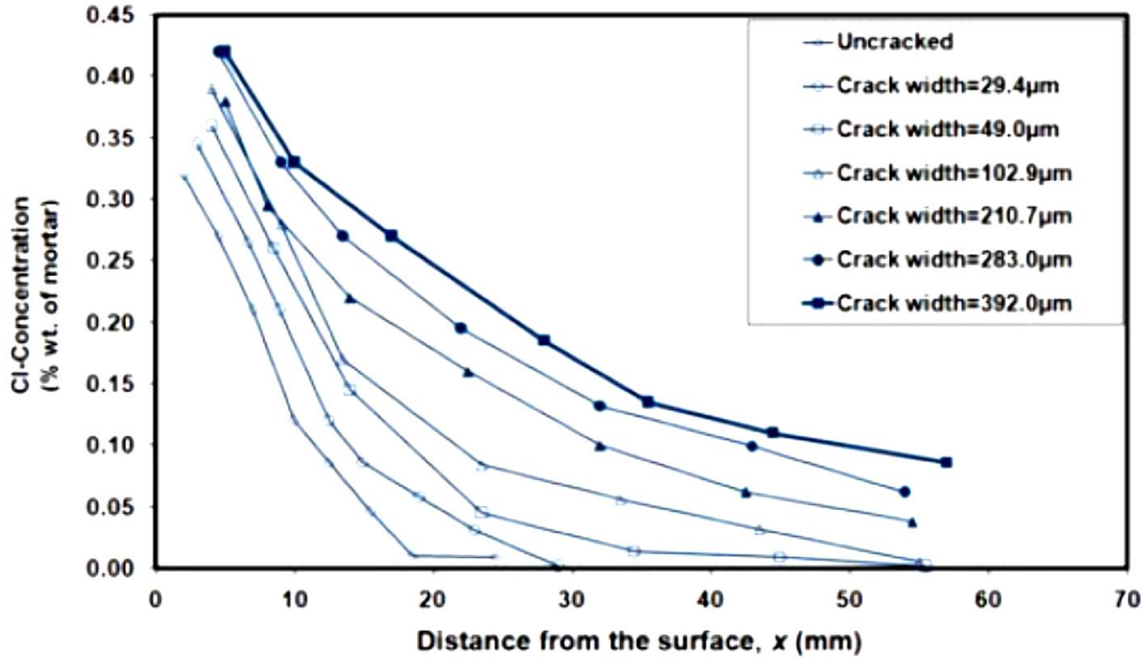

Figure 2.21: Chloride profiles for cracked concrete after 30 days exposure (Sahmaran, 2007)

2.6.4 Self-healing of Cracks

The research findings on cracked concrete behavior identified that self-healing is a viable mechanism for limiting the ingress of chloride ions into a cracked concrete section. Lauer and Slate (1955) performed studies by cracking prism specimens in flexure and holding together with a rubber band and exposing to water then retesting the strength gain across the crack due to self-healing. The investigation revealed that samples experienced larger strength recovery when having a high w/cm and when initial cracking was performed at early ages. Additionally, it was noted that fly ash was detrimental to the healing process and it was hypothesized that this was due to the smaller

amount of CH present, which normally serves as nucleation sites for calcium carbonate which is the primary component of self healing observed.

Research by Ismail, et al. (2008) investigated the ingress of chlorides into cracked sections using an expansive ring to generate controlled crack sizes. It was found that young specimens exhibited greater self-healing and lower effective diffusion coefficients than specimens with the same crack size at later ages, which shows a similar trend to the strength recovery findings of Lauer and Slate (1955).

Jacobsen, et al. (1996) also investigated the chloride resistance of self-healed concrete. Tests were performed by inducing freeze thaw damage into specimens and then allowing them to heal. After healing, electrical migration tests were performed to quantify the effect of self-healing on chloride ingress. It was found that specimens where the cracks (crack width < 0.0004 in (0.012 mm)) were not allowed to heal had ingress rates an order of magnitude higher than virgin concrete. Self-healed cracks exhibited an ingress rate of approximate 25% of the unhealed cracks, but never returned to the rates observed in virgin concrete, which was also found by Parks, et al. (2010).

Edvardsen (1999) studied the influence of self-healing on water permeability of cracked samples. The research showed that smaller crack widths led to lower flow rates and quicker sealing of cracks, as is shown in Figure 2.22. It was concluded from the study that the primary form of self-healing is the precipitation of calcium carbonate, and that mix design plays a secondary role in self-healing.

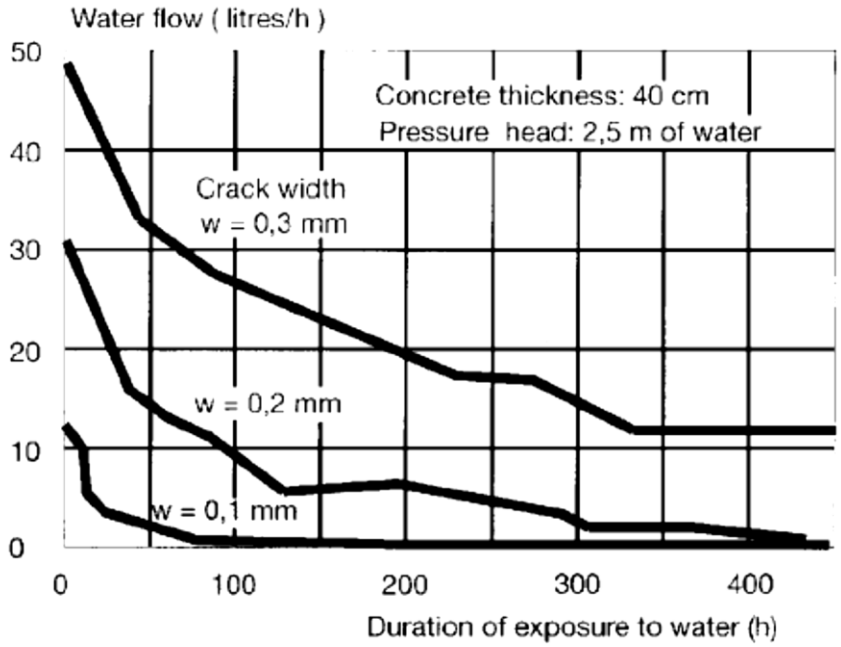

Figure 2.22: Water flow versus duration for different crack widths (Edvardsen, 1996)

Rodriguez (2001) investigated the diffusion of chlorides into cracked concrete sections. Experiments were performed by creating through specimen cracks, sealing of all sides except the top surface, and exposing to a salt water solution. Profile grinding was performed to diagnose 2-D diffusion around crack sites. Results showed that 25% slag replacement specimens were better at resisting chloride ingress in cracked sections than portland cement only specimens. The author noted that more research is needed in the area of flexure cracks with a V-shape.

Heide (2005) investigated the influence of self-healing on strength recovery through the use of artificial flexure cracks. It was found that lower degrees of hydration led to increased self-healing capabilities, which is in agreement with the findings of Lauer and Slate (1955). The author found that mix designs containing slag performed

well on the recovery strength compared to plain portland cement concrete. The author recognized the need for more research on the influence of slag contents on self-healing, as well as the influence of other SCMs.

Termkhajonkit, et al. (2009) investigated the effect of self-healing of shrinkage cracks on chloride ingress. Electrical migration tests were performed on specimens subjected to drying and autogenous shrinkage cracking after 28 and 91 days of moist curing. It was found that 25% replacement of cement with low CaO fly ash had significantly lower apparent diffusion coefficients than plain portland cement samples. The authors identified the need for investigation on the effect of fly ash on the self-healing of larger cracks that are formed at early ages.

Sahmaran, et al. (2008) studied the behavior of high volume fly ash self-consolidating concrete (SCC) subjected to microcracking from compressive loading. Cylinder samples were loaded to 70% and 90% of the max compression stress, then soaked in water for up to 30 days; then the rapid chloride permeability and compressive strength were measured for samples containing 0, 35, and 55% cement replacement with a low CaO fly ash. The results of the study are shown in Figure 2.23. It was found that fly ash samples recovered significantly more of the chloride resistance after 15 and 30 days of healing than plain portland cement concrete samples. It was proposed that the cause of this was that the high volume replacement with fly ash led to unhydrated fly ash being available along the crack surface for self-healing and the formation of secondary C-S-H across the crack.

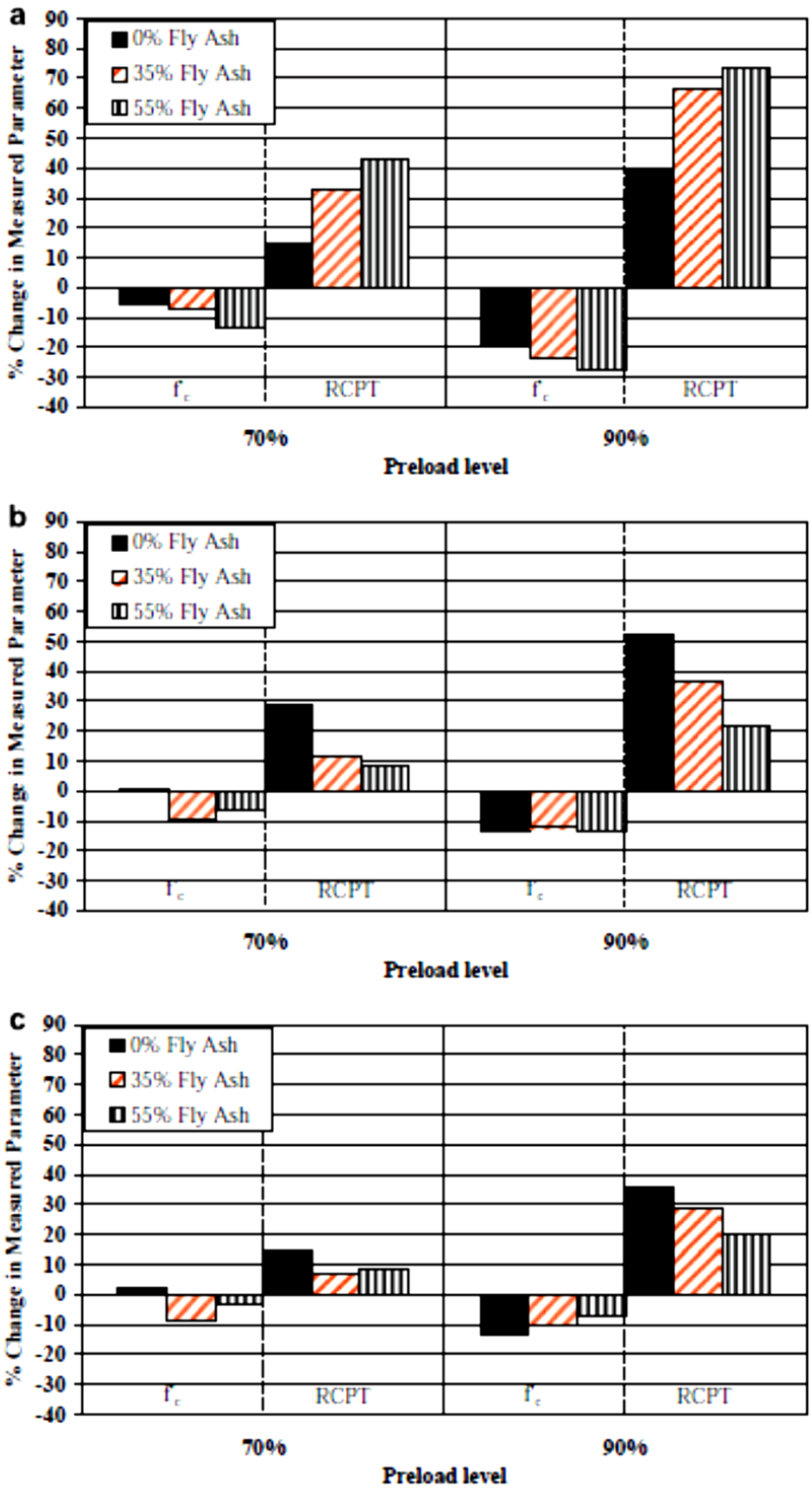

Figure 2.23: Effect of self-healing on RCPT samples before (a) no healing, (b) 15 days of healing, and (c) 30 days of healing (Sahmaran, et al., 2008)

2.7 Summary

The literature review of chloride induced corrosion, carbonation, sulfate attack, biological attack, and cracked concrete behavior of structures exposed to marine environments established the current foundation of knowledge available and the areas where research is needed. Research was identified as being needed on the following topics:

- The chloride ingress behavior of ternary blend cements containing metakaolin or silica fume
- The carbonation behavior of low water-to-cementitious material ratios
- Determination of the influence of silica fume replacement of cement on carbonation behavior
- The behavior of ternary blend cements exposed to carbonation
- Carbonation performance of blended cements containing metakaolin
- The sulfate resistance of ternary blend cements containing metakaolin and low CaO fly ash
- The influence of slag and fly ash on the self-healing and chloride ingress of cracked concrete sections
- The self-healing behavior of V-shaped cracks subjected to chloride ingress
- Determination of the self-healing behavior of ternary blend cements subjected to chloride ingress

(This page intentionally left blank.)

CHAPTER 3

Forensic Investigation of I-95 at Turtle River Bridge

3.1 Introduction

The objective of this research was to characterize the degradation mechanisms present in prestressed concrete piles exposed to marine environments in Georgia. With an in-depth understanding of relevant degradation phenomena, novel methods to increase the durability of coastal bridges can be developed with the goal of increasing bridge service lives to 100+ years. To better identify the pile deterioration mechanisms, piles from the I-95 at Turtle River Bridge in Brunswick, Georgia were investigated.

The deterioration of prestressed concrete piles in marine environments is a growing expense for the Georgia Department of Transportation (GDOT). Bridges are having to be replaced after less than 40 years in service, which is significantly less than the 75 to 100 year service life desired by the Federal Highway Administration (FHWA). For example, the substructure of the I-95 at Turtle River Bridge was replaced after only 32 years in service.

The exposure of structural concrete to the harsh Georgia coastal environment can cause several forms of degradation. The forms of attack vary with the exposure zone on the piling, as shown in Figure 3.1. Corrosion of the prestressing steel typically occurs in the tidal and splash zones, while carbonation and sulfate attack may occur in the submerged regions of the piles (Mehta, 1991). The piles recovered from the Turtle River Bridge upgrade were investigated for these damage mechanisms, in addition to inspection

for any other potential degradation hazards. Section 3.2 investigates damage caused by corrosion of the prestressing steel. Section 3.3 examines the degradation of the piles due to sulfate attack. Section 3.4 investigates the biological attack that occurred on the concrete piles. Section 3.5 presents the conclusions and recommendations drawn from this study and suggest future research in certain areas.

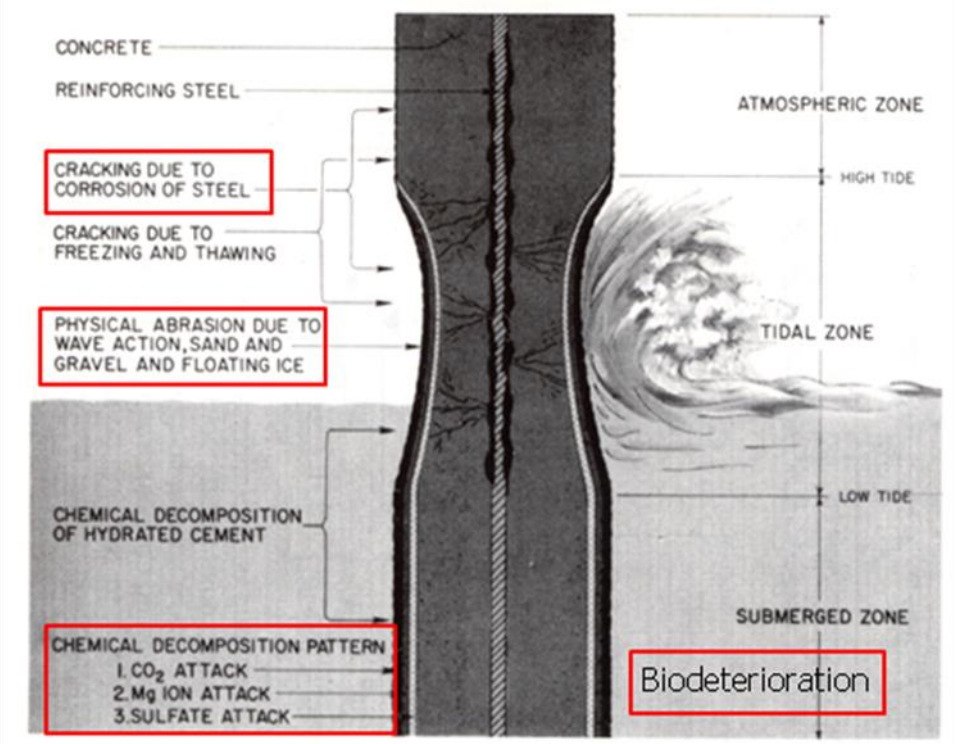

Figure 3.1: Typical degradation mechanisms in coastal concrete piling (Mehta, 1991)

3.1.1 Bridge Description

The I-95 at Turtle River Bridge (Structure ID: 127-0052-1) is located approximately 10 miles from the Atlantic coast, near Brunswick, GA, in Glynn County, as shown in Figures 3.2 and 3.3. The original bridge was constructed in 1977, and upgraded in 2009 by replacing the heavily damaged substructure. The damage observed

by inspection teams is presented in section 3.1.2. Figure 3.3 shows the original and upgraded Turtle River Bridge. The bridge has 43 spans and has a total length of 3,488 ft. The bridge has a concrete road deck. The bridge has three primary spans, which are approximately 200 ft in length and are supported by steel I-girders. The remaining 40 spans are supported by prestressed concrete girders. The girders rested on elastomeric bearing pads on pier caps. The substructure consisted of 30"x30" hollow prestressed concrete piles, which supported the pier caps.

The piles were constructed with 9/16" prestressing strands and a 0.50 water-to-cement (w/c) ratio concrete using ASTM C 150 Type I cement. Natural sand was used for the fine aggregate, and a 1" maximum size aggregate (MSA) limestone for the coarse aggregate.

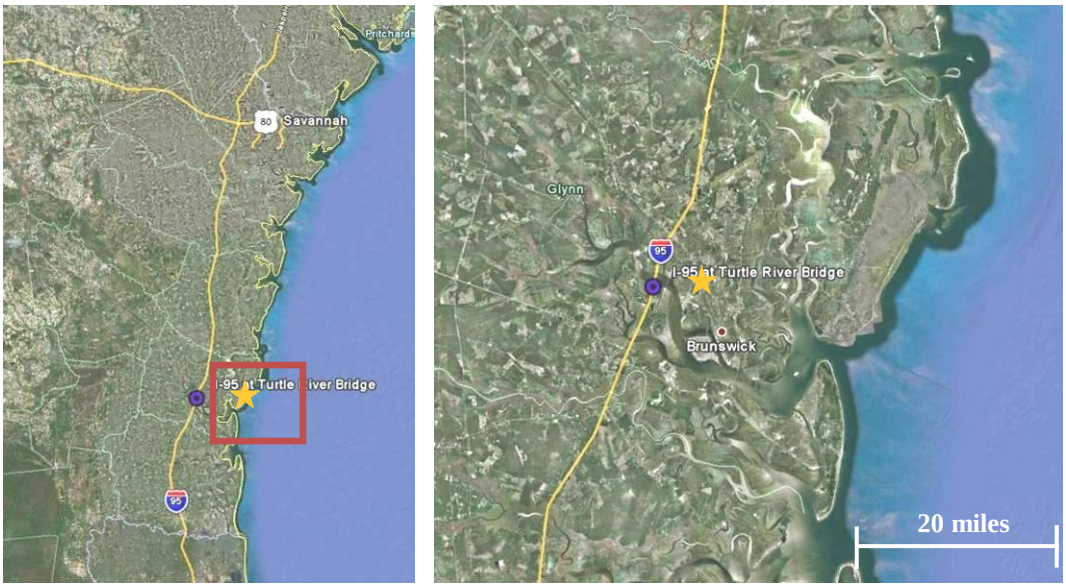

Figure 3.2: Location of I-95 at Turtle River Bridge

(a) (b)

Figure 3.3: Overall view of bridge (a) before and (b) after upgrade

The substructure on the bridge was replaced using large transfer beams and drilled caissons into the subgrade. Figure 3.4 shows the original and upgraded substructure. The piles used for the forensic investigation were removed during construction so that the new caissons could be built. Only existing piles that interfered with the new substructure were removed. In Figure 3.4 (b), the old piling can be seen in place under the new bridge structure.

(a)

(b)

(c)

Figure 3.4: View of bridge substructure (a) before, (b) transfer girder after upgrade, and (c) drilled caisson support after upgrade

Four piles were delivered to the Georgia Tech in February 2010. Figure 3.5 shows the piles upon delivery. Three of the piles contained the splash, tidal, and submerged regions, and the fourth was a fully submerged section. Figure 3.6 shows a pile after cleaning the biological growth off of the surface. The splash, tidal, and submerged zones are labeled.

Figure 3.5: Piles from Turtle River Bridge

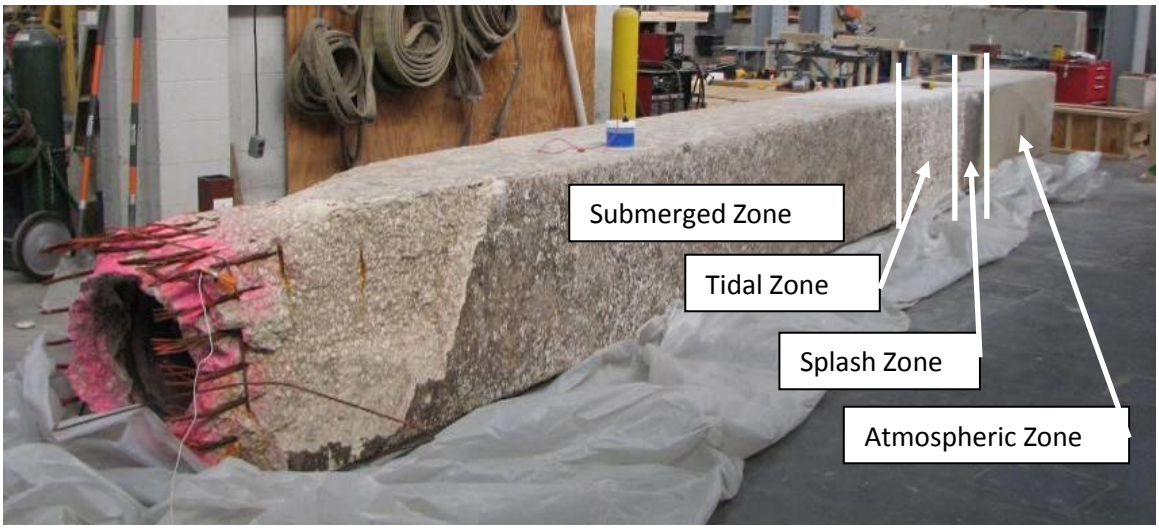

Figure 3.6: Pile after removal of biological growth

3.1.2 Inspection Report Data for Original Substructure

Access to the most recent inspection reports for the Turtle River Bridge was provided by GDOT. The most recent inspection of the substructure before replacement was performed in 2005, along with notes from previous inspections. The bridge inventory listing and bridge inspection reports are given in Appendix A.

In the splash and tidal zones of piles, visual inspection of the piles showed heavy marine growth, moderate scaling and abrasion, vertical cracking, spalling, exposed prestressing steel, rust staining, and delaminations. The reported vertical cracks varied in width from hairline to 1/4 in. For the submerged region of the piles, it was noted that the concrete piles were "soft" and that the concrete could be easily chiseled off. Also, several piles had vertical cracks in the corners that ran from the mudline up to 6 ft to 12 ft, with a width varying from hairline to 1/32 in. (0.030-in.) in width. Additionally, according to the report, multiple piles had been encased in a fiberglass sheath with epoxy as a rehabilitation method.

The inspection reports suggest visual signs of degradation consistent with chloride-induced corrosion of the reinforcement plus chemical attack and potential biological attack of the concrete. The forensic investigation of the recovered piles characterized the deterioration mechanisms present that caused the observed damage.

3.2 Corrosion of Prestressing Steel

Concrete's highly alkaline environment allows for the formation of a thin oxide layer on the surface of reinforcing steel. The thin passive film protects the steel from

corrosion in alkaline environments. If the passive layer is destroyed, active corrosion can occur. The passive film can be broken down by decreasing the pH of the surrounding environment, local attack from aggressive ions, or a concurrence of both (Bertolini, et al., 2004).

Chlorides from the surrounding marine environment are able to ingress into the concrete over time through various transport mechanisms. The protective oxide film that forms on the surface of the steel in the alkaline concrete environment is broken down locally by the presence of a sufficient local chloride concentration, and pitting corrosion can result. Pitting is a localized form of corrosion which initiates when chlorides attack defect sites in the passive film. Two reactions that occur in breaking down the passive film are given below in Eq. 3.1 and Eq. 3.2 (Bertolini, et al., 2004).

$$Fe^{3+} + 6Cl^- \rightarrow FeCl_6^{-3} \quad \text{(Eq. 3.1)}$$

$$FeCl_6^{-3} + 2OH^- \rightarrow Fe(OH)_2 + 6Cl^- \quad \text{(Eq. 3.2)}$$

The reactions do not consume the chlorides, and lower the pH at the pitting site by depleting the OH^- ions in the formation of the iron oxides. In concrete, the surrounding regions remain alkaline, and hydroxide ions are available in the pore solution which causes the surrounding regions to act as cathodes for the corrosion reactions. As the pit grows, it gains a net positive charge from the hydrogen and metal ions which attract more chlorides into the pit, causing an autocatalytic reaction. At the surface, a porous cap can form from the corrosion products that further allow the pit to grow.

The corrosion of the prestressing steels leads to a loss of steel section. Additionally, the corrosion of steel leads to the formation of iron oxides which are less dense than the original steel and occupy more volume. The formation of oxides causes tensile forces in the surrounding concrete and can lead to cracking and delamination of the cover concrete, as well as rust staining on the surface of the piles.

The causes and extent of damage produced by chloride-induced corrosion were investigated by performing a visual assessment of the damage (section 3.2.1), mapping the corrosion potentials (section 3.2.2), and determining the chloride profiles (section 3.2.3). The chloride profiles were used for service life modeling.

3.2.1 Visual Assessment of Damage

A visual inspection of the splash and tidal zones of the piles showed vertical cracks along the corners of the piles as shown in Figure 3.7. The average crack widths were approximately 0.01", but were as large as 0.05". Additionally, delamination of the cover concrete had occurred over the corner strand on one pile. The exposed surface showed extensive corrosion damage to the strand and staining of the surrounding concrete (Figure 3.8). The delamination occurred normal to the surface of the concrete through the corner strand location as illustrated in Figure 3.9.

(a) (b)

Figure 3.7: (a,b) Corrosion induced longitudinal cracking of piles

(a) (b)

Figure 3.8: (a,b) Corrosion induced delamination, loss of steel section, and staining of piles

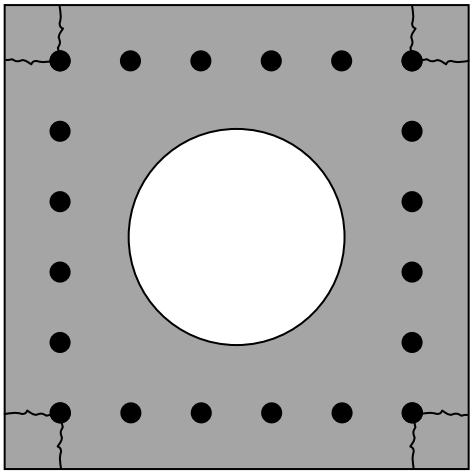

Figure 3.9: Cracking and delamination pattern on the cross-section in splash and tidal zone

Inspection of corroded strands indicated the presence of pits and preferential locations in the crevices between the braided wires of the strand. Figure 3.10 shows a core through a corroded strand and a magnified image of the corrosion products around the strand.

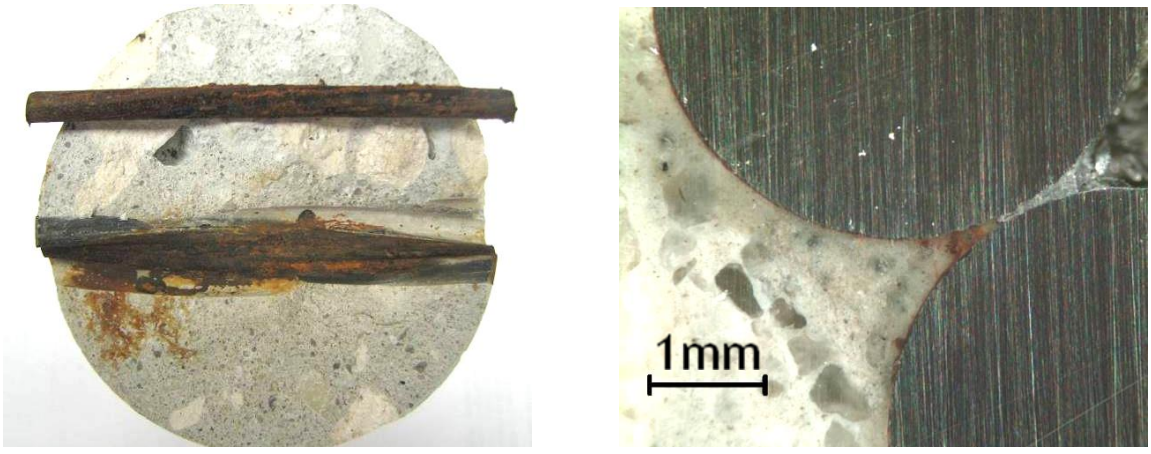

(a) (b)

Figure 3.10: Corrosion of prestressing steel in extracted core

The pH of the concrete cover was studied by using a phenolphthalein indicator solution on freshly cut surfaces of the piles. The indicator solution turns pink if the pH is above approximately 9.2, representing uncarbonated concrete. The carbonation front can be seen in Figure 3.11. The carbonation front was found to be approximately 1" beneath the exposed surface of the piling, both in the submerged and tidal regions. This limited depth suggests that it is unlikely that corrosion of the reinforcement was caused by carbonation, but that a combination of decreased pH and ingress of chlorides caused pitting corrosion to occur.

Although carbonation of the concrete did not cause general corrosion of the reinforcement, it may have contributed to degradation of the cover concrete. Carbonation of concrete leads to the depletion of calcium hydroxide, which causes the decrease in pH, and can lead to a loss of calcium silicate hydrate (C-S-H), which is the primary strength giving component of hydrated cement paste (Neville, 1997). Additionally, ettringite is unstable at a pH below 11 (Neville, 1997).

(a) (b)

Figure 3.11: (a) Phenolpthalein indicator solution on sawn surface of pile, and (b) measurement of carbonation front

3.2.2 Half-cell Corrosion Potentials

The half-cell potential of the imbedded steel strands was used to identify regions where corrosion was occurring in accordance with ASTM C 879 (2009). The measurements were performed by measuring the half-cell potential of a strand versus a $Cu/CuSO_4$ electrode (CSE) using a voltmeter and by measuring the potential at one-foot intervals along the length of the pile. An electrical contact solution consisting of liquid dish detergent mixed with water was used to wet the surface for readings. Figure 3.12 shows the experimental set-up used.

Figure 3.12: Half-cell potential measurement set-up

Figure 3.13 shows the half-cell corrosion potentials from all four sides of a pile. According to ACI Committee 222 (2001), a half-cell potential greater than 350 mV indicates a 90% or greater probability of corrosion occurring. A half-cell potential less than 200 mV indicates a 10% or less probability of corrosion occurring. The results suggest that from 2 ft above high tide and lower, there is a strong probability that corrosion is occurring. The rate of corrosion cannot be determined using this method. Therefore, a half-cell potential in excess of 350 mV does not indicate that corrosion is occurring at a highly deleterious rate. The corrosion rate is heavily influenced by environmental factors, including adequate presence of moisture and oxygen. If insufficient oxygen is present, then the corrosion rate can be orders of magnitude smaller.

The lack of oxygen in the submerged zones of piles explains why no corrosion induced damage was seen, even though the half-cell potential suggests that corrosion is occurring. The tidal and splash zones of piles have adequate access to moisture and

oxygen due to the wetting and drying cycles present. This leads to a significantly faster corrosion rate, which could be the reason for the large amount of damage found.

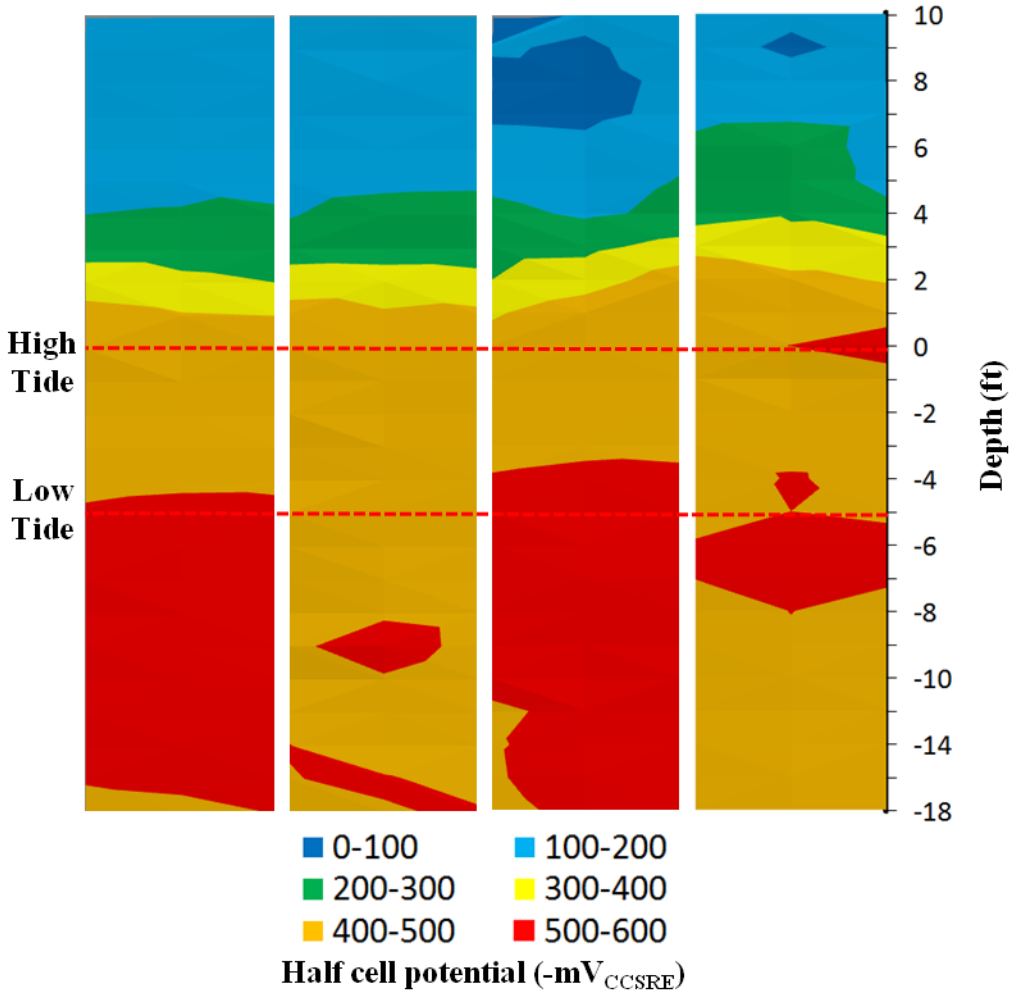

Figure 3.13: Half-cell potential map of the four faces of a Turtle River Bridge pile

3.2.3 Chloride Profiles

The concentration of chloride ions near the reinforcement surface is critical in causing the onset of pitting corrosion and in furthering the corrosion reactions; therefore, it is important to understand the migration of chloride ions through the concrete and to

understand the interactions between those ions and the cementitious system. Chlorides ingress into the concrete piles from the surrounding brackish water. Their movement through the concrete is often modeled with Fick's second law of diffusion. However, other transport mechanisms, like capillary action, can affect the transport of chlorides through the cement paste. The apparent diffusion coefficient of a concrete mix exposed to chlorides can be determined experimentally and used for service life estimation in a given environment (Bertolini, et al., 2004).

Within the concrete, chlorides exist in a free or uncombined form and in bound forms, where they may combine with existing hydration products or unhydrated cementitious phases. In the bound form, the most common product formed is Friedel's salt [$Ca_2Al(OH)_6Cl \cdot 2H_2O$]. When the concentration of chlorides reaches a threshold value at the surface of the reinforcing steel, corrosion will initiate when the passive film is broken down. There is considerable debate as to how to define the chloride threshold limit (CTL) and what the value should be (Mohammed and Hamada, 2003). The threshold values are typically reported as the total or free chlorides as a percent mass of concrete (or cement) or by the ratio of the concentration of chloride ions to the concentration of hydroxyl ions ($[Cl^-]/[OH^-]$).

In practice, the total chloride content is used more frequently for threshold values, even though it is generally believed that the free chlorides are responsible for the initiation of corrosion (Mohammed and Hamada, 2003). The CTL is typically assumed to be between 0.4% to 1% mass of binder, or approximately 0.05% to 0.2% by mass of concrete, for total chloride content (Bertolini, et al., 2004). However, reported values for the CTL have varied from 0.04% to 8.34% by mass of binder based upon total chloride

content (Angst, et al., 2009). The CTL is difficult to define since the reported values vary with cement composition, water to cement ratio, exposure temperature, internal pH, and type of steel used (Angst, et al., 2009).

3.2.3.1 Test Methodology

The total chloride concentration was measured using the ASTM C 1152 (2004) procedure, which was performed by taking 3" diameter cores through the depth of the cross-section, drilling at 1/2" increments using a 3/8" masonry bit, and collecting the powder. The concrete powder was ground using a mortar and pestle and sieved until a minimum of 30 g passed through the 850 mm sieve for each depth increment. The acid soluble chloride testing was performed by measuring 10 g of the powder into a beaker and adding 75 ml of reagent water. Next, 25 ml of dilute (1:1) nitric acid was added to the beaker. The sample was stirred until any lumps were broken up. Next, the sample was rapidly heated to a boil for 10 seconds, then removed from heat. The sample was then filtered using a Buchner funnel and filtration flask with suction through a Grade 41 coarse-textured filter paper. The sample was then allowed to cool to 25 °C. The sample was titrated with Silver nitrate solution (0.1 N) to determine the acid soluble chloride content.

The free chloride concentration was measured using the ASTM C 1218 (1999) procedure, which was performed by taking 3" diameter cores through the depth of the cross-section, drilling at 1/2" increments using a 3/8" masonry bit, and collecting the powder. The concrete powder was ground using a mortar and pestle and sieved until 30 g passed through the 850 mm sieve for each depth increment. The water soluble chloride

testing was performed by measuring 10 g of the powder into a beaker and adding 50 ml of reagent water. Next, the sample was covered and brought to a rapid boil for 5 minutes. The sample was allowed to sit for 24 hours. Next, the sample was filtered using a Buchner funnel and filtration flask with suction through a Grade 40 Class G filter paper. After filtering, 3 ml of (1:1) nitric acid and 3 ml of hydrogen peroxide (30% solution) were added to the sample, which was then covered and allowed to stand for 1 minute. The sample was then brought to a boil for 10 seconds while still covered, then removed from heat. The sample was then allowed to cool to 25 °C. The sample was titrated to determine the water soluble chloride content.

Titrations were performed using the Metrohm 798 MPT Titrino. A silver/silver chloride standard electrode was used. Silver nitrate solution (0.1 N) was added in 0.1 ml aliquots to the sample until an equivalence point was achieved. Figure 3.14 shows the filtration and titration methods. The chloride content was then determined using Eq. 3.3 to compute the percent chlorides by mass of sample.

$$Cl, \% = 3.545 * V * N/W \qquad \text{(Eq. 3.3)}$$

Where,

V = milliliters of $AgNO_3$ solution used for titration at equivalence point

N = exact normality of $AgNO_3$ solution

W = mass of sample, g

(a) (b)

Figure 3.14: (a) Filtration of chloride sample, and (b) titration of sample

2.3.2 Results, Chloride Concentrations

Total and free chloride concentrations were determined at various heights along the pile, as shown in Figure 3.15. The locations were chosen to coincide with the atmospheric, splash, high and low tide, and submerged regions of the pile. The notation used for identifying samples was that a positive value indicated a depth below high tide, and a negative value was above high tide. Cores were taken in the center of the pile to avoid the effect of 2-D transport from another surface of the pile.

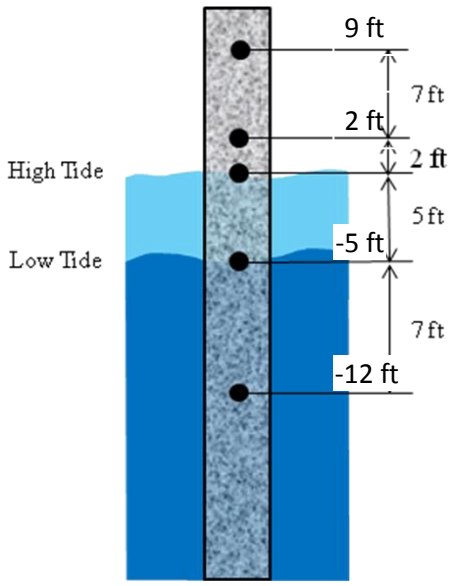

Figure 3.15: Locations of chloride concentration sampling

Figure 3.16 shows the total chloride concentrations from each sampling location with respect to depth into the cross-section. The results suggest that the concentration of total chlorides at the level of the reinforcement is significantly higher than the CTL values given in the literature. The concentrations were in agreement with the half-cell corrosion potentials, which suggested that active corrosion was occuring due to depassivation and destruction of the passive film on the surface of the steel. The chloride profiles for high tide, -5 ft, and -12 ft elevations were very similar. However, the concentration at the surface varied widely between the elevations and may be due to the presence of wetting and drying cycles in the tidal zone compared to the fully saturated condition in the submerged region. The 2 ft above high tide profile had a greatly reduced chloride content compared to submerged regions. Additionally, it was observed from the 9 ft above high tide data that the background chloride content in the mix was 0.01% by mass of concrete. The low background content suggested that the mix did not use

seawater for mixing, dredged fine aggregate, or large quantities of chloride containing admixtures.

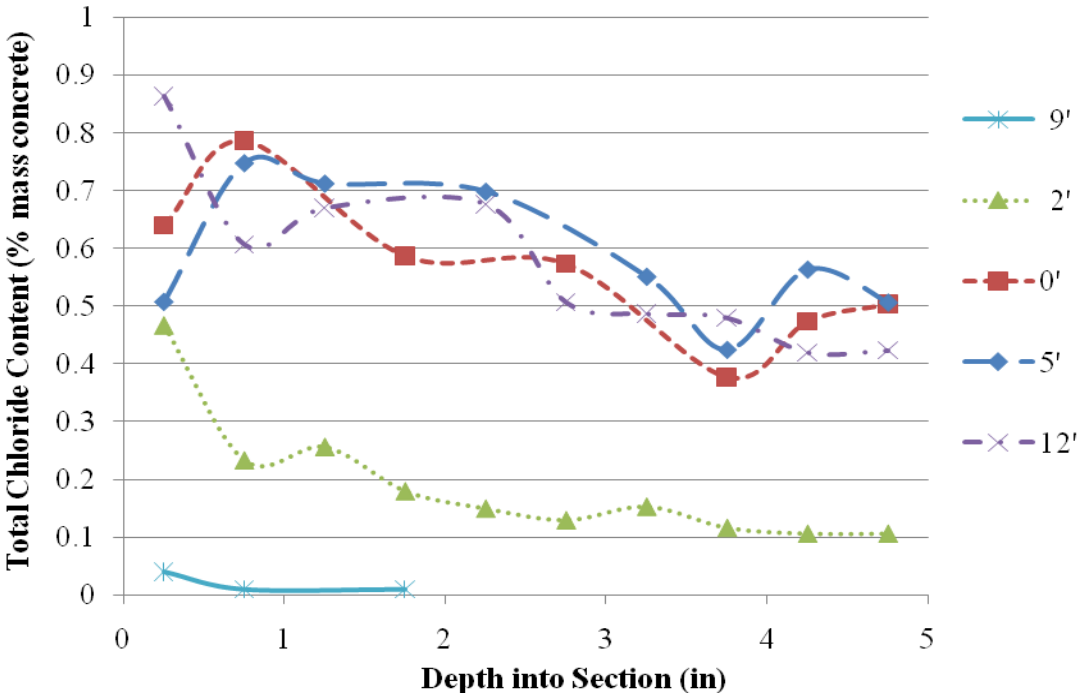

Figure 3.16: Total chloride content of concrete columns at various depths

Figure 3.17 shows the free chloride concentration profile at the selected locations along the length of the pile. The results suggest that the concentration of free chlorides at the level of the reinforcement is significantly higher than the CTL values given in the literature. The free chloride profiles follow a similar trend to the total chloride profile at each depth. The profile for 9 ft above high tide shows that all chlorides present over ½ in. into the section were bound.

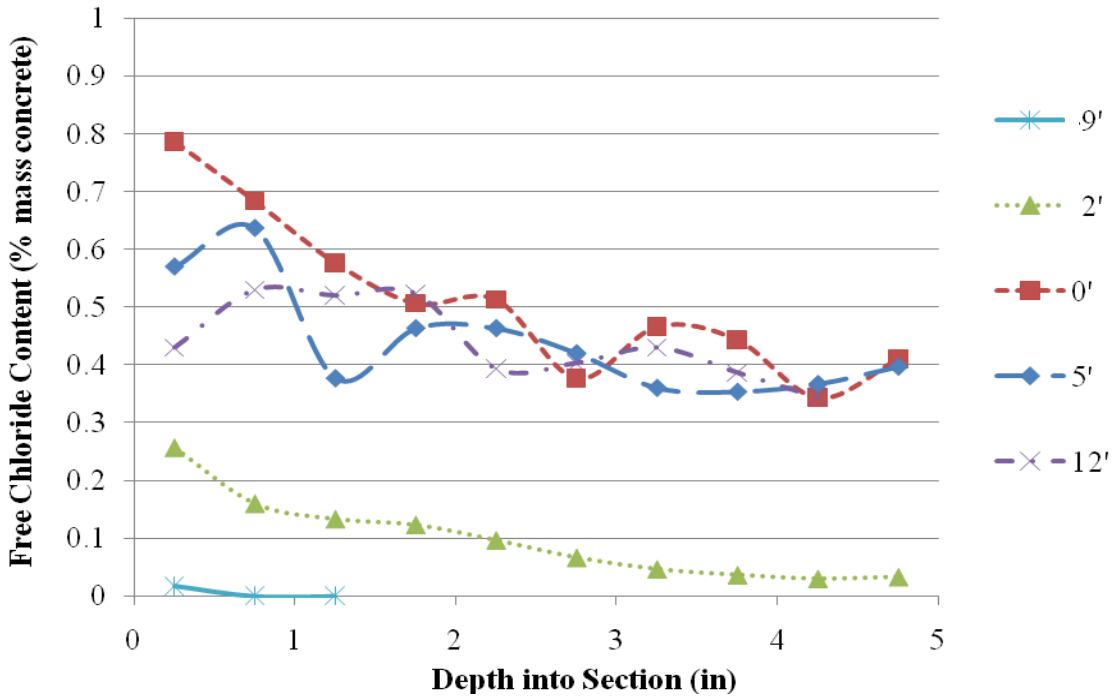

Figure 3.17: Free chloride content of concrete columns at various depths

A comparison of the total to free chloride content measured at each increment from the piles is given in Figure 3.18. From a simple linear regression between the total and free chloride concentrations, it was found that 18.6% of the total chloride content is bound. There is a large scattering of data, but the percent bound chlorides is consistent with the value of 18.7% found by Mohammed and Hamada (2003) from field exposure measurements.

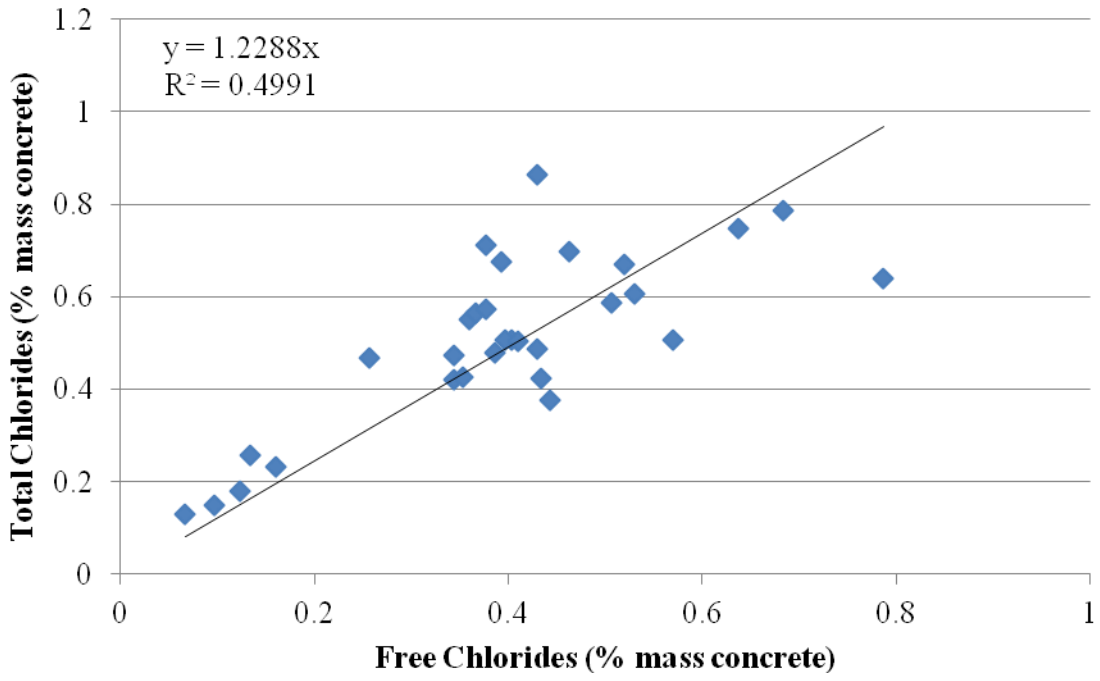

Figure 3.18: Comparison of total to free chloride concentrations

Figures 3.19 shows the free and total chloride concentrations at -12 ft, -5 ft, high tide, and +2 ft. The free chloride content follows a similar profile to the total chlorides, but the value is reduced due to binding of chlorides. The concentrations near the surface were highly variable between acid and water samples for the same depth, and could be due to variable surface conditions of cores due to biological attack and coring induced damage.

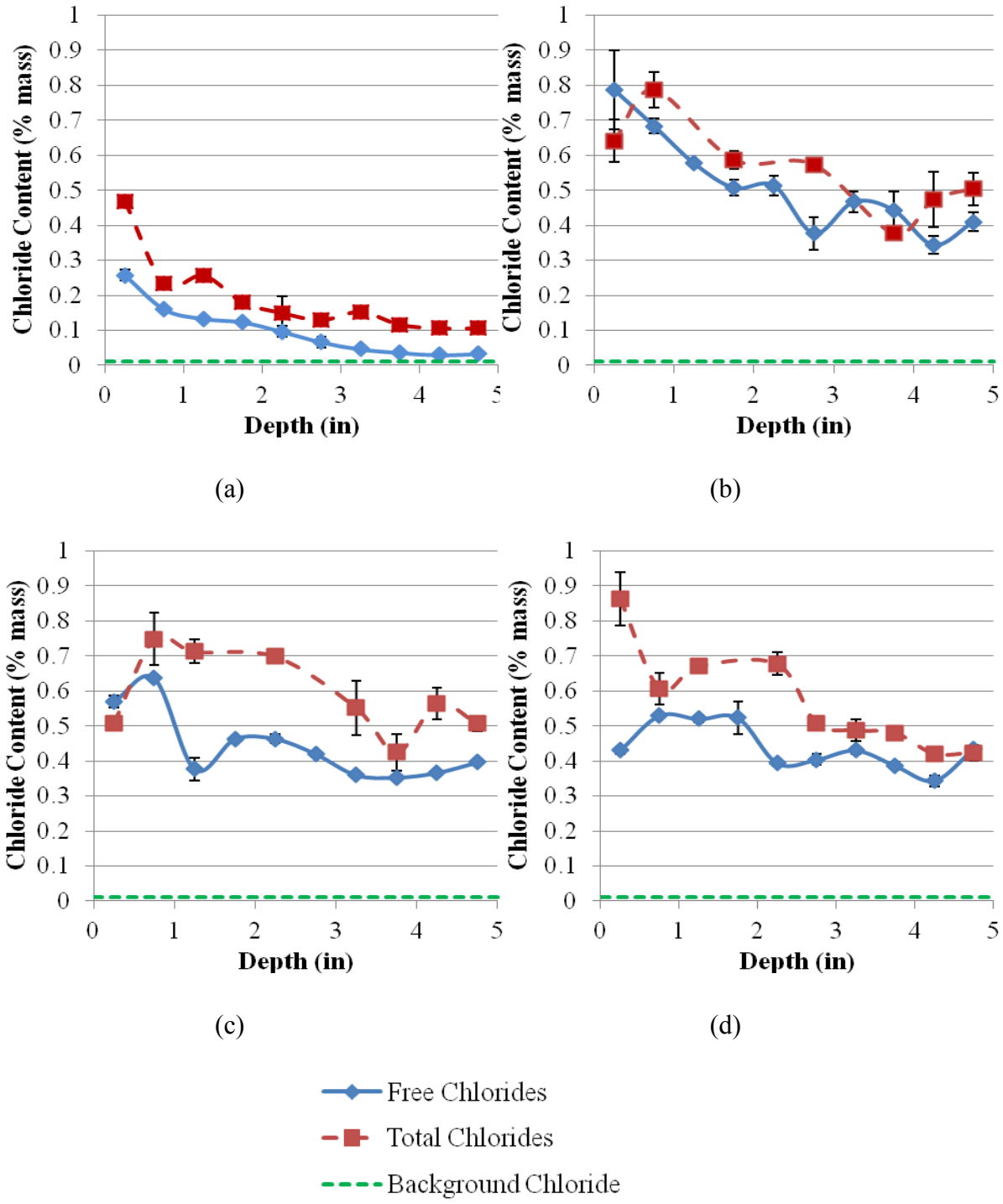

Figure 3.19: Chloride profiles at (a) 2 ft above high tide, (b) high tide, (c) 5 ft below high tide, and (d) 12 ft below high tide

3.2.3.3 Chloride Ingress Modeling

The ingress of chlorides into a structure is often treated as a diffusion-based transport phenomenon (Bertolini, et al., 2004). Fick's second law can be used with experimental data to determine the diffusion coefficient that characterizes the diffusion-based transport properties of a concrete mix. Additionally, if the diffusion coefficient and environmental parameters are known, the time necessary for the CTL to be reached can be determined and used for service life modeling.

The chloride profiles were used to determine the apparent chloride diffusion coefficient by performing a non-linear regression analysis, using the method of least squares to fit to the equation given by Eq. 3.4 (ASTM C 1152, 2004).

$$C(x,t) = C_s - (C_s - C_i) * erf\left(\frac{x}{\sqrt{4*D_a*t}}\right) \qquad \text{(Eq. 3.4)}$$

Where,

$C(x,t)$ = chloride concentration, measured at depth x and exposure time t, mass %

C_s = projected chloride concentration at the interface between the exposure liquid and test specimen that is determined by the regression analysis, mass %

C_i = initial chloride-ion concentration of the cementitious mixture prior to submersion in the exposure solution, mass %

x = depth below the exposed surface, m

D_a = apparent chloride diffusion coefficient, m^2/s

t = the exposure time, s

erf = $\frac{2}{\sqrt{\pi}} * \int_0^z exp(-u^2)\, du$

An approximation developed by Winitzki (2006) for the error function was used to perform the regression analysis. The approximation, given in Eq. 3.5, results in a maximum relative error of less than 1.3%.

$$\operatorname{erf}(x) \approx \left[1 - \exp\left(-x^2\left(\frac{\frac{4}{\pi} + 0.147x^2}{1 + 0.147x^2}\right)\right)\right]^{\frac{1}{2}} \quad \text{(Eq. 3.5)}$$

Life 365 Service Life Prediction Model (Ehlen, 2009) was used to estimate the diffusion coefficient and expected service life of the structure. The primary parameters necessary for using Life 365 are the structure location, exposure type, concrete cover distance to reinforcing steel, and mix design details, including w/cm, percent replacement of cement with supplementary cementitious materials, and use of corrosion inhibitors. The results of the nonlinear regression diffusion coefficient results compared to the Life 365 estimates are shown in Table 3.1.The Life 365 estimates were based upon a marine tidal zone exposure in Savannah, Georgia for a 0.50 w/c mix design using only Portland cement. The experimentally determined data were compared to the Life 365 data for the estimated time to corrosion initiation based upon a CTL of 0.05% by mass of concrete, which is the default value used by Life 365 (Ehlen, etal., 2009).

Table 3.1: Comparison of Life 365 estimates to experimental data

	Experimental	Life 365	% Difference
Diffusion Coefficient ($in^2/s * 10^{-8}$)	2.56	2.14	16.44
Surface chloride concentration (% mass concrete)	0.797	0.800	0.44
Time to corrosion initiation (years)	3.1	3.7	19.35

Overall, Life 365 gave reasonable predictions of diffusion coefficient, surface chloride concentration and time to corrosion (Table 3.1). Life 365 underestimated the diffusion coefficient that was observed from curve fitting. However, the diffusion coefficient observed could be influenced by other damage mechanisms that were occurring in the piles. The observed biological attack, sulfate attack, and potential cracking from construction practices could all lead to an increased permeability and diffusion coefficient. The discrepancy between diffusion coefficients is responsible for the variation in time to corrosion initiation. Life 365 and the experimental data were in agreement on the surface concentration for this exposure zone. The time to corrosion initiation was significantly less than the 75+ year lifespan desired by GDOT. After corrosion initiates, the time until repair or replacement is required varies heavily on the corrosion rate, which can vary by orders of magnitude. The Life 365 program assumes a 6 year propagation time in the program's service life calculations (Ehlen, et al., 2009). However, frequently, the failure of a structure due to chloride-induced corrosion is assumed to occur at corrosion initiation for service life modeling (Bertolini, et al., 2004).

3.2.4 Conclusions, Corrosion of Prestressing Steel

The piles from the Turtle River Bridge showed extensive damage from chloride-induced corrosion. The half-cell corrosion potentials indicated that the prestressing strands were undergoing active corrosion from the tidal zone to mudline. The chloride profiles indicated that the concentration of chlorides at the reinforcement, 0.35% to 0.45% by mass of concrete, was significantly higher than the 0.05% necessary to initiate pitting corrosion. The large amount of concrete cracking and spalling and of steel corrosion damages were limited to the tidal and splash zones on the piles, due to the limited availability of oxygen in the fully submerged regions of the piles.

The diffusion coefficient for chloride transport in the concrete showed that the concentration of chlorides at the level of the steel would exceed the threshold value after only 3.1 years of service in the marine environment. This suggests that the concrete mix used is not adequate for long-term exposure to this environment. The service life analysis program Life 365 was able to predict the diffusion coefficient to within 16% of the measured value. The measured was higher, likely due to contributions of additional forms of degradation to increased permeability in the concrete piles.

3.3 Sulfate Attack

Concrete piling in seawater and brackish water can be exposed to high concentrations of sulfates. In addition to sulfates present in the water, it is being investigated if additional sulfates may be produced by bacteria on the surface of the piles. The primary forms of sulfates present are $NaSO_4$ and $MgSO_4$ (Skalny, et al., 2002).

Damage to the concrete due to various reactions between the ingressing sulfate ions and hydration products and anhydrous cement phases in the cement paste is termed “sulfate attack”. Two primary mechanisms are associated with sulfate attack. First, sulfate ions can react with monosulfoaluminatate or available tricalcium aluminate to form ettringite. The formation of ettringite can be expansive and lead to cracking and spalling. The calcium consumed in this reaction comes from the dissolution of available portlandite. In addition, sulfate ions may react with available calcium hydroxide to form gypsum. If there is no portlandite present, then the calcium comes from the decomposition of the calcium silicate hydrate phase (C-S-H). The loss of calcium from the C-S-H leads to a reduction in strength (Skalny, et al., 2002).

In the case of magnesium sulfate attack, additional reaction mechanisms are possible. Magnesium sulfate reacts with portlandite to form brucite, in addition to gypsum. Simultaneously, C-S-H is decomposed and converted to an amorphous hydrous silica or magnesium silicate hydrate phase. The decomposition of C-S-H is significantly faster with exposure to magnesium sulfate compared to sodium sulfate (Skalny, et al., 2002).

Visible signs of sulfate-induced damage include a whitish appearance of the cement paste in damaged areas, as well as cracking (due to expansion), softening of the paste, delaminations, and spalling, with the damage typically starting at corners and edges. In addition, loss of strength and modulus can be measured (Neville, 1997). The sulfate attack damage to the bridge piles was characterized by performing a visual inspection of the piles, hardness measurements, and TGA (thermo-gravimetric analysis) and XRD (x-ray diffraction) analysis.

3.3.1 Visual Assessment of Damage

A visual assessment of the submerged region was performed. Cracks were found near the corners of the piles that extended from the mudline up to low tide. The width of these crack varied widely, with a maximum of 0.05 in., but most were approximately 0.025 in. in width. Spalling and abrasion were also apparent at the surface. Additionally, marine life had grown along the cracks, and that growth may have led to increased deterioration. Figure 3.20 shows the measurement of a crack, along with marine growth inside of a crack.

(a) (b)

Figure 3.20: (a) Cracking along corner of pile, and (b) marine growth in crack

A core taken through the cross-section revealed a visible whitish discoloration of the cement paste near the surface in the submerged region of the pile as shown in Figure 3.21. The depth of the color change was consistent with the cracking location along the corners of the piles.

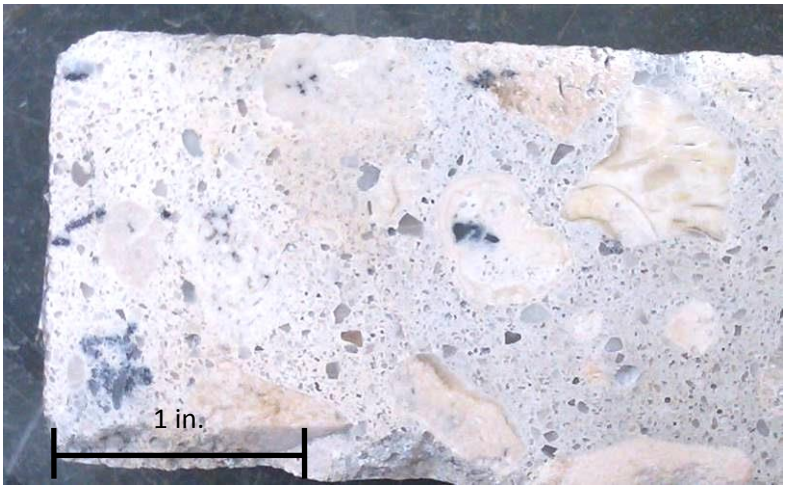

Figure 3.21: Whitish discoloration near surface in submerged region

3.3.2 Hardness Measurements

To determine if a variation existed between the different exposure regions, the hardness of the concrete was measured using two different methods - rebound hammer to measure coarser variations in hardness along the length of the piles and Vickers hardness to measure finer variations in hardness through the depth of the pile. Rebound hammer testing was performed at 1 ft increments along the length of the pile in accordance with ASTM C 805 (2008). A minimum of 10 readings were taken at each location on a smooth surface. Any reading outside the average by more than 6 units was discarded. The calibration from rebound number to strength (or hardness) is provided by the manufacturer for each orientation of testing. The calibration is affected by moisture condition of the concrete, depth of carbonation, and other environmental factors that make the relationship highly variable. However, the rebound hammer number was correlated to a strength for interpreting results to correct for the orientation of the hammer

during testing, which affects the rebound number. The calibration from rebound number to strength (or hardness) was provided by the manufacturer (Figure 3.22).

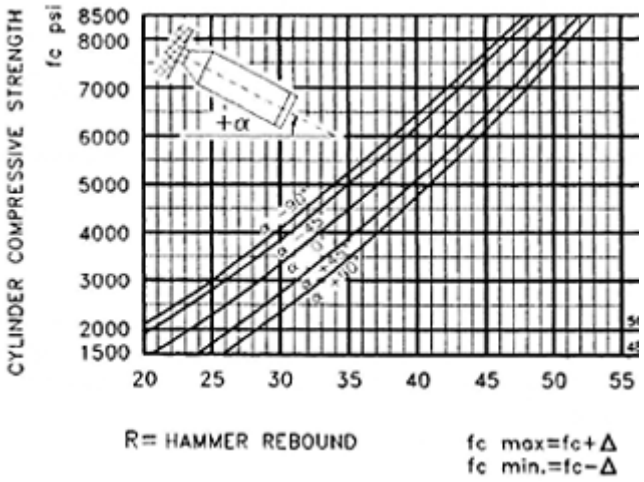

Figure 3.22: Rebound hammer calibration

The results from the rebound hammer testing performed on two piles have been converted into compressive strengths, as previously described, and are shown in Figure 3.23. A negative depth represents above high tide; a positive depth is below high tide. The results suggest a large change in surface hardness, and potentially strength, that occurs in between the splash and low tide region of the piles. The results show an average reduction in strength of approximately 50% from the region of the pile exposed to the atmosphere to the submerged concrete. The reduction in strength occurred rapidly near the high tide region of the piles, and continued to decrease at a gradual rate with increasing depth.

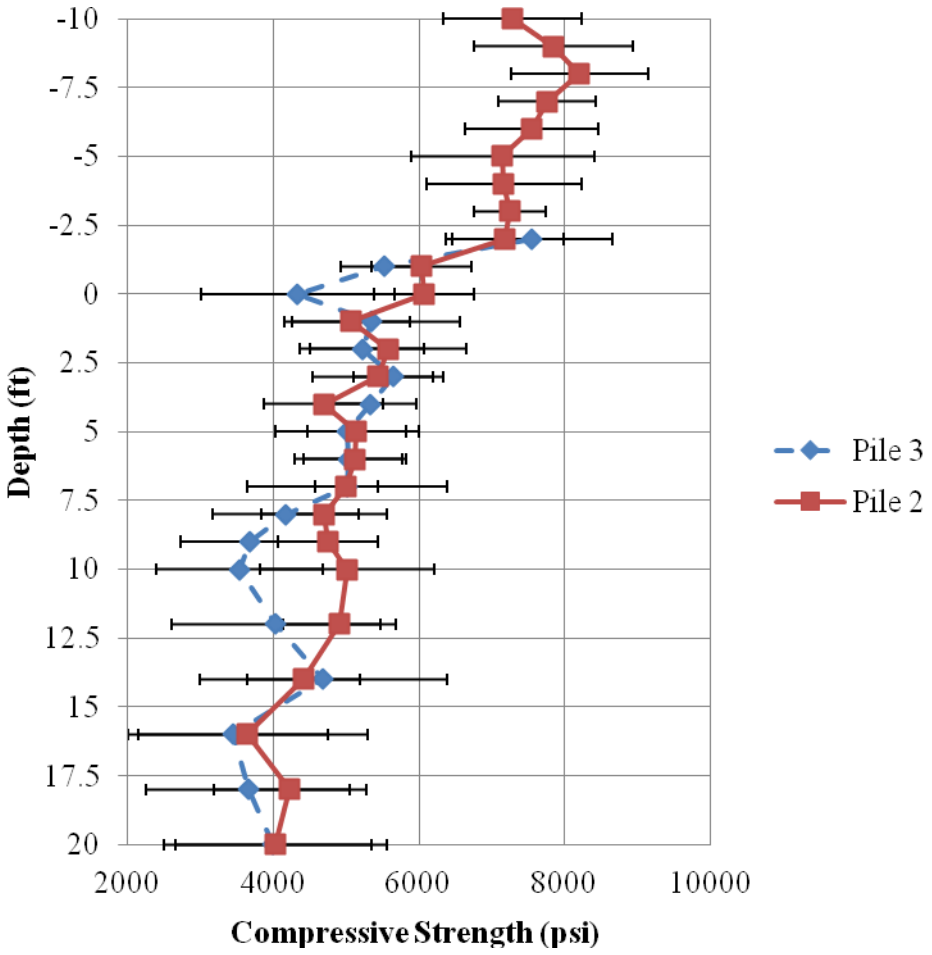

Figure 3.23: Rebound hammer results

Vicker's indentation measurements were performed on polished slices of cores to determine the variation in micro-hardness of the cement paste with depth into the section. Vicker's indentations were performed in accordance with ASTM C 1327 (2008) using 1 kg mass applied for 15 seconds. A minimum of 5 indentations were made at ¼ in. increments into the section on sections polished with 1 micron alumina.

The indentations were measured using a Leica TCS NT confocal microscope. Measurements were made to the nearest micrometer across both diagonals, then the average used for calculating the hardness number. Figure 3.24 shows the results of the

measurements for 2 ft above high tide and 12 below in the submerged region. The outer 2 in. of the submerged region had a reduced hardness compared to the 2 ft above high tide sample. The depth at which the hardness significantly increased coincided with the location of the whitish color change on the samples.

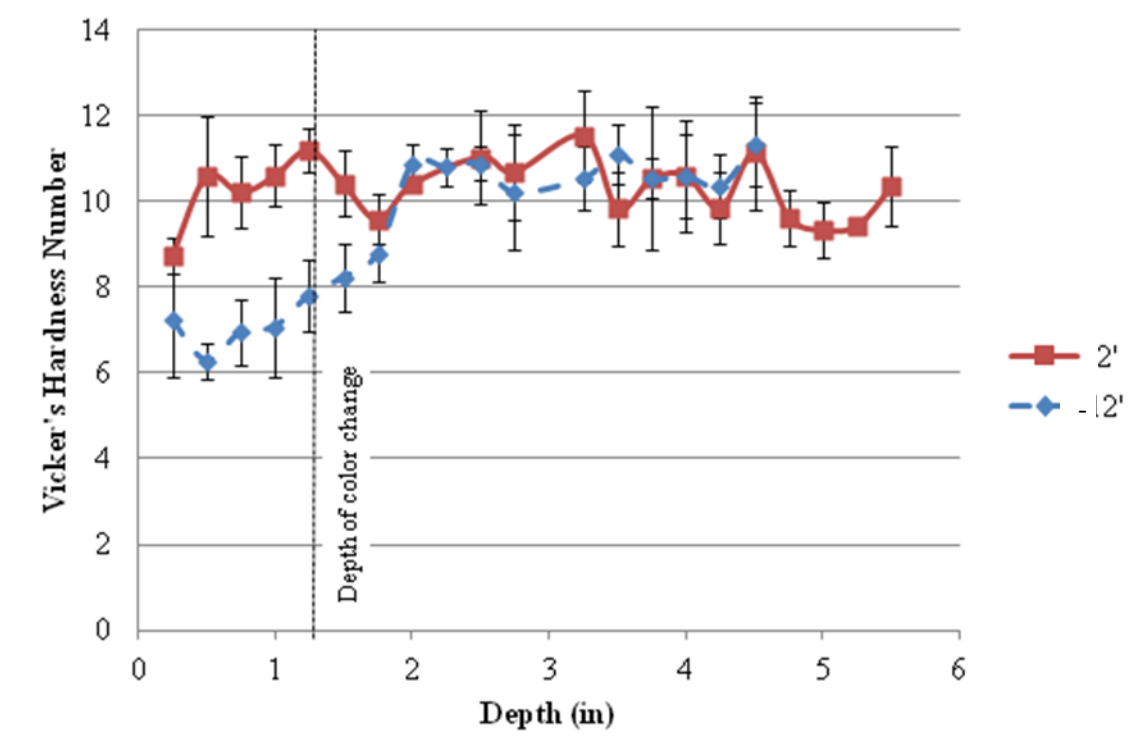

Figure 3.24: Vicker's hardness measurements

3.3.3 Compressive Strength Testing

The compressive strength of the piles was determined in accordance with ACI 214.4R-10 (ACI Committee 214, 2010) and ASTM C 39 (2005). Two sets of tests were performed. First, three 3 in. diameter cores were obtained away from the surface of the pile, as shown in Figure 3.25. Three sets of cores were taken along the length of the pile in the atmospheric, tidal, and submerged zones for comparison of the undamaged

concrete along the length of the piles. The specimens were cut to a 6 in. length using a wet cut concrete saw.

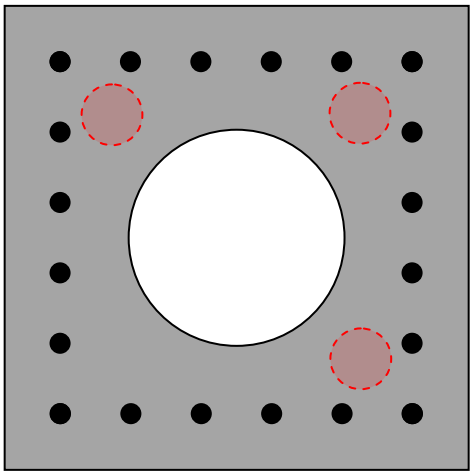

Figure 3.25: Compressive strength core locations

Also, cores were taken through the section to determine if there was a variation between concrete near the surface and the interior undamaged concrete. Cores were taken at +9 ft, high tide, -5 ft, and -12 ft depth. Four 3 in. diameter cores were taken through the section and cut to 3 in. lengths, one at the surface and a section near the center of the pile at each location tested. The location and diagram of the stub specimens are shown in Figure 3.26.

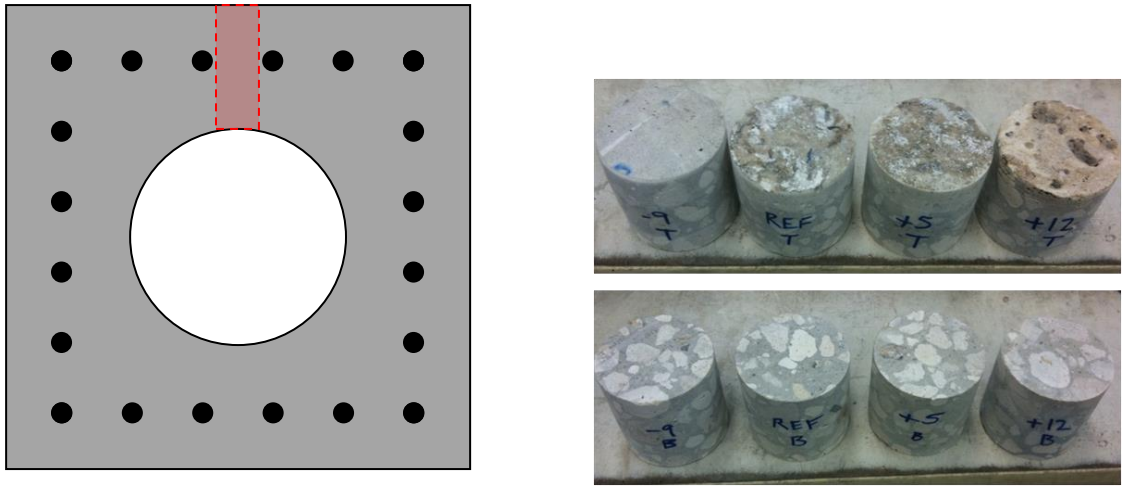

(a) (b)

Figure 3.26: (a) Compressive strength core locations, and (b) surface (top) and interior samples (bottom)

The results of the compressive strength testing of undamaged interior concrete along the length of the piles are given in Figure 3.27. The average compressive strength from all three locations was 5.92 ksi, which is above the design strength of 5 ksi. ANOVA testing, using an alpha of 0.1, showed that the concrete from all three locations at the interior of the pile was statistically equivalent. Since the undamaged interior concrete was shown to be the same in the submerged, tidal, and atmospheric zones of the pile, the data suggested that the variation in rebound hammer results was due to a softening of the surface, and not a variation in undamaged concrete properties.

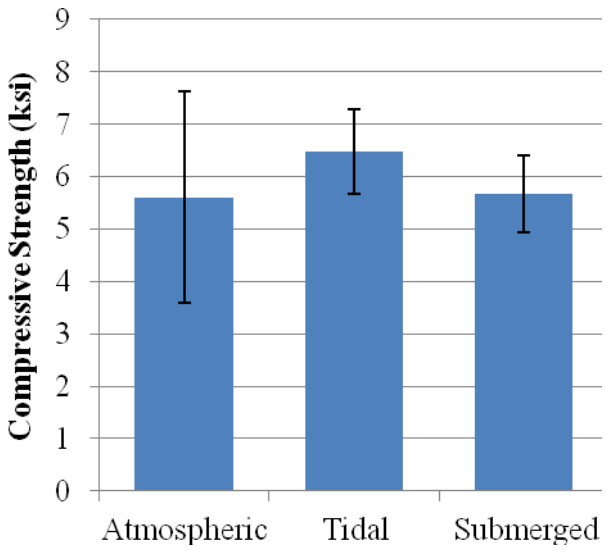

Figure 3.27: Compressive strength of undamaged interior concrete

The results of the stub compression tests comparing the surface to interior concrete are shown in Figure 3.28. The compressive strengths of the interior samples at all depths were determined to be statistically equivalent using ANOVA testing with alpha equal to 0.1. ANOVA analysis between the surface and interior concrete at each depth showed that only the +9 ft and high tide sections were statistically equivalent. The -5 ft and -12 ft samples both had statistical evidence to show the average compressive strengths were not the same. At -5 ft depth, the surface compressive strength was 80% of the interior concrete's strength. In the submerged region, the surface compressive strength was 55% of the interior concrete's strength. The strengths measured were consistent with the strengths determined from the impact hammer measurements.

The large reduction in compressive strength may be explained by a loss of C-S-H from sulfate attack or other forms of degradation, including carbonation. All of the surface samples from 12 ft below high tide failed due to a crushing near the surface and a

single large crack through the remainder of the sample. The paste portion in the crushed region was a powdery consistency after failure.

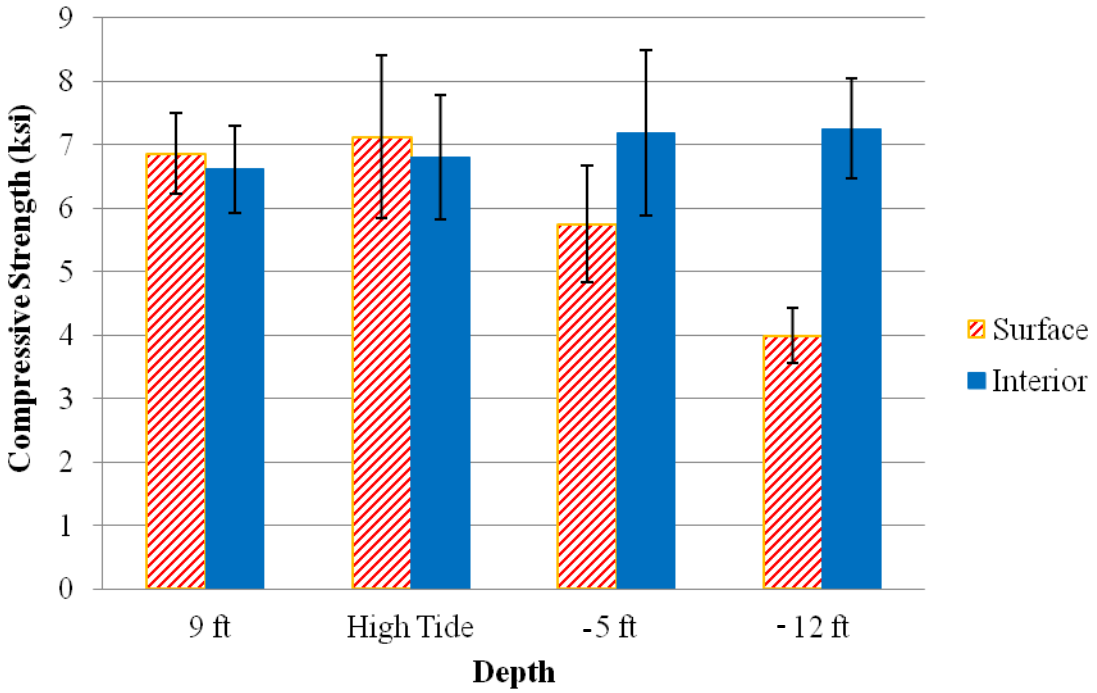

Figure 3.28: Compressive strength of surface versus interior concrete

3.3.4 X-Ray Diffraction

Powder X-ray diffraction (XRD) was performed on ground concrete samples to identify variances in the composition at various heights and depths into the cross section. Samples were taken at 9 ft. 2 ft, high tide, -5 ft, and -12 ft. Powder was obtained by taking a 3 in. diameter core through the section and then drilling at controlled increments using a 3/8 in. masonry bit. Powder was collected from the surface at ½ in. increment, then at 1 in. increments into the cross-section. The powder samples were then ground

with mortar and pestle and sieved through an 850 μm (No. 20) sieve. Figure 3.29 shows a prepared XRD sample.

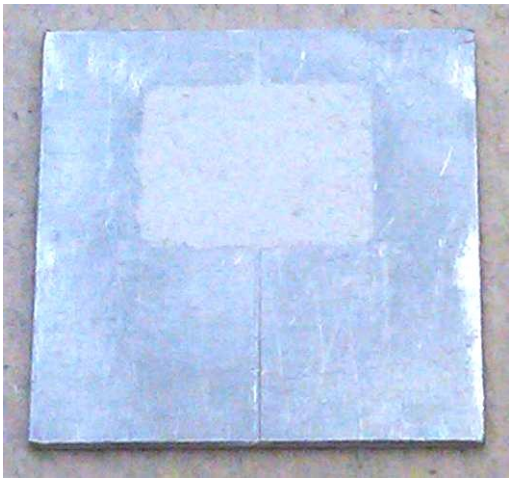

Figure 3.29: XRD sample

XRD analysis was performed using a Philip's X'Pert XRD system. The scan was performed over a 2θ range of 5˚ to 75˚ using a scan rate of 0.05˚ per second under Cu K-α radiation. Table 3.2 gives the notation used in labeling the peaks on the XRD profiles for each sample. In multiple incidences, peak locations for two or more phases overlapped. If other unique peaks for each phase were identified, then the shared peak was labeled for both phases.

The calcium carbonate (defined herein as Ca) phase represented the coarse aggregate in the concrete, as well as carbonated cement and calcium hydroxide. The quartz phase represented the fine aggregate used. The calcium hydroxide, ettringite, and gypsum phases occurred in the hydrated cement paste fraction of the sample. Calcium

silicate hydrate, the predominant product of portland cement hydration, is largely amorphous, producing a broad peak around 30^{o} on the 2θ scale.

Table 3.2: Chemical Symbols with Correlated Composition for XRD Profiles

Symbol	Composition
CH	Calcium Hydroxide
Ca	Calcium Carbonate (Calcite)
Q	Quartz
E	Ettringite
G	Gypsum

3.3.4.1 XRD Results from 9 ft above High Tide

The results at 9 ft above high tide are given in Figures 3.30 and 3.31 for the 0 to 0.5 in. and 0.5 to 1.5 in. increments, respectively. The results from these samples serve as a reference for samples located in the exposure zones of the piles. The 9 ft above high tide samples showed the same compositions at both depth increments. Quartz and calcium carbonate were present due to the coarse and fine aggregate. The peaks from the aggregate are more intense than the paste phases due to their increased volume fraction. Calcium hydroxide was detected, but no residual ettringite from hydration or gypsum. Additionally, the amorphous rise is present from a 2θ of approximately 20˚ to 75˚ and indicates the presence of non-crystalline phases like calcium silicate hydrate.

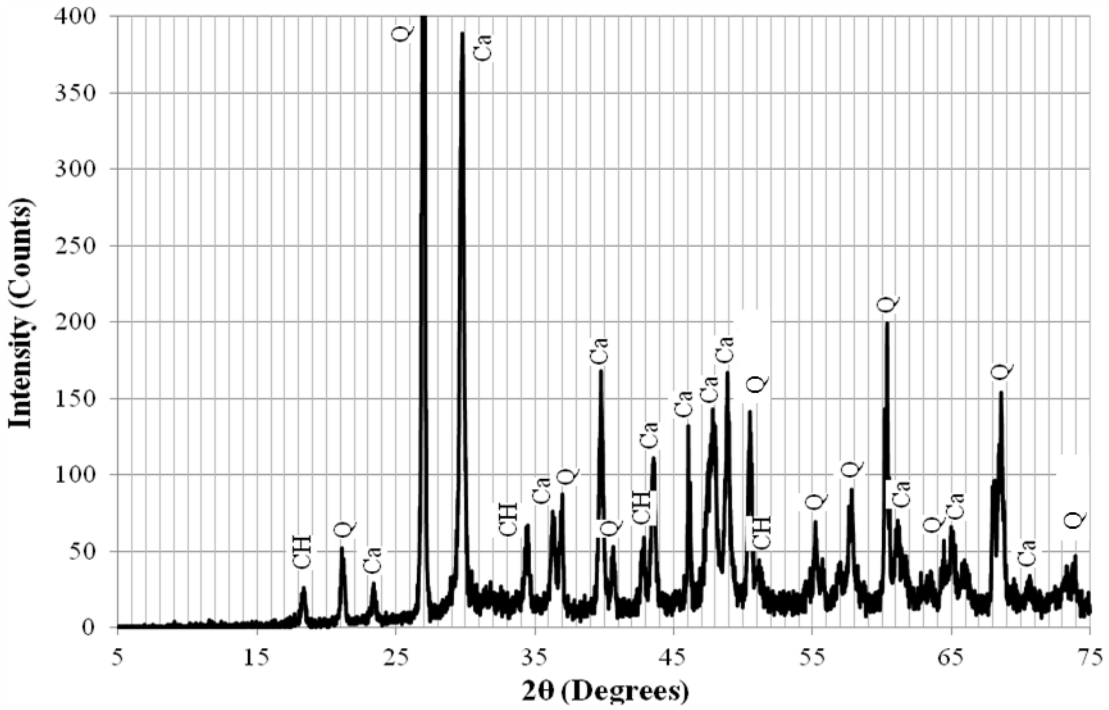

Figure 3.30: XRD profile for 9 ft above high tide at 0 – 0.5 in. increment into section

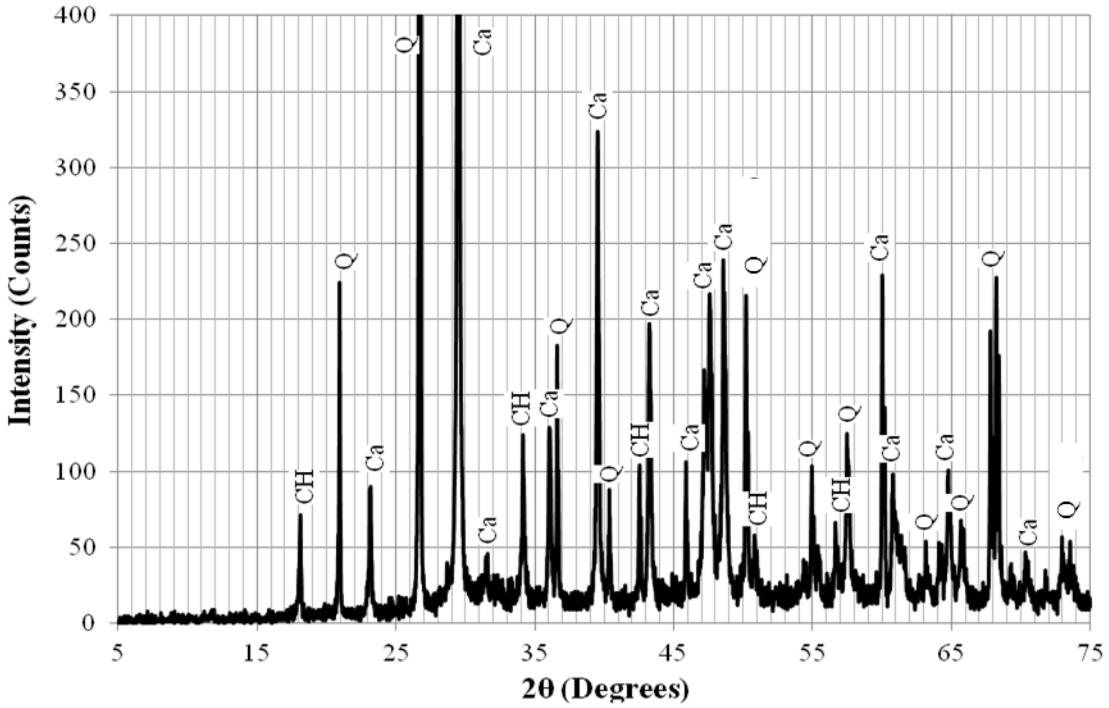

Figure 3.31: XRD profile for 9 ft above high tide at 0.5 – 1.5 in. increment into section

3.3.4.2 XRD Results from 2 ft above High Tide

Samples from 2 ft above high tide were taken to characterize the splash zone of the piles. Table 3.3 provides a summary of the results from all increments tested, where a check-mark represents the phase was present and an x-mark if not found in the increment. Calcium carbonate and quartz were detected in all samples.

Table 3.3: XRD results summary for 2 ft above high tide

	0-0.5"	0.5-1.5"	1.5-2.5"	2.5-3.5"	3.5-4.5"
Calcium Hydroxide	✓				
Ettringite	×				
Gypsum	✓	✓	✓	×	×
Calcite	✓				
Quartz	✓				

The XRD profiles for the 0-0.5 in., 0.5-1.5 in., 1.5-2.5 in., 2.5-3.5 in., and 3.5-4.5 in. increments are given in Figures 3.32, 3.33, 3.34, 3.35, and 3.36, respectively. The results show the presence of gypsum near the surface, but it was not detected deeper than 2.5 in. into the section, and no ettringite was detected. The presence of gypsum may result from prolonged exposure to brackish water, which contains large amounts of sodium sulfate and magnesium sulfate. The sulfate concentration was measured to be 1527 mg/L at the Turtle River Bridge during high tide. Calcium hydroxide was present at all depths sampled, suggesting that an alkaline pH was maintained. The XRD profiles deeper than 2.5 in. into the section are identical to the reference samples from 9 ft above high tide at the 1.5-in. depth, which suggest that no significant changes to the microstructure have occurred in those increments. At +9-ft., no samples were taken at depths more than 1.5 in.

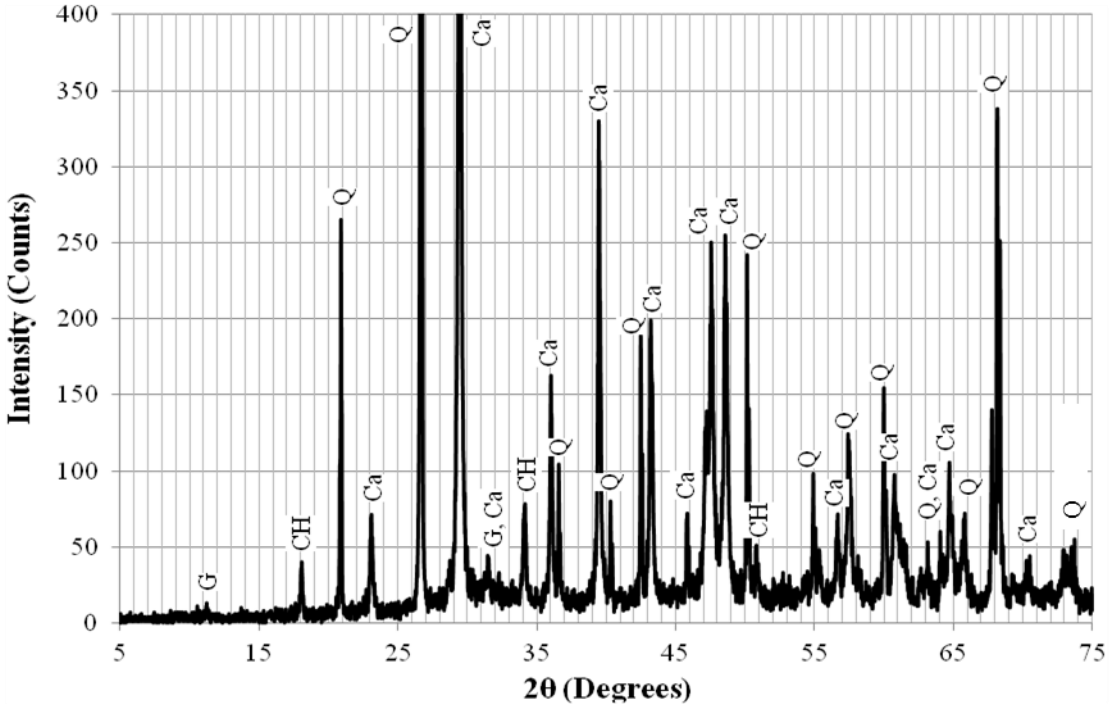

Figure 3.32: XRD profile for 2 ft above high tide at 0 – 0.5 in. increment into section

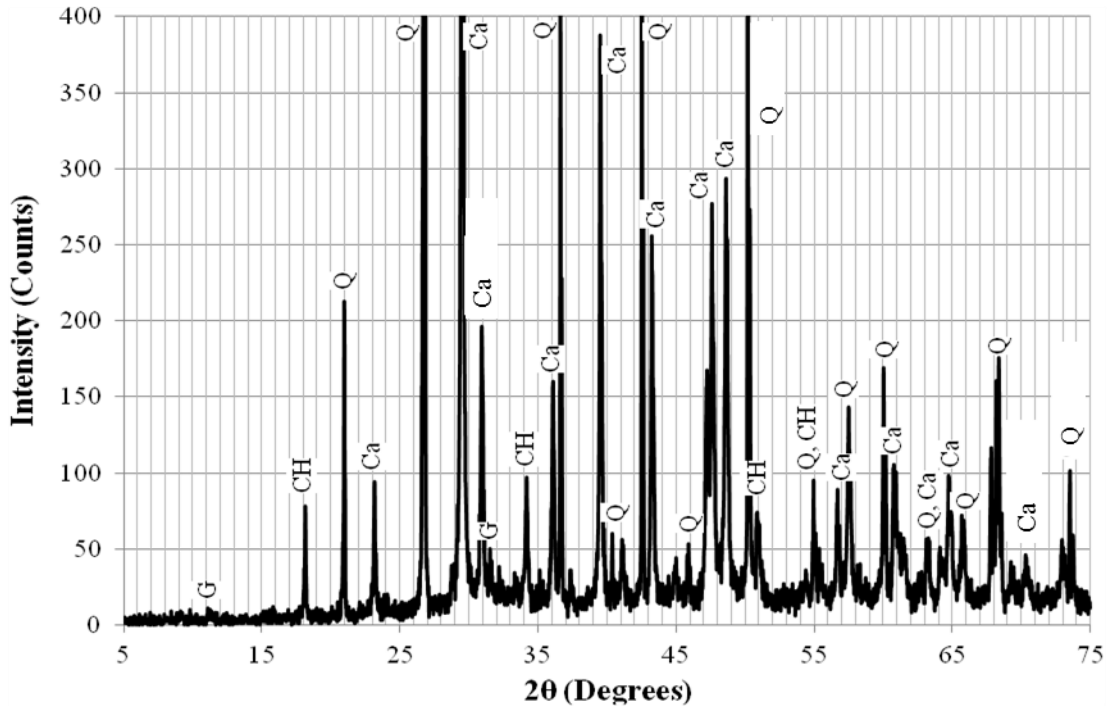

Figure 3.33: XRD profile for 2 ft above high tide at 0.5 – 1.5 in. increment into section

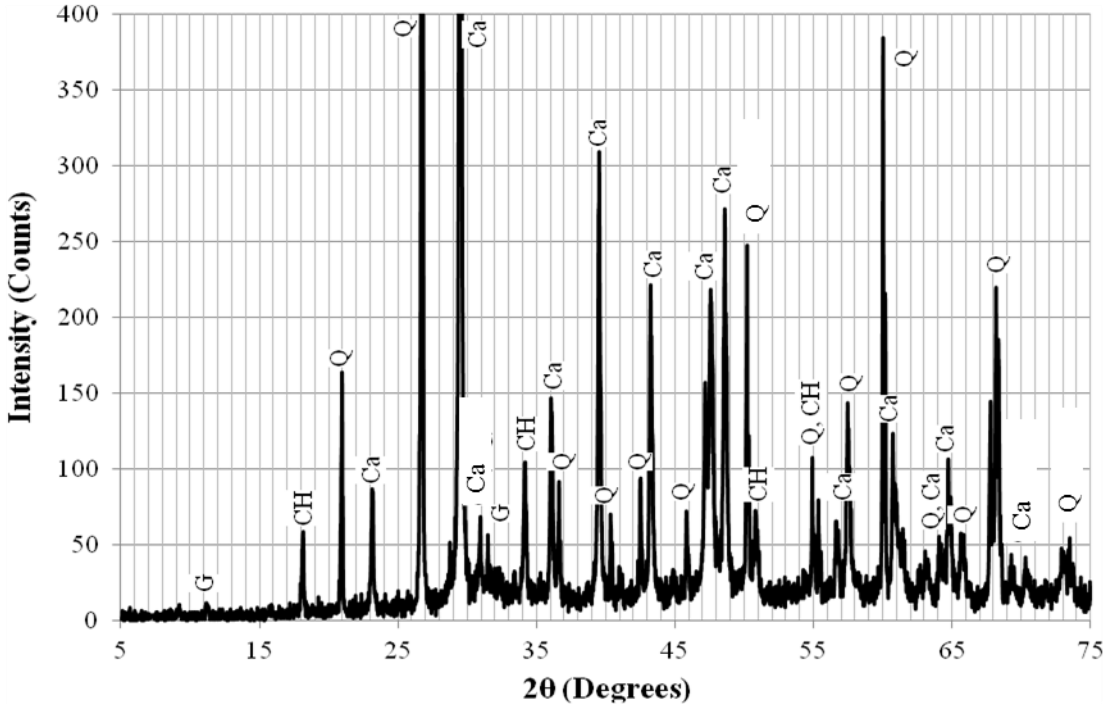

Figure 3.34: XRD profile for 2 ft above high tide at 1.5 – 2.5 in. increment into section

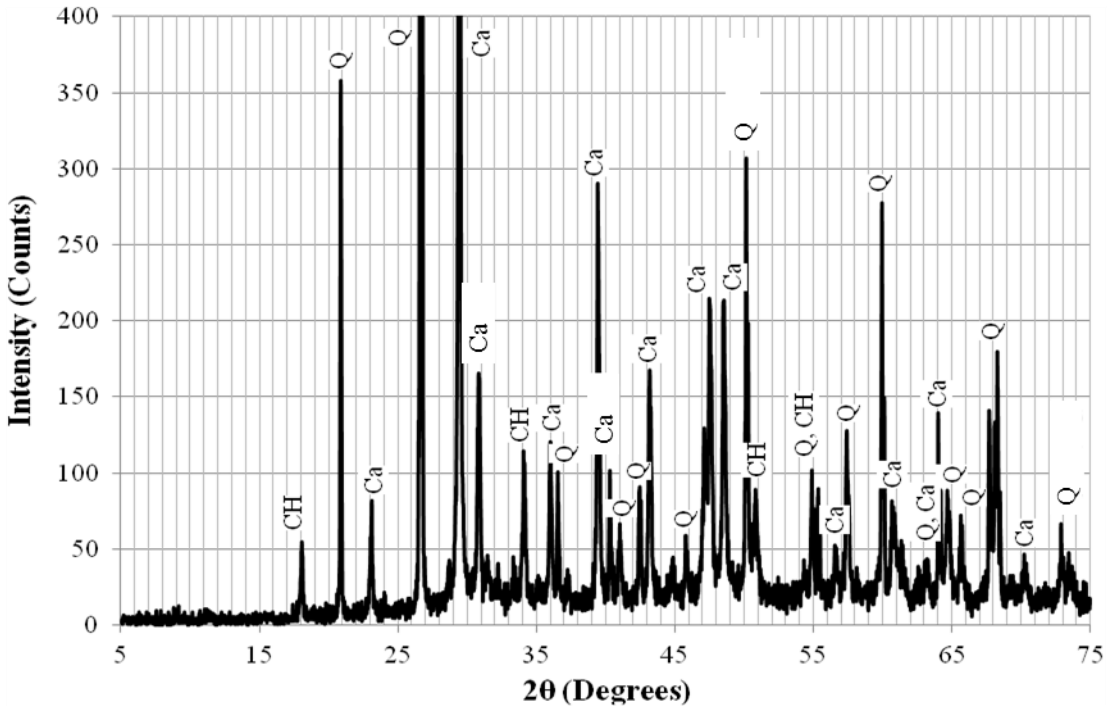

Figure 3.35: XRD profile for 2 ft above high tide at 2.5 – 3.5 in. increment into section

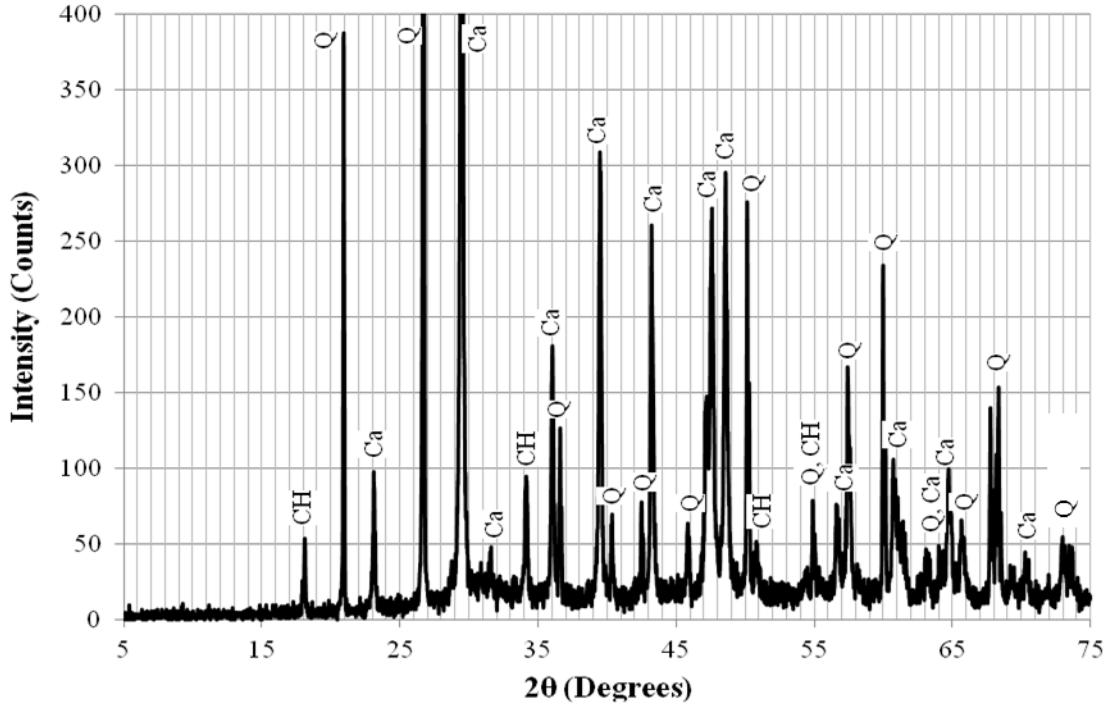

Figure 3.36: XRD profile for 2 ft above high tide at 3.5 – 4.5 in. increment into section

3.3.4.3 XRD Results from High Tide Region

Table 3.4 provides a summary of the results from all increments tested at the high tide region of the pile.

Table 3.4: XRD results summary for high tide

	0-0.5"	0.5-1.5"	1.5-2.5"	2.5-3.5"	3.5-4.5"
Calcium Hydroxide	✓				
Ettringite	✓	✓	×	✓	×
Gypsum	✓				
Calcite	✓				
Quartz	✓				

The XRD profiles for the 0-0.5 in., 0.5-1.5 in., 1.5-2.5 in., 2.5-3.5 in., and 3.5-4.5 in. increments can be found in Figures 3.37, 3.38, 3.39, 3.40, and 3.41, respectively. The results show a small presence of ettringite in the surface to 3.5 in. depth increments, and gypsum throughout the depth. Calcium hydroxide was present at all depths, but the intensity near the surface is greatly reduced from the other increments. These results suggest changes in the microstructure from the reference samples that are consistent with sulfate attack. The presence of ettringite at depths nearer to the surface and gypsum throughout the section depth suggest that sulfate ions were able to penetrate through much of the depth of the pile at the high tide location.

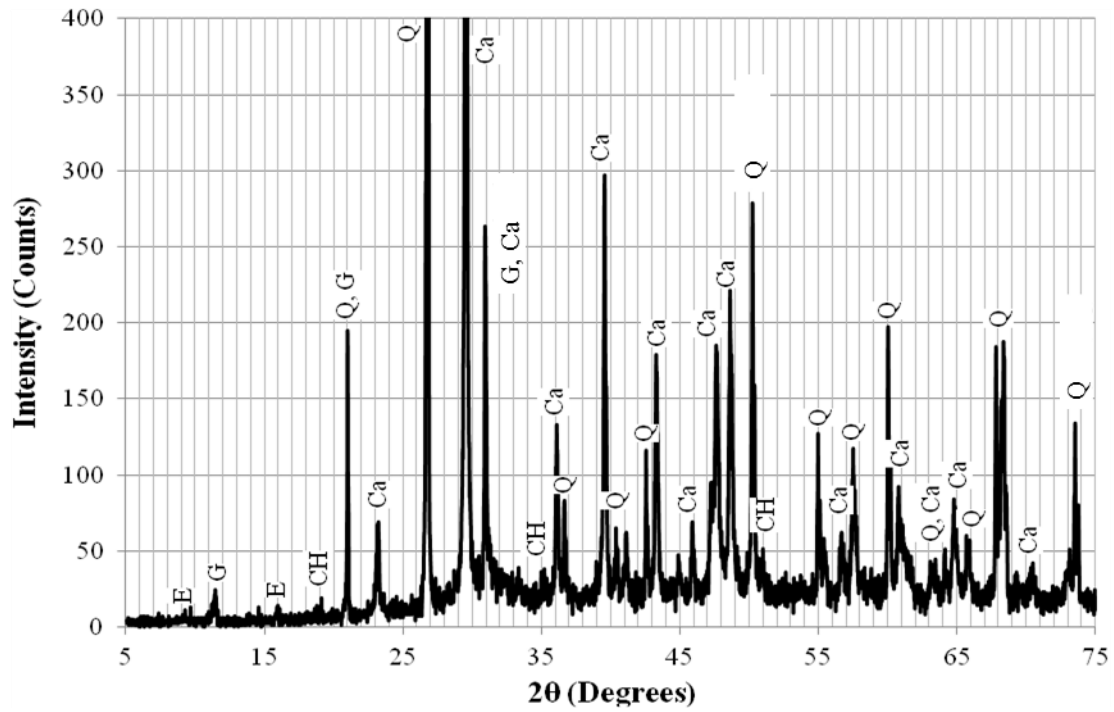

Figure 3.37: XRD profile for high tide region at 0 – 0.5 in. increment into section

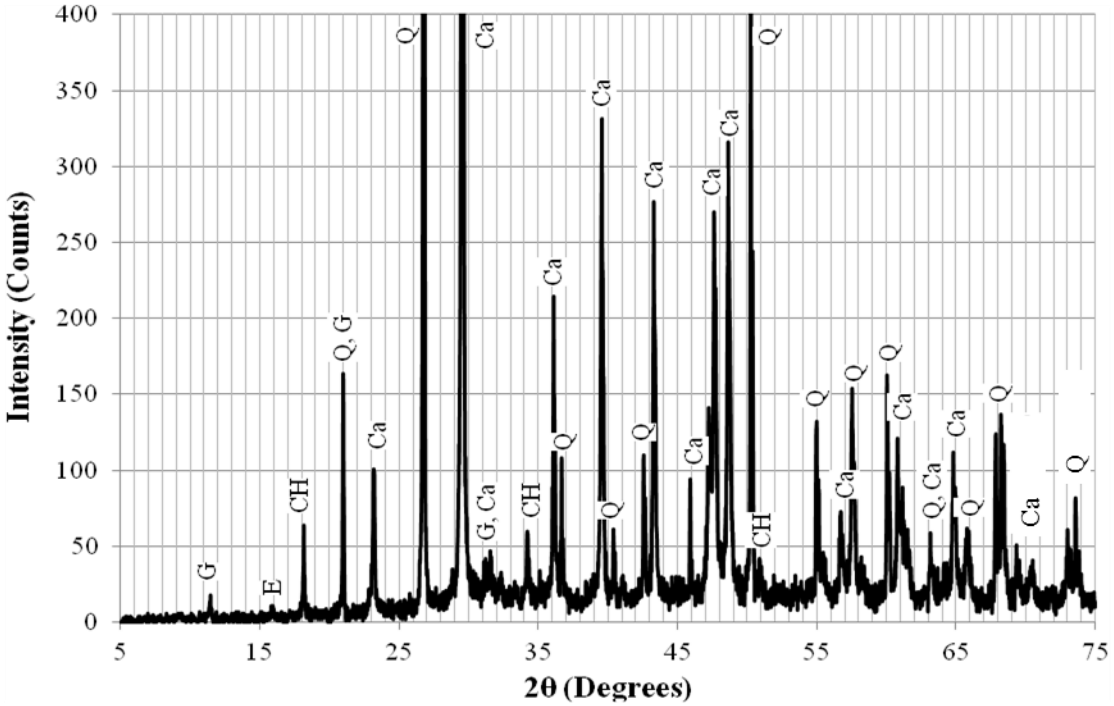

Figure 3.38: XRD profile for high tide region at 0.5 – 1.5 in. increment into section

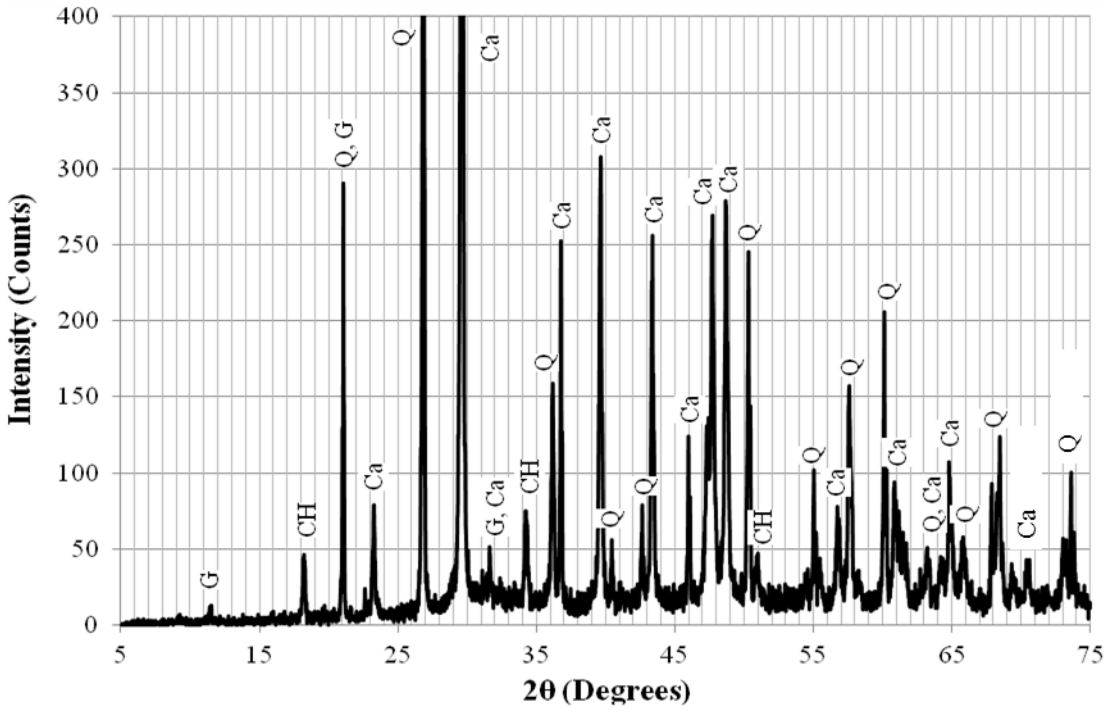

Figure 3.39: XRD profile for high tide region at 1.5 – 2.5 in. increment into section

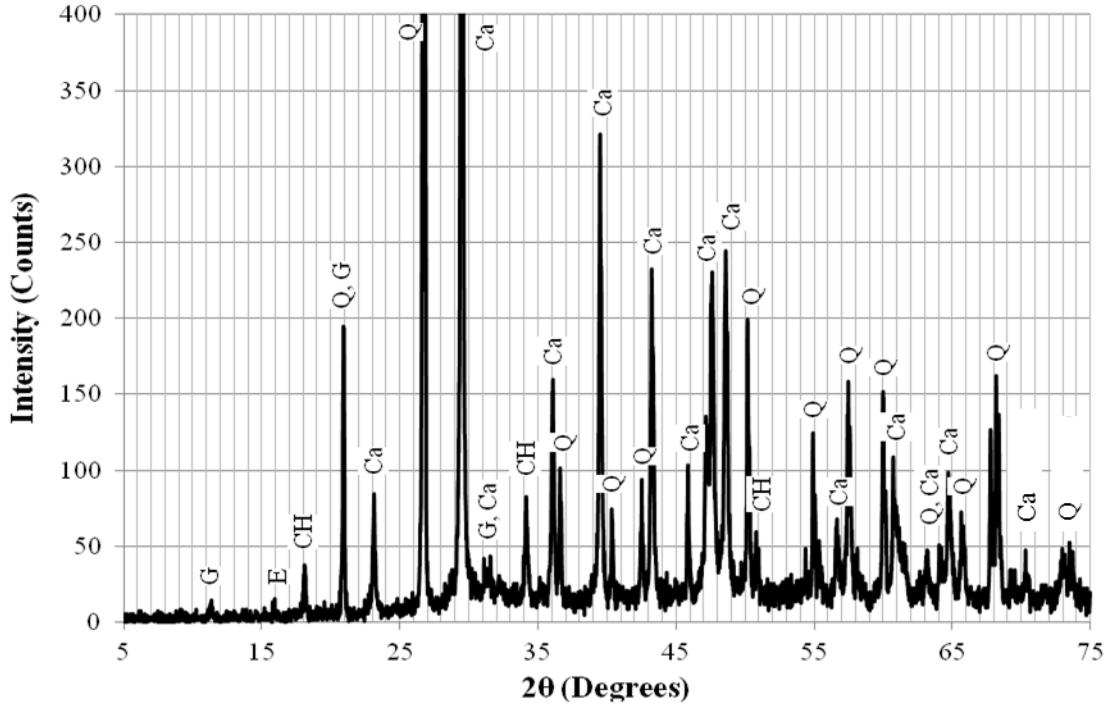

Figure 3.40: XRD profile for high tide region at 2.5 – 3.5 in. increment into section

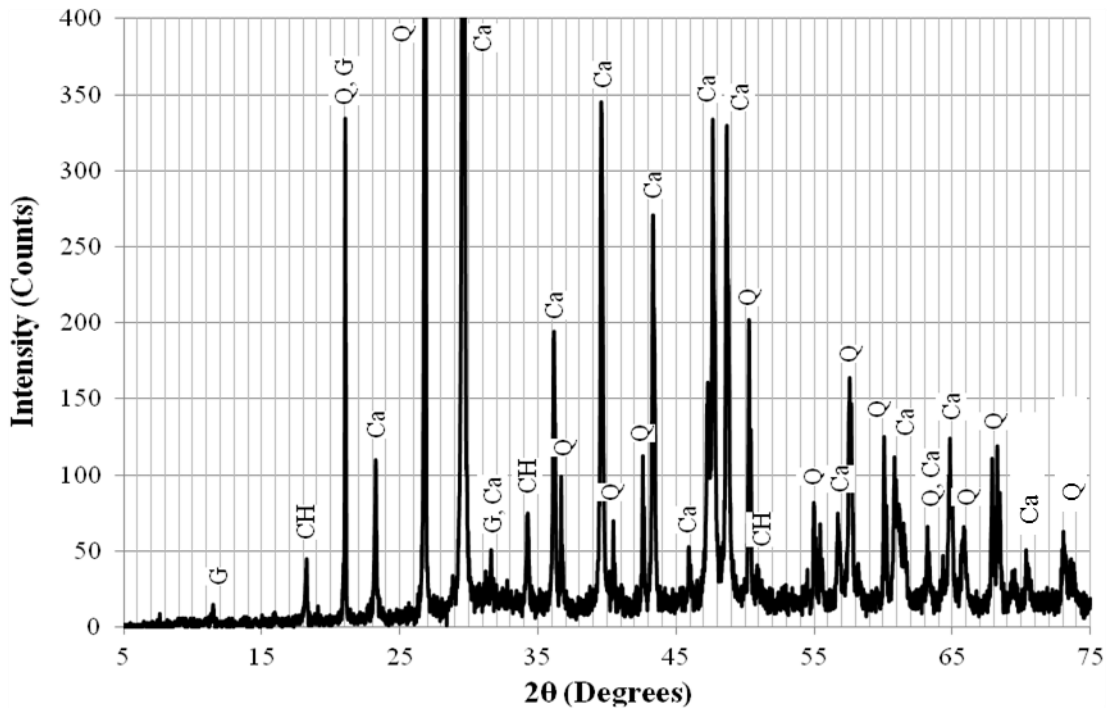

Figure 3.41: XRD profile for high tide region at 3.5 – 4.5 in. increment into section

3.3.4.4 XRD Results from 5 ft below High Tide

Samples from 5 ft below high tide were taken to characterize the low tide region of the piles. Table 3.5 provides a summary of the results from all increments tested.

Table 3.5: XRD results summary for 5 ft below high tide

	0-0.5"	0.5-1.5"	1.5-2.5"	2.5-3.5"	3.5-4.5"
Calcium Hydroxide	×	×	✓	✓	✓
Ettringite	✓	×	×	×	×
Gypsum	✓				
Calcite	✓				
Quartz	✓				

The XRD profiles for the 00-0.5 in., 0.5-1.5 in., 1.5-2.5 in., 2.5-3.5 in., and 3.5-4.5 in. increments can be found in Figures 3.42, 3.43, 3.44, 3.45, and 3.46, respectively. The results show a small presence of ettringite at the surface, and gypsum throughout the depth. Calcium hydroxide was not detected in the outer 1.5 in. of the section, but was present in depth increments farther into the section. These results, like the others presented previously, suggest changes in the microstructure compared to the reference samples that are consistent with sulfate attack and carbonation.

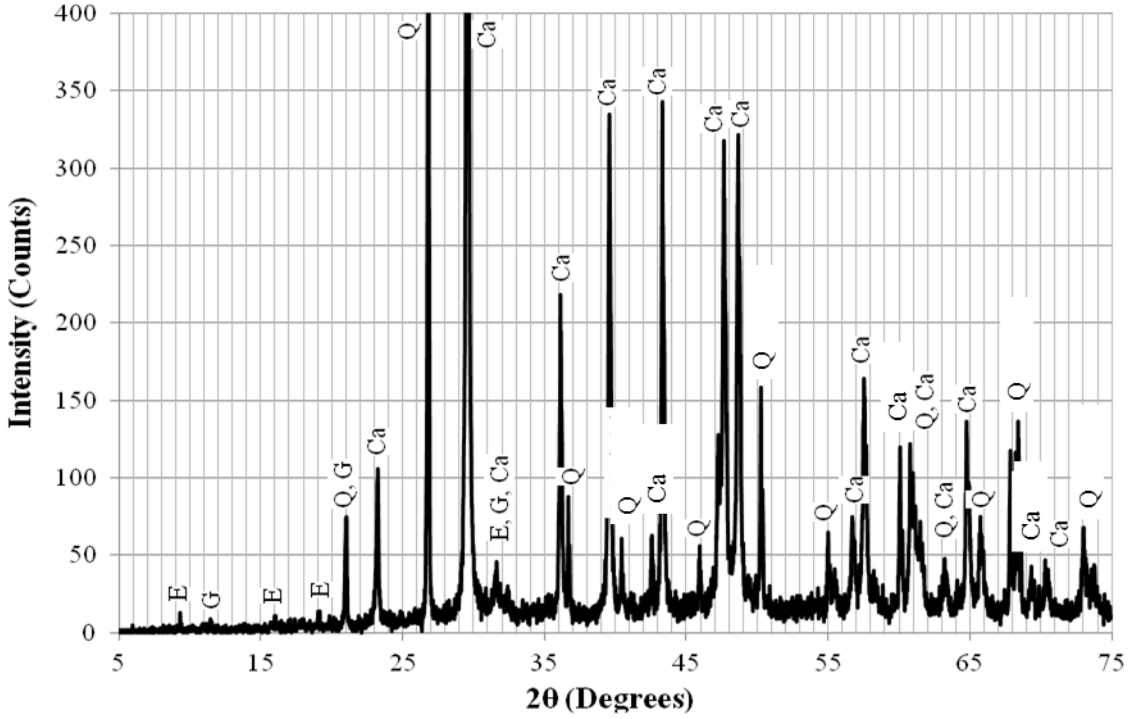

Figure 3.42: XRD profile for 5 ft below high tide at 0 – 0.5 in. increment into section

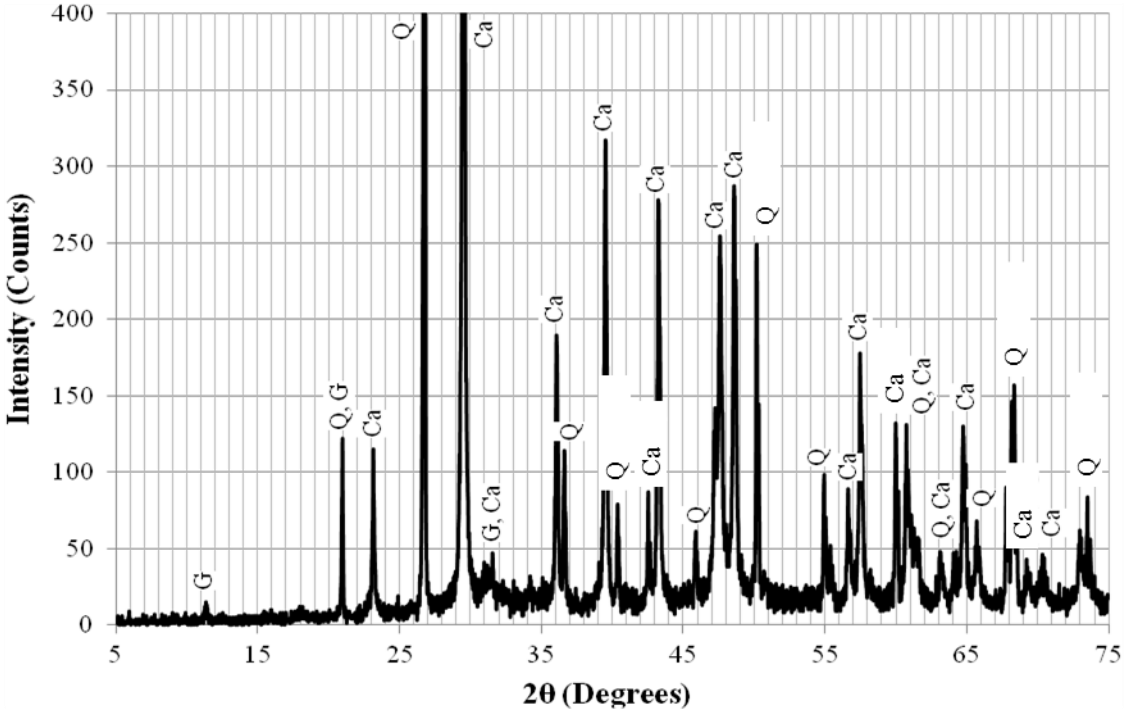

Figure 3.43: XRD profile for 5 ft below high tide at 0.5 – 1.5 in. increment into section

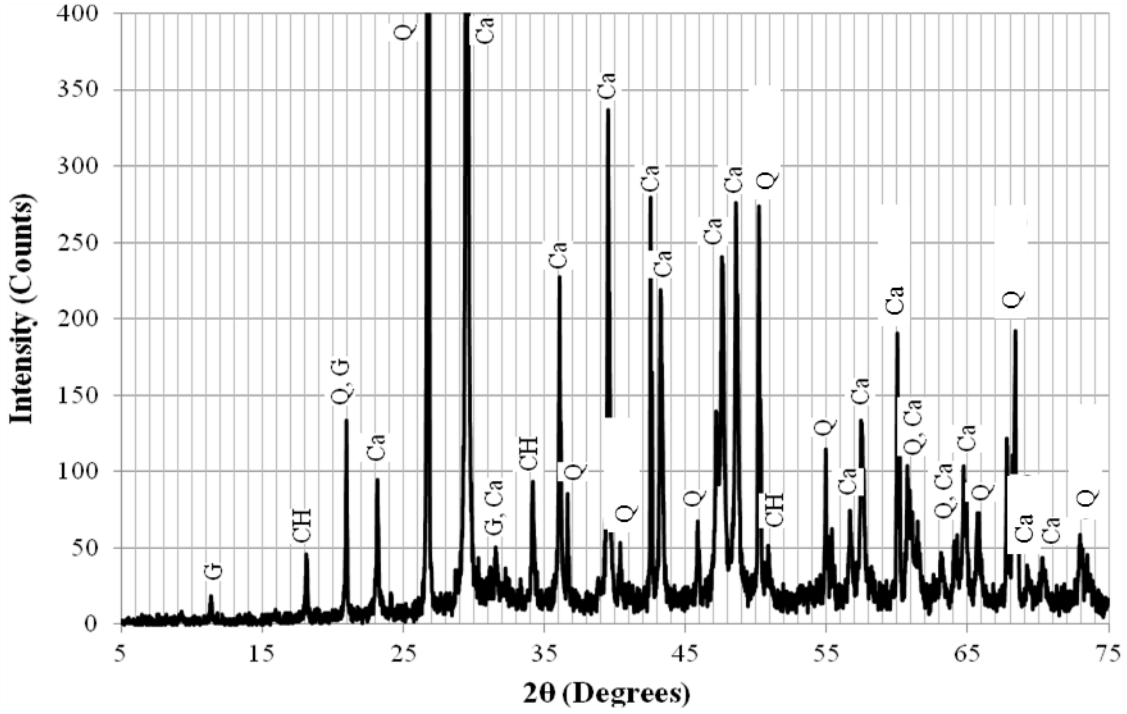

Figure 3.44: XRD profile for 5 ft below high tide at 1.5 – 2.5 in. increment into section

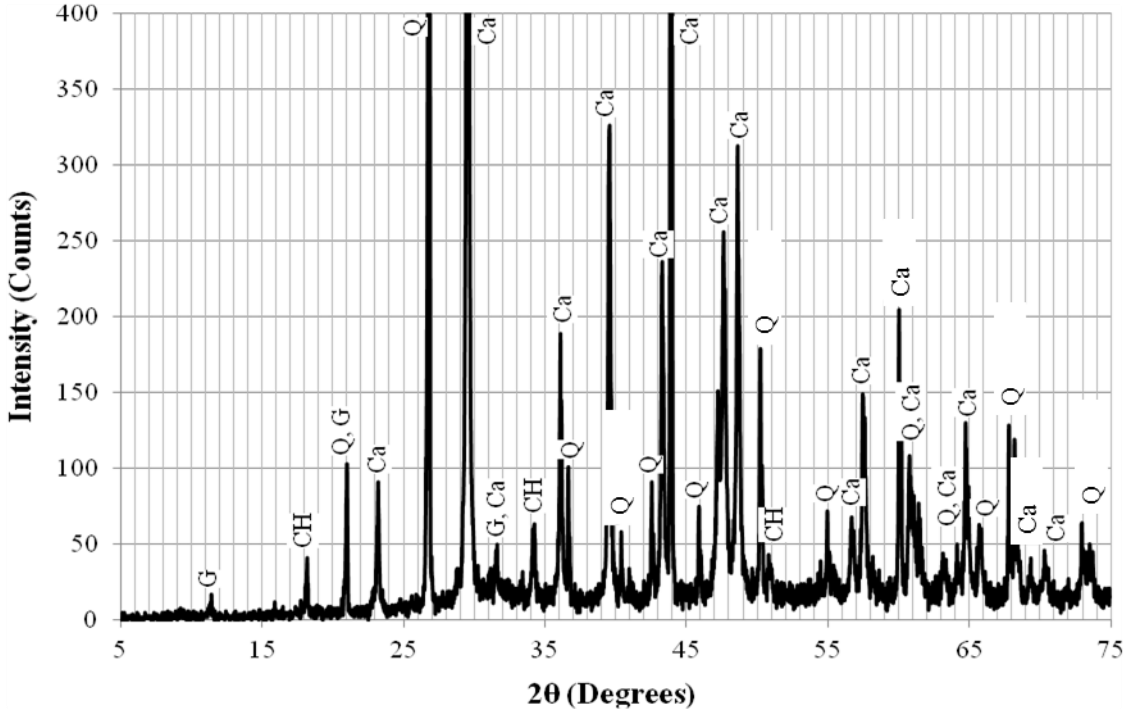

Figure 3.45: XRD profile for 5 ft below high tide at 2.5 – 3.5 in. increment into section

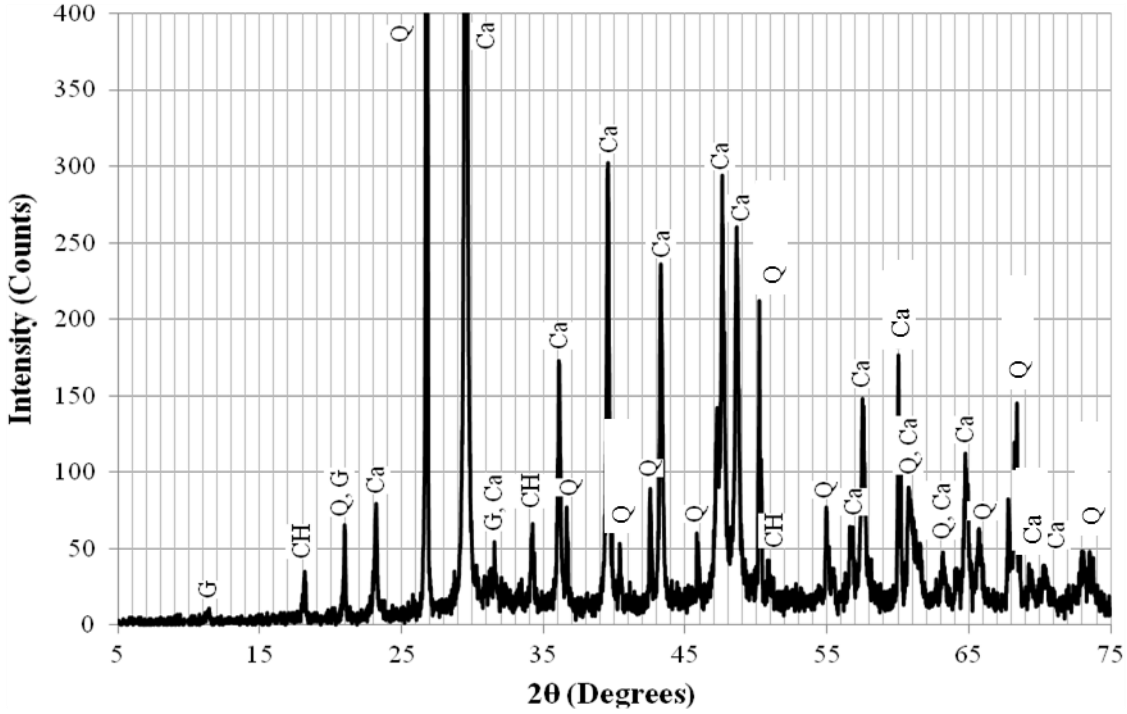

Figure 3.46: XRD profile for 5 ft below high tide at 3.5 – 4.5 in. increment into section

3.3.4.5 XRD Results from 12 ft below High Tide

Samples from 12 ft below high tide were taken to characterize the submerged region of the piles. Table 3.6 provides a summary of the results from all increments tested.

Table 3.6: XRD results summary for 12 ft below high tide

	0-0.5"	0.5-1.5"	1.5-2.5"	2.5-3.5"	3.5-4.5"
Calcium Hydroxide	×	×	✓	✓	✓
Ettringite	✓	✓	×	×	×
Gypsum	✓				
Calcite	✓				
Quartz	✓				

The XRD profiles for the 0-0.5 in., 0.5-1.5 in., 1.5-2.5 in., 2.5-3.5 in., and 3.5-4.5 in. increments can be found in Figures 3.47, 3.48, 3.49, 3.50, and 3.51, respectively. The results show a presence of ettringite near the surface, and gypsum throughout the depth. Calcium hydroxide was not detected in the outer 1.5 in. of the section, but was present at deeper depths into the section. These results suggest changes in the microstructure compared to the reference samples that are consistent with sulfate attack. The lack of calcium hydroxide near the surface also suggests carbonation and/or leaching.

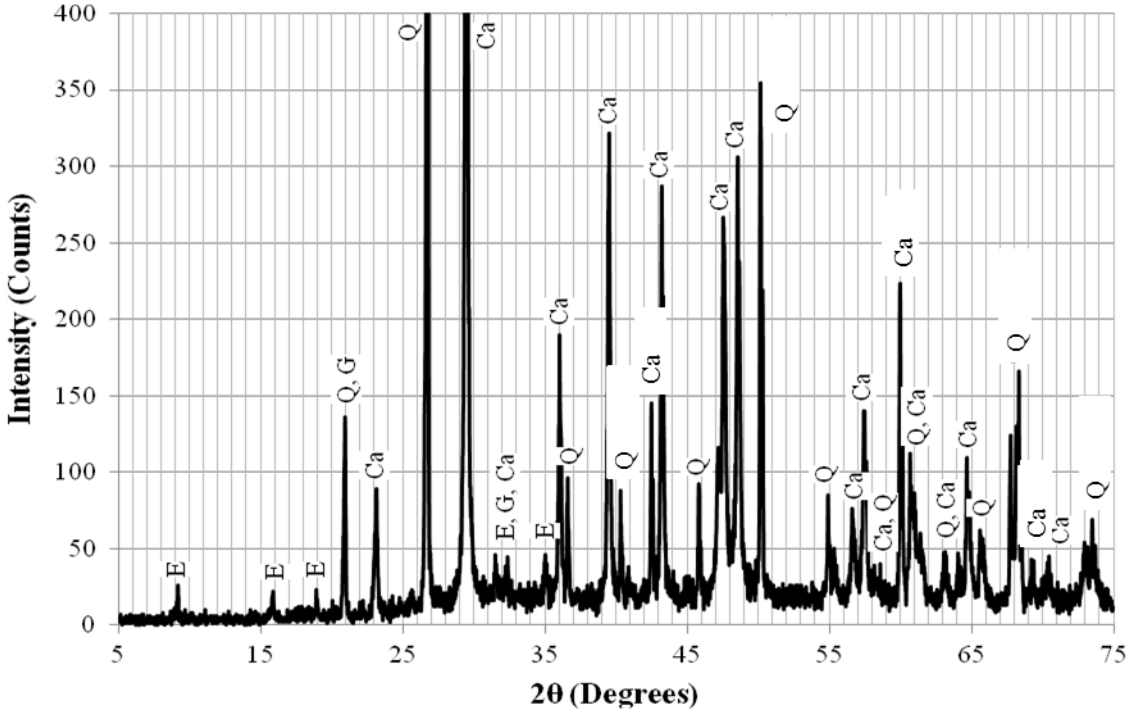

Figure 3.47: XRD profile for 12 ft below high tide at 0 – 0.5 in. increment into section

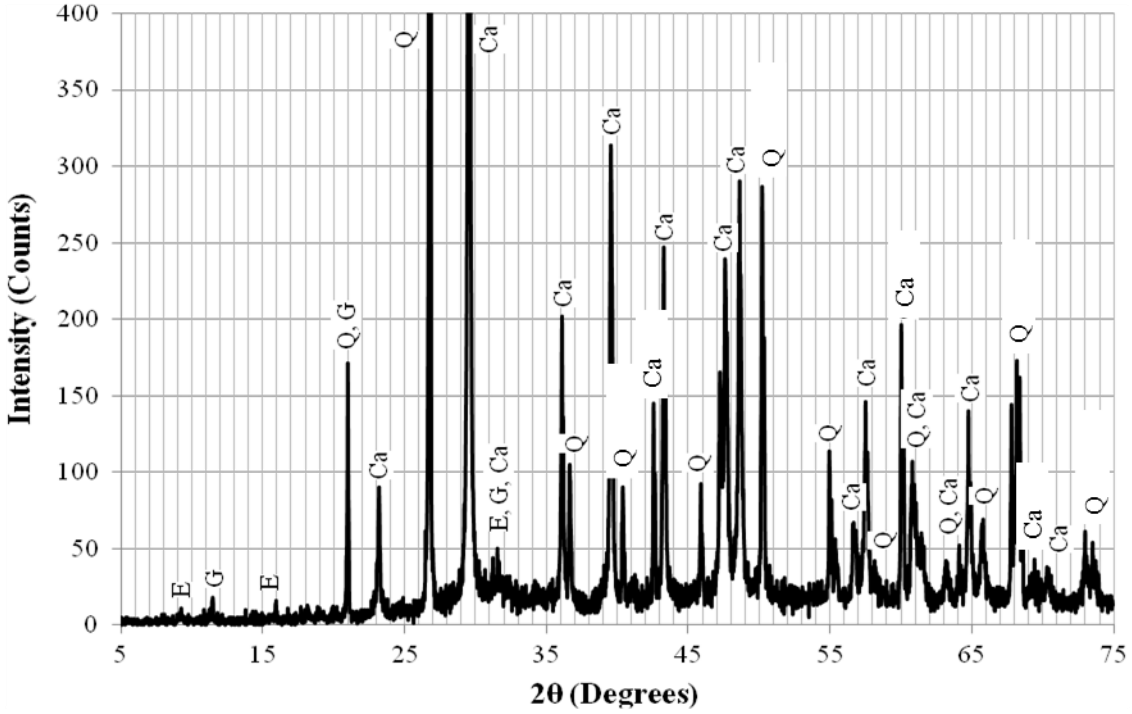

Figure 3.48: XRD profile for 12 ft below high tide at 0.5 – 1.5 in. increment into section

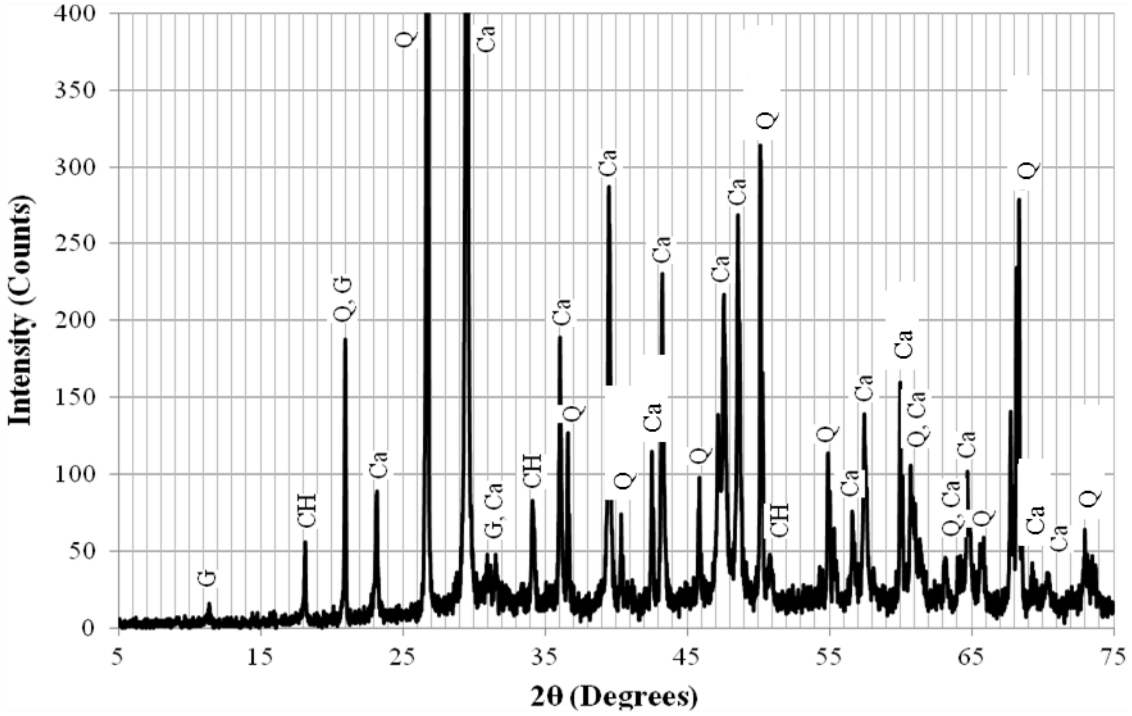

Figure 3.49: XRD profile for 12 ft below high tide at 1.5 – 2.5 in. increment into section

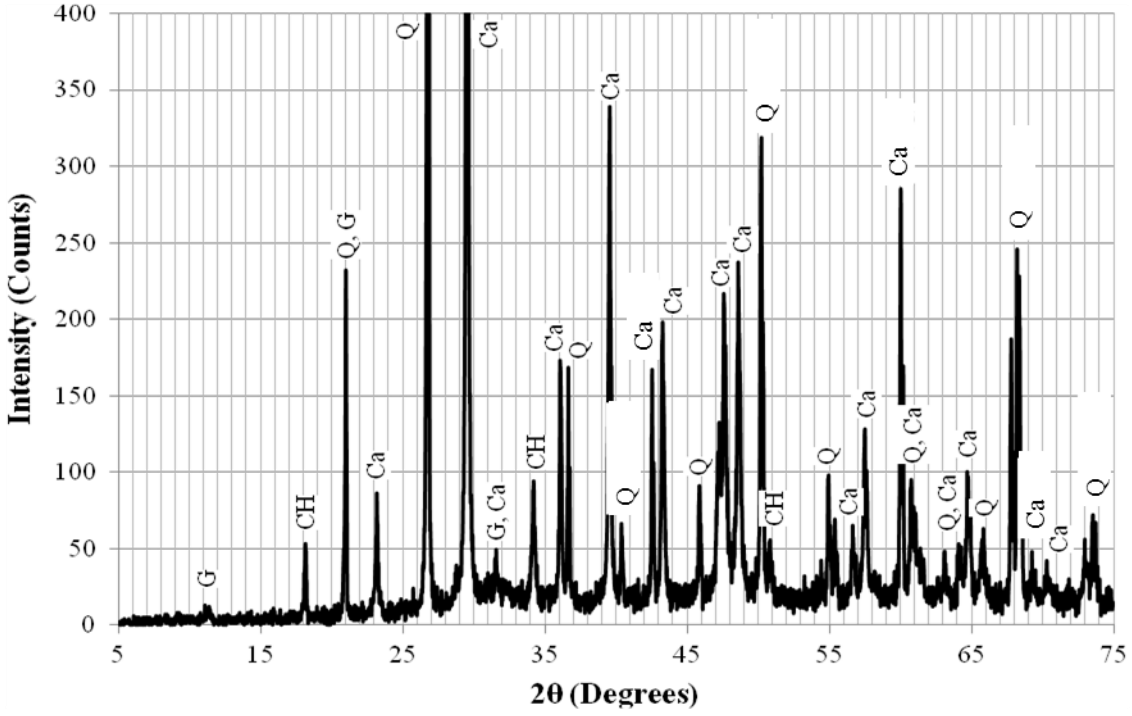

Figure 3.50: XRD profile for 12 ft below high tide at 2.5 – 3.5 in. increment into section

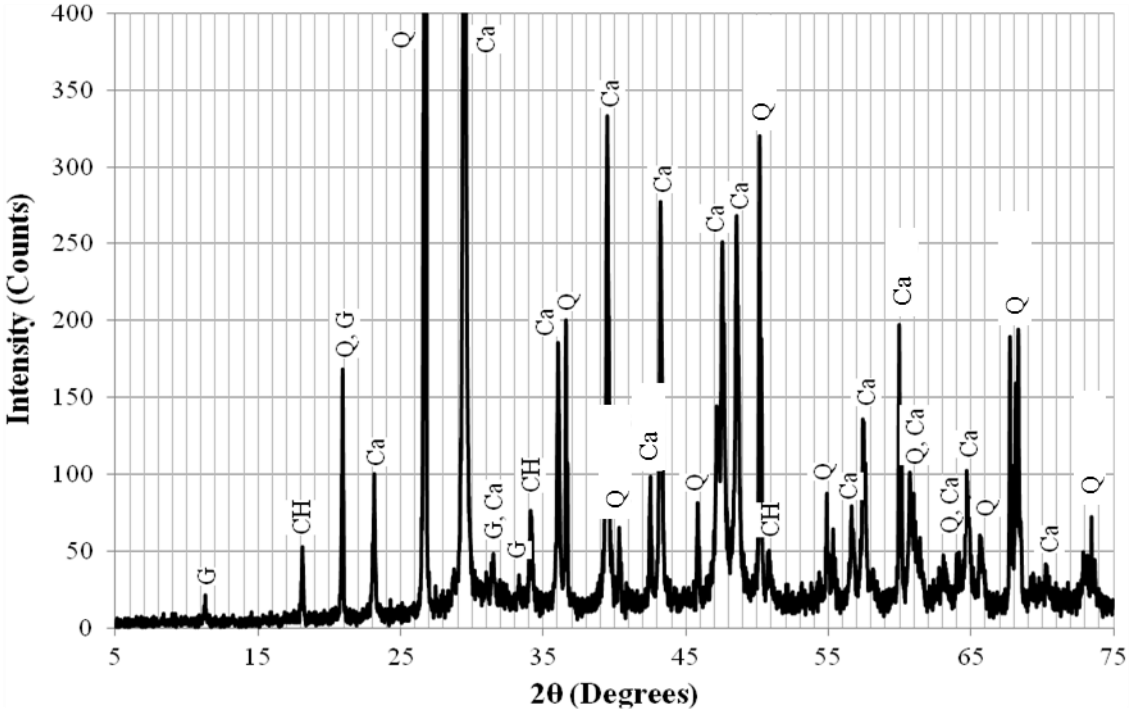

Figure 3.51: XRD profile for 12 ft below high tide at 3.5 – 4.5 in. increment into section

3.3.5 Thermo-Gravimetric Analysis

Thermo-gravimetric analysis (TGA) was performed on ground concrete samples to identify variations in the composition at various heights and depths into the cross section. Samples were taken at 9 ft. and 2 ft above high tide, at high tide, and at -5 ft, and -12 ft. Powder was obtained by taking a 3 in. diameter core through the section and then drilling at controlled increments using a 3/8 in. masonry bit. Powder was collected from the surface in ½ in. increment, then in 1 in. increments into the cross-section. The powder samples were then ground with mortar and pestle and sieved through an 850 μm (No. 20) sieve.

The analysis was performed using a Seiko TG/DTA in accordance with ASTM E 1131 (2008). Approximately 30 mg of sample powder were placed in platinum pans and

brought to 100˚C and held for one hour to remove any remaining free water from the sample. After the initial hold period, the sample was heated at a rate of 10˚C per minute up to a maximum temperature of 950˚C, while continually measuring the mass of the sample.

TGA analysis allows for determination of phases present based upon mass loss over their degradation temperatures. Ettringite decomposes at temperatures less than 115˚C and is not easily determined using TGA due to degradation temperature coinciding with the evaporation of free water. C-S-H undergoes dehydration between 100˚C to 200˚C, and a decomposition and change in structure between 200˚C and 400˚C. Portlandite ($Ca(OH)_2$) undergoes dehydroxylation between 425˚C and 600˚C. Above 750˚C, calcium carbonate degrades. However, because the coarse aggregate used was primarily calcium carbonate, the mass loss in this temperature range does not represent only a degradation of calcium carbonate in the cement paste.

Figures 3.52 and 3.53 show the TGA mass loss curves for the 9 ft and 2 ft above high tide samples, respectively. Both curves show a consistent mass loss in the regions due to alteration of C-S-H and decomposition of portlandite. The mass loss due to alteration of C-S-H is a gradual change over the thermal range. The decomposition of portlandite occurs over a small temperature range near 425˚C. A consistent mass loss of 1% occurred in all of the samples at these depths due to the loss of portlandite. The presence of portlandite in all of the depths tested is consistent with the XRD results.

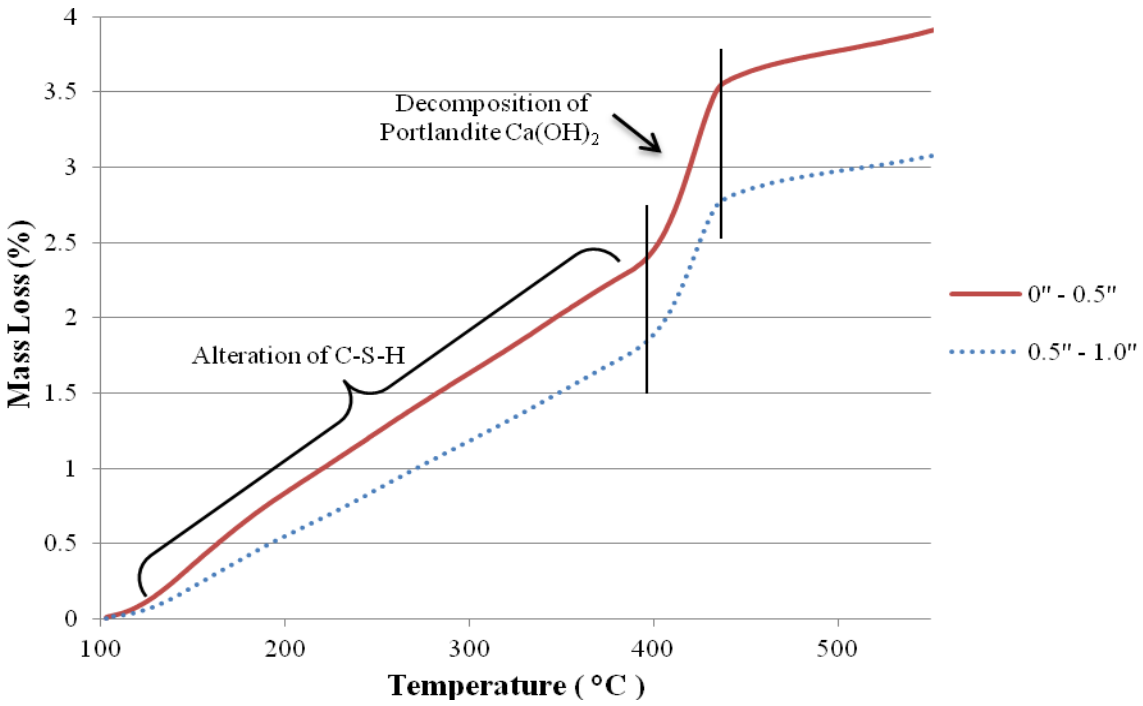

Figure 3.52: TGA for 9 ft above high tide

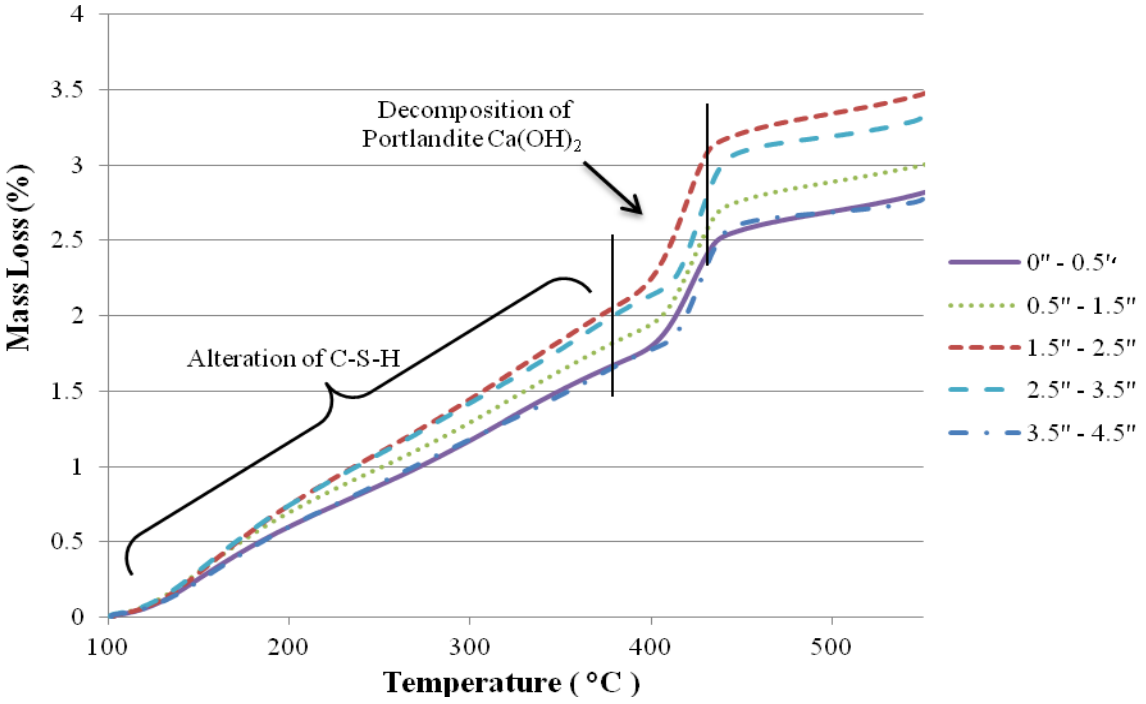

Figure 3.53: TGA for 2 ft above high tide

The results of TGA on the high tide region are shown in Figure 3.54. The samples from 0.5 in. and farther into the section are consistent with the 9 ft and 2 ft above high tide samples. There is a consistent mass loss due to degradation of portlandite present. The surface interval sample does not show an appreciable mass loss due to portlandite degradation. This is not in complete agreement with XRD results, which suggested a small amount of portlandite was present compared to the other increments tested at the depth. The TGA data may be more accurate due to the test giving quantitative characterization of phases present and being more sensitive to small amounts of phases present.

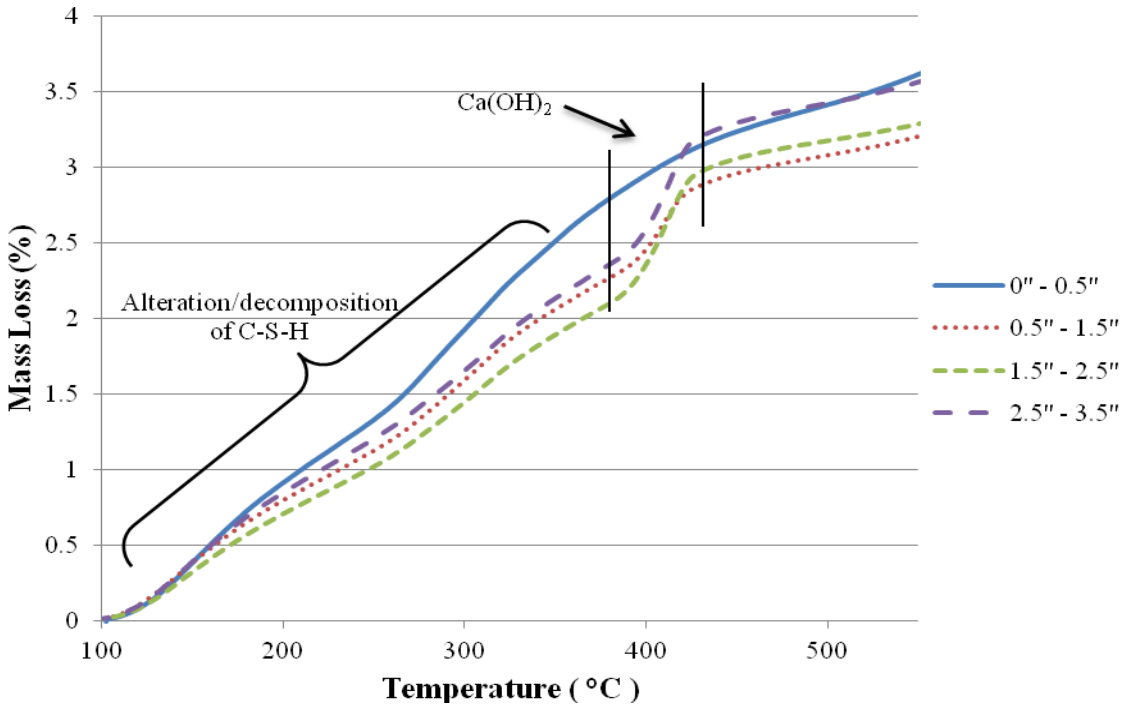

Figure 3.54: TGA for high tide region

The TGA results for 5 ft and 12 ft below high tide are shown in Figure 3.55 and 3.56, respectively. The surface interval on both data sets showed a decreased rate of mass loss between 100˚C and 400˚C than samples farther into the cross-section and at unsubmerged depths. This suggests that C-S-H was lost on the surface of the piles, most likely due to sulfate attack and carbonation. Additionally, the outer 1.5 in. of both samples showed an absence of portlandite. This is consistent with XRD results for these depths. Additionally, the mass loss during the degradation of portlandite decreased from the loss at 9 ft above high tide samples, suggesting a decreased amount present. These results are consistent with the damage patterns that would occur with sulfate attack.

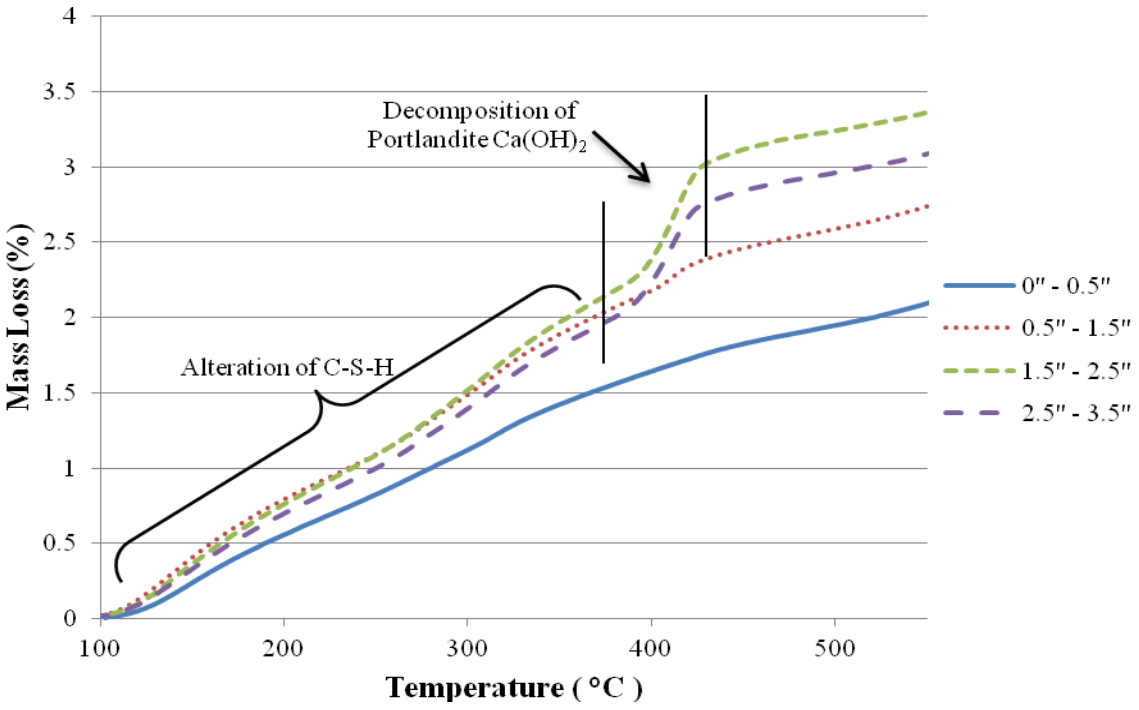

Figure 3.55: TGA for 5 ft below high tide

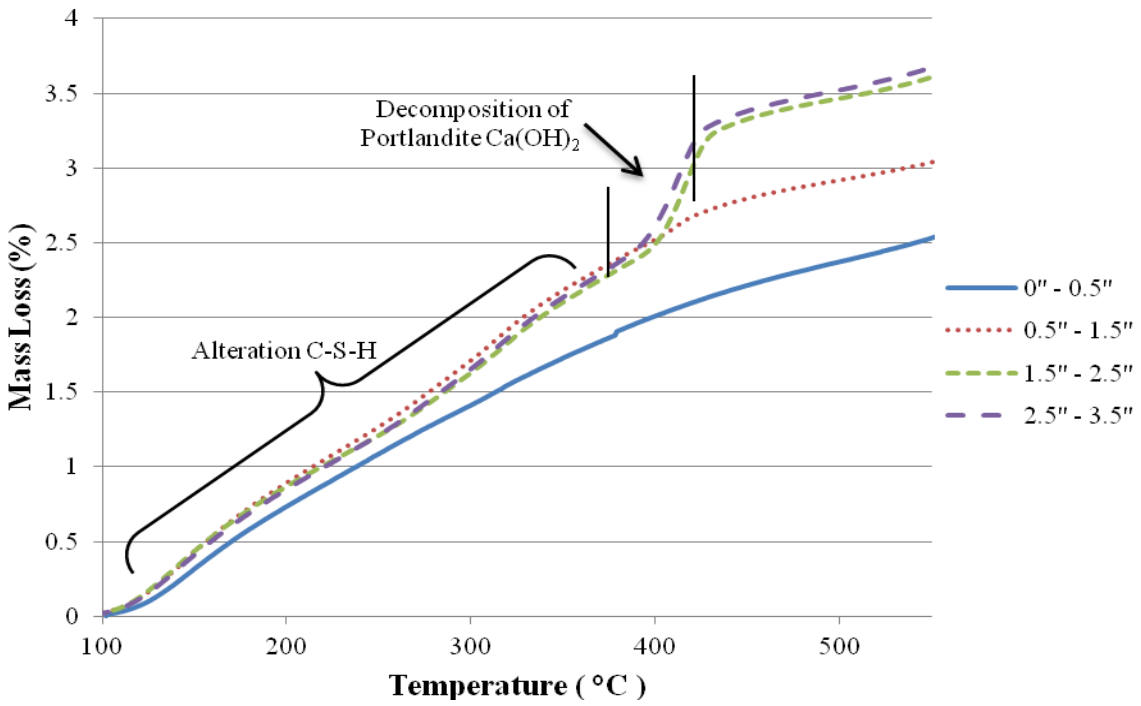

Figure 3.56: TGA for 12 ft below high tide

3.3.5 Conclusions, Sulfate Attack

The piles from the I-95 at Turtle River Bridge exhibited several characteristics of sulfate attack. The submerged regions of the piles showed an absence of calcium hydroxide near the surface, and the presence of gypsum and ettringite. This result is consistent with sulfate attack, which would lead to a decrease in calcium hydroxide near the surface, and the presence of ettringite and gypsum. Additionally, TGA suggested a decrease in C-S-H near the surface that is also consistent with carbonation and which would cause decreased compressive strength. Testing of cores for compressive strength showed a decrease of 45% near the surface of the pile in the submerged regions. The use of ASTM C 150 (2009) Type I cement, an ordinary rather than sulfate-resisting cement,

and a w/c of 0.50 could have allowed the sulfates from the surrounding water to ingress into the section over time and cause the extensive damage found.

3.4 Biodeterioration

There have been few reported cases of biological attack on coastal concrete structures. Here, a visual inspection and microscopic analysis techniques were used to characterize the biological attack on the piles.

3.4.1 Visual Inspection of Damage

A visual inspection was performed on the submerged region of the piles. No significant deterioration was visible until after cleaning the marine growth off of the surface of the piles. After removal of biological growth, large amounts of surface damage were visible. The damage, as seen in Figure 3.57, consisted of large pits on the surface of the piles. The damage was more pronounced along the corners of the piles, where the presence of boreholes and spalling were present. The pits occurred where coarse aggregate had been present on or near the surface of the piles.

(a)

(b)

Figure 3.57: Surface damage to concrete piling

Cores taken in the submerged region showed extensive damage to aggregate within 1.0 in. of the surface of the piles, as shown in Figure 3.58. Boreholes were present in aggregate near the surface in over 70% of cores taken. Damage was observed at over 1 in. depth into the section.

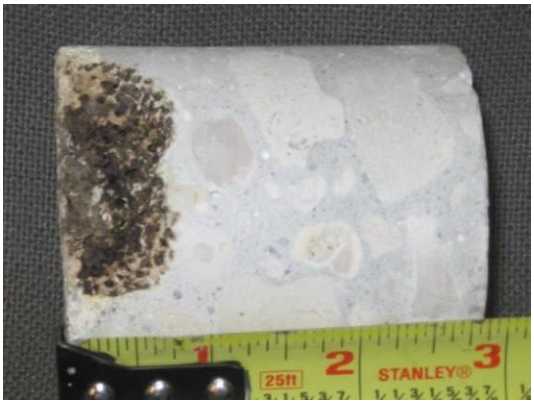

(a)

(b)

Figure 3.58: Boreholes in limestone aggregate of cores

The damage pattern observed visually was consistent with reported descriptions of Cliona borings on limestone and coral. A reported case of boring sponge attack was reported in Jamaica due to *Cliona lampa* (Scott, et al., 1988). The sponges burrowed through the limestone aggregate of concrete masonry blocks. The damage was primarily at the corners, and irregular shaped bore holes occurred in the aggregate. The sponges use etching secretions to penetrate calcium carbonate and form the boreholes (Nicol and Reisman, 1976). The genus *Cliona* sponges leave silicate spicules near the surface of their borings. The length of the spicules varies by species but is typically between 200 μm to 400 μm (Zea and Weil, 2003). Figure 3.59 shows spicules from *Cliona caribbaea*.

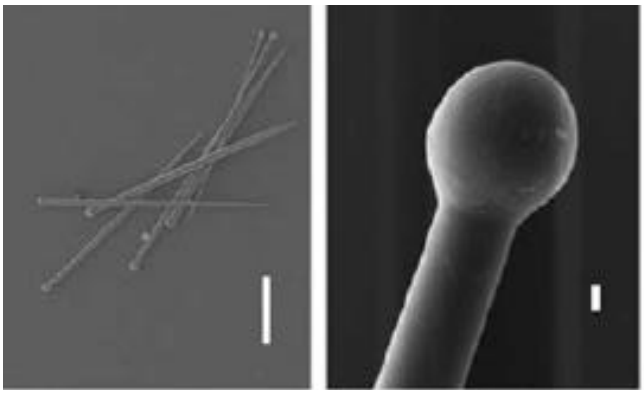

Figure 3.59: Spicules of *Cliona caribbea* (Zea and Weil, 2003)

There have been reports of *Cliona* sponges at Gardiner's Island, New York (Nicol and Reisman, 1976), along the coast of Virginia (Hopkins, 1962), Corpus Christi, Texas (Miller, et al., 2010), and off the coast of Jamaica (Scott, et al., 1988). Studies on the erosion rate of the sponge show that the rate may exceed 1 mm (0.04 in.) per year of ingress in solid limestone (Neumann, 1966). The rate of biological degradation of the limestone aggregate in these piles, >1 in. in 35 years, is consistent with the rate of attack

measured by Neumann (1966) for *Cliona* on solid limestone. The boring sponge is shown in Figure 3.60 on a coral reef.

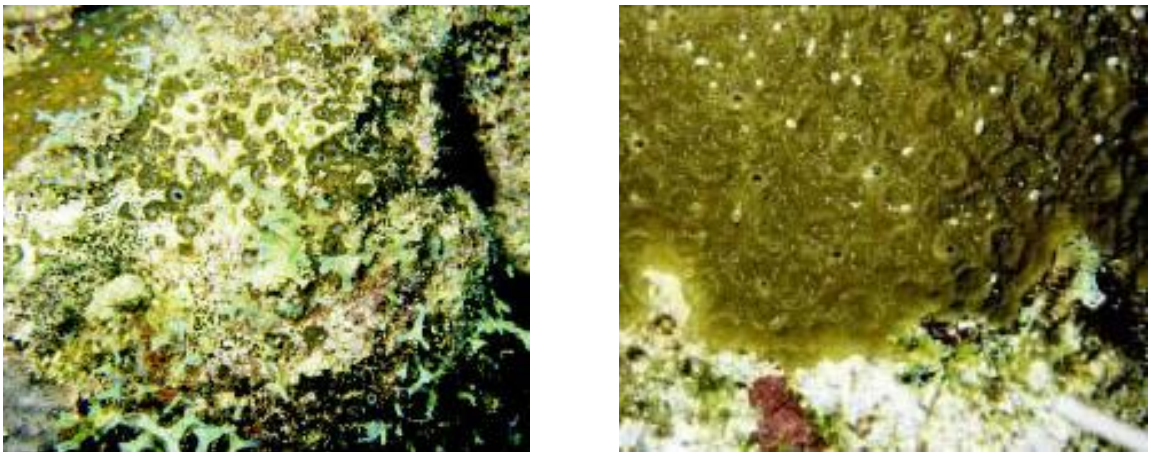

(a) (b)

Figure 3.60: *Cliona caribbaea* boring sponge (Zea, 2003)

3.4.2 Microscopy Characterization

Further investigation of the boreholes using environmental scanning electron microscopy at (ESEM) revealed the presence of rod-like structures. Energy dispersive x-ray analysis (EDS) of the rod-like structures revealed them to be highly silicate in composition. The rod-like structures inside of a borehole in the aggregate are shown in Figure 3.61, and the corresponding EDS spectrum is shown in Figure 3.62.

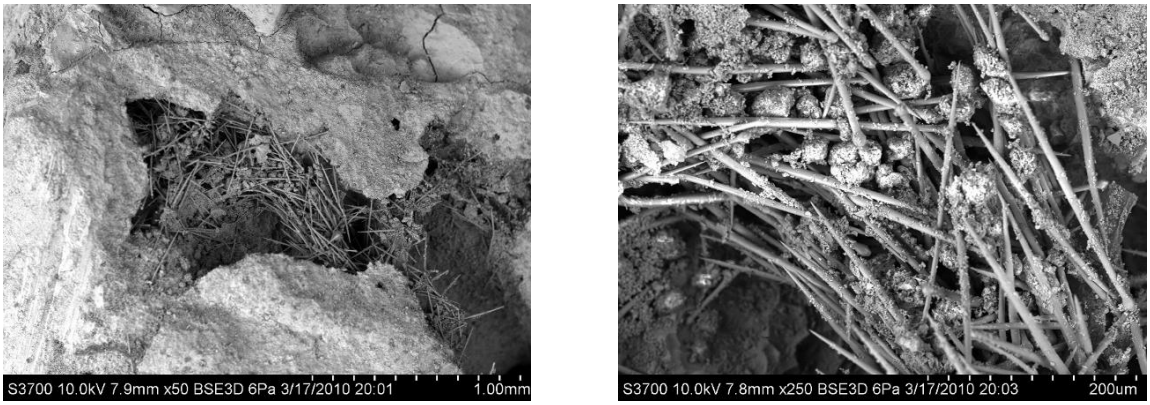

(a) (b)

Figure 3.61: (a,b) Silicate rod-like structures inside of boreholes through aggregate

(Courtesy of Robert Moser)

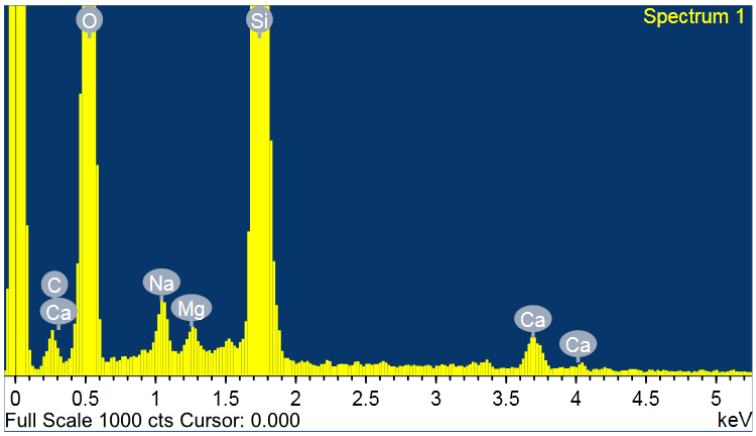

Figure 3.62: EDS spectrum of rod-like structures

(Courtesy of Robert Moser)

Characterization of the limestone aggregate by EDS showed that the aggregate was composed primarily of calcium carbonate. The types of calcite present were in agreement with XRD results. The composition of the aggregate suggests it is a Pleistocene limestone that is commonly found in southern Florida and the Bahamas.

Morphological and chemical comparison suggests that the rod-like structures resemble the siliceous spicules of *Cliona* boring sponges. The bioerosion patterns were similar to those reported by Scott (1988) in submerged concrete structures in Jamaica subjected to bioerosion from *Cliona caribbaea*. The patterns suggest that boring sponges are the most likely source of this form of damage to the piles. Further research is needed to better understand how the boring sponge damages the aggregate and to develop mitigation techniques for preventing damage in new construction.

3.5 Conclusions

3.5.1 Summary of Results

The forensic investigation of the I-95 at Turtle River Bridge piles revealed extensive damage from multiple deterioration mechanisms. Chloride-induced corrosion of the prestressing strands in the splash and tidal zones of the piling had induced cracking and delamination of the cover concrete as well as a loss of steel cross-section. The level of ingress of chloride ions suggested that the concrete was inadequate to provide 100+ year service life in the marine environment. Additionally, severe deterioration of the concrete due to sulfate attack and carbonation occurred in the submerged regions of the piles. A loss of over 40% of the compressive strength near the surface of the piles occurred due to loss C-S-H and the formation of ettringite and gypsum. Also, in the submerged regions of the piles, extensive damage to the coarse aggregate had occurred. This damage was likely caused by the presence of *Cliona* boring sponges. The piles exhibited extensive damage that led to the discovery of unexpected threats to bridge

substructures in marine environments, and the study emphasized the need for adequate protection from known environmental hazards.

3.5.2 Future Research Topics and Recommendations

The forensic investigation of the damage to the piles from the I-95 at Turtle River Bridge indicated a need for research in several areas as follows: (1) the development of high performance, normal strength concretes capable of withstanding sulfate attack, carbonation and chloride ingress to ensure service lives exceeding 100+ years while also meeting strength and design criteria necessary for precast concrete applications; (2) the development and implementation of corrosion resistant metallurgies possessing the mechanical properties necessary for use as prestressing strand; and (3) the investigation of biological attack on piles and assessment of a foundation of knowledge on the species causing attack, the rate and effects of their ingress, as well as methods of preventing and mitigating damage to existing piles.

The forensic investigation also demonstrated a need for changes in the construction materials used. First, eliminate the use of calcium carbonate-based (Limestone) aggregate to prevent a large source of nutrients for the biological life that attacked the surface of the piles. The use of limestone powder in cement has not yet been examined, but may also provide a source of nutrients for the biological life. Second, use an ASTM C 150 (2009) Type II or ASTM C 1157 (2004) Class MS cement in place of an ASTM C 150 (2009) Type I or III cement to mitigate the risk of sulfate attack on future concrete structures as recommended by ACI Committee 201 (2008). An ASTM C 150 (2009) Type III Cement can be used in conjunction with supplementary cementitious

materials or admixtures if the expansion for the ASTM C 1012 (2009) test meets the limits given by ACI Committee 201 (2008). Future research to be performed will develop draft design recommendations and concrete specifications to mitigate damage from the marine environment and allow for longer service lives.

(This page intentionally left blank.)

CHAPTER 4

Mix Design Development and Mechanical Properties

4.1 Development of Concrete Mix Designs

High performance marine concrete (HPMC) mix designs were developed with the goal of providing a 100+ year service life in Georgia's marine environment. This was performed by using the results of the forensic report (Chapter 3), coast trip report (Appendix A), and GDOT personnel interviews (Appendix B) to determine the durability characteristics and requirements that must be met to achieve this goal.

4.1.1 Concrete Mix Design

The mix designs investigated were developed to resist carbonation, sulfate attack, and to mitigate chloride induced corrosion of reinforcement as the primary durability concerns. Additionally, from the GDOT personnel interviews, it was recognized that the presence of cracking should be considered for its effect on the above degradation mechanisms. The mix designs developed and tested represent the current concretes being used by the Georgia Department of Transportation (GDOT), a mix design meeting the minimum ACI 201.2R-08 (2008) durability requirements, and new mix designs which may be capable of meeting the durability requirements for a 100+ year life-span in an aggressive marine environment.

4.1.1.1 Mix Design Development

Mix designs were proportioned using the ACI 211.4R-08 (2008) procedure. The ACI 211.4R-08 (2008) process for developing mix designs is presented in Figure 4.1. The ACI 211.4R-08 (2008) was used in place of the ACI 211.1-91 (1991) document due to

the required strength, f_{cr}', of 6,200 psi exceeding the values given for proportioning when following the recommendations from Table 5.3.2.2 in ACI 318R-11 (2011) for a design strength of 5,000 psi, which is the minimum strength requirement for precast prestressed concrete piles in Georgia at 28 days (GDOT, 2004).

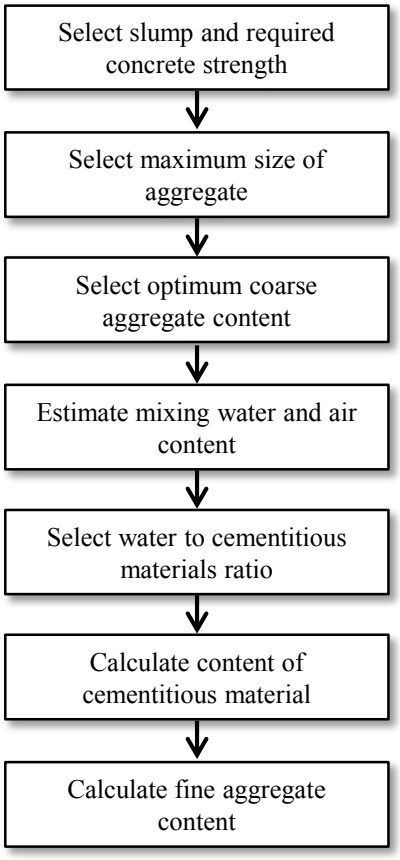

Figure 4.1: ACI 211.4R-08 (2008) Mix Design Procedure

The mix design meeting the minimum ACI 201.2R-08 (2008) durability requirements (T2) was developed by selecting a 2-4 inch slump. Next, a 3/4 inch maximum-size coarse aggregate (MSA) was selected based upon the 6,200 psi design strength and locally available aggregate gradations. Next, a coarse aggregate content of 0.72 was selected. A water content of 305 lb/yd^3 was selected based upon the MSA and desired slump. The water to cement ratio of 0.4 was selected based upon the durability

requirements for a seawater exposure. An ASTM C 150 (2009) Type II cement was selected to meet sulfate exposure requirements. The final mix design for T2 is given in Table 4.1.

Table 4.1: ACI durability criterion mix design (T2)

Material	**Weight (lb/yd^3)**
Water	305
Type I/II cement	763
Natural Sand	1096
#67 Stone	1905
w/cm	0.4

For all other mix designs, the notation of SCM – replacement level was used, unless a cement type other than an ASTM C 150 (2009) Type II cement was used, where the type of cement was denoted by T3 or T5 for a Type III or V cement. SCM's were abbreviated with the following notation: Fly Ash (F), slag (S), silica fume (SF), and metakaolin (MK).

Table 4.2 gives the mix design for a typical GDOT high performance concrete (T3-F15) currently being used for piles in the state of Georgia, which contains both an air entraining admixture and a super plasticizer. This mix design was provided by GDOT.

Table 4.2: Current HPC mix design (T3-F15)

Material	**Weight (lb/yd^3)**
Water	307
Type III cement	789
Type F Fly Ash	140
Natural Sand	1003
#67 Stone	1606
w/cm	0.33

For all potential HPMC mix designs, a high range water reducing admixture (HRWRA) was utilized; therefore, an initial slump of 1-2 inches was selected before the addition of the HRWRA. Next, a 3/4 inch MSA was selected since the required strength was below 9,000 psi, and is a readily available size in Georgia. Next, a coarse aggregate content of 0.72 was selected based upon the MSA. A water content of 285 lb/yd^3 was selected based upon the MSA and desired slump. Lastly, a w/cm of 0.3 was selected based upon previous findings in the literature for durability requirements. From the literature review (Chapter 2), it was found that decreasing the water to cementitious materials ratio and the addition of supplementary cementitious materials (SCM's) increased the durability of concrete by creating a denser microstructure. Table 4.3 shows the base mix design to be investigated for potential HPMC.

Table 4.3: Base experimental mix design

Material	**Weight (lb/yd^3)**
Water	285
Binder	950
Natural Sand	866
#67 Stone	1905
w/cm	0.30

This research will investigate the use of binary and ternary blended cements containing slag, Class F fly ash, silica fume, and metakaolin with an ASTM C 150 (2009) Type II moderate sulfate resistance cement. The binder compositions to be investigated are given in Table 4.4. The dosages of air-entraining and high-range water reducers will be determined during mixing to attain desired workability and air content values. Five of the mix designs will also be investigated for the effect of self-healing capabilities on the ingress of chlorides. These mix designs are designated with a check mark by their binder compositions.

Table 4.4: Binder compositions for experimental mix designs

Mix ID	Cement (%)	Cement Type	Fly Ash (%)	Slag (%)	Silica Fume (%)	Metakaolin (%)	w/cm	Self-Healing
T2	100	II	0	0	0	0	0.4	-
T3-F15	85	III	15	0	0	0	0.33	✓
TypeII	100	II	0	0	0	0	0.3	✓
F25	75	II	25	0	0	0	0.3	✓
F25-SF5	70	II	25	0	5	0	0.3	-
F25-MK5	70	II	25	0	0	5	0.3	-
F25-SF10	65	II	25	0	10	0	0.3	-
F25-MK10	65	II	25	0	0	10	0.3	-
S35-MK5	60	II	0	35	0	5	0.3	✓
S50-MK5	45	II	0	50	0	5	0.3	✓
S35-SF5	60	II	0	35	5	0	0.3	-
S50-SF5	45	II	0	50	5	0	0.3	-

4.1.2 Raw Material Properties

4.1.2.1 Cement

Oxide analysis and particle size distributions for each cement utilized in the project were measured. ASTM C 150 (2009) Type II cement and Type III cement were provided by National Cement. An ASTM C 150 (2009) Type V cement was acquired from TXI Riverside. Table 4.5 presents the results of the oxide analysis on the cement samples and the Bogue compositions.

Table 4.5: Oxide analysis and Bogue compositions of cement samples

Sample		Type II OPC	Type III OPC	Type V OPC
SiO2	%	20.51	20.80	20.81
Al2O3	%	4.65	4.96	4.30
Fe2O3	%	3.35	3.30	4.14
CaO	%	62.60	63.74	63.52
MgO	%	2.81	1.06	1.40
SO3	%	2.99	3.46	2.55
LOI	%	1.85	1.50	2.08
Na2O	%	0.07	0.11	0.22
K2O	%	0.75	0.53	0.44
TiO2	%	0.28	0.26	0.20
P2O5	%	0.04	0.14	0.15
MnO	%	0.05	0.03	0.12
SrO	%	< 0.01	< 0.01	< 0.01
C3S	%	54	54	58
C2S	%	18	19	16
C3A	%	6.7	7.6	4.4
C4AF	%	10	10	13
Gypsum	%	6.4	7.5	5.5

Each of the cements met their respective ASTM C 150 (2009) limits for each component of the Bogue composition. The C_3A content of the Type III cement was low, in the range of what is expected from a Type I/II. The C_3A content of the Type V mix was 4.4%, which is slightly lower than the limit of 5%.

The particle size distribution of each cement and the Blaine fineness are given in Table 4.6. The Type III cement had the smallest median particle size and highest fineness. The gradation curves are shown in Figure 4.2. The gradations for the Type II and Type V cements were similar, with an average particle size of 14.2 and 13.83 mm, respectively.

Table 4.6: Particle size distributions and Blaine Finess Values

	Type II %	**Type III %**	**Type V %**
<1μm	1.83	2.55	2.15
<1.5μm	3.29	4.40	4.14
<2μm	4.62	5.99	6.03
<3μm	7.29	9.27	9.89
<4μm	10.36	13.21	14.06
<6μm	18.12	23.15	22.79
<8μm	26.77	34.01	30.97
<12μm	42.19	52.99	44.46
<16μm	56.09	67.70	56.24
<24μm	77.62	85.04	74.96
<32μm	88.69	91.81	86.18
<48μm	95.88	96.14	95.04
<64μm	97.68	97.47	97.58
<96μm	98.71	98.45	98.94
<128μm	99.06	98.86	99.30
<192μm	99.38	99.26	99.55
median μm	14.20	11.31	13.83
Blaine Value (m^2/kg)	433.90	630.10	429.60

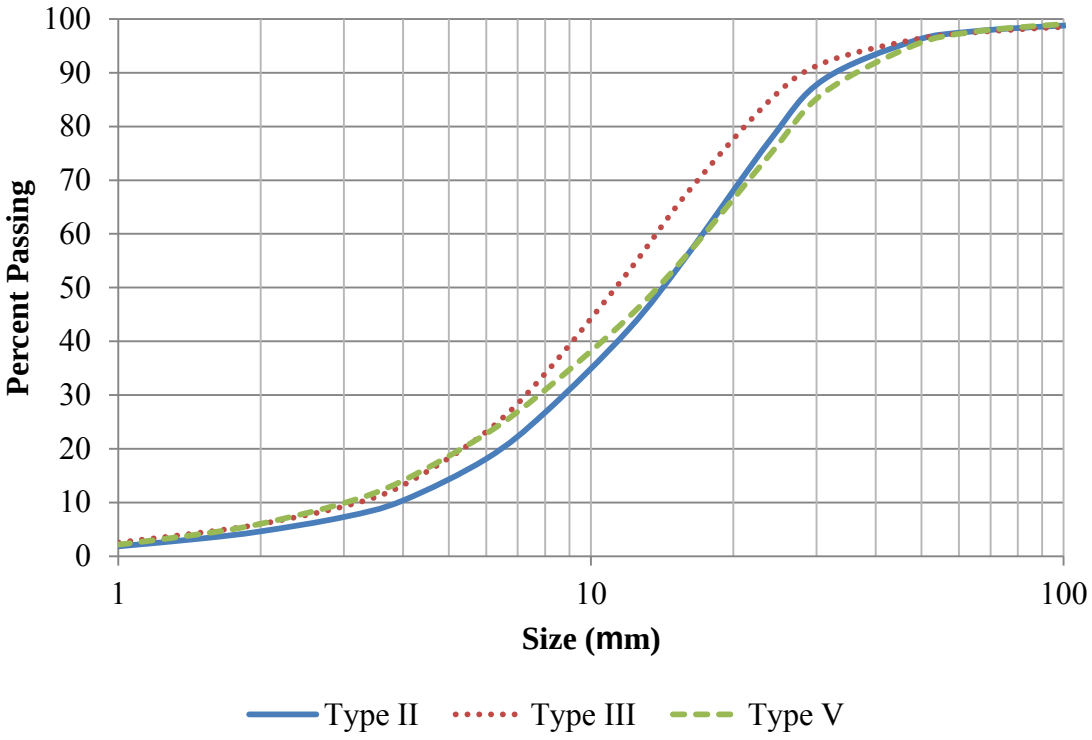

Figure 4.2: Particle size distributions for cement samples

4.1.2.2 SCM's

Oxide analysis and particle size distributions were performed on all four SCM's utilized for mix designs. Table 4.7 shows the results of the oxide analysis. The silica fume was composed of over 94% SiO_2. The slag was composed primarily of four components: SiO_2, Al_2O_3, CaO, and MgO. The fly ash was composed primarily of SiO_2 and Al_2O_3 as was the metakaolin.

Table 4.7: Oxide analysis for SCM samples

Sample		Silica Fume	Slag	Fly Ash	Metakaolin
SiO2	%	94.43	38.95	55.95	51.28
Al2O3	%	0.37	8.04	29.39	44.27
Fe2O3	%	0.09	0.41	4.91	0.40
CaO	%	0.59	37.23	1.05	0.08
MgO	%	0.37	12.10	0.86	0.17
SO3	%	0.16	1.83	0.29	0.13
LOI	%	3.00	-0.24	2.69	0.96
Na2O	%	0.08	0.28	0.29	0.41
K2O	%	0.68	0.42	2.16	0.11
TiO2	%	0.01	0.29	1.72	1.85
P2O5	%	0.12	0.01	0.48	0.29
MnO	%	0.03	0.38	0.02	0.01
SrO	%	< 0.01	0.05	0.13	0.01

The particle size distribution of each SCM is given in Table 4.8. The gradation curves are shown in Figure 4.3. From the gradations, the average particle size of metakaolin was smaller than any other SCM. The silica fume had the largest particle size due to being a densified powder.

Table 4.8: Particle size analysis of SCM samples

	Silica Fume %	**Metakaolin %**	**Slag %**	**Fly Ash %**
<1μm	0.00	3.62	2.46	0.91
<1.5μm	0.02	9.96	5.51	1.65
<2μm	0.12	17.73	8.40	2.30
<3μ	0.40	32.12	13.98	3.47
<4μm	0.79	42.86	19.69	4.71
<6μm	1.71	57.31	31.42	7.84
<8μm	2.77	66.84	42.65	12.01
<12μm	5.21	77.89	61.80	21.95
<16μm	8.24	83.36	76.18	32.03
<24μm	15.51	87.96	90.58	47.36
<32μm	23.12	89.87	95.44	57.66
<48μm	38.35	91.91	98.44	72.08
<64μm	50.68	93.35	99.34	81.83
<96μm	64.65	95.64	99.87	92.11
<128μm	73.34	97.25	99.99	96.16
<192μm	87.09	98.74	100.00	98.47
median μm	62.93	4.87	9.43	25.80

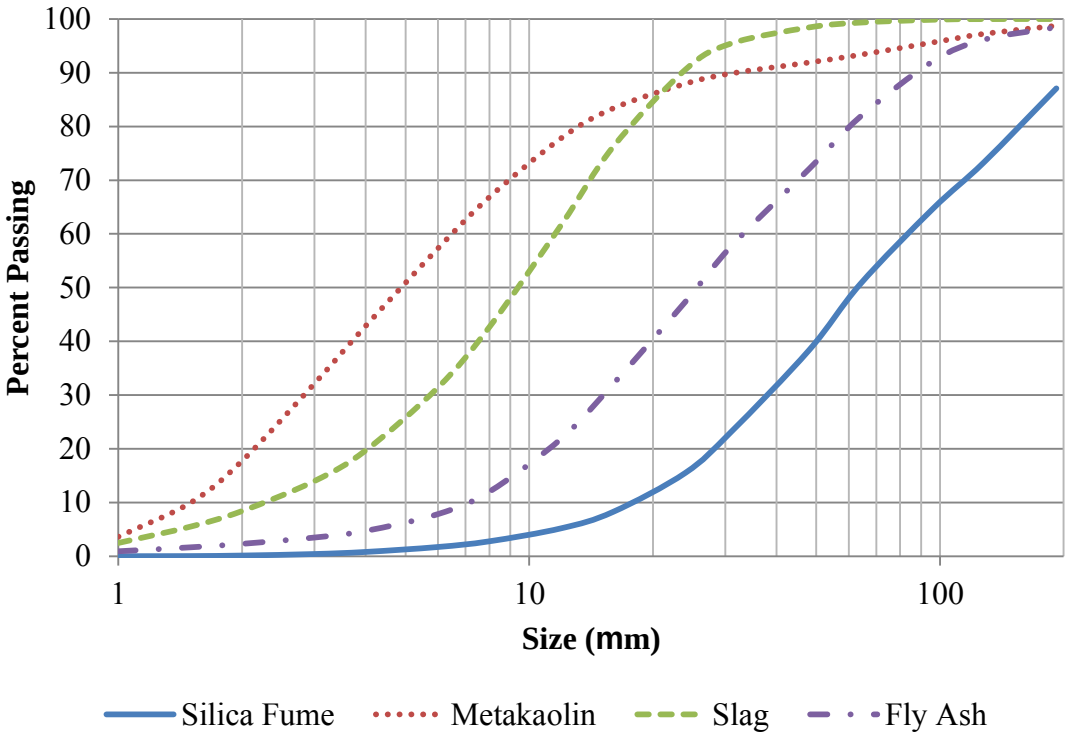

Figure 4.3: Particle size distributions for SCM samples

4.1.2.3 Fine Aggregate

A natural sand was used as the fine aggregate in the casting and development of mix designs. The gradation curve for the sand is shown in Figure 4.4. The fineness modulus was found to be 2.69. The absorption capacity was found to be 1.01% with a specific gravity of 2.597 when at the saturated surface dry (SSD) condition.

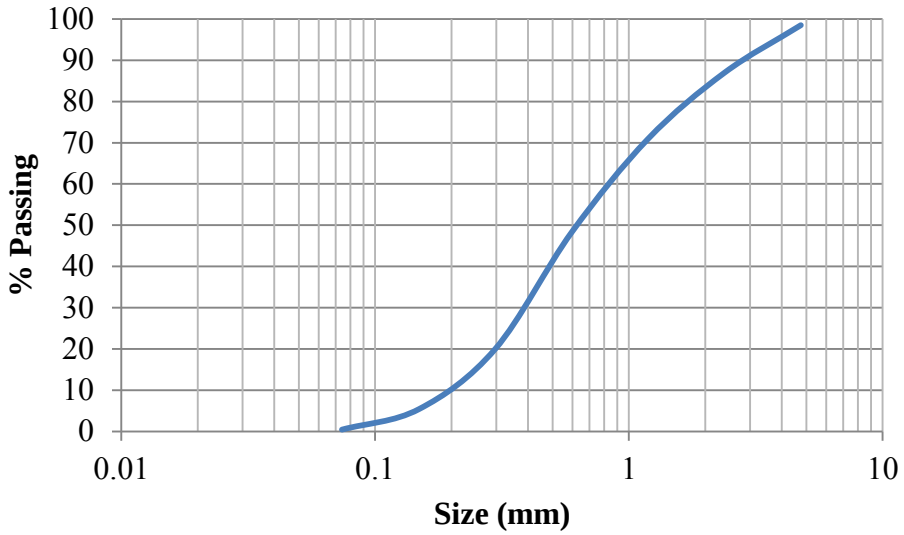

Figure 4.4: Gradation curve of natural sand

4.1.2.3 Coarse Aggregate

A crushed granite coarse aggregate was used in the casting and development of mix designs. The aggregate had an absorption capacity of 0.4% and a specific gravity of 2.745 when at SSD moisture condition. The dry rodded unit weight (DRUW) was found to be 97.8 pcf.

4.2 Mechanical Property Characterization

4.2.1 Compressive Strength

The compressive strength of each mix design was investigated. The compressive strength was measured in accordance with ASTM C 39 (2005) on 4–in. x 8–in. cylinders. Three cylinders from each mix design were tested at 3, 28, and 56 days of age to determine the strength characteristics of each mix for precast use. Figure 4.5 shows the strength gain curves. All mix designs had a compressive strength above 4,500 psi at 3 days of age.

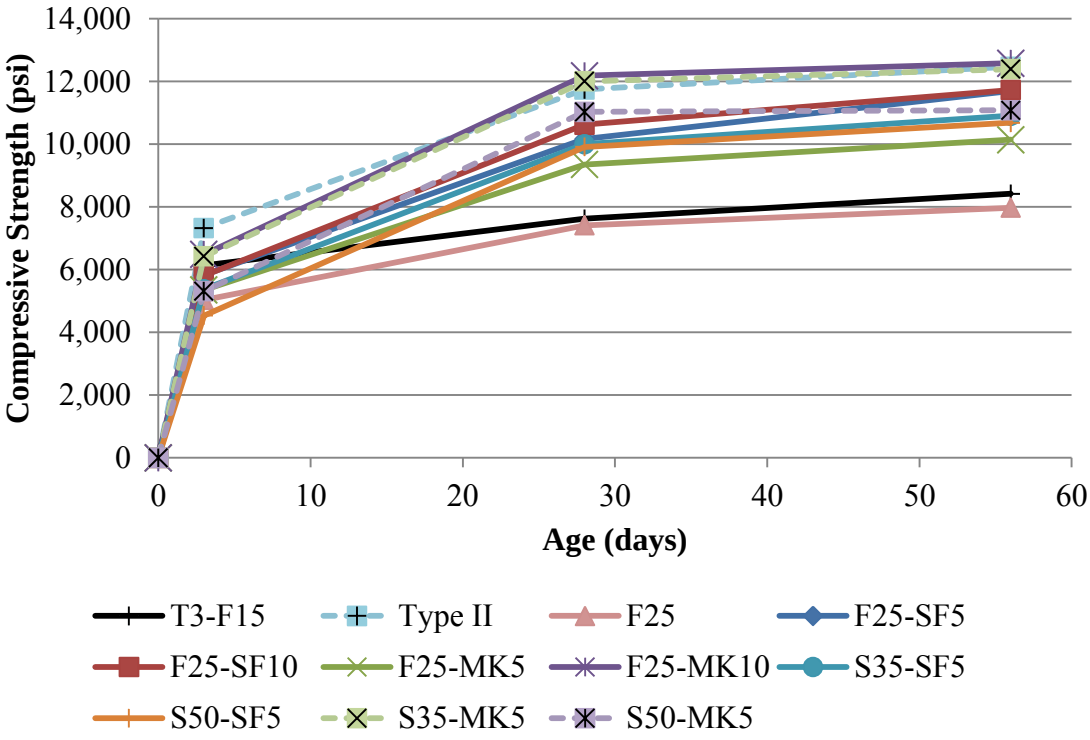

Figure 4.5: Compressive strength gain curves

GDOT currently requires a compressive strength of 4,000 psi for release of prestressing and a 5,000 psi 28-day strength for mix designs (GDOT, 2004). The longer a mix takes to develop the release strength, the longer it takes to produce each pile and increases the costs to the precast plant. The current mix design used by GDOT (T3-F15) had a 3-day strength of 6,100 psi, and two of the proposed high-performance marine concrete (HPMC) mix designs exceeded this at 3-days, F25-MK10 and S35-MK5. Further refinement and analysis of early age strength gain and the effect of curing regimes are needed. All mix designs met the 28-day strength requirement.

4.2.2 Elastic Modulus

The elastic modulus of each mix design was investigated in accordance with ASTM C 469 (2002). Figure 4.6 presents the elastic modulus results for tests performed on three 6-in.x12–in. cylinders at 56 days of age. The AASHTO (2007), ACI 363 (1997), and Rizkalla (NCHRP, 2007) estimation equations are also plotted in Figure 4.6. The ACI 363 (1997) estimator equation, which was developed for high-strength concrete, is in best agreement with the measured elastic moduli.

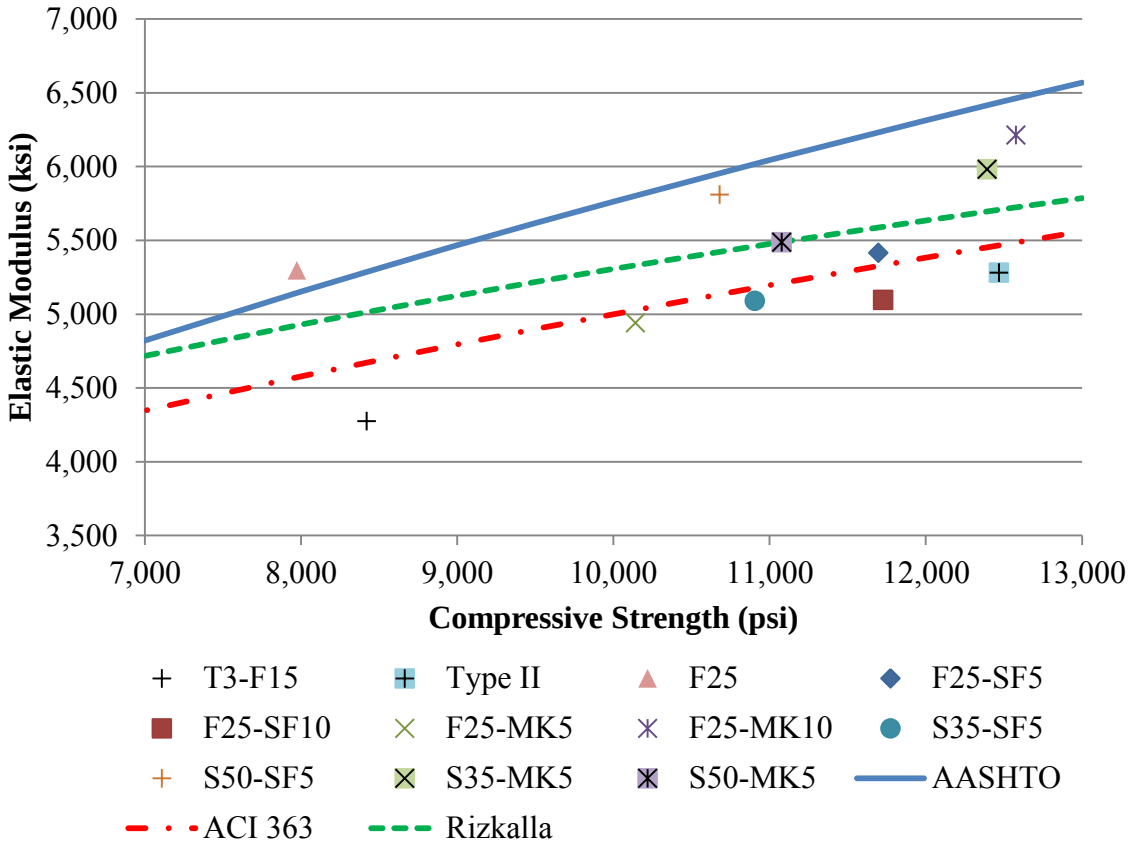

Figure 4.6: Elastic modulus vs. compressive strength and estimator equations

CHAPTER 5

Chloride Ingress Resistance of High Performance Concrete

5.1 Introduction

Chlorides from the surrounding marine environment are able to ingress into the concrete over time through various transport mechanisms, as discussed in Chapter 2. The protective oxide film that forms on the surface of the steel in the alkaline concrete environment is broken down locally by the presence of a sufficient local chloride concentration, and pitting corrosion can result. Pitting is a localized form of corrosion which initiates when chlorides attack defect sites in the passive film.

The corrosion of the prestressing steels leads to a loss of steel section. Additionally, the corrosion of steel leads to the formation of iron oxides which are less dense than the original steel and occupy more volume. The formation of oxides causes tensile forces in the surrounding concrete and can lead to cracking and delamination of the cover concrete, as well as rust staining on the surface of the piles.

The cover concrete serves as a barrier to the ingress of chloride ions to the depth of the reinforcing steel. The rate of ingress is dependent upon the cover concrete transport properties. The primary objective of this study is to develop and test the adequacy of potential HPMC mix designs to providing a 100+ year service life in a marine environment.

5.2 Experimental Program

Twelve mix designs were developed to determine the adequacy of current T3-F15 and potential HPMC mix designs for providing adequate protection to chloride ingress. These mix designs were presented in Chapter 4.

A series of experiments were performed to determine the resistance of each mix design to chloride ingress. The chloride transport properties of each concrete mix design were evaluated using a rapid migration test and a long-term ponding test. The chloride ingress resistance of each mix design was determined using ASTM C 1202 (2007) Rapid Chloride Permeability Test (RCPT) at 56 days of age on two 2 in. thick slices of 4 in. diameter concrete cylinders.

The bulk diffusion test (ASTM C 1556, 2004) was run on each mix design. Two 4in. x 8 in. cylinders were cast and fog room cured for 28 days. Next, specimens were cut and the initial chloride content determined. Specimens were fully saturated with limewater and sealed on all but one surface at the time of exposure. Profile grinding was performed on the sample after the exposure period of 180 days. The total chloride concentration of each increment is determined in accordance with ASTM C 1152 (2004). Table 5.1 shows the grinding increments utilized. A regression analysis of the results to Fick's Second Law (Eq. 2.2) was performed for the determination of an apparent diffusion coefficient.

The results of the bulk diffusion testing were used to perform service life modeling of each mix design. Life 365 (2009) was used to perform service life estimates for each mix design.

Table 5.1: Profile grinding increments

Increment	Depth (mm)
1	0-1
2	1-2
3	2-3
4	3-4
5	4-5
6	5-6
7	6-8
8	8-10

5.3 Results and Discussion

5.3.1 Chloride Ion Penetration Resistance

5.3.1.1 Rapid Chloride Permeability

The rapid chloride permeability test set-up is shown in Figure 5.1. ASTM C 1202 (2007) suggests using the rating system shown in Table 5.2 when comparing mix designs. GDOT currently requires mix designs for marine exposure to pass a 2,000 coulomb limit (GDOT, 2004). This limit corresponds to a rating of Low or better using Table 5.2.

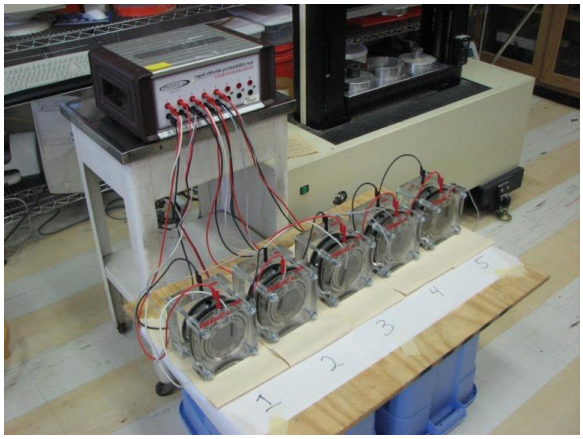

Figure 5.1: Rapid Chloride Permeability Set-up

Table 5.2: Chloride ion penetrability based on charge passed (ASTM C 1202, 2007)

Charge Passed (coulombs)	Chloride Ion Penetrability
> 4,000	High
2,000-4,000	Moderate
1,000-2,000	Low
100-1,000	Very Low
<100	Negligible

Figure 5.2 shows the results of the RCPT testing. All mix designs met the current GDOT limit. All ternary blended cement mix designs had less than 700 coulombs passed, which is considerably lower than the 1,500 coulombs measured on the current T3-F15. This suggests that the ternary blend cements provide significant improvement in chloride resistance to the mix designs currently in use.

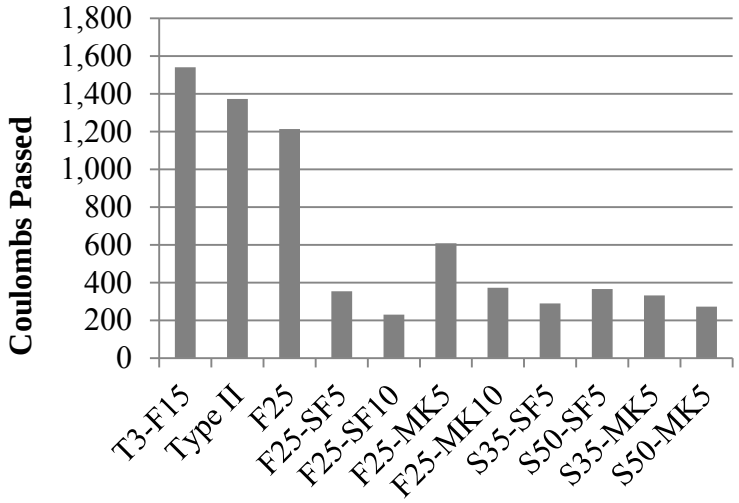

Figure 5.2: RCPT results

5.3.1.1 Bulk Diffusion

The bulk diffusion chloride profiles of each mix design were measured. Next, a regression analysis was performed fitting the results to Fick's second law of diffusion, for which the solution is given in Eq. 5.1. Previous research has shown that diffusion is the

primary transport mechanism responsible for the ingress of chlorides into the samples over long ponding periods.

$$\frac{C(x,t)}{C_o} = 1 - \text{erf}\left(\frac{x}{\sqrt{4 * D_{eff} * t}}\right) \quad \text{(Eq. 5.1)}$$

Where,

$C(x,t)$ = chloride concentration, measured at depth x and exposure time t, mass %

C_o = initial chloride-ion concentration of the cementitious mixture prior to submersion in the exposure solution, mass %

x = depth below the exposed surface (to the middle of a layer), in

D_{eff} = effective chloride diffusion coefficient, in^2/s

t = the exposure time, s

erf = error function

$$= \frac{2}{\sqrt{}} * \int_0^z \exp(-u^2)\, du$$

The apparent chloride diffusion coefficients determined from bulk diffusion testing are given in Table 5.3. The results varied by over an order of magnitude. Mix designs with a lower water to cementitious materials ratio had lower diffusion coefficients. Additionally, ternary mix designs had lower diffusion coefficients than binary mix designs.

Table 5.3: Experimental Diffusion Coefficients

Mix	D_a (in^2/s)
T2	1.13E-08
T3-F15	1.72E-09
F25	1.69E-09
F25-MK5	1.34E-09
F25-MK10	1.72E-09
F25-SF5	1.33E-09
F25-SF10	1.34E-09
S35-MK5	7.94E-10
S50-MK5	8.44E-10
S35-SF5	1.23E-09
S50-SF5	1.40E-09

The chloride profiles for all of the mix designs are given in Figures 5.3 through 5.6. The blue line with diamond markers are the experimental data points, and the red line is the result of the regression to Fick's second law. Additional increments were performed on mix designs T2 and F25 to capture the tail due to deeper penetration of chlorides into the samples.

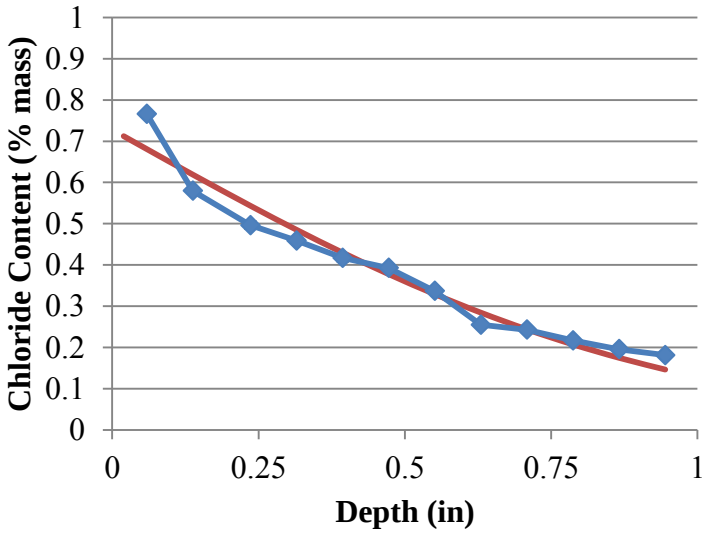

Figure 5.3: Chloride profile for T2

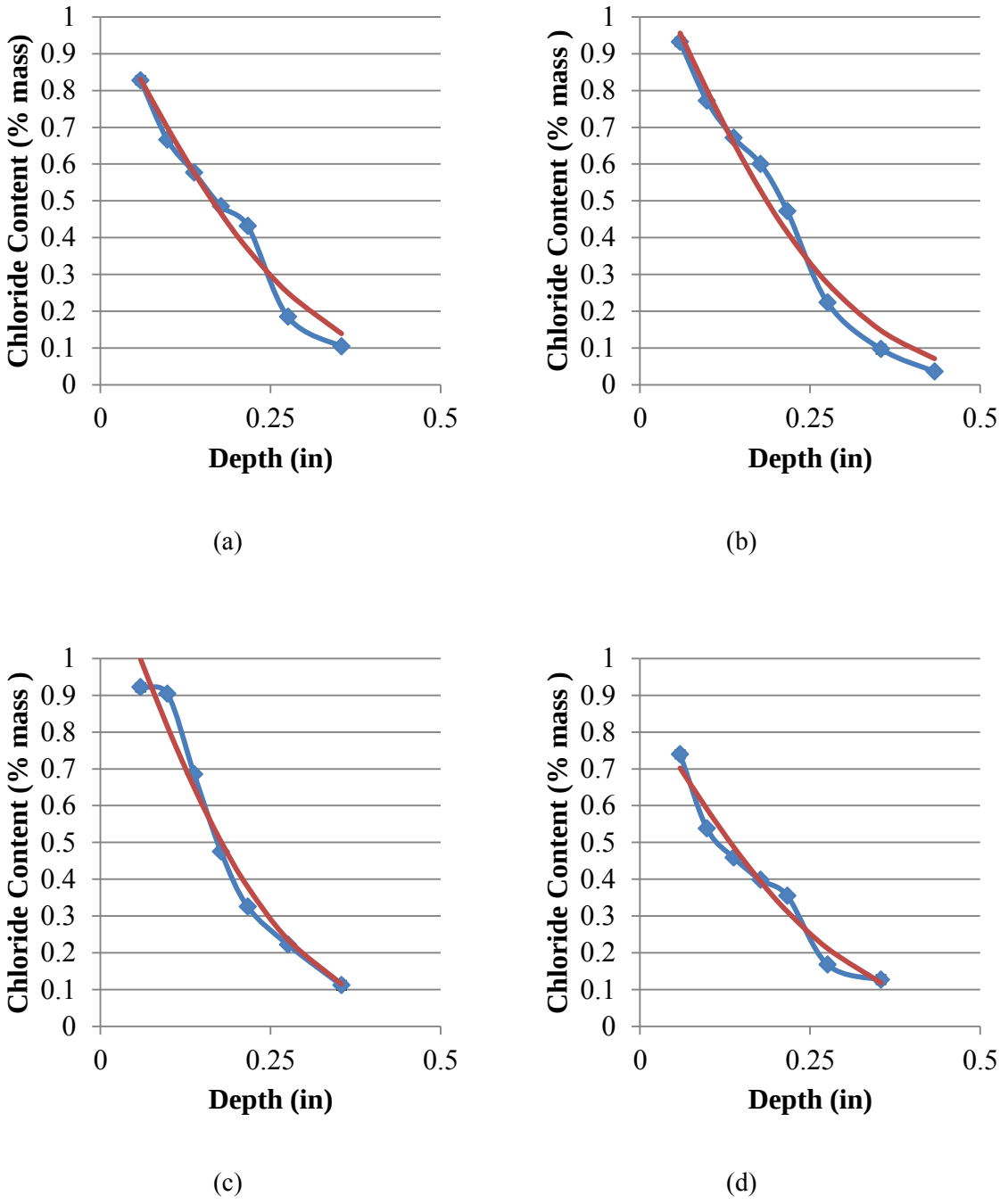

Figure 5.4: Chloride profiles for (a) T3-F15, (b) F25, (c) F25-MK5, and (d) F25-MK10

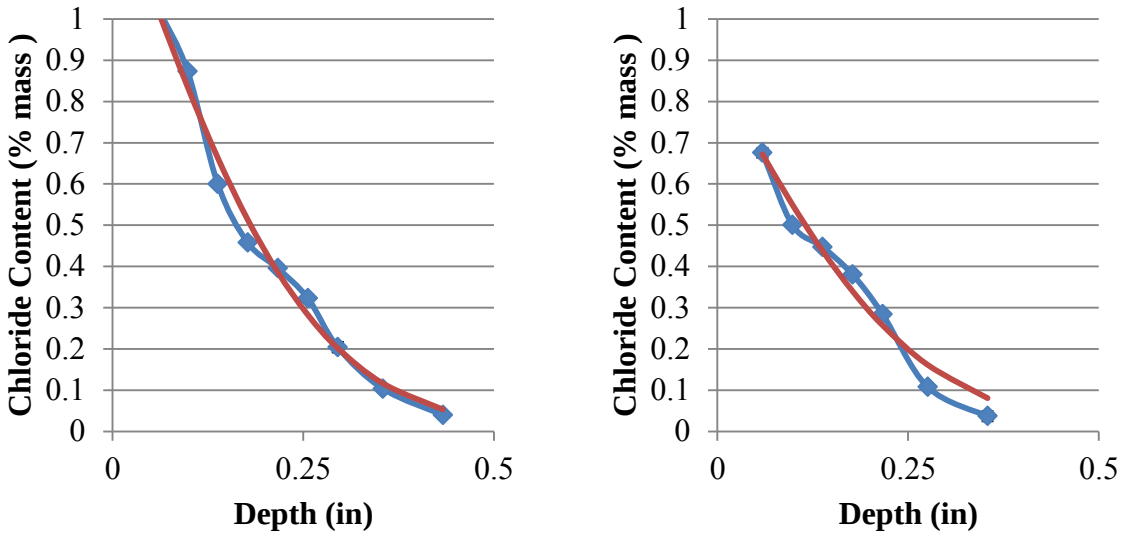

(a)

(b)

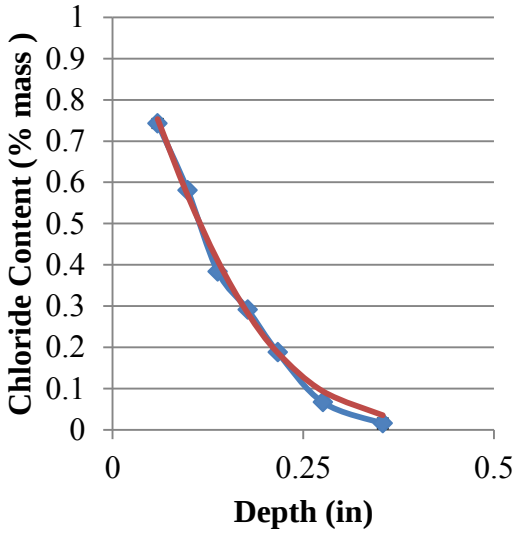

(c)

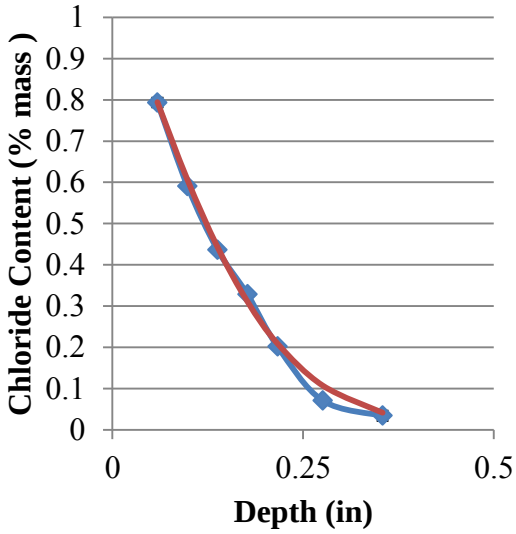

(d)

Figure 5.5: Chloride profiles for (a) F25-SF5, (b) F25-SF10, (c) S35-MK5, and (d) S50-MK5

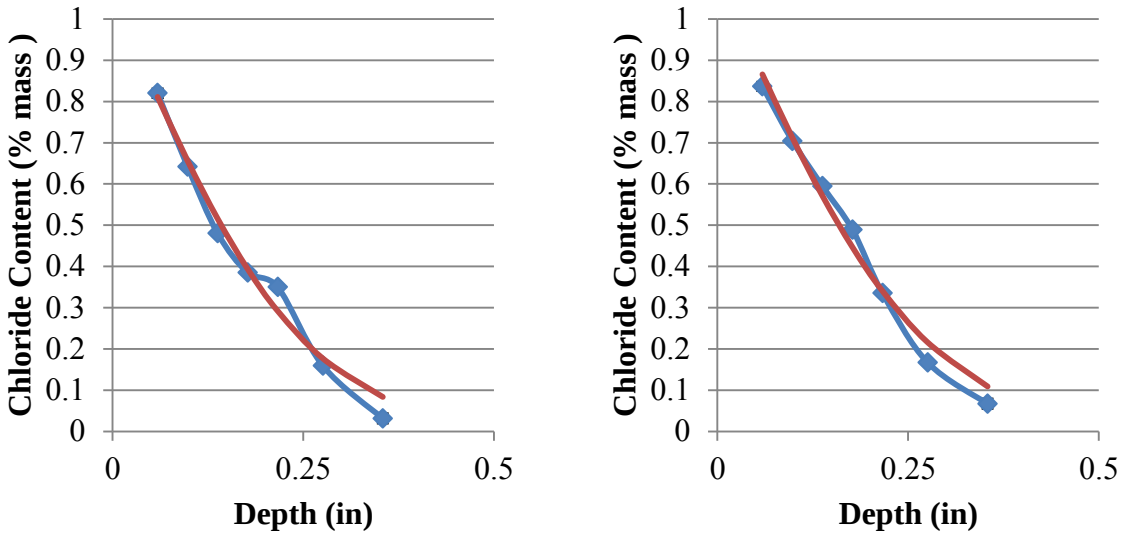

(a) (b)

Figure 5.6: Chloride profiles for (a) S35-SF5 and (b) S50-MK5

5.4 Service Life Modeling

The results of the bulk diffusion tests were used to perform service life modeling to determine the estimated corrosion initiation time. Figure 5.7 shows a basic corrosion service life model which consists of two phases: corrosion initiation time and propogation period. The initiation period is the time it takes for the chloride threshold limit (CTL) to be exceeded at the level of steel. Since diffusion is the primary transport mechanism, the time period for exceedance can be estimated. The propogation period reported in the literature varies significantly and depends upon several paremeters including the rate of corrosion and what is concluded to be the end of service life state of damage (Bertolini, et al., 2004).

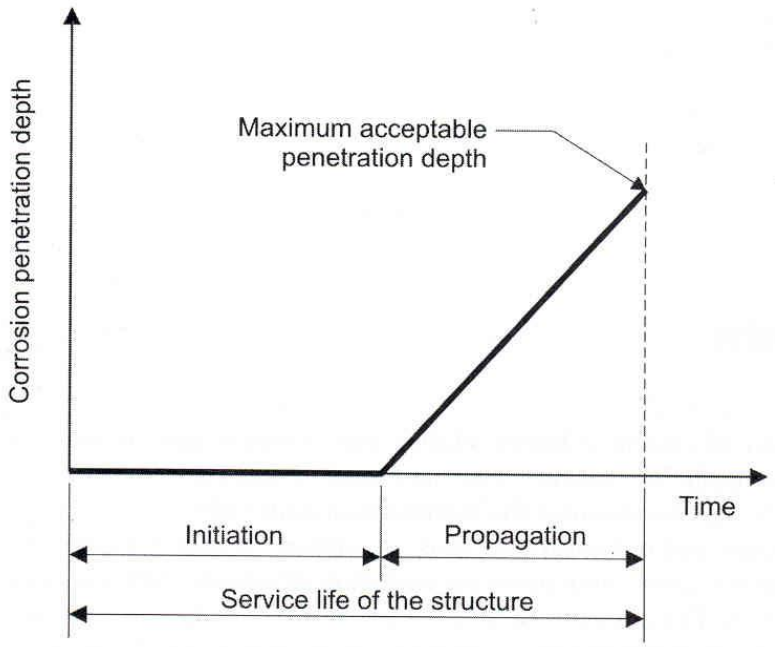

Figure 5.7: Service life model for corrosion induced damage (Bertolini, et al., 2004)

5.4.1 Diffusion Coefficient Estimation

Life 365 (2009) provides a method for estimating the diffusion coefficient of mix designs for preliminary estimates of their service life. The basis for the estimation is that the chloride diffusion coefficient is a function of time and mix design parameters. Eq. 5.2 shows the relationship assumed to account for time-dependent changes in the diffusion coefficient.

$$D(t) = D_{ref}\left(\frac{t_{ref}}{t}\right)^{m} \qquad \text{(Eq. 5.2)}$$

Where,

D(t) = diffusion coefficient at time t

D_{ref} = diffusion coefficient at time t_{ref} (t_{ref} is 28 days for Life 365)

m = diffusion decay index (0.2 for portland cement)

For estimation, a base diffusion coefficient at t_{ref} = 28 days, D_{28}, is estimated first for a straight portland cement mix design, then adjustment factors are made based upon the addition of SCM's. Eq. 5.3 gives the equation for estimating the D_{28} of a portland cement mixture based upon the w/cm.

$$D_{28} = 1 \times 10^{(-12.06+2.40*w/cm)} \quad \text{(Eq. 5.3)}$$

Where,

D_{28} = diffusion coefficient of portland cement, m^2/s

w/cm = water to cementitious materials ratio

The addition of SCM's to concrete mix designs are accounted for based upon the type of SCM utilized. Silica fume is known to react quickly and affect early age behavior by decreasing the diffusion coefficient. Life 365 accounts for this through the application of a reduction factor to the D_{PC}, which is calculated using Eq. 5.3. The method for applying the reduction factor is given in Eq. 5.4 for silica fume. Silica fume is not assumed to have an effect on the diffusion decay index, m, which accounts for long-term time-dependent reductions of the diffusion coefficient. Life 365 does not have an adjustment factor currently for the influence of metakaolin on diffusion behavior of mix designs.

$$D_{SF} = D_{PC} * e^{-0.165*SF} \quad \text{(Eq. 5.4)}$$

Where,

D_{SF} = diffusion coefficient silica fume containing concrete, m^2/s

SF = silica fume content, % (valid up to 15%)

D_{PC} = D_{28} calculated using Eq. 5.3

The addition of fly ash and slag are assumed to not have an effect on the early-age diffusion coefficient, D_{28}. Both have been shown to decrease the apparent diffusion coefficient over long-term exposures. Life 365 accounts for this through modifying the diffusion decay index, m, as shown in Eq. 5.5.

$$m = 0.2 + 0.4(FA/50 + SG/70) \quad \text{(Eq. 5.5)}$$

Where,

m = diffusion decay index

FA = fly ash content, % (valid up to 50%)

SG = slag content, % (valid up to 70%)

Using the outlined procedure above for estimating the diffusion coefficient, Table 5.4 shows the measured and estimated values for the diffusion coefficients. No estimates were made for mix designs containing metakaolin, since Life 365 currently does not have that capability. Life 365 estimated all diffusion coefficients to within an order of magnitude, which is less than the range of observed values between mix designs. Also, it appears to over-estimate the influence of silica fume contents above 5%. This may be due to the difficulty in properly dispersing high silica fume contents when mixing.

The apparent diffusion coefficient can be used to determine the chloride profile at various ages for different mix designs. Figure 5.8 shows the estimated chloride profiles for both T3-F15 and S50-MK5 at various ages when exposed to ingress from a single face. The D_{28} value of S50-MK5 was approximately 50% of the T3-F15 and had a m value of 0.48 compared to 0.32 respectively. From the visual, it can be observed that after each exposure period, the depth of penetration for S50-MK5 is significantly lower. The relationship between diffusion coefficient and depth of ingress at each age is not a linear function.

Table 5.4: Experimental and estimated reference diffusion coefficients

	D_{28} (in^2/s)	
Mix	**Experimental**	**Estimated**
T2	1.76657E-08	1.23E-08
T3-F15	3.12015E-09	8.36243E-09
F25	3.56712E-09	7.08488E-09
F25-MK5	2.81441E-09	-
F25-MK10	3.61076E-09	-
F25-SF5	2.79187E-09	3.10484E-09
F25-SF10	2.81816E-09	1.36065E-09
S35-MK5	1.67131E-09	-
S50-MK5	2.10054E-09	-
S35-SF5	2.59127E-09	3.10484E-09
S50-SF5	3.46559E-09	3.10484E-09

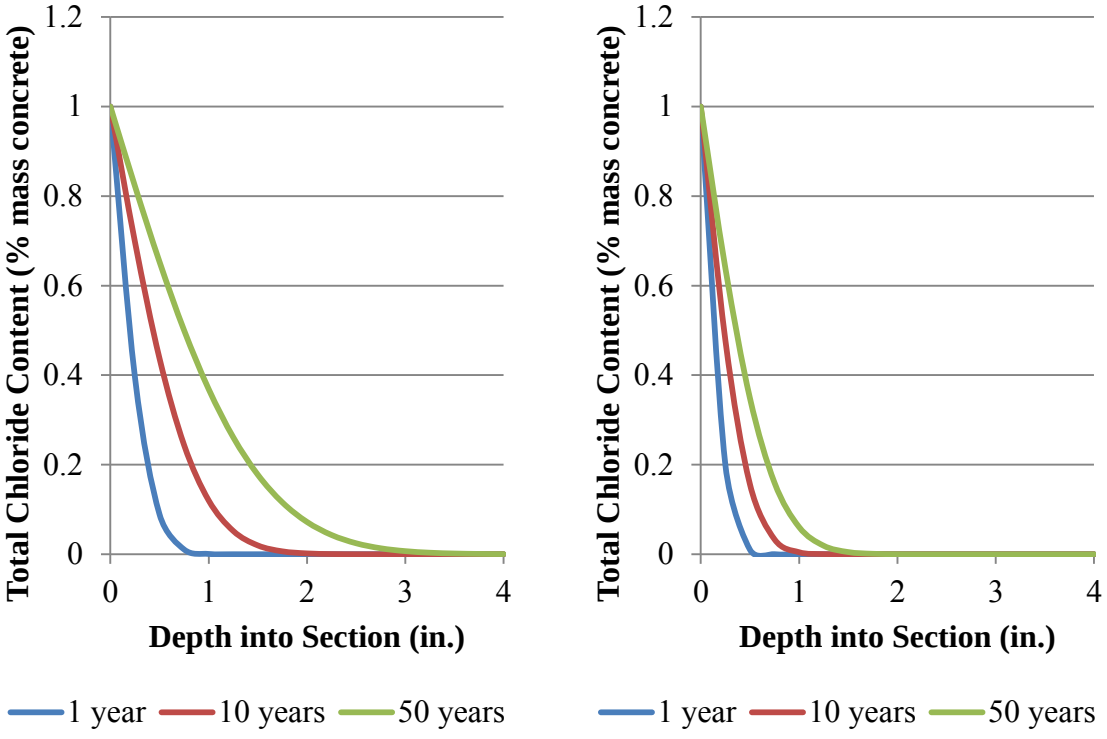

Figure 5.8: Estimated chloride profiles after various exposure periods for (a) T3-F15 and (b) S50-MK5

5.4.2 Corrosion Initiation Period Estimation

The corrosion initiation period was calculated using Life 365's internal solver and the estimated diffusion decay indexes. The program is able to account for two-dimensional flow of chlorides for the square pile geometry that Georgia currently uses using the two-dimensional Crank-Nicolson approach (Ehlen, et al., 2009). For estimation, a 3 in. cover distance was used on an 18 in. square pile. A CTL of 0.05% by weight of concrete was used as a conservative estimate.

The results of the analysis for the experimentally determined apparent diffusion coefficients are shown in Figure 5.9. The mix design T2, which would be obtained by following the minimum requirements of ACI 201.2R-08 (2008), would initiate corrosion after only 7 years. T3-F15 would initiate corrosion after approximately 55 years. All ternary mix designs would provide a minimum initiation time of 73 years. S50-MK5 provided the longest initiation time.

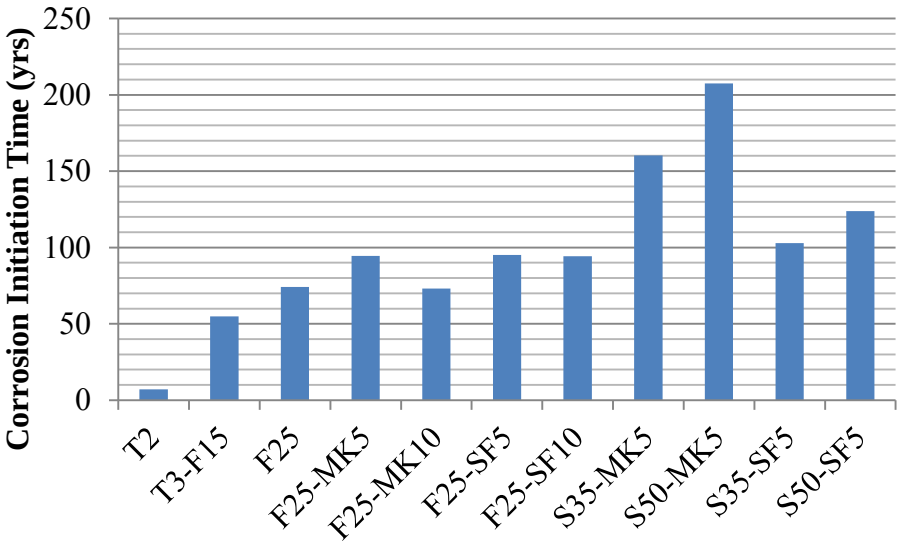

Figure 5.9: Corrosion initiation time for experimental results

Additionally, the estimated initiation times using the estimated diffusion coefficients from Life 365 were calculated. Table 5.5 shows the experimental and estimated initiation times. The Life 365 estimates were over 50% lower for T3-F15 and F25, which are both mix designs that contain only fly ash. The estimated values for ternary blends including slag and silica fume were within 17 years (~16%). The estimate for 10% silica fume was over 100% higher than the experimental value, which matches the noted difference in estimated diffusion coefficient in section 5.4.1.

Table 5.5: Corrosion initiation times

	Expected Initiation Time (years)	
Mix	**Experimental**	**Estimated**
T2	7	9.2
T3-F15	54.8	20.2
F25	74.1	36.2
F25-MK5	94.4	-
F25-MK10	73.2	-
F25-SF5	95.2	85.4
F25-SF10	94.3	197.7
S35-MK5	160.3	-
S50-MK5	207.4	-
S35-SF5	102.8	85.4
S50-SF5	123.8	138.5

Since tests were not performed to verify the validity of the diffusion decay index for each mix design, a highly conservative estimate of corrosion initiation time is to use the 180 day measured diffusion coefficient for each mix design. It is known that the actual values should be longer than the estimated values using this method. Figure 5.10 shows the results of estimated corrosion initiation time not accounting for time-dependent decreases in the diffusion coefficient.

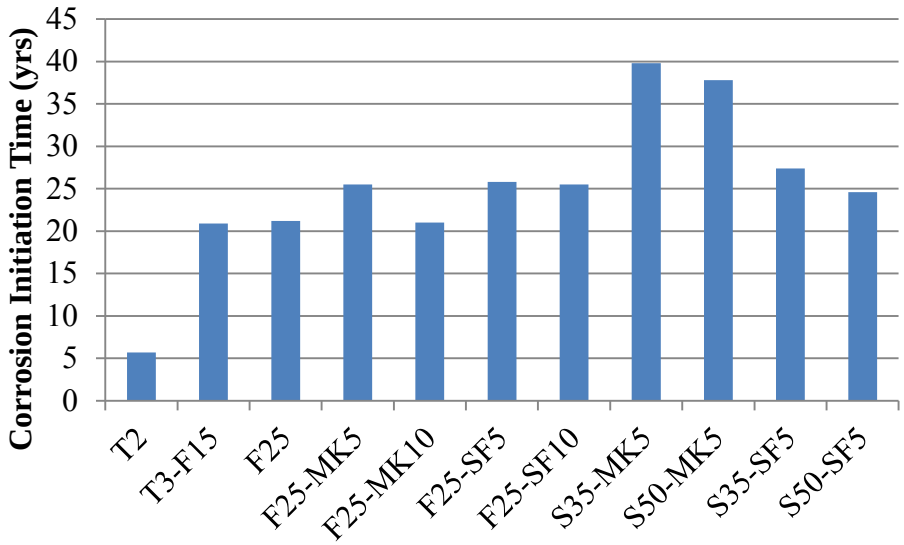

Figure 5.10: Estimated corrosion initiation times without maturity correction

Using this method, the initiation times decreased significantly as was expected. The maximum initiation times were provided by S35-MK5 and S50-MK5, with values of 39.8 and 37.8 years, respectively. The F25-SF5, F25-MK5, and F25-SF10 mix designs provided the longest service life of the fly ash mix designs.

5.5 Conclusions and Recommendations

The study into the chloride ingress resistance of binary and ternary mix designs found that ternary mix designs provide superior resistance than binary mix designs. Also, decreasing the w/cm was found to improve resistance. The RCPT demonstrated the decrease in penetrability of mix designs and agreed with the results of the bulk diffusion testing. The service life modeling showed that mix designs capable of an estimated 70 year or longer service life had a charge of less than 1000 coulombs passed during the RCPT. Bulk diffusion tests and service life modeling showed that ternary mix designs with slag and metakaolin provide the longest service lives. Additionally, estimates from

Life 365 for the diffusion coefficient and estimated service life varied widely from observed behavior.

This study has led to the following recommendations for design, quality assurance testing, and future research:

- Use S50-MK5 or F25-SF5 to maximize usable service lives of structures depending upon whether a slag or fly-ash mix is preferred.
- Use of a 1000 Coulomb limit for HPMC mix designs.
- Life 365 can be used to estimate corrosion initiation times, given that the diffusion coefficient is determined experimentally.
- Development of estimation techniques for mix designs utilizing metakaolin are needed.

(This page intentionally left blank.)

CHAPTER 6

Sulfate Resistance of High Performance Concrete

6.1 Introduction

One objective of this study was to develop and test potential HPMC binder compositions for their resistance to sulfate attack. Concrete piling in seawater and brackish water can be exposed to high concentrations of sulfates. The primary forms of sulfates present are $NaSO_4$, $MgSO_4$, and $CaSO_4$ (Skalny, et al., 2002). Damage to the concrete due various reactions between the ingressing sulfate ions and hydration products and anhydrous cement phases in the cement paste is termed "sulfate attack". Two primary mechanisms are associated with sulfate attack. First, sulfate ions can react with monosulfo-aluminate or available tricalcium-aluminate (C_3A) to form ettringite, as shown in Eq. 6.1. The formation of ettringite can be expansive and lead to cracking and spalling.

$$2SO_4^{2-} + Ca_4Al_2(OH)_{12} * SO_4 * 6H_2O + 2Ca^{2+} \rightarrow Ca_6Al_2(OH)_{12}(SO_4)_3 * 26H_2O \qquad \text{(Eq. 6.1)}$$

In addition, sulfate ions may react with available calcium hydroxide (CH) to form gypsum, as shown in Eq. 6.2. If there is no CH present, then the calcium comes from the decomposition of the calcium silicate hydrate phase (C-S-H). The loss of calcium from the C-S-H leads to a reduction in strength (Skalny, et al., 2002).

$$SO_4^{2-} + Ca^{2+} + 2H_2O \rightarrow CaSO_4 * 2H_2O \qquad \text{(Eq. 6.2)}$$

The concentration of sulfates has a large effect on the extent and rate of sulfate attack. ACI 201 (2010) provides guidelines for four exposure classes and requirements to protect against each level of exposure. Table 6.1 shows the requirements proposed by ACI 201 for a given sulfate exposure in water. The recommended cement type is based upon an ASTM C 150 (2009) cement designation. Alternatively, the performance based specification for cements (ASTM C 1157, 2011) can be used, and they require testing following the ASTM C 1012 (2009) procedure with expansion limits. For Georgia's brackish water and marine exposures, sulfate levels fall into the S1 to S2 categories based upon the results of the environmental condition survey presented in Appendix A.

Table 6.1: Exposure Classes as specified by ACI 201 (2010)

Exposure Class		**Cement Type**	**Exposure (%)**	**w/cm**
S0	Not Applicable	No Restriction	$SO_4 < 0.10$	None
S1	Moderate	Type II	$0.10 \leq SO_4 < 0.20$	w/cm < 0.5
S2	Severe	Type V	$0.20 \leq SO_4 < 2.0$	w/cm < 0.45
S3	Very Severe	Type V + Pozzolan or Slag	$SO_4 > 2.0$	w/cm < 0.40

The ACI 201 (2010) approach does not provide design guidelines based upon the source of sulfates or the cation present, but only on the concentration of sulfate ions. Additionally, the approach does not correlate the expected service life to the measured expansion at various ages. Additionally, through ASTM C 1012 (2009) expansion tests, only one of the two deleterious reactions associated with sulfate attack is being measured and may not provide a full characterization of a mix design's performance in a sulfate rich environment.

6.2 Experimental Program

The expansion and strength degradation behavior of thirteen binder compositions subjected to sulfate exposure were evaluated. The binder compositions evaluated are

given in Table 6.2. ASTM C 150 (2009) Type II, III, and V cements were used as well as binary and ternary compositions containing SCM's ; each mixture was designed to increase sulfate resistance based upon previous research findings (Chapter 2).

Table 6.2: Binder compositions

	Cement		SCM's (%)			
Mix ID	**%**	**Type**	**Fly Ash**	**Slag**	**Silica Fume**	**Metakaolin**
T2	100	Type II	0	0	0	0
T3	100	Type III	0	0	0	0
T5	100	Type V	0	0	0	0
T3-F15	85	Type III	15	0	0	0
F25	75	Type II	25	0	0	0
F25-SF5	70	Type II	25	0	5	0
F25-SF10	65	Type II	25	0	10	0
F25-MK5	70	Type II	25	0	0	5
F25-MK10	65	Type II	25	0	0	10
S35-MK5	60	Type II	0	35	0	5
S50-MK5	45	Type II	0	50	0	5
S35-SF5	60	Type II	0	35	5	0
S50-SF5	45	Type II	0	50	5	0

The sulfate resistance of each mix design was investigated using two accelerated test methods. Accelerated expansion tests were performed in accordance with ASTM C 1012 (2009) on mortar samples with the binder compositions given in Table 6.2 and compared against the expansion limits provided by ACI 201 (2010) for different exposure classes, as given in Table 6.3. Expansion tests were performed for 18 months.

Table 6.3: Maximum expansion percentages specified by ACI 201 (2010)

Exposure Class	**Expansion Percent**		
	6 Months	12 Months	18 Months
S1	0.10%	-	-
S2	0.50%	0.10%	-
S3	-	-	0.10%

Compressive strength testing was performed on paste cube samples by the method used by Kurtis, et al. (2001). Paste cube samples (0.5 in) were cast simultaneously with ASTM C 1012 (2009) samples using a 0.5 w/cm and cured in the molds for 24 hours, then moist cured for 7 days at 50˚C. After the curing period, samples were placed into a 4% Na_2SO_4 solution where the pH was maintained at 7.2. By maintaining a constant pH, the effects of leaching of calcium hydroxide were minimized and better replicated field conditions. Through the use of sulfuric acid, Brown (1981) showed that the sulfate concentration remains constant. For each mix, the compressive strength of control and exposed samples were tested at the time of exposure, as well as, at 28, 90, and 180 days after exposure. Eight samples with sulfate exposure and eight control samples were tested at each age at a load rate of 600 lb/min.

The compressive strength degradation test accounts for the deterioration of CH and C-S-H to form gypsum, which is more commonly reported in field studies of sulfate damage. The ASTM C 1012 (2009) test only accounts for the effects of ettringite formation in its expansion evaluation. Cracking caused by ettringite or gypsum formation and ettringite expansion, as well as C-S-H deterioration adversely affects the measured compressive strength; therefore, those reactions are accounted for in the compressive strength degradation test methodology.

6.3 Results and Discussion

6.3.1 ASTM C 1012 Expansion Testing

Figure 6.1 shows the expansion results for the ASTM C 150 (2009) Type II, III, and V cements (T2, T3, and T5, respectively) and a dashed red line gives the expansion limits. Only T3 failed the 12-month limit, which was expected since both T2 and T5 binders were designed for sulfate resistance. T2 and T5 failed the 18 month limit at 13 and 14 months, respectively. The 18 month limit suggests the use of an ASTM C 150 (2009) Type V cement with Pozzolan.

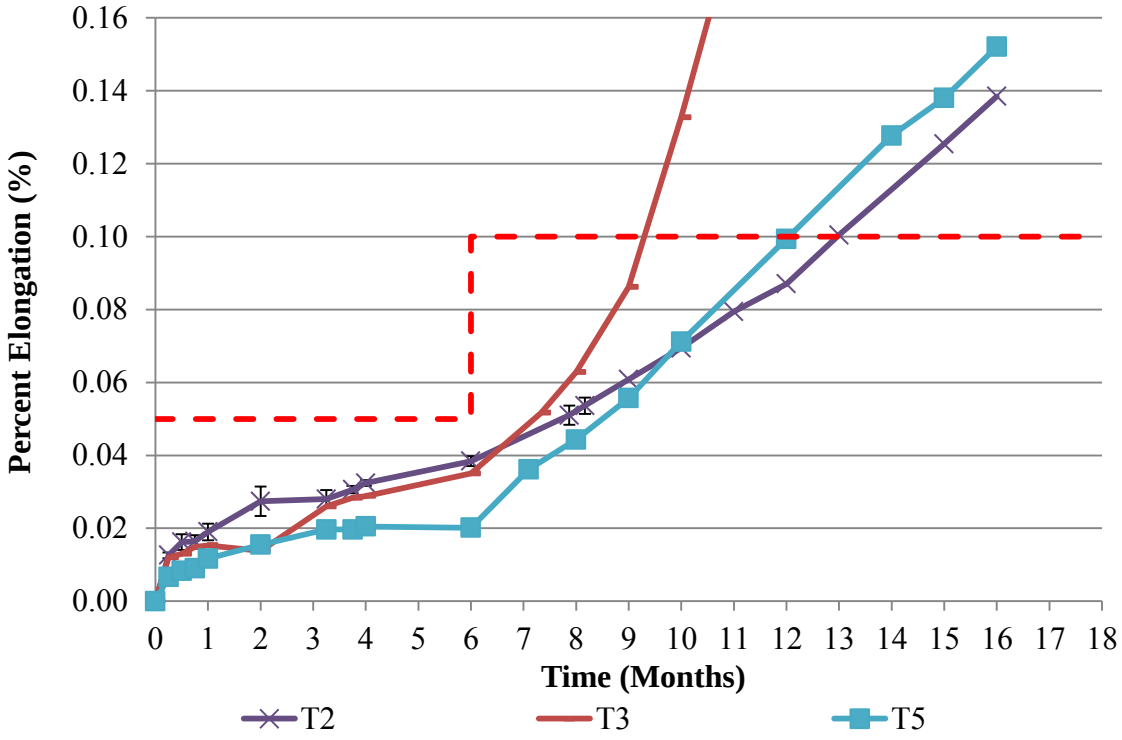

Figure 6.1: ASTM C 1012 expansion results for cement mixes

Figures 6.2 and 6.3 show the expansion results for binder compositions containing fly ash and slag, respectively, with the dashed red line representing the expansion limits. All of the blended cement mix designs (T3-F15, F25, F25-MK5, F25-MK10, F25-SF5, F25-SF10, S35-MK5, S50-MK5, S35-SF5, and S50-SF5) met the severe exposure (S2)

expansion limits, which suggests that these mix designs possess adequate resistance to sulfate attack for the marine environments in Georgia according to ACI 201. F25-MK5 failed the 18 month expansion limit, suggesting it provides lower sulfate resistance than the other ternary mix designs. F25 shows an increasing rate of expansion compared to the other samples, which have shown a stable expansion behavior, and if its current expansion behavior continues, it will fail the 0.1% expansion limit by 19 months of exposure.

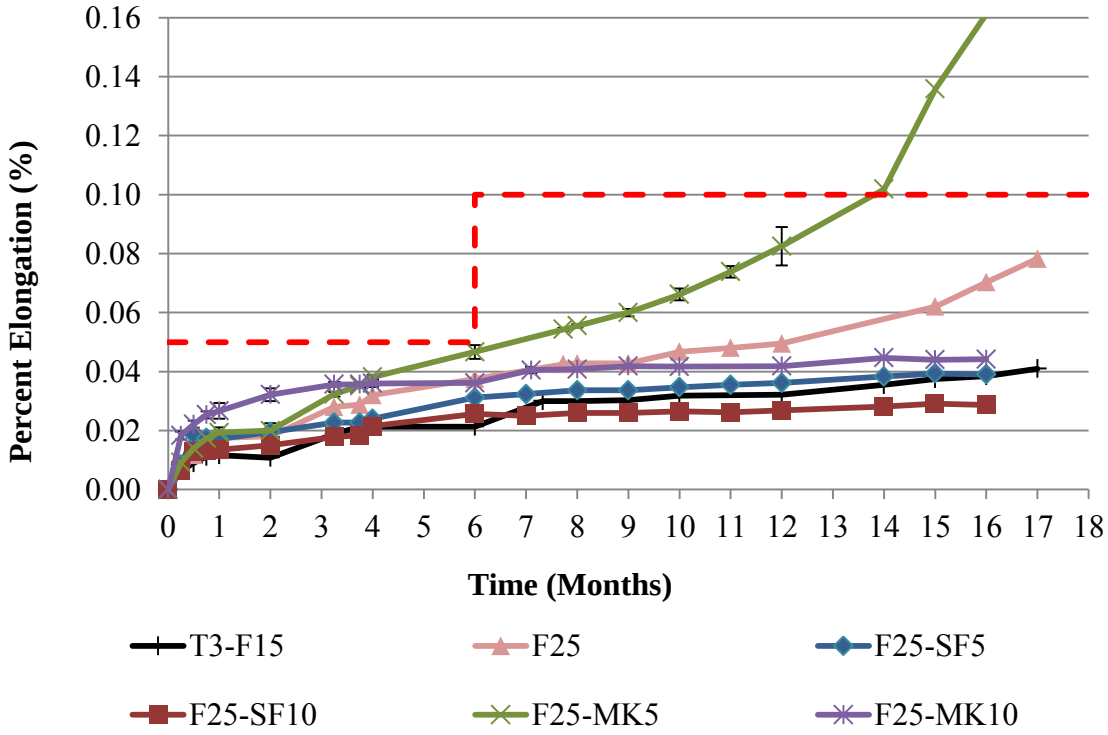

Figure 6.2: ASTM C 1012 expansion results for binder compositions containing fly ash

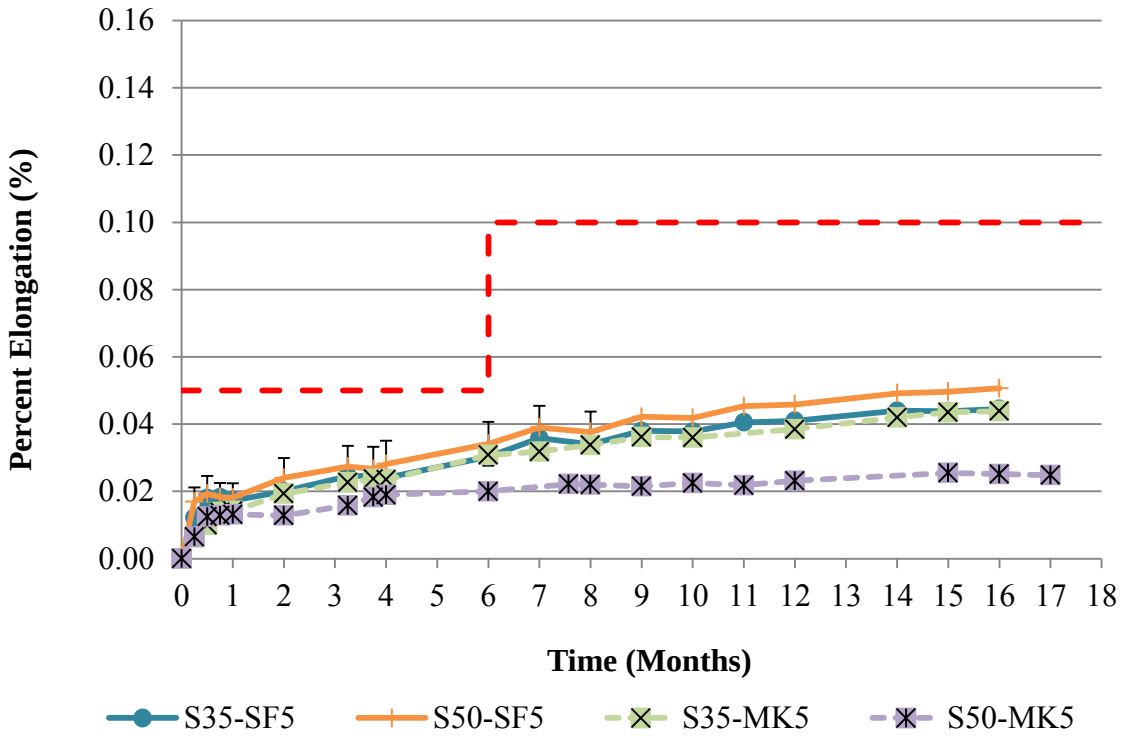

Figure 6.3: ASTM C 1012 expansion results for binder compositions containing slag

6.3.2 Compressive Strength Degradation Testing

The compressive strength degradation testing was performed for 180 days of exposure to samples. After the exposure period, varying degrees of visible damage were observed. Figure 6.4 shows a T5 control and sulfate exposure sample after 180 days. The sulfate exposure sample had cracking along the edges of the cube, but no spalling of corners or surfaces. In contrast, Figure 6.5 shows a T3 control and sulfate exposure sample. The sulfate exposure sample had extensive cracking and spalling of corners and edges.

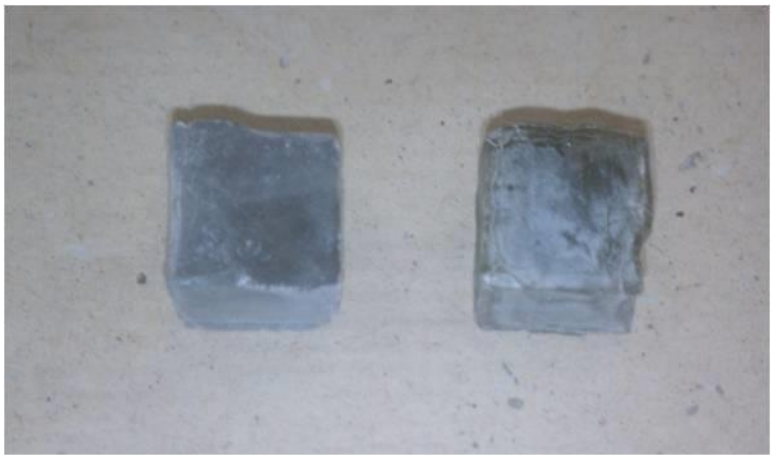

Figure 6.4: T5 control sample (left) and 180 day exposure specimen (right)

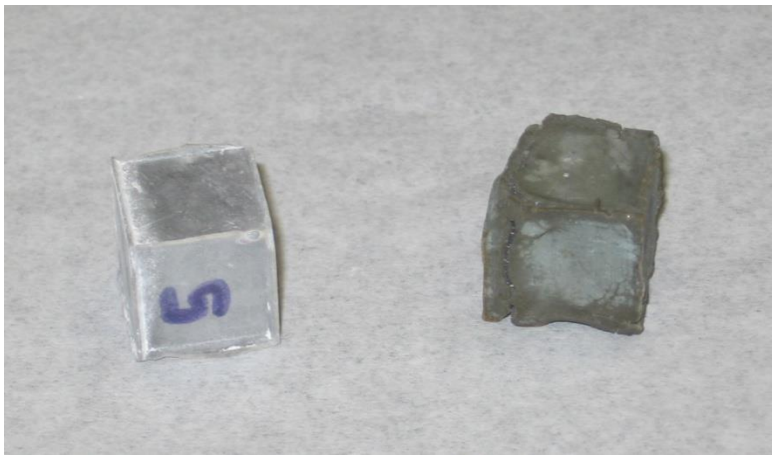

Figure 6.5: T3 control sample (left) and 180 day exposure specimen (right)

The results of the compression strength testing of each mix design are shown in Figures 6.6 to 6.9. The solid blue line represents the strength behavior of samples exposed to sulfate exposure, and the dashed red line with square markers for control samples. The T2 (Figure 6.6-a) and T5 (Figure 6.7-a) sulfate exposure samples were stronger than the control samples at all ages of exposure, but both the control and sulfate exposure samples demonstrated similar strength gain behavior. The strength gain may be attributed to the T2 and T5 mix designs having no SCM's, and therefore more CH present to serve as a buffer to the decalcification of the C-S-H (Eq. 6.1). All binder compositions

besides T2 and T5 demonstrated lower strength in sulfate exposed samples after 180 days than control specimens.

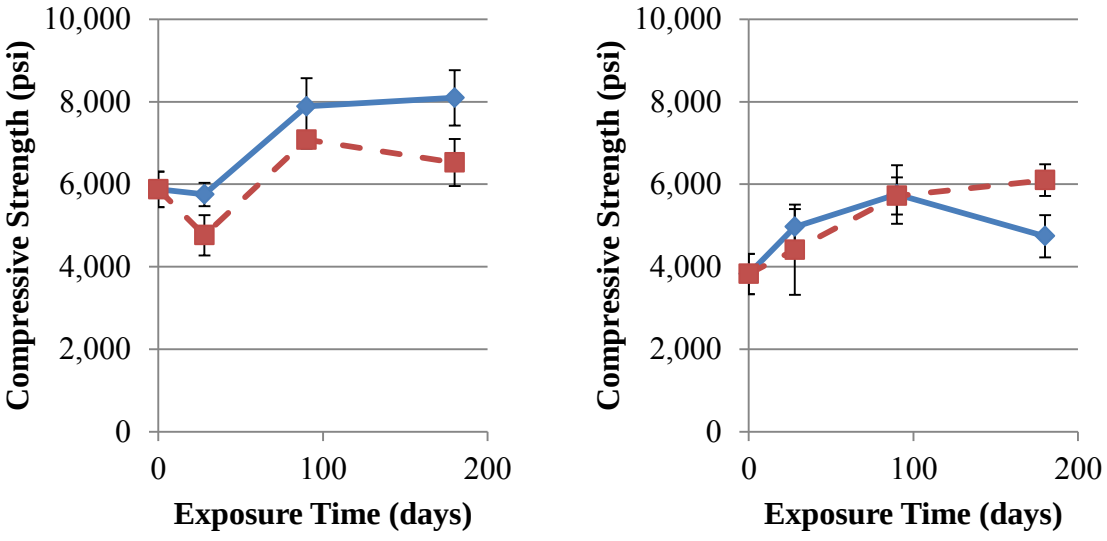

(a) (b)

Figure 6.6: Strength gain curves for control (red dashed line) and sulfate exposure (blue solid line) samples for (a) T2 and (b) T3

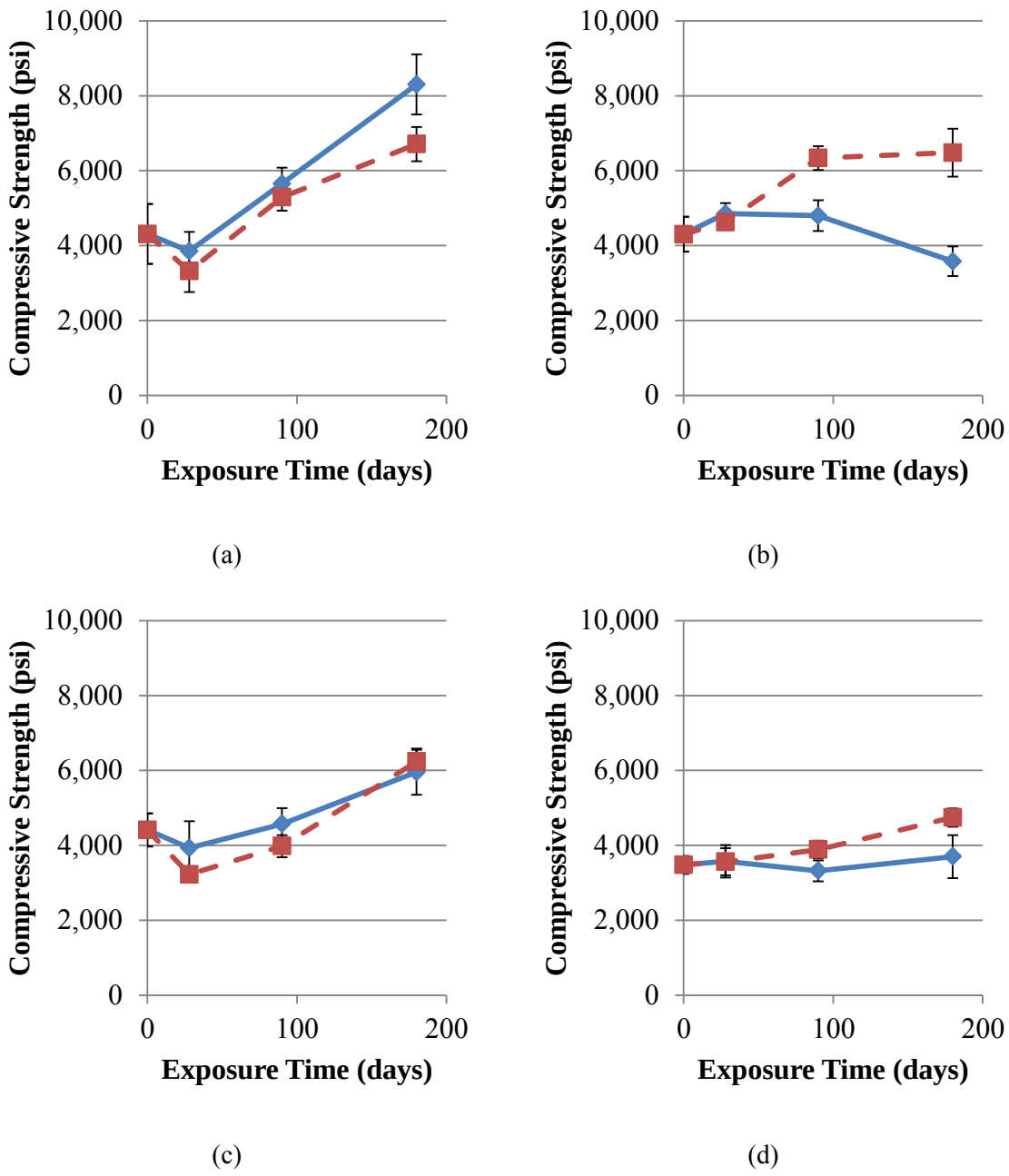

Figure 6.7: Strength gain curves for control (red dashed line) and sulfate exposure (blue solid line) samples for (a) T5, (b) T3-F15, (c) F25, and (d) F25-MK5

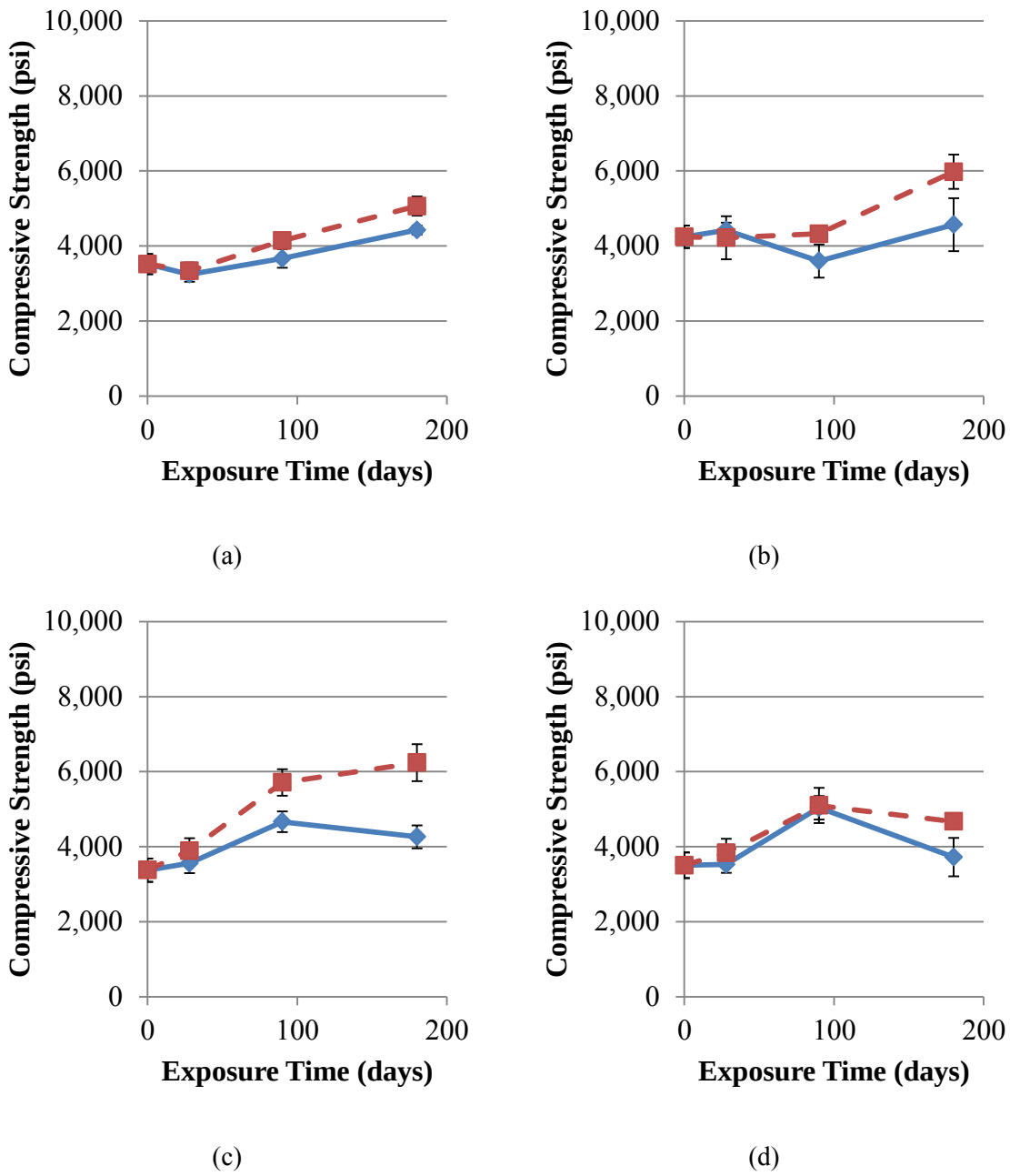

Figure 6.8: Strength gain curves for control (red dashed line) and sulfate exposure (blue solid line) samples for (a) F25-MK10, (b) F25-SF5, (c) F25-SF10, and (d) S35-MK5

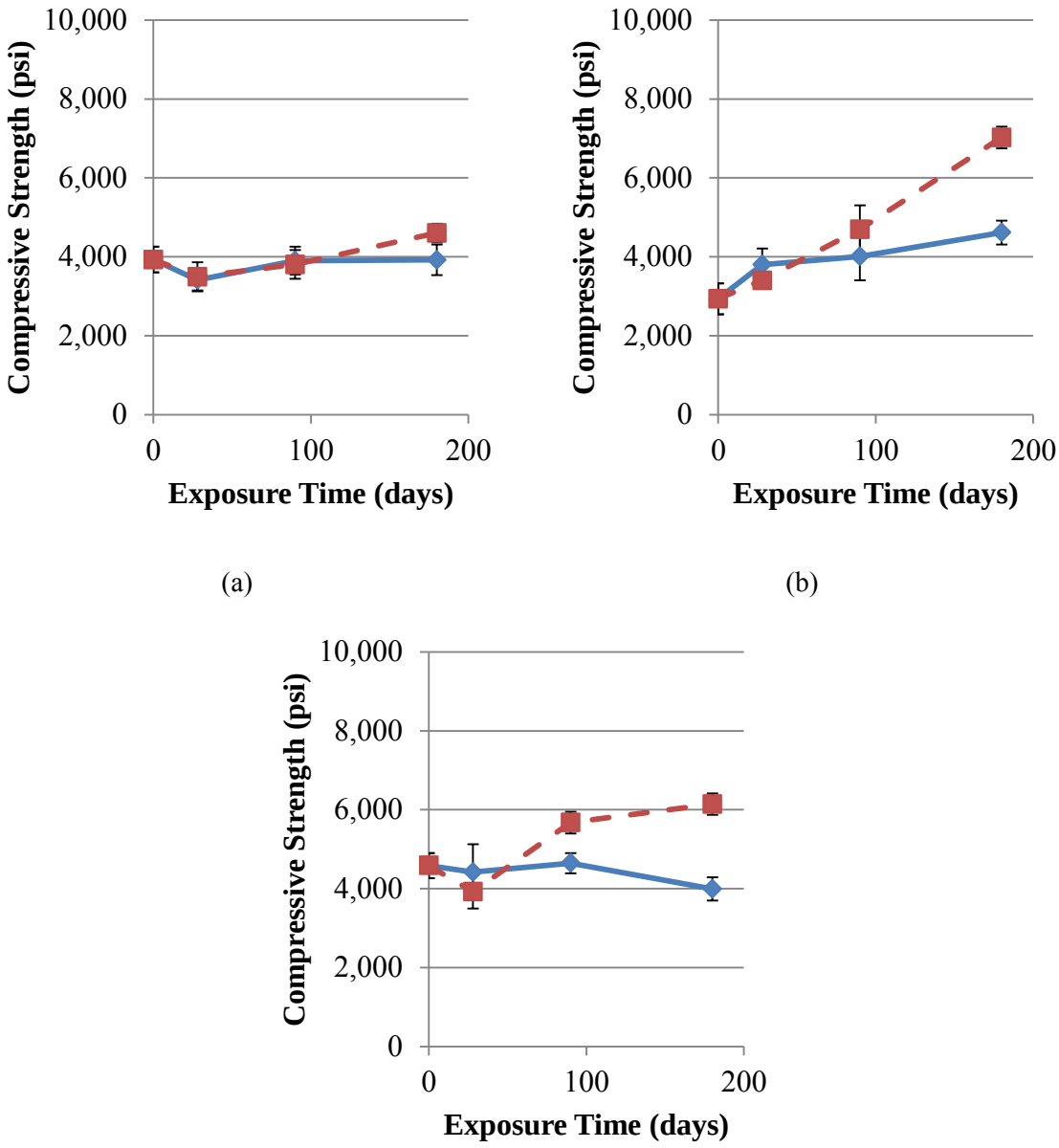

Figure 6.9: Strength gain curves for control (red dashed line) and sulfate exposure (blue solid line) samples for (a) S50-MK5, (b) S35-SF5, and (c) S50-SF5

The relative strength of each mix design compared to the control sample at the same age was calculated using Eq. 6.3 and plotted in Figures 6.10, 6.11, and 6.12 for 28,

90, and 180 days of exposure, respectively. The relative strength was determined using sulfate and control samples of the same age.

$$Relative\ Strength\ = \frac{Sulfate\ Exposure\ Strength}{Control\ Sample\ Strength} \times 100 \qquad \text{(Eq. 6.3)}$$

Hypothesis testing was performed with an α of 0.05 for statistical equivalency of sulfate exposure specimens and control specimens. After 28 days of exposure, no sulfate exposure samples showed statistically significant lower strengths than the control specimens. However, T2 sulfate exposure specimens showed a statistically significant higher strength than the control specimens.

After the 90 day exposure period, the T3-F15, F25-SF10, and S50-SF5 mix designs showed statistically significant decreases in strength. T3-F15 showed the largest decrease in strength, with a 22% decrease in strength compared to the control specimens. T2 and T5 were the only mix designs which demonstrated statistically significant higher strengths in sulfate exposure specimens than control specimens.

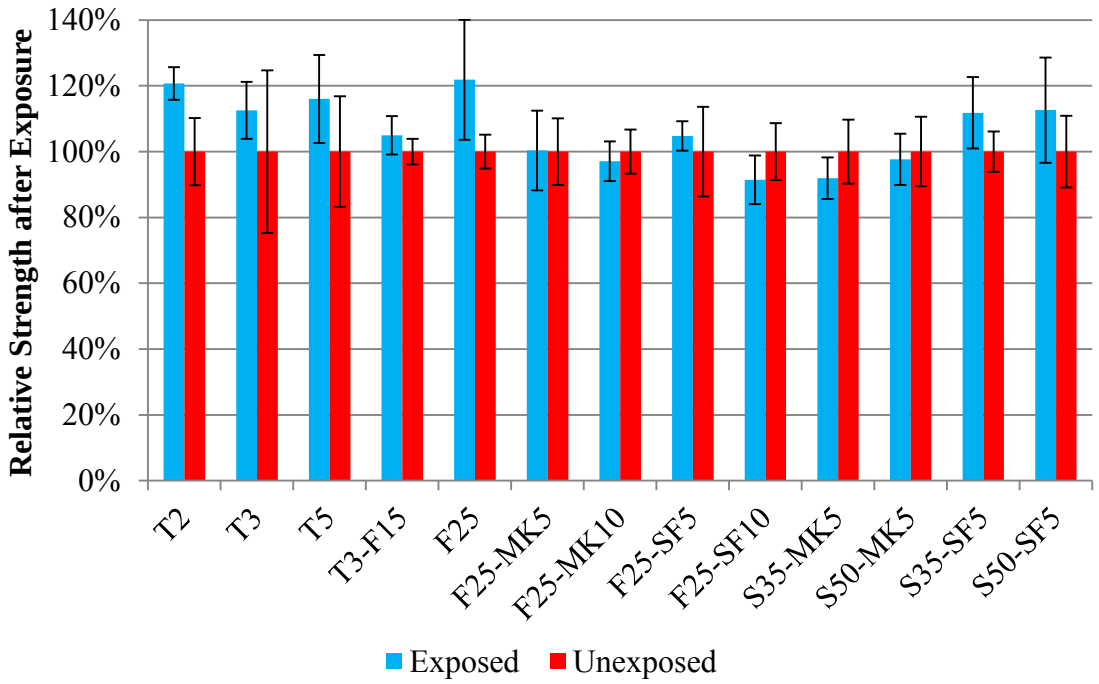

Figure 6.10: Relative strength of sulfate exposure samples after 28 days

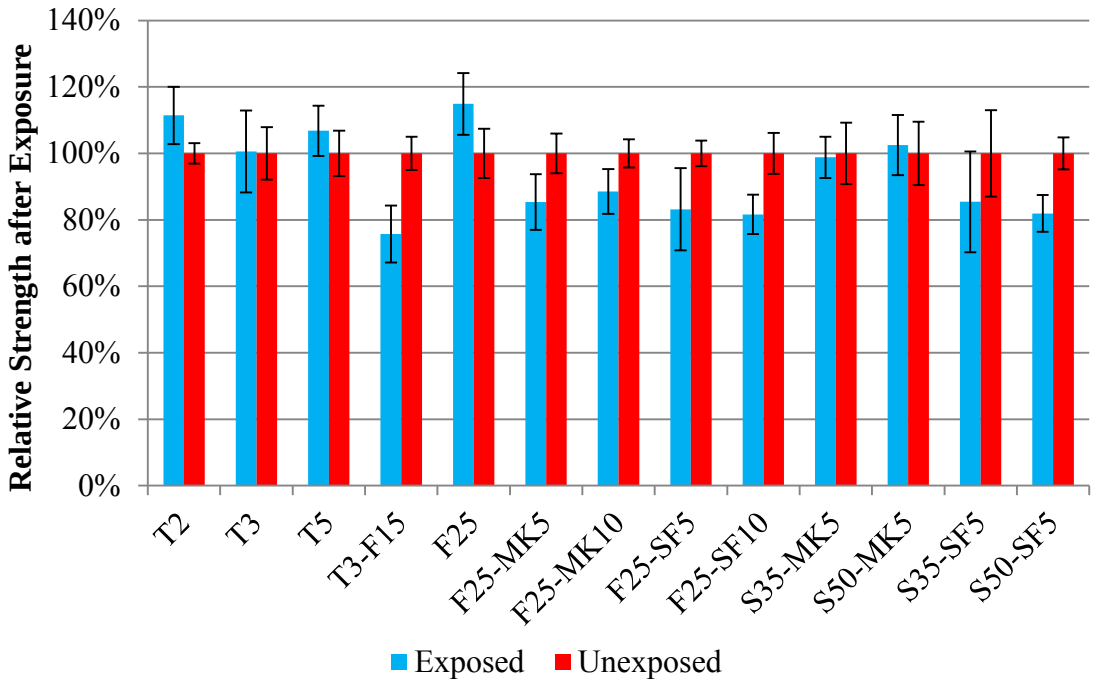

Figure 6.11: Relative strength of sulfate exposure samples after 90 days

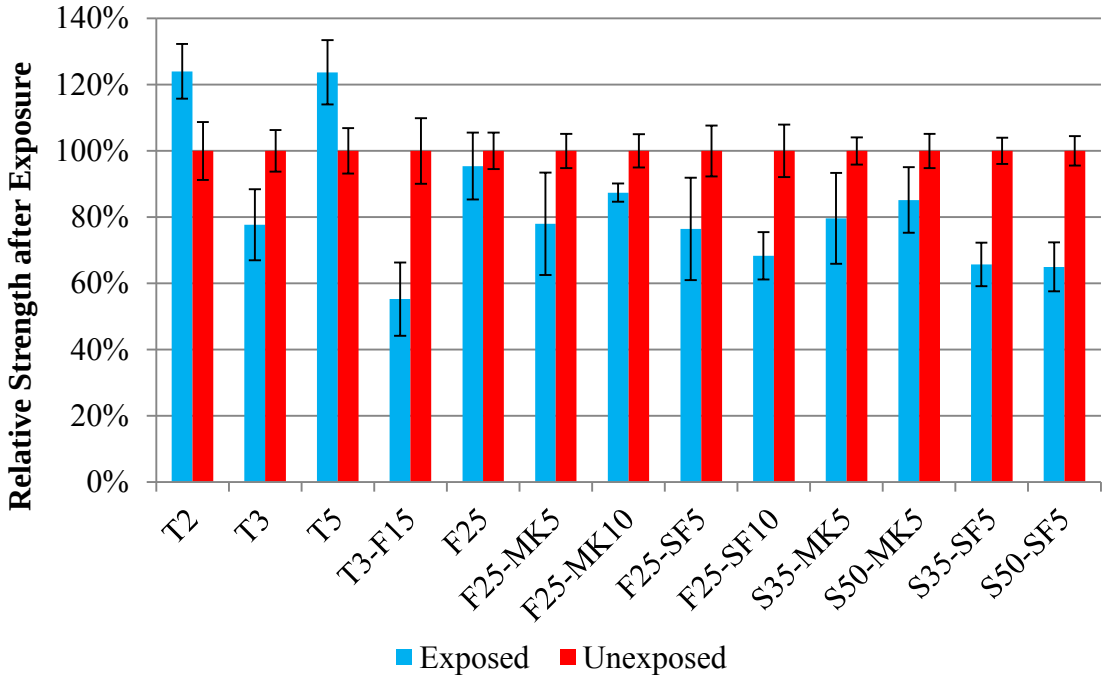

Figure 6.12: Relative strength of sulfate exposure samples after 180 days

After the 180 day exposure period, the T3, T3-F15, F25-SF10, S35-SF5, and S50-SF5 mix designs showed statistically significant decreases in strength. T3-F15 showed the largest decrease in strength, with a 42% decrease in strength compared to the control specimens. T2 and T5 demonstrated statistically significant higher strengths in sulfate exposure specimens than control specimens.

Figures 6.13 through 6.15 show the relative strength of samples at each age versus exposure time for binder compositions containing only cement (Figure 6.13), fly ash mixes (Figure 6.14), and slag mixes (Figure 6.15).

For cement only specimens, both T2 and T5 never exhibited strength loss. T3 showed increasing strength loss at 90 and 180 days. All fly ash mix designs showed a decreasing trend in strengths after the 28 days of exposure. T3-F15 showed the largest decrease in strength, and may be due to containing a ASTM C 150 (2009) Type III cement, which has a higher C_3A content than the other fly ash mix designs. For slag

specimens, mixes containing slag and silica fume performed worse than metakaolin mix designs.

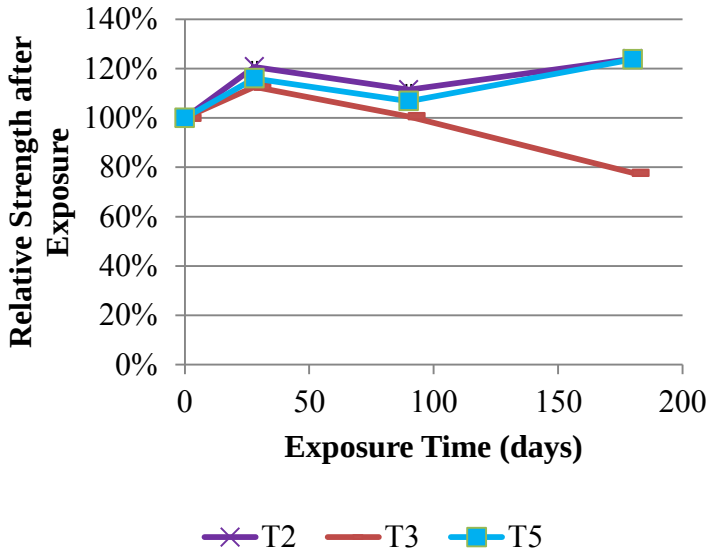

Figure 6.13: Relative strength curves for cement specimens

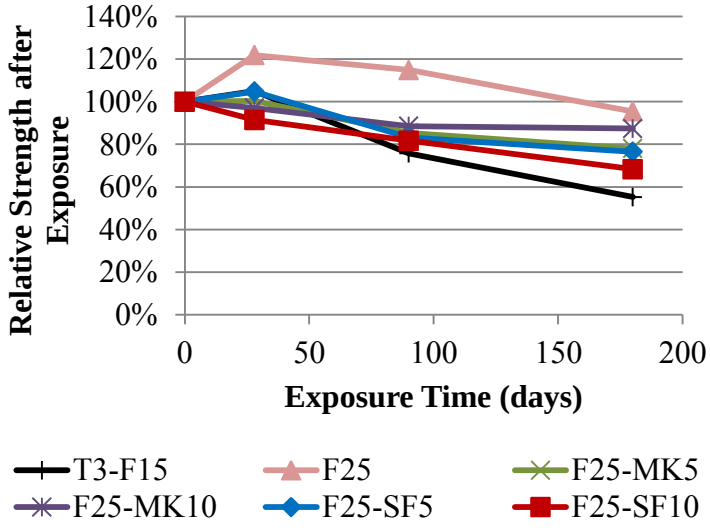

Figure 6.14: Relative strength curves for fly ash binder compositions

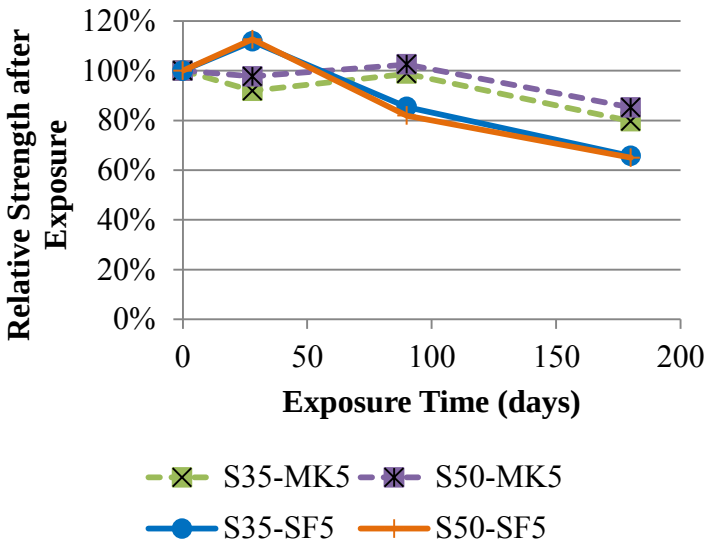

Figure 6.15: Relative strength curves for slag binder compositions

6.3.3 Discussion of Results

The performance of binder compositions exposed to sulfate solutions varied widely depending upon whether the ASTM C 1012 (2009) expansion behavior or compressive strength degradation was being measured. The heavy variance in performance demonstrates that neither test is alone adequate for determining sulfate performance. The results suggest that both the ASTM C 1012 (2009) and compressive strength degradation testing should be used to test for sulfate attack resistance, until a more adequate test method is developed. Table 6.4 provides a summary of the strength and expansion test results, as well as the rank of each mix design compared to the other binder compositions; the #1 rank had the best sulfate resistance. T2 and T5 performed the best on the strength degradation testing; however, failed the 18 month limit for expansion testing. T3 performed poorly on both tests, which is to be expected since it was not designed for sulfate resistance. Slag mix designs containing metakaolin performed well with both test methods. Mix designs containing silica fume performed

poorer at strength testing than their equivalent metakaolin mixes with the same replacement levels.

Table 6.4: Summary of sulfate testing results

	Strength Degradation 180 day strengths		ASTM C 1012 12 month expansion	
Mix	**Rank**	**Relative Strength**	**Rank**	**% Elongation**
T2	1	1.24	11	0.087
T3	8	0.78	13	0.237
T5	2	1.24	12	0.099
T3-F15	13	0.55	3	0.032
F25	3	0.95	9	0.050
F25-MK5	7	0.78	10	0.083
F25-MK10	4	0.87	7	0.042
F25-SF5	9	0.76	4	0.036
F25-SF10	10	0.68	2	0.027
S35-MK5	6	0.80	5	0.039
S50-MK5	5	0.85	1	0.023
S35-SF5	11	0.66	6	0.041
S50-SF5	12	0.65	8	0.046

6.4 Conclusions and Recommendations

The results of this sulfate resistance study demonstrated that the measured performance varied widely depending upon the measured property. The following conclusions and recommendations were supported by the results of this study:

- S35-MK5 or S50-MK5 are recommended for use in sulfate rich environments.
- Expansion testing showed that cement only samples exhibited significantly higher expansion than SCM containing compositions, which may be of concern in a prestressed concrete structure.
- Further research is needed into the cause of increased strength loss in silica fume specimens compared to those which used metakaolin.

- Quantitative X-ray Diffraction (QXRD) is needed to understand compositional changes resulting in the observed behavior.

(This page intentionally left blank.)

CHAPTER 7

Carbonation Resistance of High Performance Concrete

7.1 Introduction

The objectives of this portion of the study were to test the carbonation resistance of potential HPMC's and to perform service life modeling of each mix to determine the predicted corrosion initiation period. Carbonation of concrete can occur due the diffusion of carbon dioxide from the atmosphere and sea water through the pores of concrete. Carbonation of concrete leads to the depletion of calcium hydroxide, which causes the decrease in pH, and can lead to a loss of calcium silicate hydrate (C-S-H), which is the primary strength giving component of hydrated cement paste (Neville, 1997). Carbonation of concrete can cause strength loss of the concrete and initiate corrosion of reinforcing steel due to the decreased pH (Papadakis, et al, 1991). Therefore, maintaining high pH levels helps assure protection of embedded reinforcing steel.

7.2 Experimental Program

The carbonation resistance properties of the mix designs presented in Chapter 4 were characterized by using an accelerated exposure test based upon the procedure used by Papadakis (1991). The test was performed on concrete prisms exposed to a 20% carbon dioxide environment, at 55% relative humidity and 40˚ C in a Nuaire US Autoflow NU-4850 Incubator. Samples were moist cured for 28 days in a fog room, conditioned at 55% relative humidity and 40˚C for 7 days, and then placed into the carbonation chamber. After various exposure periods, a phenolphthalein indicator solution, as used by Kurth (2008), was applied to the cut surfaces; and the distance to the carbonation front, as defined by color change at pH of 9.2, was measured.

The results were compared with estimator equations developed by Papadakis (2000). Additionally, modeling of the carbonation depth versus time was performed to aid in service life prediction calculations for corrosion initiation.

7.3 Results and Discussion

7.3.1 Carbonation Results

The carbonation depth was measured at various ages, and the depth of carbonation versus time for each mix design is shown in Figures 7.1 through 7.3. Carbonation has been shown to be a diffusion based phenomenon by Papadakis, et al. (1991). A simple model for carbonation is that the depth of ingress is proportional to the n^{th} root of time, as given in Eq. 7.1 (Bertolini, et al., 2004). Typically, n is assumed to be 2, resulting in the depth of ingress being proportional to the square root of time. Figures 7.1 to 7.3 also show the regression curve which fit Eq. 7.1 to the experimental data. Table 7.1 gives the measured carbonation constants from the regression analysis.

$$d = Kt^{1/n} \qquad \text{(Eq. 7.1)}$$

Where,

d = depth of carbonation

K = carbonation constant

t = time

n = curve fitting factor, typically assumed to be 2

The carbonation testing showed that mix designs with higher water to cementitious materials ratios (w/cm) had significantly higher rates of carbonation. Mix design T2, which had a 0.4 w/cm had a carbonation rate an order of magnitude of higher than specimens with a 0.3 w/cm. After 28 days of exposure, T2 had carbonated over 0.75

inches. Mix designs containing fly ash and metakaolin or silica fume had the lowest rates of ingress. Slag mixes and fly ash only mix designs had similar rates of ingress. The data suggest that the use of silica fume or metakaolin helped to decrease the rate of carbonation.

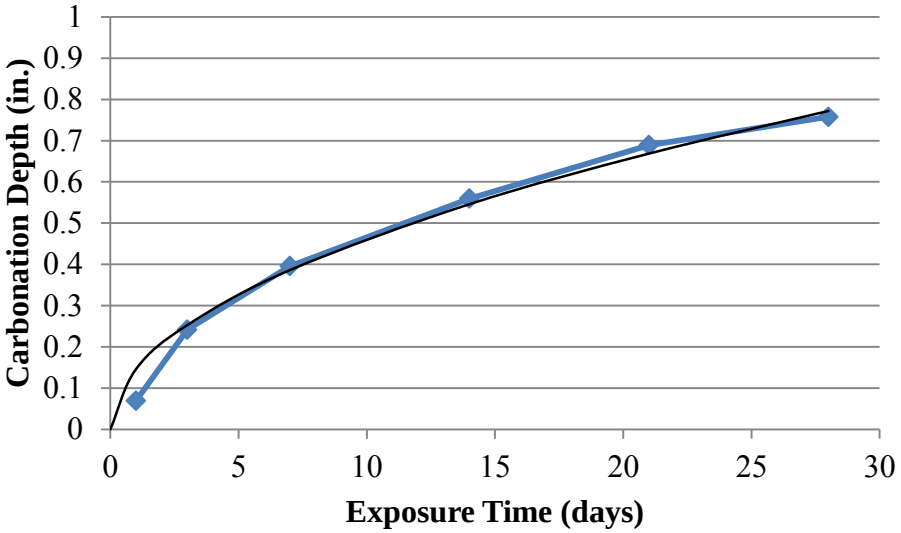

(a)

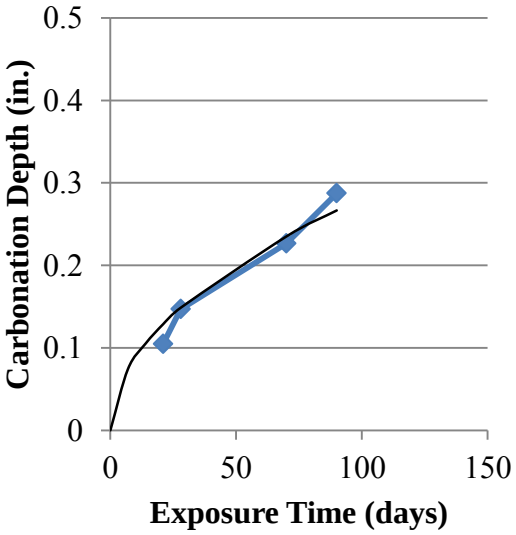

(b)

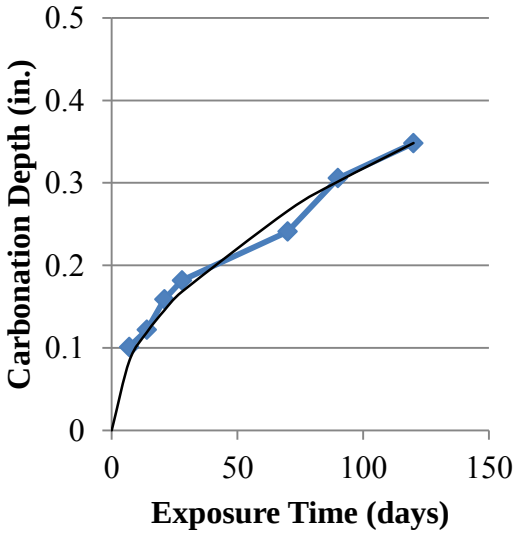

(c)

Figure 7.1: Carbonation curves for (a) T2, (b) T3-F15, and (c) F25

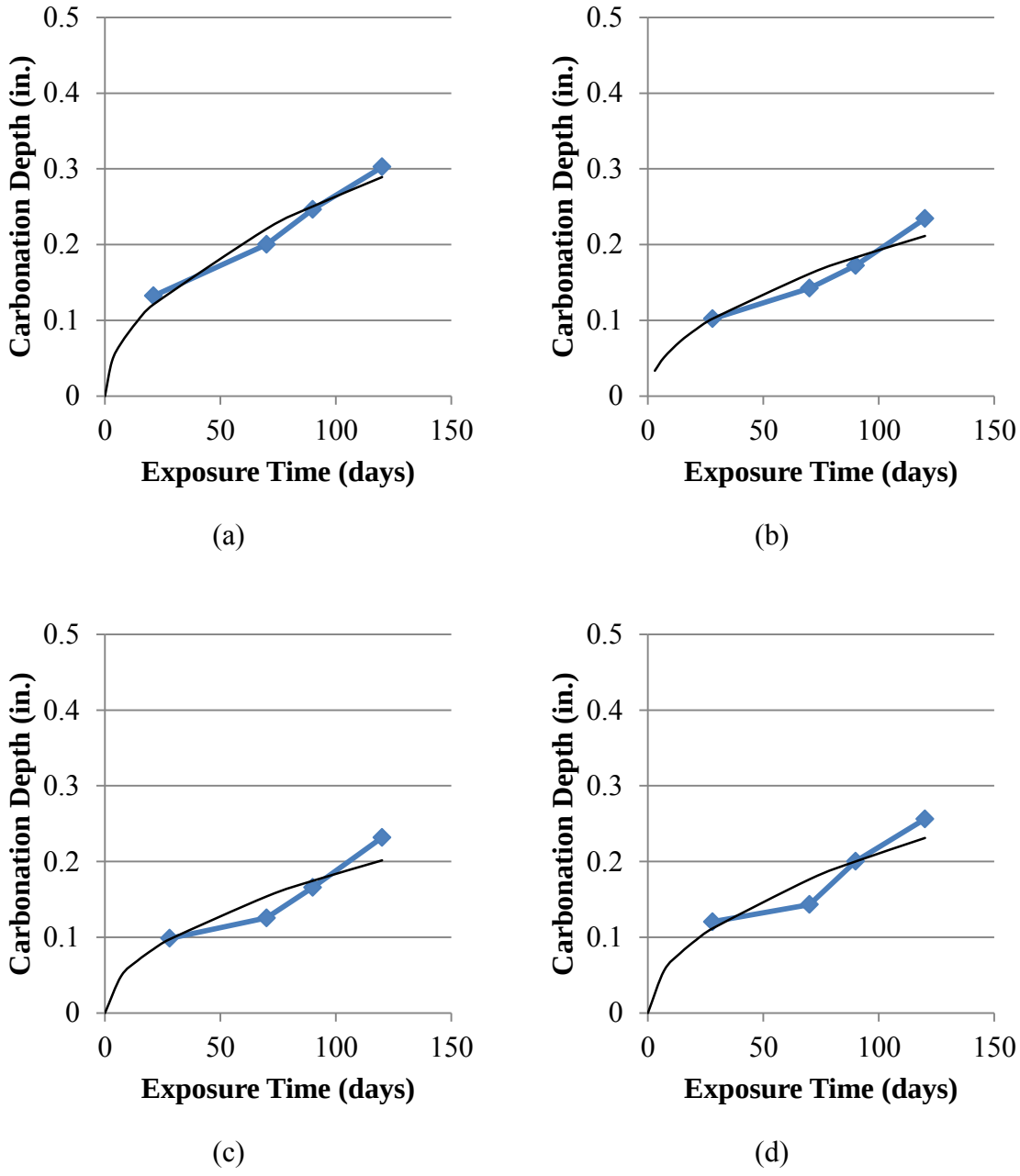

Figure 7.2: Carbonation curves for (a) F25-MK5, (b) F25-MK10, (c) F25-SF5, (d) F25-SF10

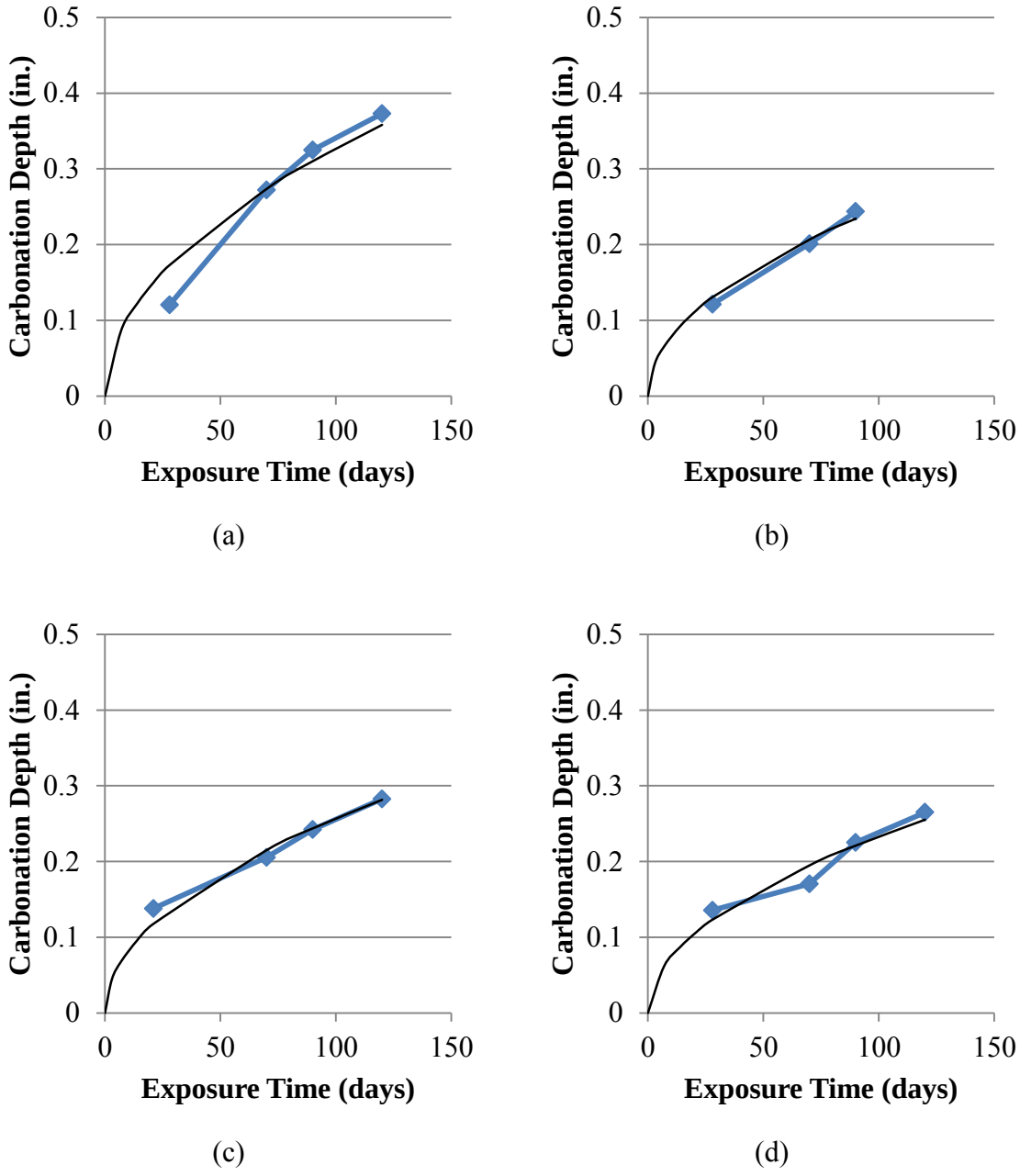

Figure 7.3: Carbonation curves for (a) S35-MK5, (b) S50-MK5, (c) S35-SF5, (d) S50-SF5

The regression analysis with R2 values of 0.82 or higher showed that there was good agreement between the experimental data and the Eq. 7.1 relationship of the depth of carbonation being proportional to the square root of the exposure period.

Table 7.1: Experimental carbonation constants

Mix	Carbonation Constant (in./day$^{0.5}$)
T2	0.1459
T3-F15	0.0281
F25	0.0318
F25-MK5	0.0364
F25-MK10	0.0193
F25-SF5	0.0184
F25-SF10	0.0211
S35-MK5	0.0327
S50-MK5	0.0247
S35-SF5	0.0257
S50-SF5	0.0233

7.3.2 Modeling

Papadakis, et al. (1991) and Papadakis (2000) presented a sophisticated model that gives a mathematical and physical meaning to the constant, K. A generic form of the Papadakis (2000) model is given in Eq. 7.2. The model provides a method for estimating the carbonation depth of mix designs containing cement and fly ash or silica fume. Additionally, the method establishes a technique for accounting for the carbon dioxide level and relative humidity.

$$d = \sqrt{\frac{2\, D_{e,CO_2}\left(\frac{CO_2}{100}\right)t}{0.33CH+0.214CSH}} \qquad \text{(Eq. 7.2)}$$

Where,

d = depth of carbonation, m.

$D_{e,CO2}$ = diffusivity of CO_2 in carbonated concrete, m^2/s

CO_2 = carbon dioxide content of ambient air at concrete surface in %

t = time, s

CH = estimated calcium hydroxide content, kg/m^3

CSH = estimated calcium-silicate-hydrate content, kg/m^3

The relationship can be simplified into the same form as presented in Eq. 7.1, where the depth of carbonation is proportional to square root time by a constant that accounts for the exposure conditions and mix design properties. Eq. 7.3 provides the relationship between the carbonation constant, K, and the calculation method presented by Papadakis (2000). This relationship was used to calculate the experimental carbonation constant for ambient carbon dioxide levels and the estimation method used to predict the carbonation constant for mix designs F25 and T3-F15. Table 7.2 shows the measured and estimated values for the carbonation constant. Only plain Portland cement concretes and binary mix designs with fly ash were able to be predicted with current estimation techniques. The Papadakis (2000) estimation technique underestimated the carbonation constant for mix design T2 by 42%, which led to an unconservative estimate for the predicted service life. The Papadakis (2000) technique overestimated the carbonation constant for fly ash mix designs, which led to a shorter predicted service life and would be conservative for design.

$$K = \sqrt{\frac{2\, D_{e,CO_2}\left(\frac{CO_2}{100}\right)}{0.33CH + 0.214CSH}} \qquad \text{(Eq. 7.3)}$$

Where,

K = carbonation constant

$D_{e,CO2}$ = diffusivity of CO_2 in carbonated concrete, m^2/s

CO_2 = carbon dioxide content of ambient air at surface,%

CH = estimated calcium hydroxide content, kg/m^3

CSH = estimated calcium-silicate-hydrate content, kg/m^3

The results of the Sulapha, et al. (2003) study suggested that the carbonation constant, K, is related to the compressive strength of the concrete by Eq. 7.4 for a 6.5% CO_2 accelerated test environment.

$$K = -0.08315 * S + 7.5127 \qquad \text{(Eq. 7.4)}$$

Where,

K = carbonation constant ($mm/week^{0.5}$)

S = compressive strength at time of exposure (MPa)

Table 7.2: Experimental and estimated carbonation constants

Mix	Carbonation constant (in./yr$^{0.5}$)	Estimated Carbonation Constant (in./yr$^{0.5}$) (Eq. 7.3)	Estimated Carbonation Constant (in./yr$^{0.5}$) (Eq. 7.4)
T2	0.088	0.050	0.091
T3-F15	0.017	0.026	0.070
F25	0.019	0.019	0.073
F25-MK5	0.022	-	0.048
F25-MK10	0.012	-	0.012
F25-SF5	0.011	-	0.038
F25-SF10	0.013	-	0.032
S35-MK5	0.020	-	0.014
S50-MK5	0.015	-	0.027
S35-SF5	0.016	-	0.040
S50-SF5	0.014	-	0.041

The results for the carbonation constant given in Table 7.2 were used to estimate the carbonation front with time for an ambient exposure. Figures 7.4 and 7.5 show the estimated carbonation front versus time for fly ash and slag mix designs, respectively. Based upon one-dimensional ingress, none of the fly ash or slag mix designs would have the carbonation front reach the level of steel with a 3 in. cover in a 200 year service life. F25-SF5 and S50-SF5 provided the lowest ingress for fly ash and slag mix designs respectively, with fly ash mix designs containing silica fume performing the best.

Figure 7.6 shows the predicted carbonation front locations for T2, T3-F15, and the best fly ash and slag mix designs. It can be observed that all mix designs provided adequate protection for carbonation, but ternary mix designs with lower water to cementitious materials ratios and fly ash performed better than the other mix designs.

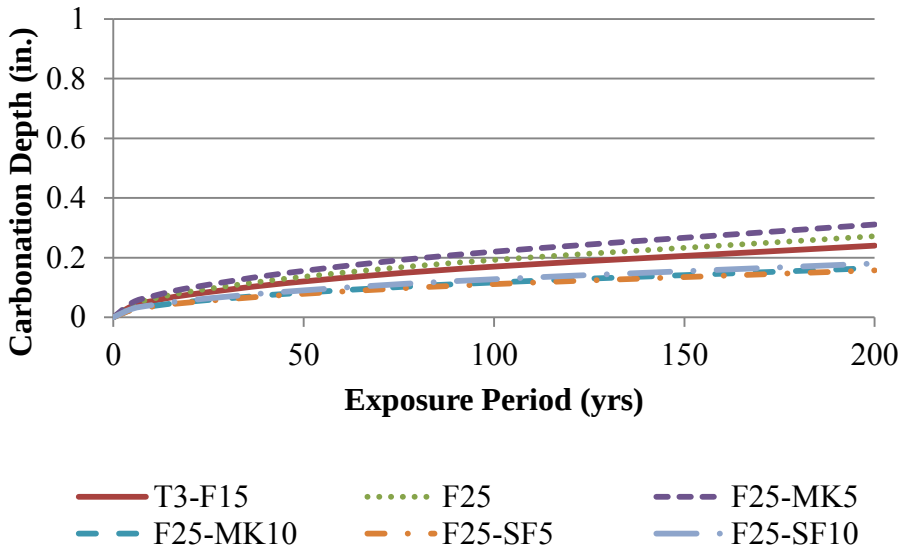

Figure 7.4: Predicted carbonation front location versus time for fly ash mix designs

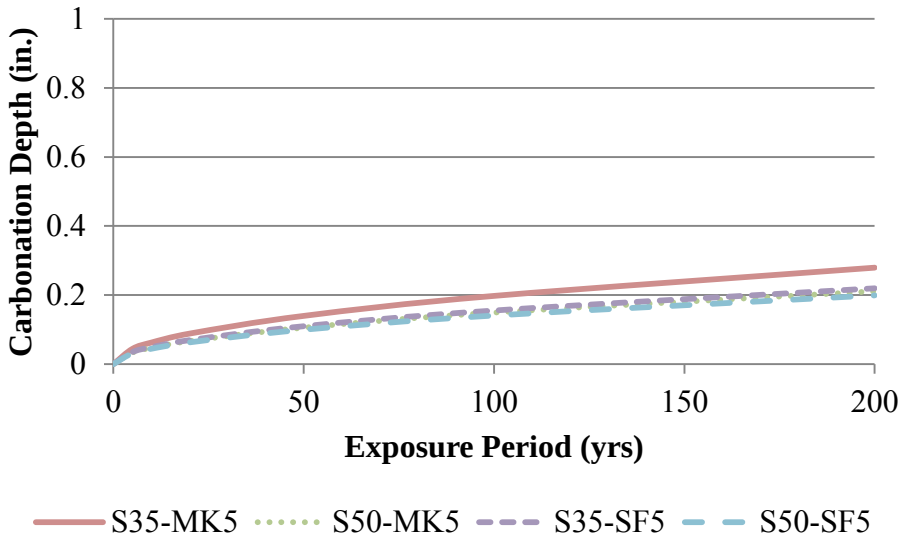

Figure 7.5: Predicted carbonation front location versus time for slag mix designs

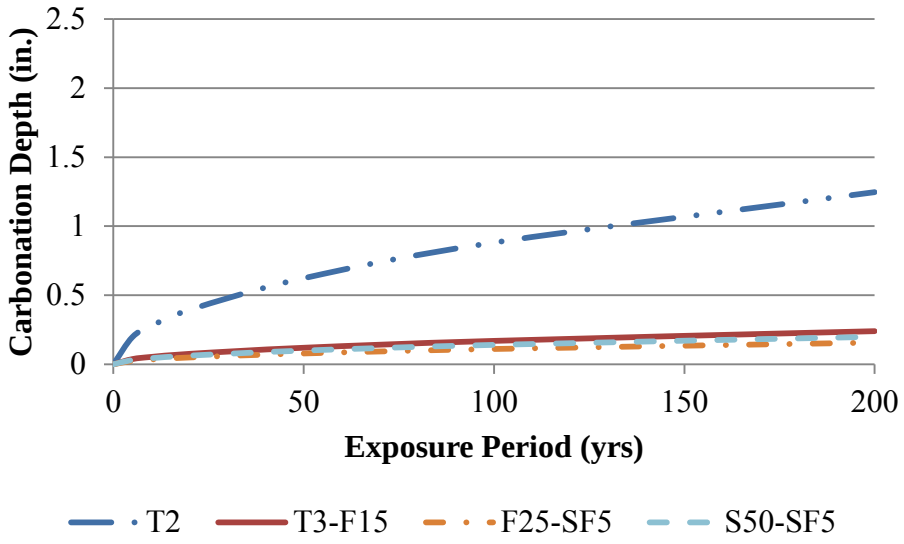

Figure 7.6: Predicted carbonation front location versus time for T2, T3-F15 and the best fly ash and slag mix designs

7.4 Conclusions and Recommendations

The study into carbonation performance of potential HPMC mix designs showed that ternary mix designs are capable of providing service lives in excess of 200 years. The results showed that estimation techniques overestimate and underestimate carbonation constants which could lead to an unconservative estimate of usable service life before corrosion initiation. The results showed that the carbonation rate decreased significantly with lowering of the w/cm ratio. Additionally, for mix designs containing SCM's, ternary mix designs with silica fume and fly ash perform the best.

The results of this study led to the following recommendations:

- Use 0.3 w/cm mix designs with fly ash and silica fume to ensure service lives in excess of 100 years.
- Future research is needed to develop service life models which account for 2-D ingress of the carbonation front.

- An estimation technique for accurately estimating the carbonation constant is needed for ternary mix designs.

CHAPTER 8

Conclusions and Recommendations

8.1 Conclusions

The results of the study on concrete materials established that a new mixture termed HPMC is needed to provide adequate resistance to chloride ingress, carbonation, and sulfate attack in order to provide a 100+ year lifespan for precast prestressed concrete piles in marine environments. The development and testing of potential HPMC mix designs found that through the use of ternary mix designs, it is possible to provide durability characteristics that allow for a service life in excess of the 100 year goal.

Studies into chloride ingress resistance demonstrated that slag mix designs containing metakaolin provided superior resistance compared to other mix designs. Additionally, it was found that accelerated test methods may be used within appropriate limits for quality assurance testing.

Sulfate resistance testing demonstrated that the performance characteristic measured during sulfate exposure had significant effect on the apparent resistantance of mix designs. Compression degradation and expansion testing both showed that slag mix designs with metakaolin performed well, regardless of the testing method for sulfate resistance.

Carbonation testing of mix designs showed that mixes with a low w/cm are capable of providing service lives in excess of 200 years, and that fly ash mix designs with silica fume performed the best.

8.2 Recommendations

The following recommendations are supported by the findings of this investigation for future design and construction of precast prestressed concrete piles in marine environments:

- Use S35-MK5, S50-MK5, or F25-SF5 to maximize the usable service life of structures exposed to chlorides.
- Implement a 1000 Coulomb limit for rapid chloride ion permeability testing (RCPT) in accordance with ASTM C 1202 (2007) for testing of HPMC.
- Use S35-MK5 or S50-MK5 in sulfate rich environments to ensure adequate protection against sulfate attack.
- Use ternary mix designs with a 0.3 w/cm to ensure service lives over 200 years for structures subjected to carbonation, and F25-SF5 for severe environments.
- Use S50-MK5 or F25-SF5 for marine environments where structures are subjected to chloride ingress, carbonation, and sulfate attack.

Additionally, the results of this study have led to the following recommendations of areas for future research and investigation:

- Estimation techniques for chloride ingress resistance of mix designs containing metakaolin are needed.
- Research into the compositional changes undergone by ternary mix designs exposed to sulfate attack, and its influence on strength loss and expansion is needed.

- Development of estimation techniques for the carbonation constant for ternary mix designs is needed.
- Development of carbonation modeling methods for 2-D ingress is needed.
- Development of performance based criterion for testing of potential HPMC for resistance to chloride ingress, sulfate attack, and carbonation is needed.
- A study into the durability requirements and service life modeling of structures utilizing duplex stainless steel prestressing strands is needed.

(This page intentionally left blank.)

Appendix A

Georgia Coastal Bridge Inspections

A.1 Overview

Bridges of interest in the coastal counties with reported damage to the concrete piling were inspected from May 2nd through the 4th, 2010. Additionally, interviews were performed with Georgia Department of Transportation (GDOT) personnel at the Savannah and Brunswick offices and with Standard Concrete Products (SCP) engineers in Savannah and summaries are presented in Appendix B.

A.2 Bridge Inspections

Eleven bridge sites shown in Figure A.1 were inspected during the trip. Table A.1 gives the bridge numbers and names. The sites were selected based on the extent and types of damage noted in inspection reports provided by the GDOT Bridge Maintenance Office, varying proximities to the coast, and distribution throughout the coastal counties of Georgia. All bridges spanned rivers or inlets with fresh or brackish waters. At each site, photos were taken of any visible damage, and water samples collected for pH, sulfate content, and chloride content testing.

Table A.1: Bridge ID Numbers and Names for Locations Inspected

Bridge Name	Bridge Number
Harriet's Bluff Road at Deep Creek Bridge	039-0049
Houlihan Bridge	051-0054
US 17 at Back River Bridge	051-0059
US 80 at Lazeratto Creek Bridge	051-0066
Island Expressway at Wilmington River Bridge	051-0132
Oatland Island Research Bridge	051-5013
Long Bridge Road at Ebenezer Creek Bridge	103-0030
I-95 at Turtle River Bridge	127-0052
Torras Causeway at Little River Bridge	127-0063
Ocean Highway at Riceboro Creek Bridge	179-0005
Ocean Highway at Champney's River Bridge	191-0005

Figure A.1: Bridges Inspected Along Georgia's Coastal Counties.

Red dots indicate bridge locations.

A.2.1 Harriett's Bluff Road at Deep Creek Bridge (Bridge No. 039-0049)

Located approximately 8 miles from the coast in Camden county, the Harriett's Bluff Road Bridge spanning Deep Creek exhibited significant corrosion-related

deterioration, primarily in its superstructure. The bridge was constructed in 1964 with a reinforced concrete superstructure and precast concrete pile-bent substructure system. The substructure looked to be in fairly good condition, with minimal surface abrasion and heavy marine growth and oyster scale in the tidal region (Figure A.2). However, given that the inspection coincided with high tide, a detailed assessment of the substructure could not be made.

Figure A.2: Substructure of Harriett's Bluff Road at Deep Creek Bridge (Bridge No. 039-0049)

The superstructure of the bridge exhibited the most significant deterioration. Cracking and spalling of concrete, especially in the cast-in-place concrete railing/barrier system, was widespread throughout the superstructure. Typical corrosion damage observed in the barrier is shown in Figure A.3 below.

Figure A.3: Corrosion Damage in Cast-in-Place Barrier of Harriett's Bluff Road at Deep Creek Bridge (Bridge No. 039-0049)

A.2.2 Houlihan Bridge (Bridge No. 051-0054)

Constructed in 1953, the Houlihan Bridge is located approximately 17 miles from the coast near Port Wentwork in Chatham county. The bridge consists of a reinforced concrete beam superstructure, a precast concrete pile-bent substructure, and a central movable steel truss span. An overall view of the bridge is shown in Figure A.4.

Figure A.4: Overall View of Houlihan Bridge (Bridge No. 051-0054)

Similar to what had been recorded in GDOT bridge inspection reports, the most significant deterioration observed on the Houlihan Bridge was found in the submerged and tidal zone of the concrete substructure. Significant surface abrasion was ubiquitous, with fully exposed aggregates from the top of the splash zone down. In some cases, abrasion was so aggressive that hourglassing of the piles could be seen even at a distance. Some typical photos of surface abrasion are shown in Figures A.5 and A.6. In Figure A.5, it should be noted that abrasion occurred on both the precast piling and the cast-in-place support for the movable bridge span in the background. Given the bridge's location fairly far inland, little oyster shell was present on the piles.

Figure A.5: Surface Abrasion of Concrete Substructure on Houlihan Bridge (Bridge No. 051-0054)

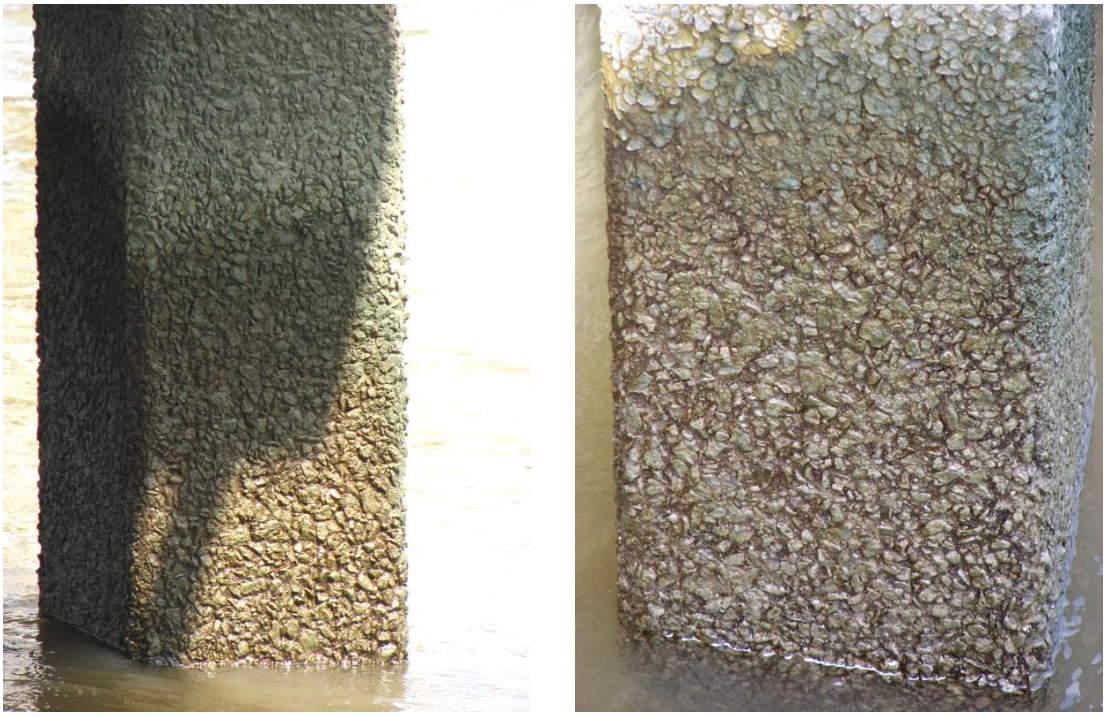

Figure A.6: Surface Abrasion Oberved in Concrete Substructure of Houlihan Bridge (Bridge No. 051-0054)

A.2.3 US 17 at Back River Bridge (Bridge No. 051-0059)

The Back River Bridge is located at the Georgia – South Carolina border just east from the Talmadge Bridge, approximately 12 miles from the coast in Chatham county. The bridge was constructed in 1954 with a reinforced concrete beam superstructure and a precast pile-bent substructure with a total length of approximately 0.5 miles. The precast pile substructure, which is shown in Figure A.7, is extensive and has been severly damaged by corrosion.

Figure A.7: Pile-Bent Substructure of US 17 at Back River Bridge (Bridge No. 051-0059)

Almost all piles have vertical cracks at the corners, extending from the waterline up to 2 to 3 feet above high tide with rust staining present. Many of the cracks appear to be much larger than hairline in width, although measurements were limited due to the marsh surrounding the bridge. Typical damage observed in the piles is shown in Figure A.8. The substructure had recently undergone a retrofit of the piles conducted by an external contractor. This retrofit consisted of fiber-reinforced polymeric (FRP) jackets being compression fitted onto the most significantly damaged piles in order to provide confinement of the cracked concrete and to limit any subsequent corrosion damage. A typical jacketed pile is shown in Figure A.9.

Figure A.8: Vertical Cracking at Corner of Concrete Pile on US 17 at Back River Bridge (Bridge No. 051-0059)

Figure A.9: Corrosion Damaged Piling with FRP Jacket Retrofit on US 17 at Back River Bridge (Bridge No. 051-0059)

A.2.4 US 80 at Lazeratto Creek Bridge (Bridge No. 051-0066)

Located adjacent to the coast at the mouth of the Savannah River in Chatham county, the US 80 Bridge spanning Lazeratto Creek was constructed in 1960 with a precast concrete and steel girder superstructure and a precast pile-bent substructure. The overall bridge structure is shown in Figure A.10 below, with only the central steel spans of the bridge over water.

Figure A.10: Overall View of US 80 at Lazeratto Creek Bridge (Bridge No. 051-0066)

Due to the marsh adjacent to the bridge and our inspection occuring at high tide, limited access to the substructure in the spans over water was available for photos. In the dry marsh approach spans, a detailed inspection of the precast piles could be made. Grout repairs of what looked to be traverse cracks likely caused during driving were observed in some piles (see Figure A.11). Poor construction in the cast-in-place pile caps was also evident with honeycombing and exposed reinforcement in some cases (see Figure A.12).

Figure A.11: Grout Repair of Traversve Crack in Precast Concrete Pile on US 80 at Lazeratto Creek Bridge (Bridge No. 051-0066)

Figure A.12: Honeycombing and Exposed Corroding Reinforcement in Pile Cap on US 80 at Lazeratto Creek Bridge (Bridge No. 051-0066)

A.2.5 Island Expressway at Wilmington River Bridge (Bridge No. 051-0132)

Located approximately 8 miles inland in Chatham County, the Island Expressway Bridge spanning the Wilmington River was constructed in 1963 using a precast concrete girder superstructure and precast pile-bent substructure. A steel moveable span is located in the center of the bridge. An overall view of the bridge as seen from the underside is shown in Figure A.13. The adjacent bridge shown on the right of Figure A.13 carrying westbound traffic appears to be much newer and constructed with piers rather than pile bents. No record of the reconstruction of the westbound lanes was found in the inspection reports.

Figure A.13: Underside of Island Expressway at Wilmington River Bridge (Bridge No. 051-0132)

At low tide, a detailed inspection of the submerged regions of the piling was performed. Limestone aggregates showed deterioration and abrasion on all piles (see

Figure A.14). The limestone aggregates were exposed on the surface of the piles due to pop-outs and and showed severe abrasion. Large longitudinal cracks at the corners with rust staining were present in most piles. Severe cases of cracking and spalling, as well as "hour-glassing" in the tidal region, are shown in Figure A.15.

Figure A.14: Deterioration of Limestone Aggregates Present at Concrete Surface on Island Expressway at Wilmington River Bridge (Bridge No. 051-0132)

Figure A.15: Severe Damage to Concrete Piling on Island Expressway at Wilmington River Bridge (Bridge No. 051-0132)

A.2.6 Oatland Island Research Bridge (Bridge No. 051-5013)

The Oatland Island Research Bridge was constructed in 1987 using precast concrete girders and a precast concrete pile bent substructure. An overall view of the bridge is shown in Figure A.16. The bridge was constructructed using a variety of corrosion mitigation methods. The following methods were used in each bent: epoxy coated strands, calcium nitrite corrosion inhibitors, and high performance concrete with SCMs. While access to the substructure for photos was limited due to the surrounding marsh and oyster shell growth on the piling, all of the piles looked to be in excellent condition with no apparent cracking and very limited surface abrasion (Figure A.17).

Figure A.16: Oatland Island Research Bridge (Bridge No. 051-5013)

Figure A.17: Pile-Bent Substructure of Oatland Island Research Bridge

(Bridge No. 051-5013)

A.2.7 Long Bridge Road at Ebenezer Creek Bridge (Bridge No. 103-0030)

Located approximately 30 miles inland in Effingham county, the Long Bridge Road Bridge spanning Ebenezer creek was constructued in 1968 with a reinforced

concrete superstructure and precast concrete pile-bent substructure. An overall view of the bridge is shown in Figure A.18.

Figure A.18: Long Bridge Road at Ebenezer Creek Bridge (Bridge No. 103-0030)

Bridge 103-0030 was selected for inspection primarily due to the mention of driving cracks in the piles recorded in its inspection report. Tranverse cracks which had been repaired with grout were observed on two piles but were not present throughout the bridge. A typical repair is shown in Figure A.19.

Figure A.19: Grout Repair of Tranverse Cracking Likely Caused by Overdriving on Long Bridge Road at Ebenezer Creek Bridge (Bridge No. 103-0030)

The most predominant deterioration observed on the bridge was degradation of the paste fraction of the concrete piling in regions from the high-water mark down. Above the high-water mark, the concrete was in good condition. Below the high-water mark, the paste was extremely friable and could be scratched easily. This condition was observed on all piles. A typical case of surface abrasion is shown in Figure A.20.

Figure A.20: Surface Abrasion of Concrete Below High-Water Mark on Long Bridge Road at Ebenezer Creek Bridge (Bridge No. 103-0030)

A.2.8 I-95 at Turtle River Bridge (Bridge No. 127-0052)

The Turtle River Bridge is located approximately 10 miles from the coast near Brunswick, GA in Glynn County. The bridge was recently upgraded but was inspected because it was the site where piles were pulled and shipped to the Georgia Tech Structural Engineering and Materials Laboratory for further forensic investigation in February 2010. The piles that used for the forensic investigation showed the following deterioration mechanisms: abrasion and "hour glassing" in the splash zone, longitudinal cracking and spalling in the tidal and submerged regions, rust staining along the corners of the piles, softening of the concrete in the submerged region, and biological attack on the limestone aggregate.

Due to the expense of pulling all the piles, only those which needed to be removed were, with the rest of the piles from the original bridge left in place underneath the new structure. The new structure consists of precast concrete girders and drilled shafts supporting large transfer beams which span to substructure of the old bridge. An overall view of the new Turtle River Bridge is shown in Figure A.21. Figure A.22 shows the substructure of the new bridge with the original piles integrated into the large transfer beam. The bridge was inspected near high-tide and limited access for photos was available under the bridge.

Figure A.21: Updated I-95 at Turtle River Bridge (Bridge No. 127-0052)

Figure A.22: Transfer Beam with Original Piles Left In-Place on I-95 at Turtle River Bridge (Bridge No. 127-0052)

A.2.9 Torras Causeway at Little River Bridge (Bridge No. 127-0063)

The Torras Causeway Bridge was constructed as part of a series of bridges in 1986 close to the coast near Brunswick, GA in Glynn county. The bridge was built to replace an older corrosion damaged bridge using precast concrete girder superstructure and a precast concrete pile-bent substructure with larger piers in the center spans over the intercoastal waterway. An overall view of the structure is shown in Figure A.23, taken from the adjacent fishing pier which is actually the remains of the original Torras Causeway Bridge constructed in the 1950s.

Figure A.23: Torras Causeway at Little River Bridge (Bridge No. 127-0063) on Right and Adjacent Fishing Pier on Left

With the heavy oyster shell growth present in the tidal zone of the piles, it was difficult to see any surface abrasion or damage from a distance. No longitudinal cracking or rust staining could be seen on any of the piles. A typical pile-bent at the waterline is shown in Figure A.24. Access to the original bridge was also available from the adjacent dry marsh. The piles under the original bridge showed significant deterioration with large longitudinal cracks, rust staining, and spalling of concrete. On many of the piles, concrete repair jackets were present. A typical pile form the older structure is shown in Figure A.25.

Figure A.24: Pile-Bent on Torras Causeway at Little River Bridge (Bridge No. 127-0063)

Approach Span

Figure A.25: Corrosion Damage in Original Torras Causeway at Little River Bridge

Substructure (Bridge No. 127-0063)

A.2.10 Ocean Highway at Riceboro Creek Bridge (Bridge No. 179-0005)

Located 20 miles inland over Riceboro Creek in Liberty County, bridge 179-005 was constructed with a reinforced concrete superstructure and precast concrete pile-bent substructure in 1957. An overall view of the bridge is shown in Figure A.26. All piles showed significant deterioration with surface abrasion of the paste fraction below the high-water mark, longitudinal cracks at the corners, and rust staining from corrosion present on most piles (see Figure A.27).

Figure A.26: Ocean Highway at Riceboro Creek Bridge (Bridge No. 179-0005)

Figure A.27: Deterioration of Precast Concrete Piles in Substructure of Ocean Highway at Riceboro Creek Bridge (Bridge No. 179-0005)

A.2.11 Ocean Highway at Champney's River Bridge (Bridge No. 191-0005)

The Ocean Highway Bridge is located approximately 10 miles inland spanning Champney's River in McIntosh county. The bridge was constructed in 1981 with a precast concrete girder superstructure and precast concrete pile-bent substructure. An overall view of the structure is shown in Figure A.28. Hollow square piles, 36"x36", were used in the substructure. Leftover piles from the bridge were piles on the bank forming a

seawall at an adjacent boat ramp. Close-up examination of these piles revealed the concrete was manufactured using limestone coarse aggregates (see Figure A.29).

Figure A.28: Overall View of Ocean Highway at Champney's River Bridge (Bridge No. 191-0005)

Figure A.29: Remaining Piles on Bank Adjacent to Ocean Highway at Champney's River Bridge (Bridge No. 191-0005)

A fishing pier attached to the side of the bridge was used to take photos of the substructure. The bridge was inspected at high tide and photos of regions of the piles well below the high water mark could not be taken. Surface abrasion, particularly at the site of limestone aggregates, was present on all of the piles. No significant cracking or rust staining was observed on any of the piles. The typical condition of the piles is illustrated in Figure A.30.

Figure A.30: Typical Surface Abrasion of Concrete on Ocean Highway at Champney's River Bridge (Bridge No. 191-0005)

A.3 Water Sample Testing

Water samples were collected at eight of the bridge sites visited. Access to collect samples at the other sites was not possible. The samples were tested for chloride content,

sulfate content, and pH. Chloride contents were obtained by diluting 1 mL of the sample with 50 mL of deionized water and titrating using the Metrohm 798 MPT Titrino. A silver / silver chloride standard electrode was used. 0.1 N silver nitrate is added in 0.1 ml steps to the sample until an equivalence point is achieved.

The sulfate content was determined by performing inductively coupled plasma atomic emission spectroscopy (ICP) on a Perkin Elmer Optima 7300 DV Optical Emission Spectrometer. The pH was measured using a Thermo Scientific Orion 3-Star Plus pH Portable Meter. The results of the tests performed on the water samples are given in Table A.2.

Table A.2: pH, Chloride, and Sulfate Contents of Water Samples

Bridge Name	**Bridge ID**	**pH**	**% NaCl (g/g)**	**Tide**	**$[SO_4^{2-}]$ (mg/L)**
Harriet's Bluff Road at Deep Creek Bridge	039-0049	7.41	2.77	High	2070.75
Houlihan Bridge	051-0054	7.04	0.05	Low	52.91
Island Expressway at Wilmington River Bridge	051-0132	7.32	1.38	Low	1058.58
Long Bridge Road at Ebenezer Creek Bridge	103-0030	5.88	0.00	Low	13.65
I-95 at Turtle River Bridge	127-0052	7.47	1.99	High	1527.54
Torras Causeway at Little River Bridge	127-0063	7.41	2.34	Mid	1746.22
Ocean Highway at Riceboro Creek Bridge	179-0005	7.25	0.38	Low	219.95
Ocean Highway at Champney's River Bridge	191-0005	7.18	0.00	High	22.65

The salt content of water is used to differentiate between fresh, brackish, and saline (sea) water. Table A.3 shows the general ranges of NaCl concentrations as given by the USGS (2010). From Table A.3, it can be seen that all of the bridges except for the 051-0054, 103-0030, and 191-0005 are in brackish water. The three bridges considered to be in fresh water were located further inland than the rest investigated and no signs of corrosion induced damage were noticed.

Table A.3: Water Salinity Based on Dissolved Salt (NaCl) Concentration

Fresh water	Brackish water	Ocean Water
<0.1 %	0.1-3.5 %	3.5 %

The pH of water is highly variable. According to the USGS (2010), seawater has a pH of between 8 and 9. However, the average field pH is 4.7 for coastal Georgia (USGS, 2010). The values of pH observed at the inspected bridge sites fell between the two reported values. Only bridge 103-0030 was located in acidic water. The damage observed on the bridge was consistent with the signs of acid attack, including the observations of exposed coarse aggregates on the surface due to the loss of paste, and severe softening of the paste content. The other bridge locations had a near neutral pH, typically measuring in the range of 7.1 to 7.4.

The sulfate contents varied significantly among the water samples. Seawater has an average sulfate content of 2,700 mg/L (Bertolini, et al., 2004), and a study by Murata, et al. (1997) suggests that the sulfate content in brackish water is typically in excess of 1,000 mg/L. The measured values of sulfate concentrations at the bridge sites varied by two orders of magnitude. The wide spread of observed concentrations could be due to

both varying distance from the coast as well as the tide when measured (USGS, 2010). ACI 201.2 (2008) provides design requirements based upon the sulfate content in water, and requires preventative measures to protect against damage to the concrete by sulfate attack for a concentration above 150 mg/L. Additional measures are required for concentrations exceeding 1500 mg/L, which would apply to three of the bridges visited. ACI 201.2 (2008) states that for concentrations less than 150 mg/L, no special requirements are necessary for sulfate resistance. For concentrations between 150 and 1,500 mg/L, the w/c should be no greater than 0.50 and an ASTM C 150 Type II or ASTM C 1174 Class MS cement should be used. For concentrations between 1,500 and 10,000 mg/L, the w/c should be no greater than 0.45 and an ASTM C 150 Type V or ASTM C 1174 Class HS cement should be used.

X-ray diffraction was performed on piles from the Turtle River Bridge (127-0052) to examine if sulfate attack was the cause of the softening of the surface concrete. The concentration of sulfates in the water appears to be sufficient to cause significant sulfate attack, but other local sources of sulfates, particularly biological sources, may contribute to the degradation as well.

The concentrations of sulfates and chlorides in the water can vary widely with variations in rainfall and seasonal effects. Regional data will be investigated further to determine the extent of this variation, and how the data collected compares with historical data.

A.4 Summary

The inspections of bridges along the coast suggest that the causes of damage observed during the forensic investigation of piling from the Turtle River Bridge is representative of other bridges located along the coast. The types of damage observed were cracking and staining due to corrosion, abrasion and "hour-glassing" in splash and tidal zones, loss of limestone aggregates, and severe biological growth in tidal zones. The interviews of GDOT field personnel and SCP employees suggest that driving practices for piles have improved over the last several decades; however, when damage is noticed during driving, there is no standard method of repair or rejection criterion.

The current HPC mix design requirements being used by GDOT lead to a significantly more durable concrete than the concrete mixes used in the past. However, GDOT limits the replacement of cement with SCM's to lower levels than currently being employed by Florida; therefore, the benefits of higher replacement levels need to be evaluated. Additionally, GDOT does not require the use of an ASTM C 150 Type II or ASTM C 1174 Class MS cement in coastal concrete piling, but there is evidence that sulfate attack may occur in this environment if preventative measures are not taken.

Appendix B

Interview Summaries

B.1 GDOT Preconstruction and Maintenance Division Interviews

Interviews were performed with staff from the GDOT preconstruction and maintenance divisions to establish observed damage, current design methods and criterion, and research areas of interest. Interviews were later conducted with GDOT field office employees in District 5, Savannah and Brunswick. Mr. Richard Potts of Standard Concrete Products, Savannah, was also interviewed because that company supplies prestressed concrete piles to GDOT.

B.2 Paul Liles and Mike Clements

Messrs. Paul Liles and Mike Clements were interviewed on January 25th, 2010 at the Georgia Department of Transportation's One Georgia Center location. Topics discussed in the meeting were the goals that the Georgia Department of Transportation (GDOT) hopes to achieve from this project, observed trends of corrosion induced damage in coastal Georgia bridges, GDOT experience with mitigation techniques, and current design practices.

It was established the desired goals of the project for GDOT are as follows: (1) the development and implementation of corrosion resistant stainless steel strands for prestressed concrete piles in the substructure of coastal bridges; (2) development of service life and damage estimation capabilities based on salinity maps for concrete mix designs; and (3) provide design recommendations to achieve service lives in excess of 100 years.

Corrosion induced damage has been observed primarily in simple pile bent bridges in coastal and marsh regions. The damage is localized primarily in the piles, not in the pile or pier caps. This may partially be due to the fact that most of the bridges have the pile caps directly below the girders and elevated from the water. GDOT prefers to use prestressed concrete piles over steel H-piles and sheet piling in aggressive environments. The damage on the concrete piles is mostly found in the splash zone, extending approximately 18" to either side of the mean water level in most cases. There is also a concern that piles may be damaged during driving which may lead to cracking. No testing has been done to verify this, but driving guidelines are given in the GDOT specifications to prevent this damage. The state currently does not have requirements for the jetting of piles for placement except in special soil conditions.

GDOT is currently employing the following design practices to provide corrosion resistance in prestressed concrete piling: (1) Use of high performance concretes that contain supplementary cementitious materials, a low water to cementitious material ratio, and are limited to a maximum of 2000 coulombs charge passed on the rapid chloride permeability test; (2) a minimum cover distance of 2 inches is required for increased durability, and no piling less than 12" in width is used; and (3) the superstructures of bridges are built a minimum of 1 to 2 ft above the 50 year storm water level. Additional information on the standard pile sections is available through AASHTO and the GDOT website. Currently no service life modeling efforts are used in the design of prestressed concrete piles.

GDOT has attempted to implement several other methods for providing corrosion resistance, but have discontinued the use for various reasons. A bridge in Chatham country was constructed using corrosion inhibitors, epoxy coated rebars, and supplementary cementitious materials on individual piles. A report was written in the 1980's on this project, but no

monitoring after construction was completed. Cathodic protection was implemented on the Sidney Lanier Bridge in Brunswick, Georgia. The system proved to have large maintenance issues and GDOT no longer will use electrochemical methods of protection for future projects. Epoxy coated rebar was briefly used in concrete piles, but discontinued after poor performance was observed by the Florida DOT.

B.3 Mike Clements and Andy Doyle

Messrs. Mike Clements and Andy Doyle were interviewed on February 1st, 2010 at the Georgia Department of Transportation's Confederate Avenue office. Topics discussed included inspection techniques used, typical damage to concrete piles observed, and repair techniques for damaged piles.

GDOT performs inspections of prestressed concrete piles using a dive team of inspectors. The submerged regions of piles are inspected by visually scanning the surface of each face of the pile along the length while also feeling along surface for damage. A small hammer is used to tap at the surface if damage is suspected. If cracks are observed, the size is noted an attempt to open them is made. The atmospheric and splash zones of the piles are visually inspected for damage, and a hammer is used to tap the surfaces of the piles.

Typical types of damages that have been observed are as follows: (1) degradation and softening of concrete starting at 1 to 2 ft below the water line and extending to the mudline; (2) longitudinal cracks along the corners of the piles extending from mudline to low tide region of pile; and (3) color change and spalling of concrete along corners of piles in submerged region.

If damage is observed, GDOT does not have standard methods of repair. The repair methods employed vary by district, and are only performed in response to damage. Currently no preventative repair is performed on concrete piles.

B.4 Myron Banks and Jeff Carroll

Messrs. Myron Banks and Jeff Carroll were interviewed on February 8th, 2010 at the GDOT Materials and Research Branch facility. Topics discussed included GDOT mix design specifications for prestressed concrete piles, reported damage patterns to concrete piles, and areas of research needed.

GDOT has two mix design specifications for prestressed concrete piles. Any piling in an aggressive environment has been required to follow the high performance concrete (HPC) specifications for the last 2 to 3 years. The HPC guidelines require a maximum of 2,000 coulombs passes on the rapid chloride permeability test, a maximum water to cementitious materials ratio of 0.35, and a 28 day strength of at least 5,000 psi. Fly ash can be used as a cement replacement up to 15%, without any restrictions on whether Type C or F is used. If alkali silica reaction (ASR) is a concern, then Type F is used with a CaO limit of 5%. Silica fume is allowed as a replacement up to 10%. Mix designs meeting these criteria often contain air entraining admixtures and super-plasticizers. For other regions, a Class AAA concrete can be used. The specification for this mix has been in place and unchanged for over 25 years. The mix has a minimum cement requirement of 675 lb/yd^3, a maximum water to cementitious materials ratio of 0.44, an air content of 2.5 to 6%, and a minimum strength of 5,000 psi at 28 days of age.

The prestressed concrete piles are typically placed at between 7 to 14 days of age. Standard designs utilize a 3 in. cover distance for strands. No life cycle modeling is currently

employed, but is an area of interest. GDOT has not attempted to implement mitigation methods that are available or in use in other states. South Carolina requires the use of a calcium nitrite corrosion inhibitor in their mix designs. GDOT does allow the use of fibers and slag, but neither are being utilized.

The following types of damages have been reported or observed: (1) transverse cracking with a spacing of 3 to 5 ft, possibly due to over-driving or reflective cracking; (2) spalling of corners of the piles down to the level of the corner strand in the splash zone; (3) surface wear from wave action; and (4) delamination of cover concrete due to corrosion.

Areas of interest for research are as follows: (1) development of lower permeability concrete mix designs; (2) the effect of micro-cracking during driving practices on the durability of prestressed concrete piles; and (3) feasibility of self-healing concrete for improved durability characteristics.

B.5 GDOT Savannah

Messrs. Mike Garner and Slade Cole were interviewed on May 3, 2010 in the Savannah GDOT District 5 office. The damage patterns in piles were discussed, as well as the repair techniques employed. Until recently, overdriving of piles was not considered or heavily monitored. Contractors would continue to attempt to drive the piles without regard to a "refusal" limit, which is approximately 10 blows per ½ in. Overdriving in the coastal region is typically a concern only when a hard layer of soil or lime rock layer is reached, but the refusal limits are monitored.

The reflective cracking of piles is still an area of concern for GDOT. It most commonly occurs when a soft layer of soil is hit immediately following a hard layer, or when the contractor

is not following standard practice (bad pads or oversized hammer). Reflective cracking is identified by "dusting" of the piles where a small amount of powdery material is lost from the cracked region. The cracks are typically very small, and hard to find (hairline) due to prestressing effects. If a reflective crack occurs in the Savannah region, the procedure for repair varies, depending on the location in the pile. If the crack location is below the mud line, then no repair is made; however, if the crack is located above the mud line, then it is patched with epoxy. The 18" square piling is the most common size to have reflective cracking occur. The hypothesized reasoning for this is that the 18" design has a lower precompression stress than the other sizes and therefore is more susceptible to developing tensile forces during driving.

Once piles begin showing major signs of deterioration, there are two primary methods of repair that are used. The first method is to encase the piling in concrete, by either placing a corrugated steel tube around it and filling with concrete, or by using a plastic jacket and pumping concrete into it. The second method of repair is to epoxy jacket the piles, which is expensive to perform. This technique was employed on the Back River Bridge. These are not long-term solutions to bridge deterioration, but simply methods to add a short amount of time before the bridge will require replacement.

For future research, construction is about to begin on a project which will have over 1000 piles driven, and the GDOT is willing to help in attempting to determine the effects of driving on permeability due to microcracking. Additionally, for future trips, it may be possible to use a boat to inspect a few bridges of interest.

B.6 Standard Concrete Products

Messrs. Richard Potts and Alan Pritchard of Standard Concrete Products – Savannah were interviewed on May 3, 2010 at the plant. Concrete mix designs and their variability between requirements of different states were discussed. In Georgia, any piling going into "aggressive" coastal environments is required to be cast using a high performance concrete. The HPC mix specifications require a rapid chloride permeability of less than 2000 Coulombs, which is the upper limit for the rating of "Low Chloride Ion Penetrability" according to ASTM C 1202. Fly ash can be used as up to 15% cement replacement and silica fume for up to 10%. Additionally, once cast, the concrete must age at least 18 hours or until the release strength is met, which is between 3,500-4,000 psi depending on the pile size. The piles must meet 5,000 psi design strength requirements before placement and must also be at least 5 days of age.

The mix design that SCP uses contains 15% Class F fly ash replacement, no silica fume, and a high paste content of approximately 900 lb/yd^3 of cementitious material. The mix design has an ultimate strength of 8,000 to 10,000 psi. Silica fume is avoided due to its higher cost and an increased susceptibility to shrinkage cracking. All of Standard Concrete's mix designs specify a granite coarse aggregate and a natural sand fine aggregate. The piles are typically delivered and placed at 7-14 days of age.

The normal strength standard mix that is produced for piling in regions other than the "aggressive" environment is a 750 lb/yd^3 cement content mix with no supplementary cementitious materials and no requirement on the rapid chloride permeability.

The mix designs for other states vary considerably with those for Georgia. The mix design for Florida employs 18% fly ash replacement and a variable design strength which is typically 6,000 to 8,000 psi. Florida also allows for the use of ultra-fine fly ash. South Carolina

utilizes a calcium nitrite corrosion inhibitor in several of SCDOT mixes. Alan Pritchard agreed to email the mix designs and state specifications that are used for these states.

The concrete piles that were forensically investigated from the I-95 at Turtle River Bridge were most likely produced at Gates Precast in Jacksonville, Florida. The mix designs at the time of construction typically used a 0.5 w/c with no SCM addition. Richard Potts will contact the former plant manager there and attempt to find out more specific information.

It was reiterated that overdriving of piles in Georgia was previously not heavily controlled or monitored. Also, Mr. Potts said that the 18" piling is understressed compared to the other size designs in Georgia with an effective P/A of approximately 700 psi after losses compared to most having 800-900 psi, and he believed that such understressing is the cause of increased amount of reflective cracks noticed when using 18" piling.

The use of epoxy coated or stainless steel prestressing strand to increase the corrosion resistance of piles was also discussed. Richard stated that SCP had used epoxy coated strand briefly. Temperature control problems (which influence the properties of the epoxy) were found to be a concern in addition to the sand grit embedded in the epoxy to increase bond. The sand grit causes excessive wear on the beds and grips. SCP expressed interest in the use of stainless steel strand for the construction of "highly" corrosion resistant piling, although SCP was concerned that the high cost to produce the piles (~40% of cost is steel currently) would limit the economic feasibility of their use in bridge construction.

B.7 GDOT Brunswick

Messrs. Lisa Sikes and Brian Scarbrough were interviewed on May 4, 2010 in the GDOT Brunswick office. Damage and construction practices of piling were discussed. It was reiterated

again that the 18" piling is problematic with reflective cracking. In contrast to the Savannah office, the Brunswick office personnel will reject piling if "dusting" is seen during driving. The commonplace practice of overdriving in older construction was again discussed. When asked about a few of the bridges of interest, it was noted that there were paper mills present in close proximity and that run-off from them may be partially responsible for some damage seen on the piles. Brian Scarbrough agreed to email pictures of damaged piling on another bridge, which was not visited, over the South Brunswick River on I-95.

The I-95 at Turtle River piles that were delivered to the Georgia Tech Structures Laboratory were battered piles located on the edge of the bents. The remainder of the piling is still in place, although no longer in a load carrying capacity. Photos are shown in Chapter 3.

(This page intentionally left blank.)

APPENDIX C

CHLORIDE INGRESS RESULTS

The data from the rapid chloride permeability testing is presented in section C.1. The titration data for bulk diffusion testing is given in section C.2 for each mix design. The 0.5 mm (0.02 in.) increment was not used in regression analysis performed to determine diffusion coefficients with measured data.

C.1 Rapid Chloride Permeability

Table C.1: Rapid chloride permeability charge passed and initial current measurements for all mix designs, tests at 56 days

	Charge Passed (Coulombs)			Initial Current (Amps)		
Mix Design	**#1**	**#2**	**Average**	**#1**	**#2**	**Average**
T2	9,071	7,313	8,192	265.4	217.9	241.7
Type II	1,460	1,284	1,372	52.1	58.6	55.4
T3-F15	1,623	1,459	1,541	64.6	60.6	62.6
F25	1,220	1,207	1,214	57.1	56.3	56.7
F25-MK5	624	590	607	26.7	25.0	25.9
F25-MK10	371	375	373	16.1	16.0	16.1
F25-SF5	371	337	354	16.2	14.2	15.2
F25-SF10	222	239	231	9.3	10.0	9.7
S35-MK5	330	335	333	15.2	15.4	15.3
S50-MK5	289	257	273	12.6	11.7	12.2
S35-SF5	285	292	289	13.1	13.3	13.2
S50-SF5	358	372	365	15.1	15.5	15.3

C.2 Bulk Diffusion Raw Data

Tables C.2 though C.11 provide the raw titration data from the bulk diffusion tests where the depth in mm (1 in. = 25.4 mm) is to the midsection of the interval. Samples were sealed at 28 days and exposed for 180 days prior to grinding.

Table C.2: T2 bulk diffusion results

	Chloride Content (% mass concrete)		
Depth (mm)	**Sample 1**	**Sample 2**	**Average**
0.5	0.93	0.91	0.92
1.5	0.77	0.76	0.77
3.5	0.59	0.57	0.58
6	0.50	0.50	0.50
8	0.45	0.47	0.46
10	0.42	0.42	0.42
12	0.39	0.39	0.39
14	0.34	0.33	0.34
16	0.26	0.25	0.26
18	0.24	0.24	0.24
20	0.22	0.22	0.22
22	0.20	0.19	0.20
24	0.18	0.18	0.18

Table C.3: T3-F15 bulk diffusion results

	Chloride Content (% mass concrete)		
Depth (mm)	**Sample 1**	**Sample 2**	**Average**
0.5	1.19	1.17	1.18
1.5	0.83	0.83	0.83
2.5	0.66	0.67	0.67
3.5	0.57	0.58	0.58
4.5	0.49	0.48	0.49
5.5	0.43	0.43	0.43
7	0.18	0.19	0.18
9	0.12	0.09	0.10

Table C.4: F25 bulk diffusion results

	Chloride Content (% mass concrete)		
Depth (mm)	**Sample 1**	**Sample 2**	**Average**
0.5	0.91	0.89	0.90
1.5	0.94	0.93	0.93
2.5	0.77	0.77	0.77
3.5	0.67	0.67	0.67
4.5	0.60	0.60	0.60
5.5	0.47	0.47	0.47
7	0.23	0.21	0.22
9	0.10	0.10	0.10
11	0.04	0.04	0.04

Table C.5: F25-MK5 bulk diffusion results

	Chloride Content (% mass concrete)		
Depth (mm)	**Sample 1**	**Sample 2**	**Average**
0.5	1.31	1.31	1.31
1.5	0.98	0.86	0.92
2.5	0.87	0.93	0.90
3.5	0.73	0.64	0.69
4.5	0.53	0.42	0.48
5.5	0.28	0.37	0.33
7	0.21	0.23	0.22
9	0.10	0.13	0.11

Table C.6: F25-MK10 bulk diffusion results

	Chloride Content (% mass concrete)		
Depth (mm)	**Sample 1**	**Sample 2**	**Average**
0.5	0.85	0.87	0.86
1.5	0.73	0.75	0.74
2.5	0.54	0.54	0.54
3.5	0.45	0.46	0.46
4.5	0.39	0.41	0.40
5.5	0.35	0.36	0.35
7	0.16	0.18	0.17
9	0.12	0.13	0.13

Table C.7: F25-SF10 bulk diffusion results

	Chloride Content (% mass concrete)		
Depth (mm)	**Sample 1**	**Sample 2**	**Average**
0.5	1.02	1.04	1.03
1.5	1.02	1.03	1.03
2.5	0.86	0.88	0.87
3.5	0.58	0.62	0.60
4.5	0.44	0.47	0.46
5.5	0.39	0.40	0.40
6.5	0.32	0.33	0.32
7.5	0.20	0.20	0.20

Table C.8: S35-MK5 bulk diffusion results

	Chloride Content (% mass concrete)		
Depth (mm)	**Sample 1**	**Sample 2**	**Average**
0.5	0.87	0.85	0.86
1.5	0.69	0.67	0.68
2.5	0.51	0.50	0.50
3.5	0.44	0.45	0.45
4.5	0.38	0.38	0.38
5.5	0.28	0.29	0.28
7	0.09	0.12	0.11
9	0.04	0.03	0.04

Table C.9: S50-MK5 bulk diffusion results

	Chloride Content (% mass concrete)		
Depth (mm)	**Sample 1**	**Sample 2**	**Average**
0.5	0.85	0.84	0.84
1.5	0.74	0.75	0.74
2.5	0.58	0.58	0.58
3.5	0.37	0.39	0.38
4.5	0.28	0.30	0.29
5.5	0.19	0.18	0.19
7	0.06	0.07	0.07
9	0.00	0.03	0.02

Table C.10: S35-SF5 bulk diffusion results

	Chloride Content (% mass concrete)		
Depth (mm)	**Sample 1**	**Sample 2**	**Average**
0.5	0.82	0.84	0.83
1.5	0.79	0.79	0.79
2.5	0.59	0.59	0.59
3.5	0.44	0.44	0.44
4.5	0.32	0.33	0.33
5.5	0.19	0.21	0.20
7	0.07	0.07	0.07
9	0.02	0.05	0.03

Table C.11: S50-SF5 bulk diffusion results

	Chloride Content (% mass concrete)		
Depth (mm)	**Sample 1**	**Sample 2**	**Average**
0.5	1.02	0.99	1.00
1.5	0.79	0.85	0.82
2.5	0.64	0.65	0.64
3.5	0.49	0.47	0.48
4.5	0.39	0.38	0.39
5.5	0.35	0.35	0.35
7	0.15	0.17	0.16
9	0.04	0.02	0.03

APPENDIX D

CARBONATION TESTING RESULTS

D.1 Carbonation Depth Measurements

D.1.1 Carbonation Depth Data

The carbonation depth on samples was measured relative to exposure at 28 days, after a 21 day moist curing, and 7 day conditioning period.

Table D.1: Mean carbonation depth as indicated by phenolphthalein indicator solution (1 in. = 25.4 mm)

Exposure Time (days)	**3**	**7**	**14**	**21**	**28**	**70**	**90**	**120**	**180**	**300**	**350**
Mix Design	**Carbonation Depth (mm)**										
T2	6.1	10.2	14.2	17.5	19.3	-	-	-	-	-	-
T3-F15	-	-	-	2.5	3.8	5.8	7.4	7.1	-	9.9	10.7
F25	-	2.5	3.0	4.1	4.6	6.1	7.9	8.9	10.4	12.2	13.2
F25-MK5	-	-	-	3.3	-	5.1	6.4	7.6	9.4	11.7	12.2
F25-MK10	-	-	-	-	2.5	3.6	4.3	5.8	6.9	8.9	9.4
F25-SF5	-	-	-	-	2.5	3.3	4.3	5.8	6.4	8.1	8.6
F25-SF10	-	-	-	-	3.0	3.6	5.1	6.6	6.9	9.1	10.2
S35-MK5	-	-	-	-	3.0	6.9	8.1	9.4	10.4	12.7	13.5
S50-MK5	-	-	-	-	3.0	5.1	6.1	-	-	8.9	9.7
S35-SF5	-	-	-	3.6	-	5.3	6.1	7.1	8.4	10.7	11.4
S50-SF5	-	-	-	-	3.6	4.3	5.8	6.9	8.1	9.7	10.7

Table D.2: Standard deviation of carbonation depth as indicated by phenolphthalein indicator solution (1 in. = 25.4 mm)

Exposure Time (days)	**3**	**7**	**14**	**21**	**28**	**70**	**90**	**120**	**180**	**300**	**350**
Mix Design	**Carbonation Depth (mm)**										
T2	0.5	0.5	0.8	1.3	0.5	-	-	-	-	-	-
T3-F15	-	-	-	0.3	0.5	0.3	0.5	0.3	-	0.5	0.5
F25	-	0.3	0.3	0.3	0.3	0.3	0.8	0.8	0.3	0.5	0.5
F25-MK5	-	-	-	0.3	-	0.3	0.3	0.5	0.3	0.5	0.3
F25-MK10	-	-	-	-	0.3	0.3	0.3	0.5	0.5	0.5	0.5
F25-SF5	-	-	-	-	0.3	0.5	0.5	0.3	0.3	0.3	0.3
F25-SF10	-	-	-	-	0.3	0.3	0.3	0.5	0.5	0.5	0.5
S35-MK5	-	-	-	-	0.5	0.3	0.5	0.5	0.5	0.3	0.8
S50-MK5	-	-	-	-	0.5	0.3	0.3	-	-	0.8	0.3
S35-SF5	-	-	-	0.3	-	0.3	0.3	0.3	0.3	0.3	0.3
S50-SF5	-	-	-	-	0.3	0.3	0.5	0.5	0.3	0.3	0.8

D.1.2 Photos of Carbonation Samples

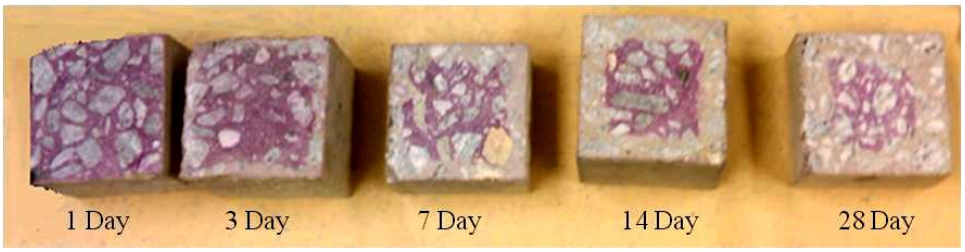

Figure D.1: T2 carbonation samples (76.2 x 76.2 mm (3 x 3 in.))

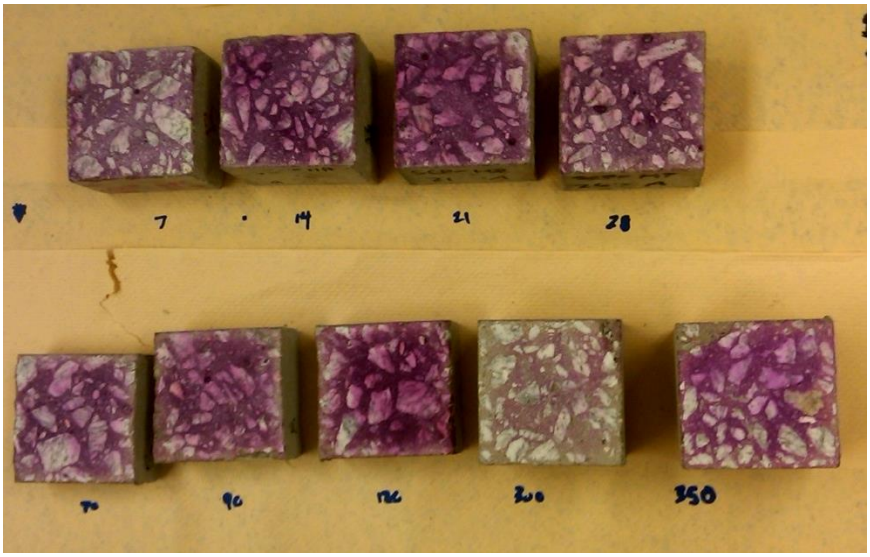

Figure D.2: T3-F15 carbonation samples (76.2 x 76.2 mm (3 x 3 in.))

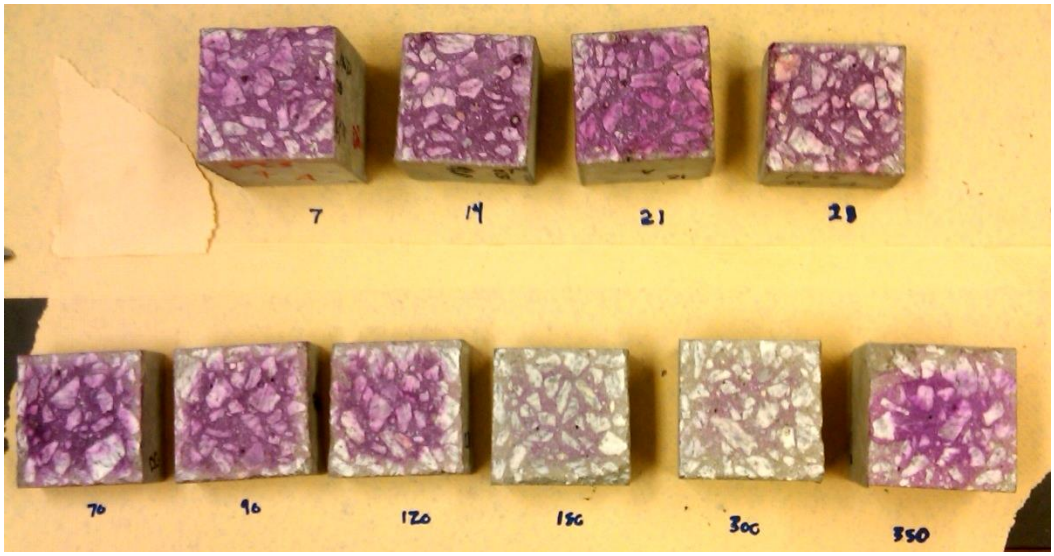

Figure D.3: F25 carbonation samples (76.2 x 76.2 mm (3 x 3 in.))

Figure D.4: F25-MK5 carbonation samples (76.2 x 76.2 mm (3 x 3 in.))

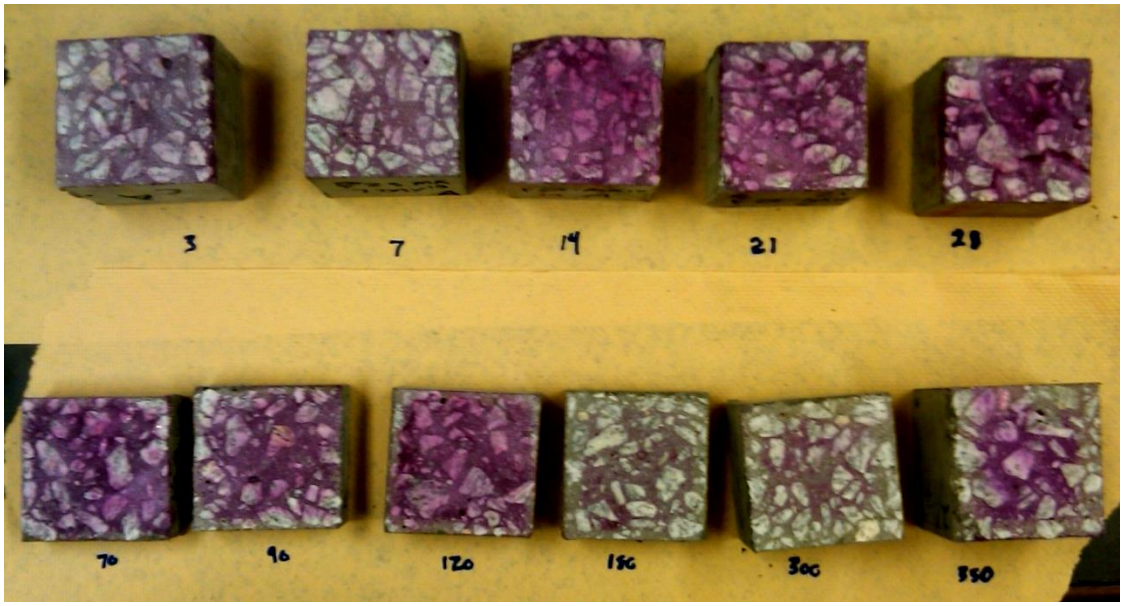

Figure D.5: F25-MK10 carbonation samples (76.2 x 76.2 mm (3 x 3 in.))

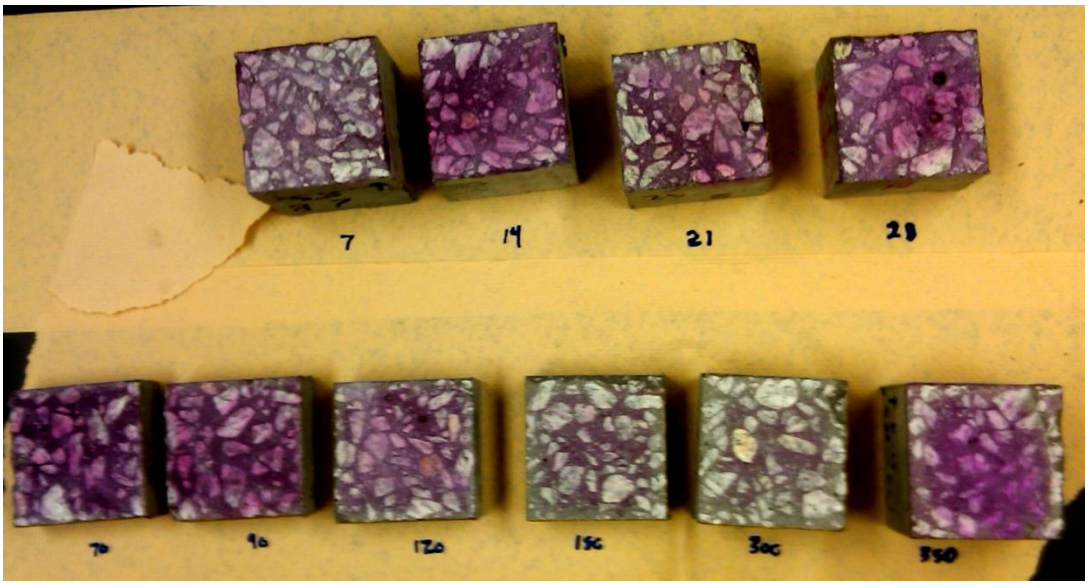

Figure D.6: F25-SF5 carbonation samples (76.2 x 76.2 mm (3 x 3 in.))

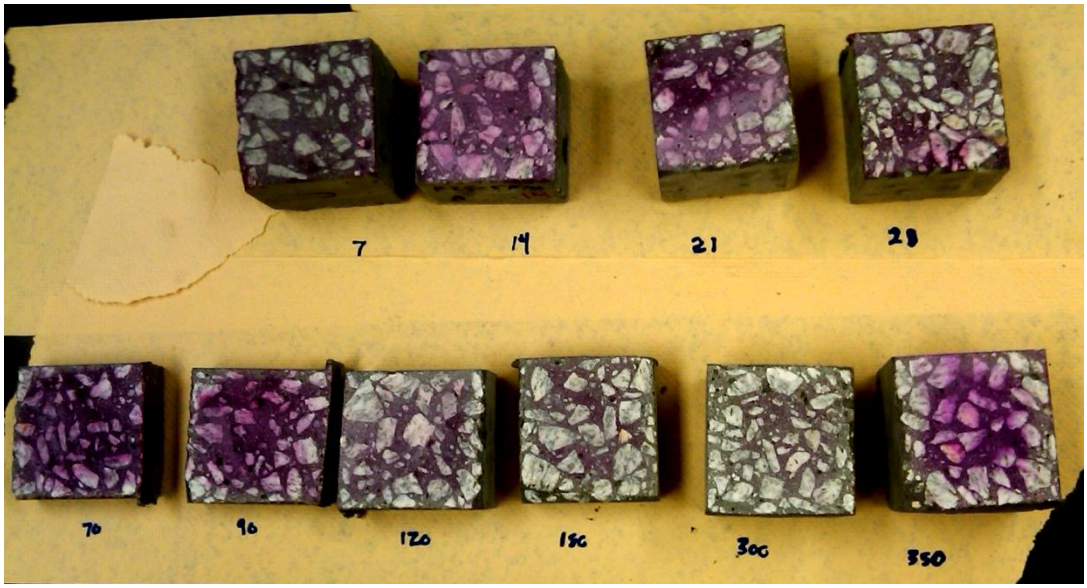

Figure D.7: F25-SF10 carbonation samples (76.2 x 76.2 mm (3 x 3 in.))

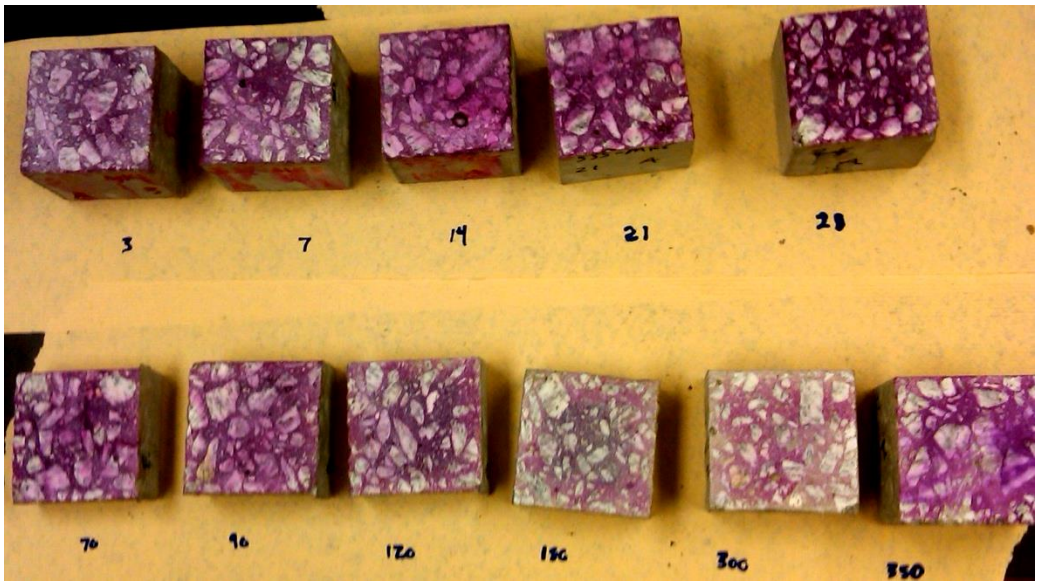

Figure D.8: S35-MK5 carbonation samples (76.2 x 76.2 mm (3 x 3 in.))

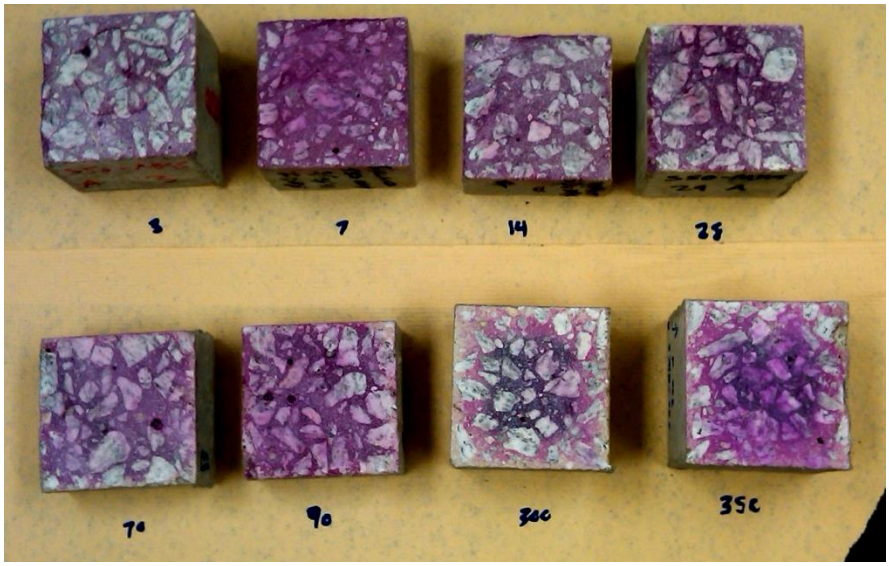

Figure D.9: S50-MK5 carbonation samples (76.2 x 76.2 mm (3 x 3 in.))

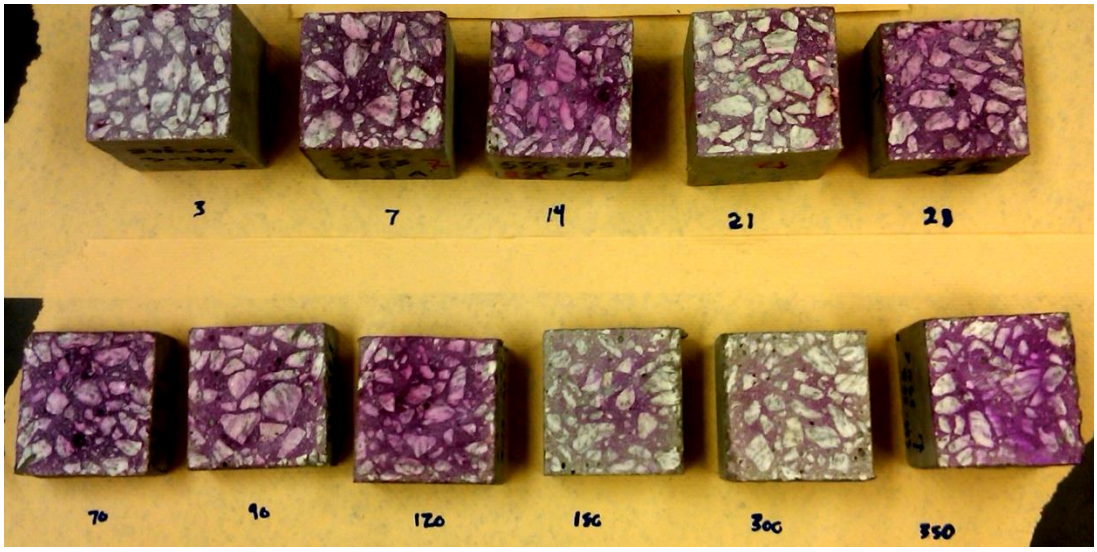

Figure D.10: S35-SF5 carbonation samples (76.2 x 76.2 mm (3 x 3 in.))

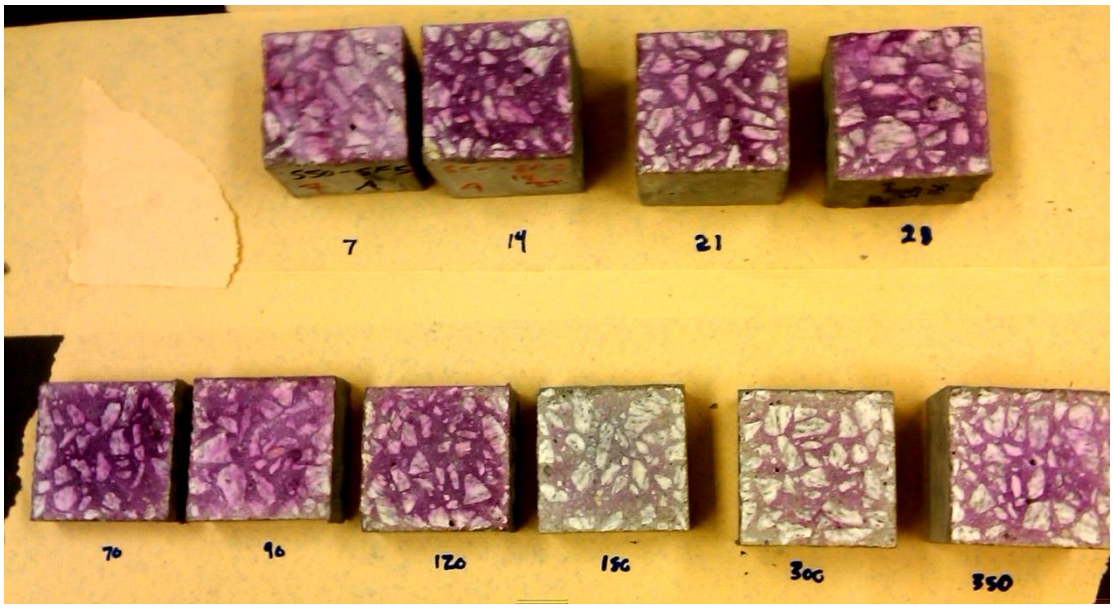

Figure D.11: S50-SF5 carbonation samples (76.2 x 76.2 mm (3 x 3 in.))

D.2 Carbonation Regression Parameters

Table D.3: Experimentally determined carbonation constant and R^2 values
(1 in. = 25.4 mm)

Mix Design	Carbonation Constant, K ($mm/yr^{0.5}$)	R^2
T2	3.71	0.981
T3-F15	0.61	0.921
F25	0.75	0.972
F25-MK5	0.67	0.989
F25-MK10	0.50	0.982
F25-SF5	0.47	0.966
F25-SF10	0.54	0.970
S35-MK5	0.76	0.936
S50-MK5	0.54	0.941
S35-SF5	0.63	0.988
S50-SF5	0.58	0.983

APPENDIX E

SULFATE ATTACK RESISTANCE TESTING

E.1 ASTM C 1012 Expansion Testing

E.1.1 Expansion Results

Table E.1: ASTM C 1012 expansion readings from initial to 15 weeks

	Expansion after exposure period (%)						
Mix Design	**1 week**	**2 week**	**3 week**	**4 week**	**8 week**	**13 week**	**15 week**
T2	0.013	0.016	0.016	0.019	0.027	0.028	0.031
T3	0.012	0.013	0.015	0.015	0.014	0.026	0.028
T5	0.007	0.008	0.009	0.012	0.016	0.020	0.020
T3-F15	0.006	0.009	0.011	0.012	0.011	0.019	0.021
F25	0.008	0.012	0.017	0.018	0.018	0.028	0.029
F25-MK5	0.009	0.014	0.017	0.019	0.020	0.032	0.035
F25-MK10	0.018	0.022	0.025	0.027	0.032	0.036	0.036
F25-SF5	0.008	0.019	0.018	0.017	0.020	0.023	0.023
F25-SF10	0.007	0.013	0.013	0.014	0.015	0.018	0.018
S35-MK5	0.006	0.010	0.014	0.014	0.019	0.023	0.024
S50-MK5	0.007	0.013	0.013	0.013	0.013	0.016	0.018
S35-SF5	0.012	0.018	0.018	0.017	0.020	0.025	0.025
S50-SF5	0.017	0.019	0.018	0.018	0.024	0.027	0.027

Table E.2: ASTM C 1012 expansion readings from 4 months to 11 months

	Expansion after exposure period (%)						
Mix Design	**4 month**	**6 month**	**7 month**	**8 month**	**9 month**	**10 month**	**11 month**
T2	0.032	0.038	0.051	0.054	0.061	0.069	0.079
T3	0.029	0.035	0.052	0.063	0.086	0.133	-
T5	0.021	0.020	0.036	0.044	0.056	0.071	-
T3-F15	0.021	0.021	0.030	0.030	0.030	0.032	-
F25	0.032	0.038	0.043	0.043	0.043	0.047	0.048
F25-MK5	0.038	0.047	0.054	0.056	0.060	0.066	0.074
F25-MK10	0.036	0.036	0.041	0.041	0.042	0.042	-
F25-SF5	0.024	0.031	0.032	0.034	0.034	0.035	0.036
F25-SF10	0.022	0.026	0.025	0.026	0.026	0.027	0.026
S35-MK5	0.024	0.031	0.032	0.034	0.036	0.036	-
S50-MK5	0.019	0.020	0.022	0.022	0.022	0.023	0.022
S35-SF5	0.024	0.030	0.036	0.034	0.038	0.038	0.041
S50-SF5	0.028	0.034	0.039	0.038	0.042	0.042	0.045

Table E.3: ASTM C 1012 expansion readings from 12 months to 18 months

	Expansion after exposure period (%)						
Mix Design	**12 month**	**13 month**	**14 month**	**15 month**	**16 month**	**17 month**	**18 month**
T2	0.087	0.100	-	0.125	0.138	0.158	0.177
T3	0.237	-	0.428	0.527	0.637	0.738	0.907
T5	0.099	-	0.128	0.138	0.152	0.175	0.201
T3-F15	0.032	-	0.036	0.038	0.039	0.041	0.041
F25	0.050	-	-	0.062	0.070	0.078	0.090
F25-MK5	0.083	-	0.102	0.136	0.161	0.190	0.218
F25-MK10	0.042	-	0.045	0.044	0.044	0.045	0.045
F25-SF5	0.036	-	0.038	0.039	0.039	0.041	
F25-SF10	0.027	-	0.028	0.029	0.029	0.029	
S35-MK5	0.039	-	0.042	0.044	0.044	0.048	0.047
S50-MK5	0.023	-	-	0.026	0.025	0.025	0.026
S35-SF5	0.041	-	0.044	0.044	0.045	0.046	
S50-SF5	0.046	-	0.049	0.050	0.051	0.053	

E.1.2 Compressive Strength Gain Data

Table E.4: Compressive strength gain of mortar cubes for ASTM C 1012 criterion

	Compressive Strength (MPa)					
Mix Design	**1 Day**	**2 Day**	**3 Day**	**4 Day**	**5 Day**	**6 Day**
T2	27.7	-	-	-	-	-
T3	35.2	-	-	-	-	-
T5	29.4	-	-	-	-	-
T3-F15	28.5	-	-	-	-	-
F25	15.5	18.9	18.5	-	19.0	23.3
F25-MK5	17.4	18.7	-	18.7	27.5	-
F25-MK10	15.6	-	22.7	-	-	-
F25-SF5	19.4	22.4	-	-	-	-
F25-SF10	22.2	-	-	-	-	-
S35-MK5	16.8	-	22.9	-	-	-
S50-MK5	11.6	-	20.7	-	-	-
S35-SF5	8.8	-	-	19.4	24.5	-
S50-SF5	9.7	-	-	16.4	19.0	21.1

E.2 Compressive Strength Degradation

Table E.5: Initial strength of paste cube samples at beginning of exposure
(1 ksi = 6.89 MPa)

Mix Design	Initial Compressive Strength (MPa)
T2	40.5
T3	26.4
T5	29.7
T3-F15	29.7
F25	30.4
F25-MK5	24.0
F25-MK10	24.3
F25-SF5	29.3
F25-SF10	23.3
S35-MK5	24.2
S50-MK5	27.1
S35-SF5	20.2
S50-SF5	31.6

Table E.6: 28 day strength of control and sulfate exposure specimens (1 ksi = 6.89 MPa)

	28-Day Compressive Strength (MPa)			
	Average		Std. Dev.	
Mix Design	Exposed	Control	Exposed	Control
T2	39.7	32.9	2.0	3.4
T3	34.2	30.4	3.0	7.5
T5	26.6	22.9	3.6	3.8
T3-F15	33.5	31.9	2.0	1.2
F25	27.1	22.2	4.9	1.1
F25-MK5	24.6	24.6	3.0	2.5
F25-MK10	22.3	23.0	1.3	1.5
F25-SF5	30.5	29.1	1.4	4.0
F25-SF10	24.5	26.8	1.8	2.3
S35-MK5	24.3	26.4	1.5	2.6
S50-MK5	23.5	24.1	1.8	2.5
S35-SF5	26.2	23.4	2.8	1.4
S50-SF5	30.5	27.1	4.9	2.9

Table E.7: 90 day strength of control and sulfate exposure specimens (1 ksi = 6.89 MPa)

	90-Day Compressive Strength (MPa)			
	Average		Std. Dev.	
Mix Design	Exposed	Control	Exposed	Control
T2	54.4	48.8	4.7	1.5
T3	39.7	39.4	4.9	3.1
T5	39.0	36.5	2.9	2.5
T3-F15	33.1	43.7	2.8	2.2
F25	31.5	27.4	2.9	2.0
F25-MK5	22.9	26.8	1.9	1.6
F25-MK10	25.3	28.6	1.7	1.2
F25-SF5	24.8	29.8	3.1	1.2
F25-SF10	32.2	39.4	1.9	2.4
S35-MK5	34.7	35.2	2.2	3.2
S50-MK5	26.9	26.2	2.4	2.5
S35-SF5	27.7	32.4	4.2	4.2
S50-SF5	32.0	39.1	1.8	1.9

Table E.8: 180 day strength of control and sulfate exposure specimens (1 ksi = 6.89 MPa)

	180-Day Compressive Strength (MPa)			
	Average		Std. Dev.	
Mix Design	Exposed	Control	Exposed	Control
T2	55.8	45.0	4.6	3.9
T3	32.7	42.1	3.5	2.6
T5	57.3	46.3	5.6	3.2
T3-F15	24.7	44.7	2.7	4.4
F25	41.1	43.0	4.2	2.4
F25-MK5	25.5	32.7	4.0	1.7
F25-MK10	30.5	34.9	0.8	1.8
F25-SF5	31.5	41.2	4.9	3.2
F25-SF10	29.4	43.0	2.1	3.4
S35-MK5	25.7	32.2	3.5	1.3
S50-MK5	27.0	31.8	2.7	1.6
S35-SF5	31.8	48.4	2.1	1.9
S50-SF5	27.5	42.3	2.0	1.9

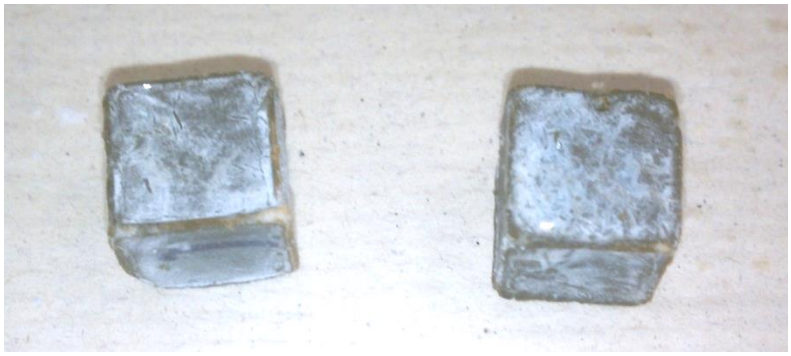

(a)

(b)

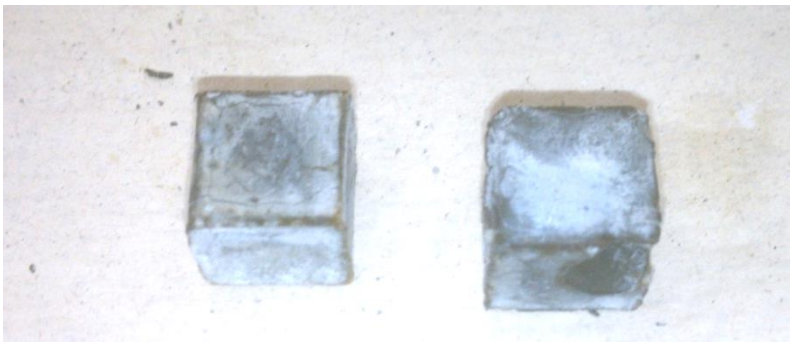

(c)

Figure E.1: Control (left) and 180-day sulfate exposure specimen for (a) T2, (b) T3, and (c) T5 (12.7 mm cubes (0.5 in.))

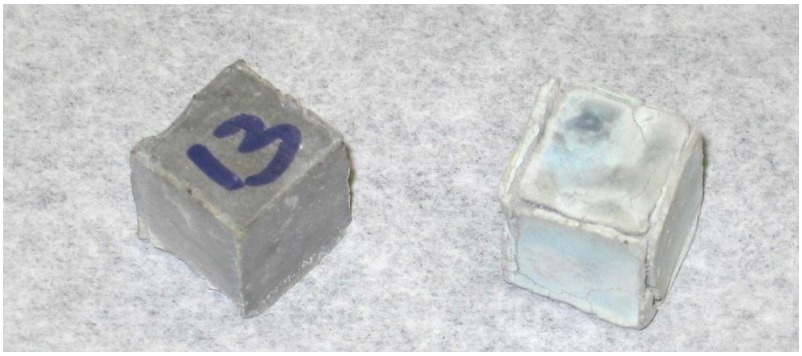

(a)

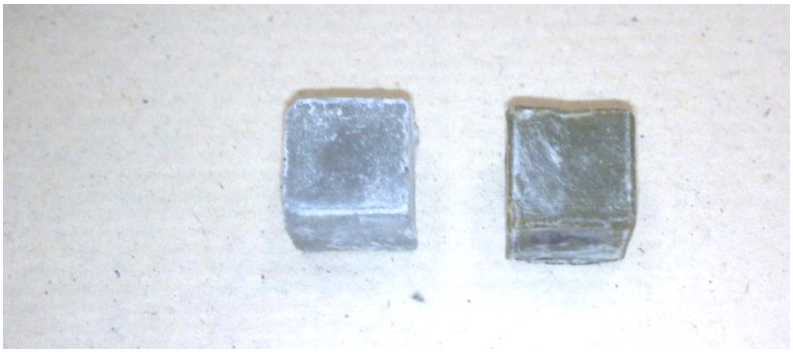

(b)

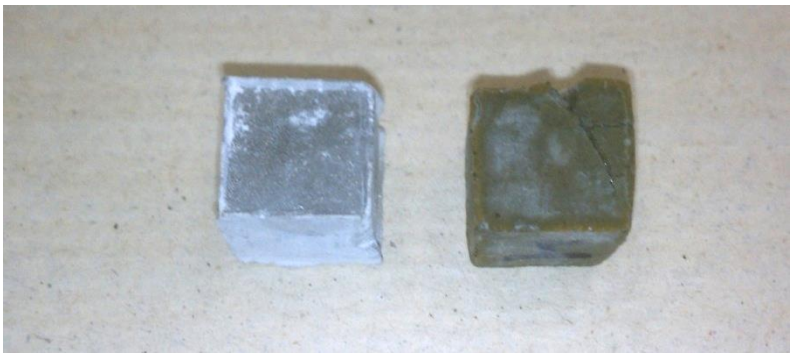

(c)

Figure E.2: Control (left) and 180-day sulfate exposure specimen for (a) T3-F15, (b) F25, and (c) F25-MK5 (12.7 mm cubes (0.5 in.))

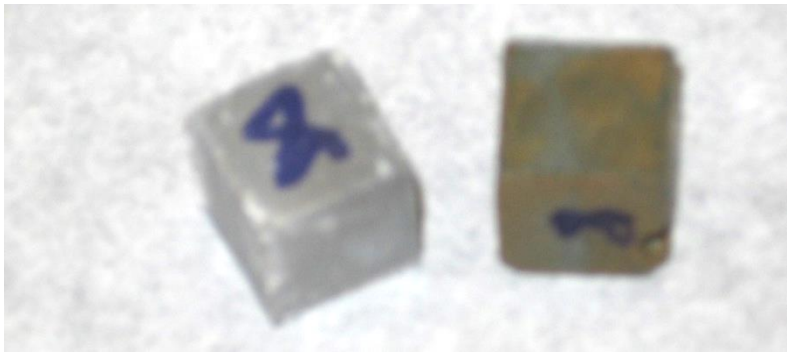

(a)

(b)

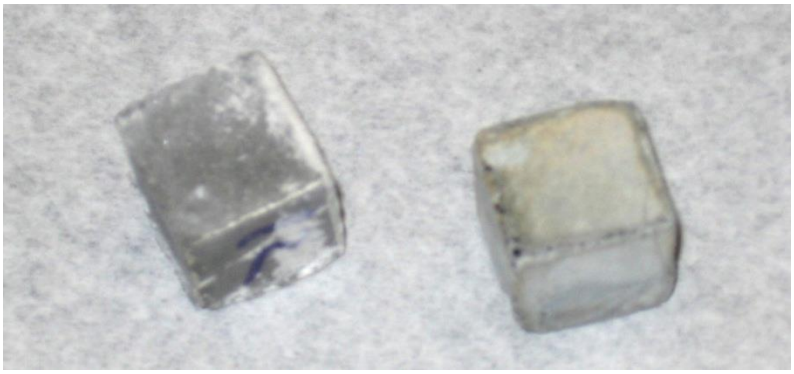

(c)

Figure E.3: Control (left) and 180-day sulfate exposure specimen for (a) F25-MK10, (b) F25-SF5, and (c) F25-SF10 (12.7 mm cubes (0.5 in.))

(a)

(b)

(c)

Figure E.4: Control (left) and 180-day sulfate exposure specimen for (a) S35-MK5, (b) S50-MK5, and (c) S35-SF5 (12.7 mm cubes (0.5 in.))

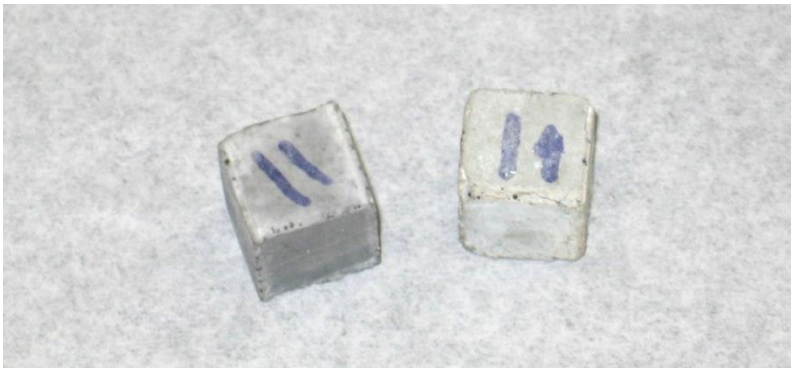

Figure E.5: Control (left) and 180-day sulfate exposure specimen for S50-SF5 (12.7 mm cubes (0.5 in.))

E.3 Quantitative X-Ray Diffraction

E.3.1 Diffraction Patterns

E.3.1.1 180-day Control Specimens

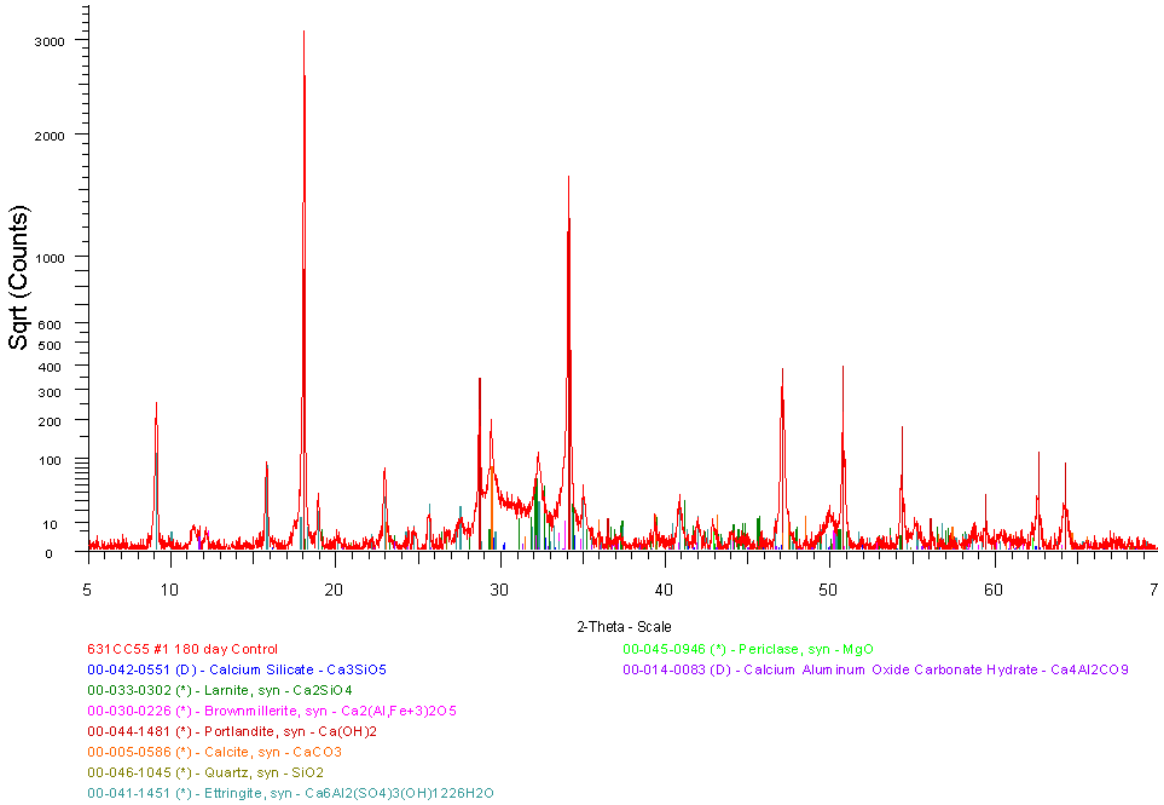

Figure E.6: T2 180-day Control XRD Pattern

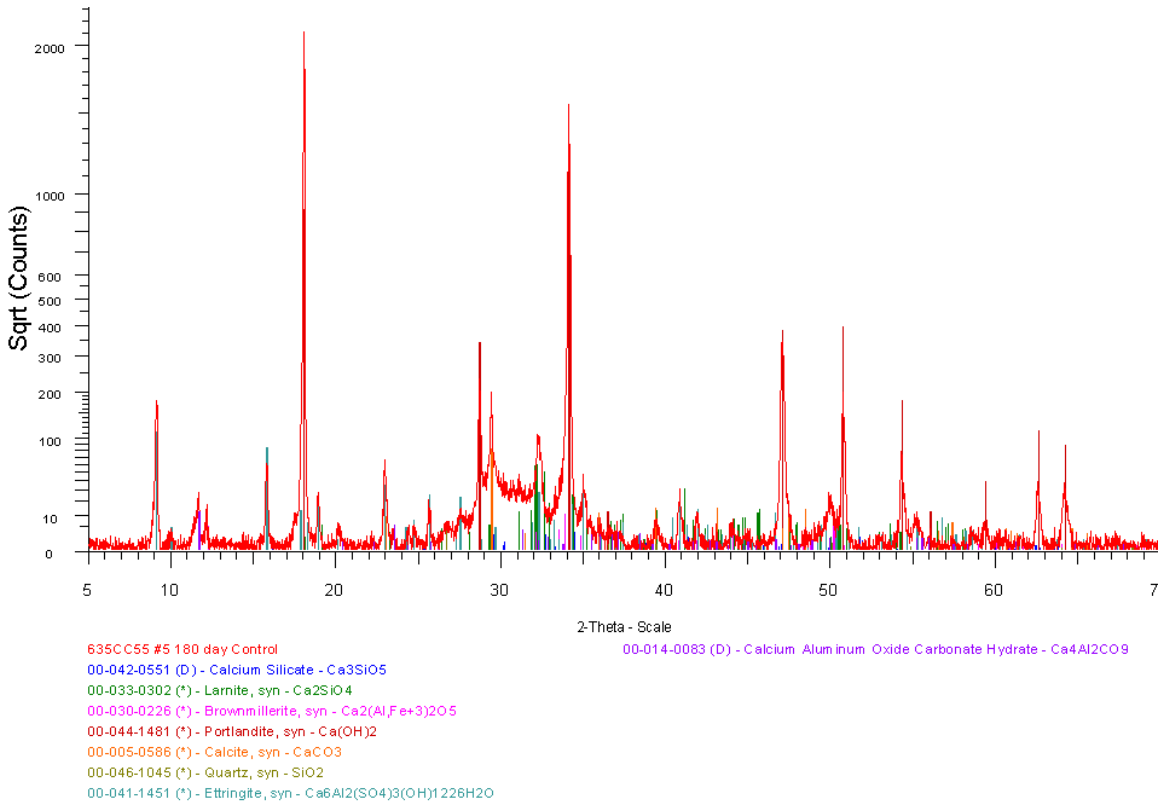

Figure E.7: T3 180-day Control XRD Pattern

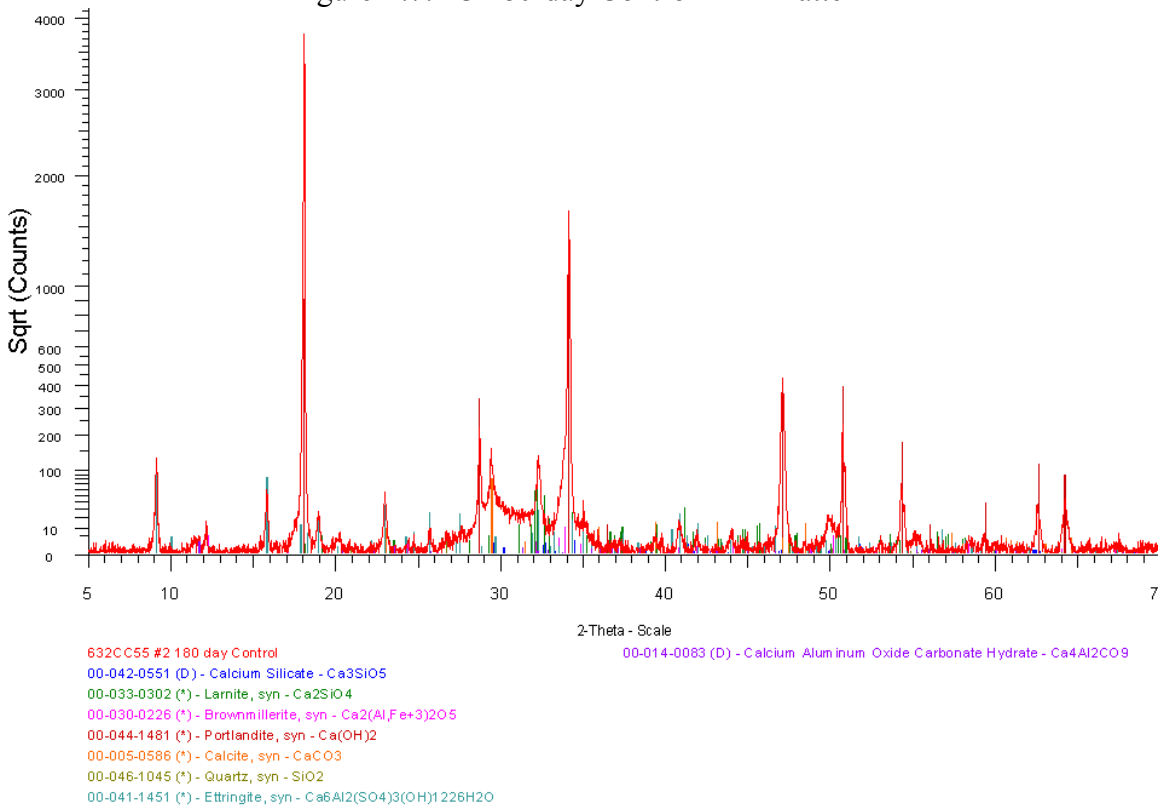

Figure E.8: T5 180-day Control XRD Pattern

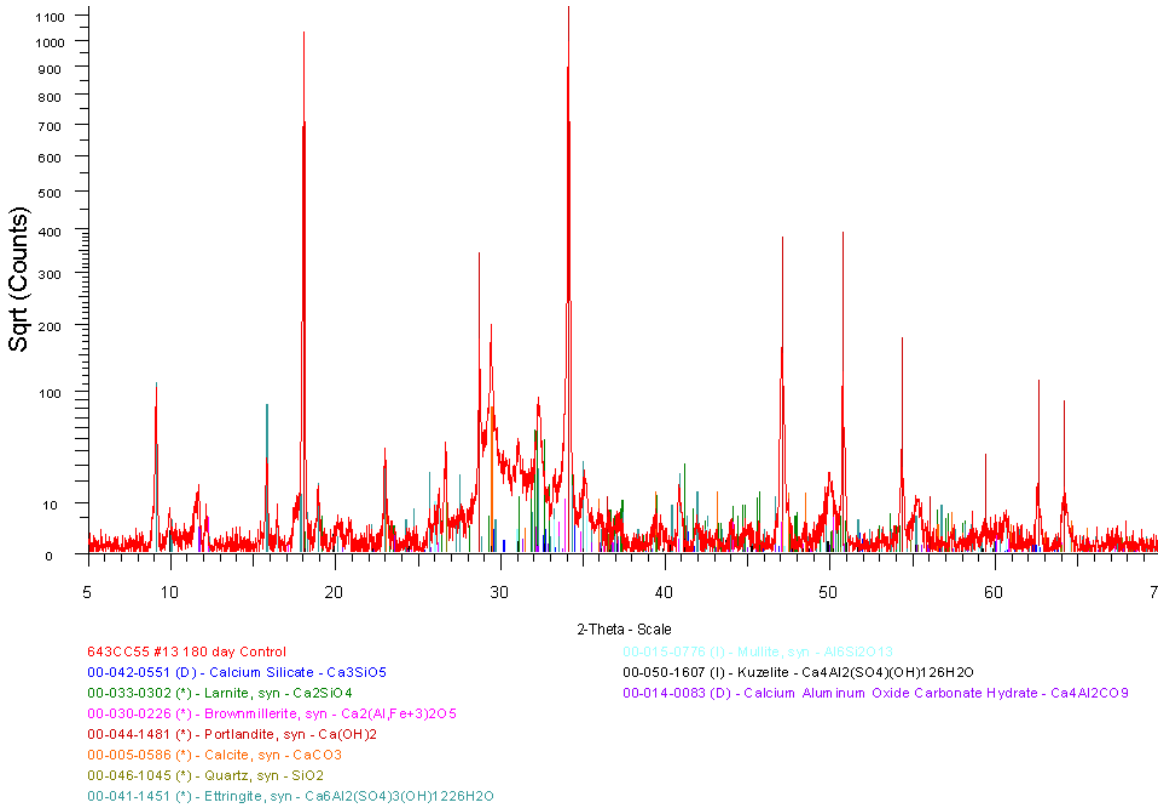

Figure E.9: T3-F15 180-day Control XRD Pattern

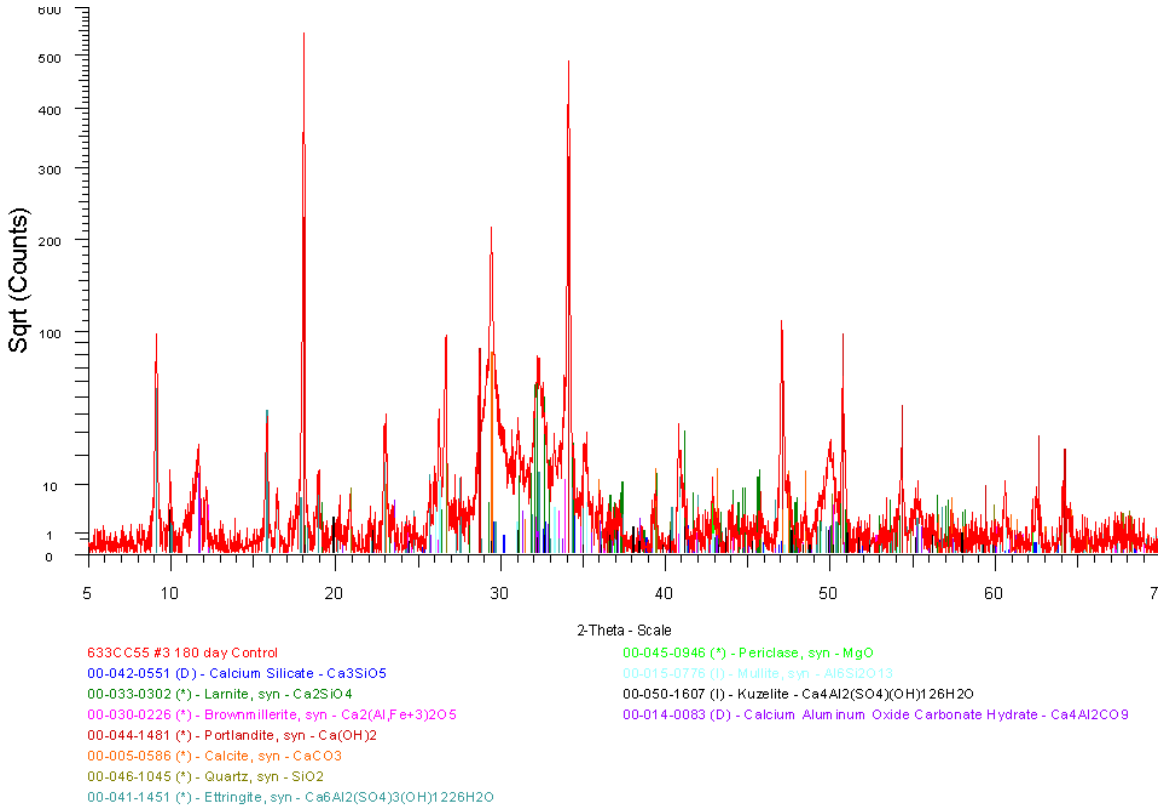

Figure E.10: F25 180-day Control XRD Pattern

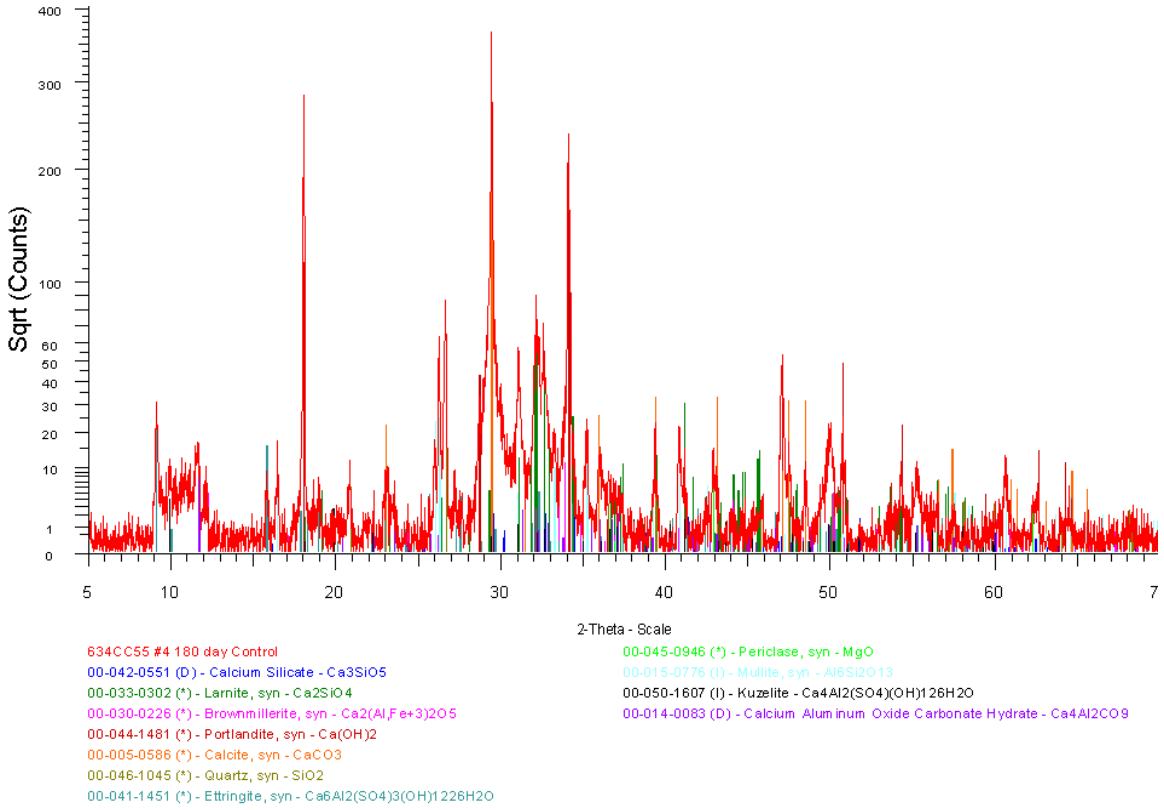

Figure E.11: F25-MK5 180-day Control XRD Pattern

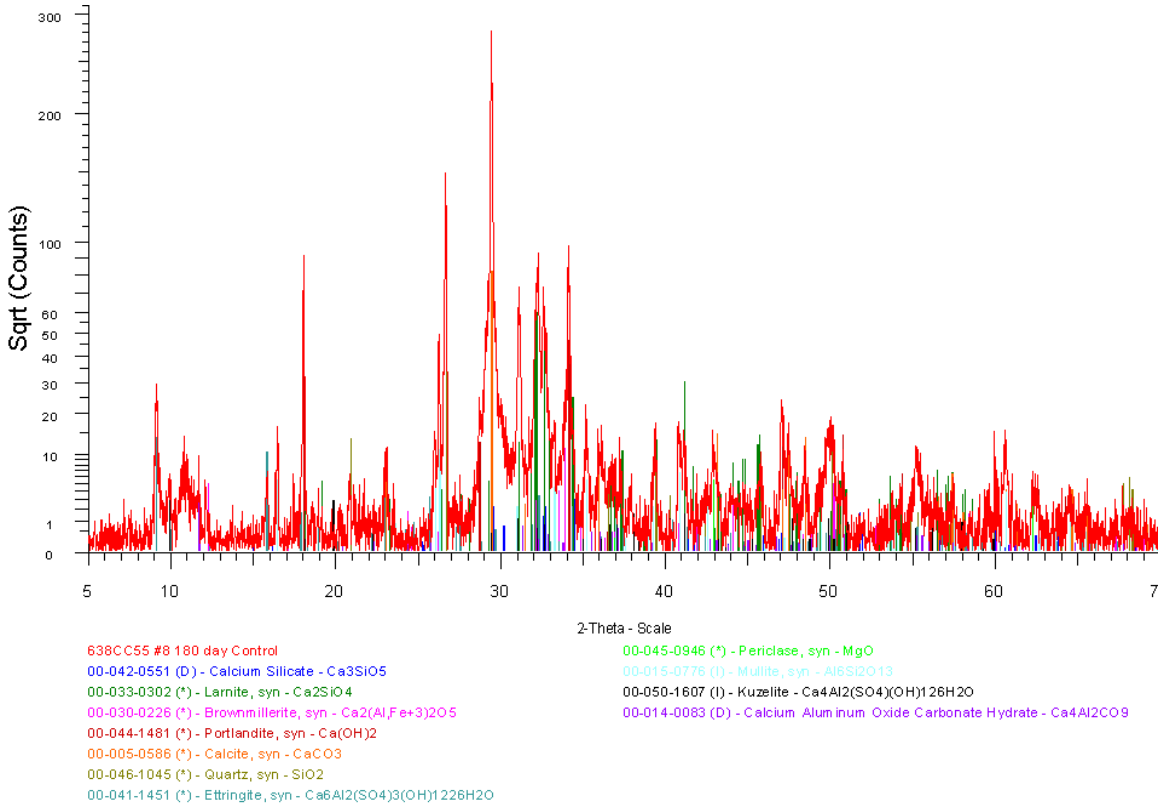

Figure E.12: F25-MK10 180-day Control XRD Pattern

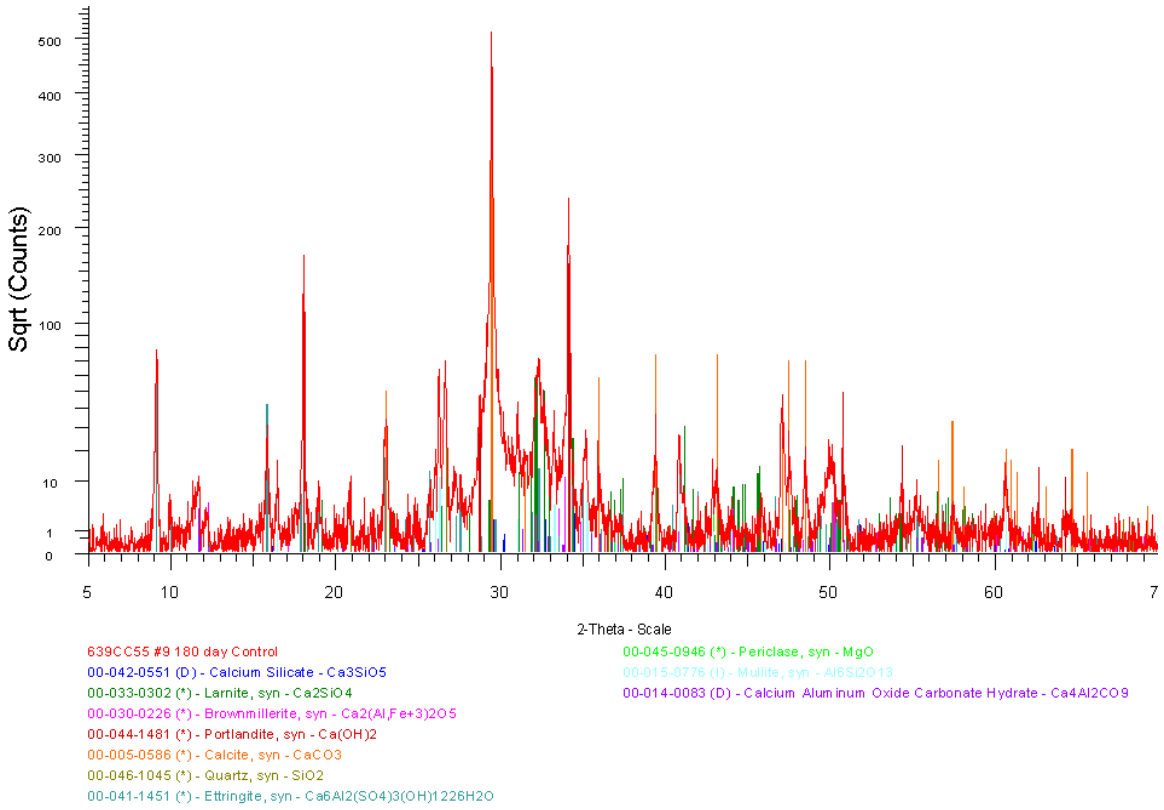

Figure E.13: F25-SF5 180-day Control XRD Pattern

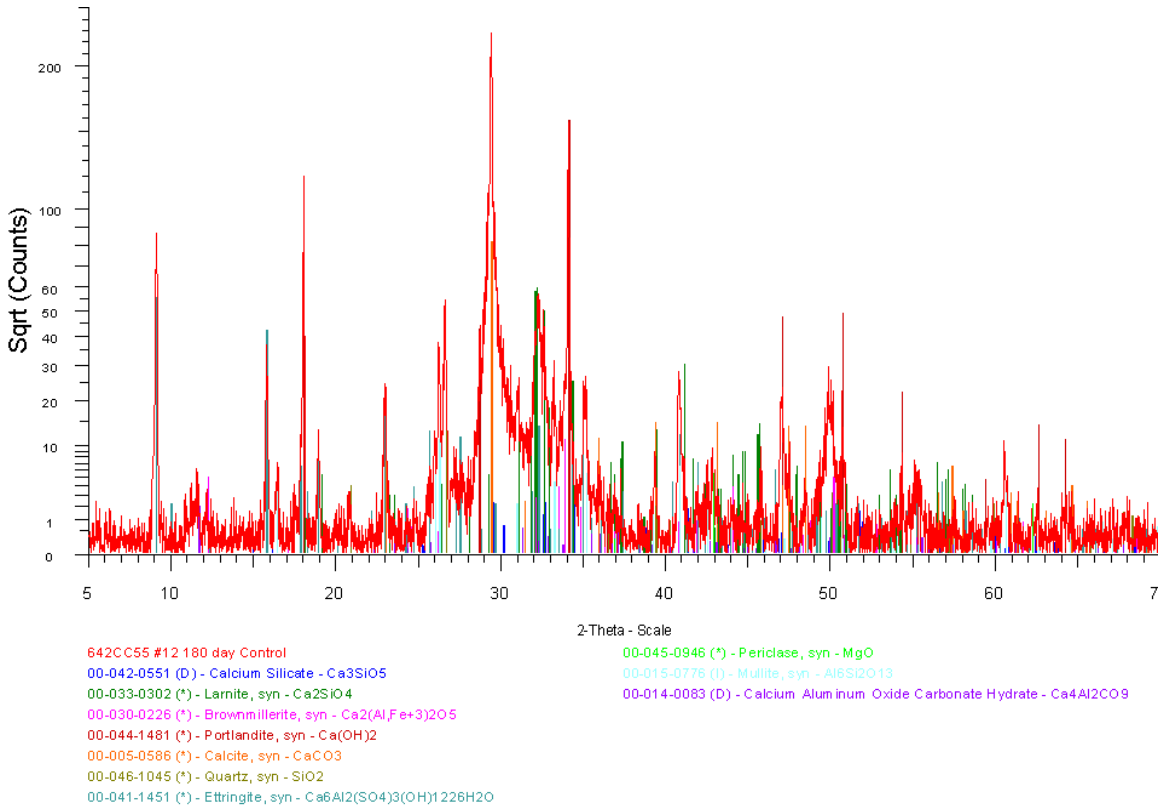

Figure E.14: F25-SF10 180-day Control XRD Pattern

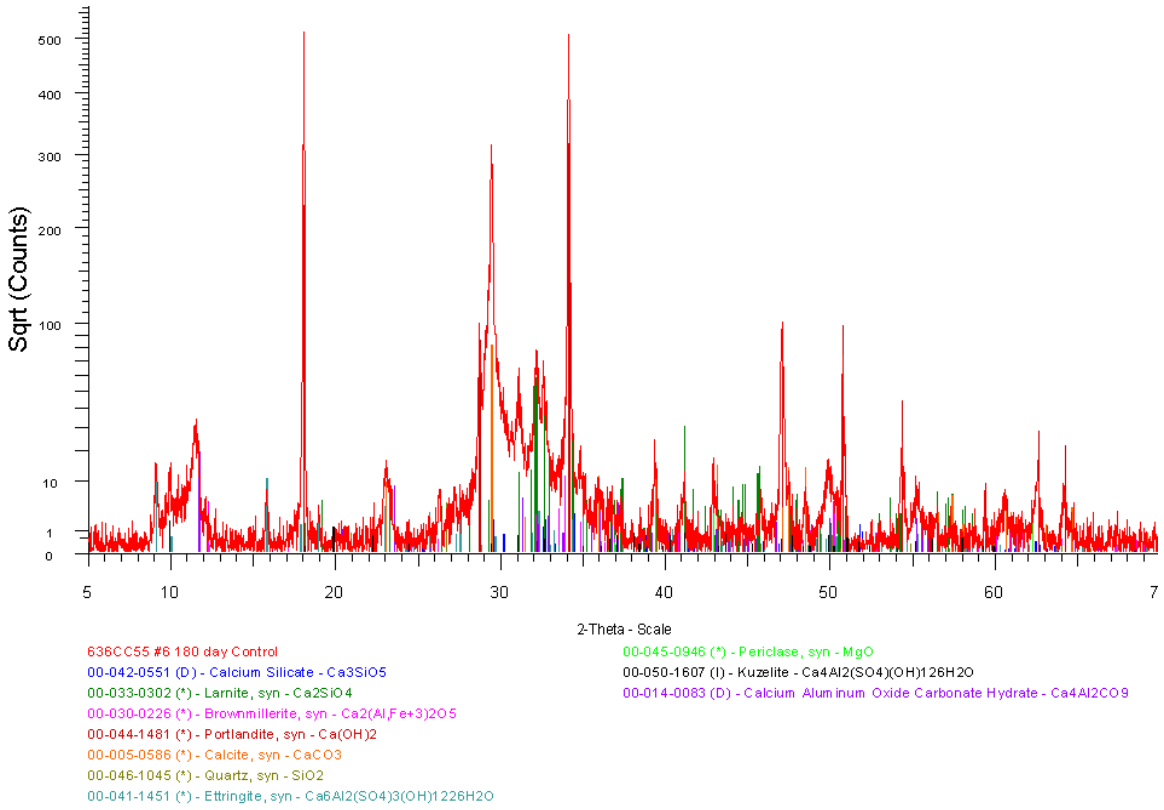

Figure E.15: S35-MK5 180-day Control XRD Pattern

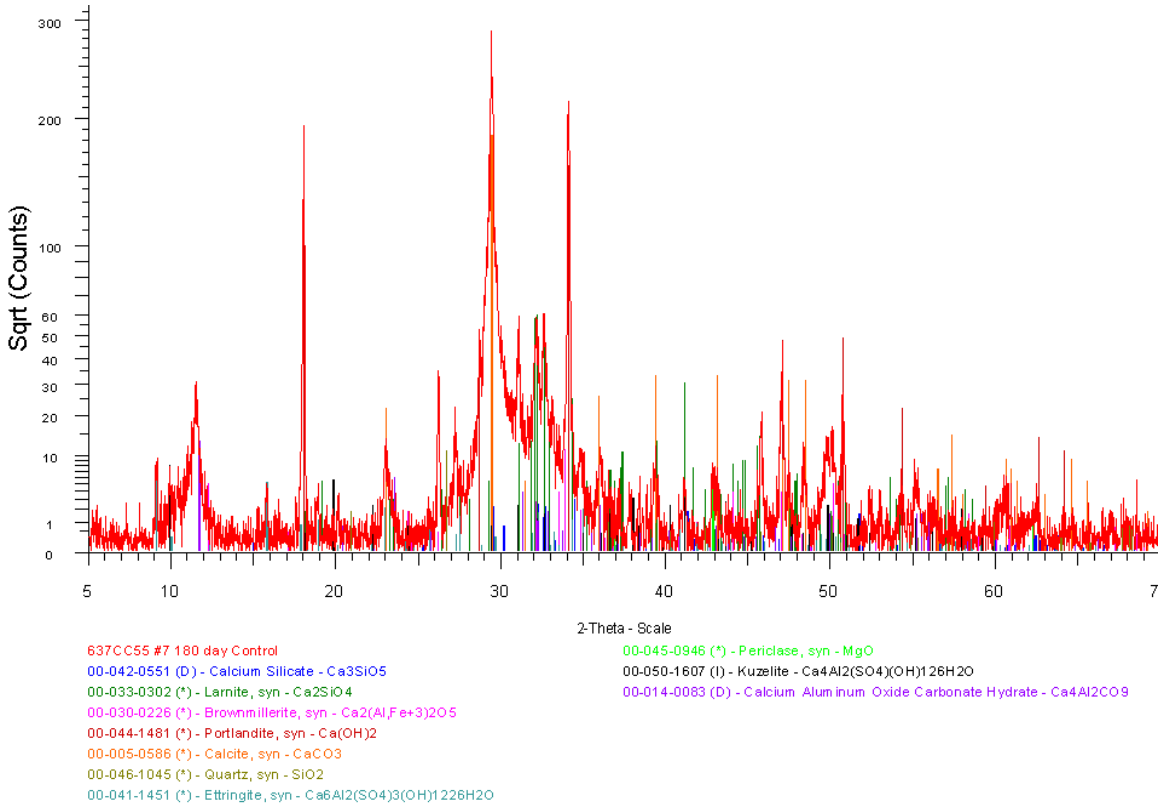

Figure E.16: S50-MK5 180-day Control XRD Pattern

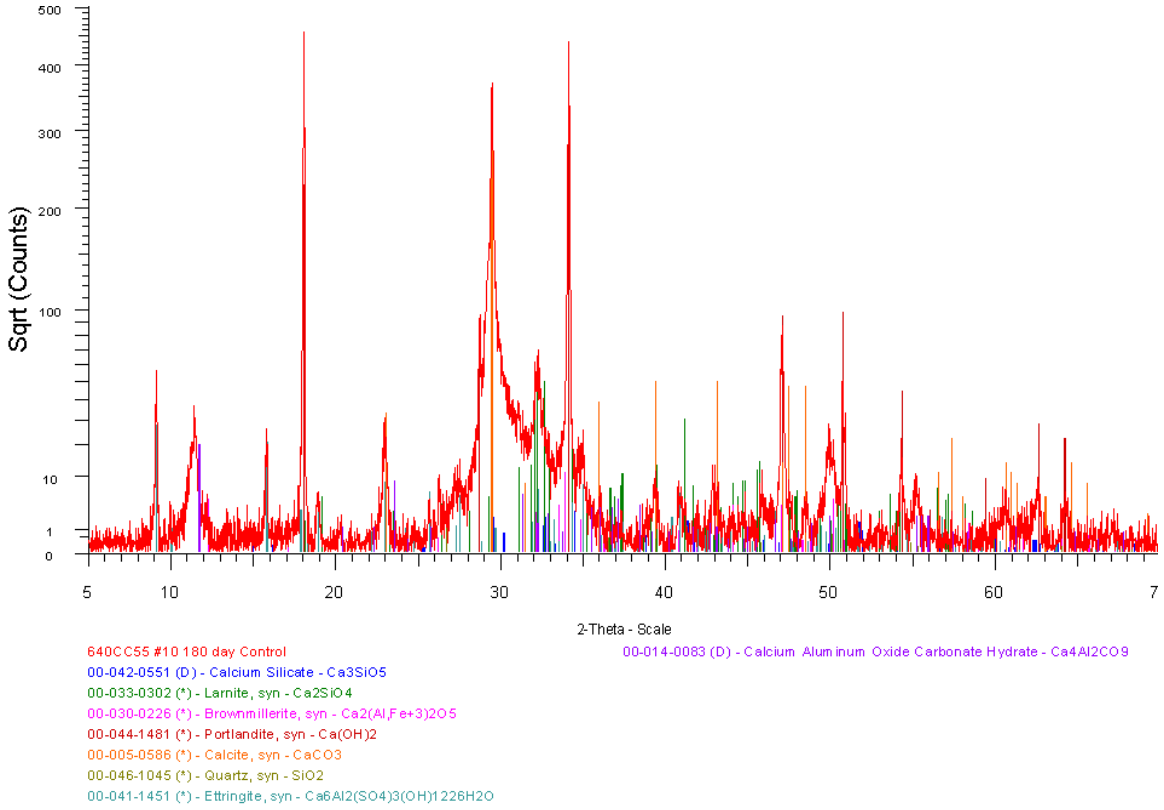

Figure E.17: S35-SF5 180-day Control XRD Pattern

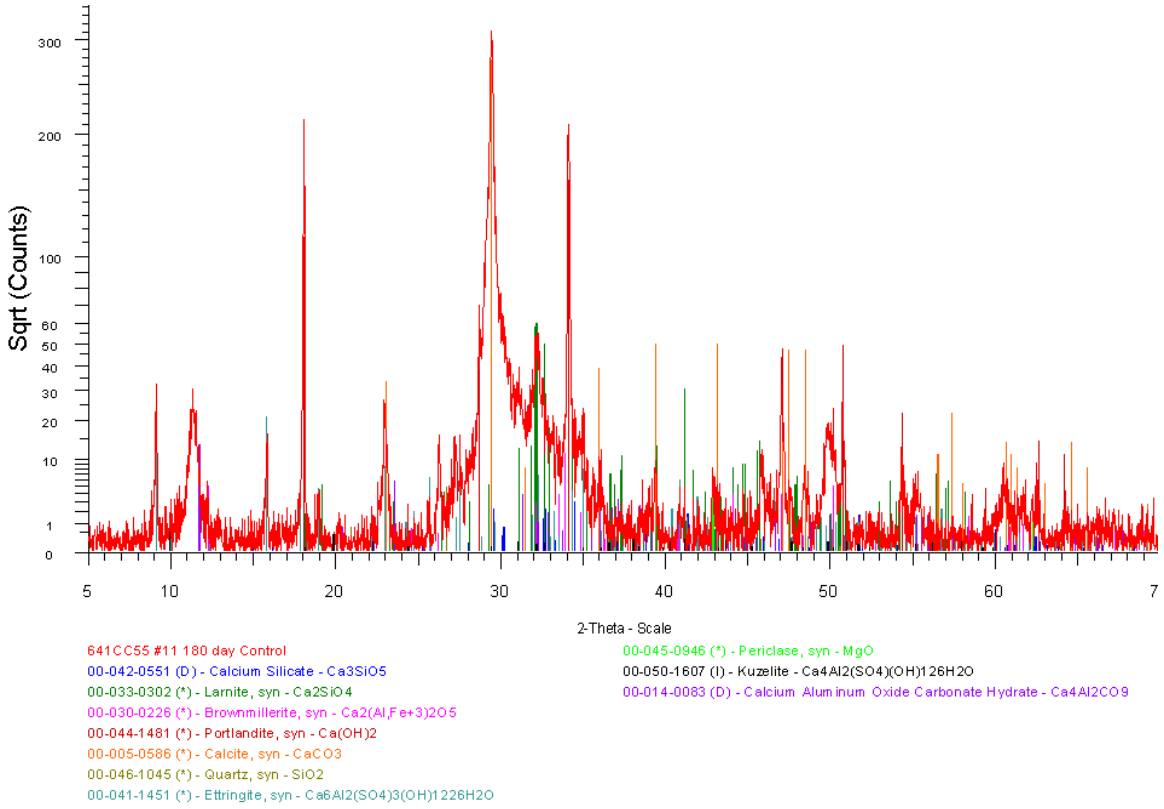

Figure E.18: S50-SF5 180-day Control XRD Pattern

E.3.1.2 90-day Sulfate Exposure Specimens

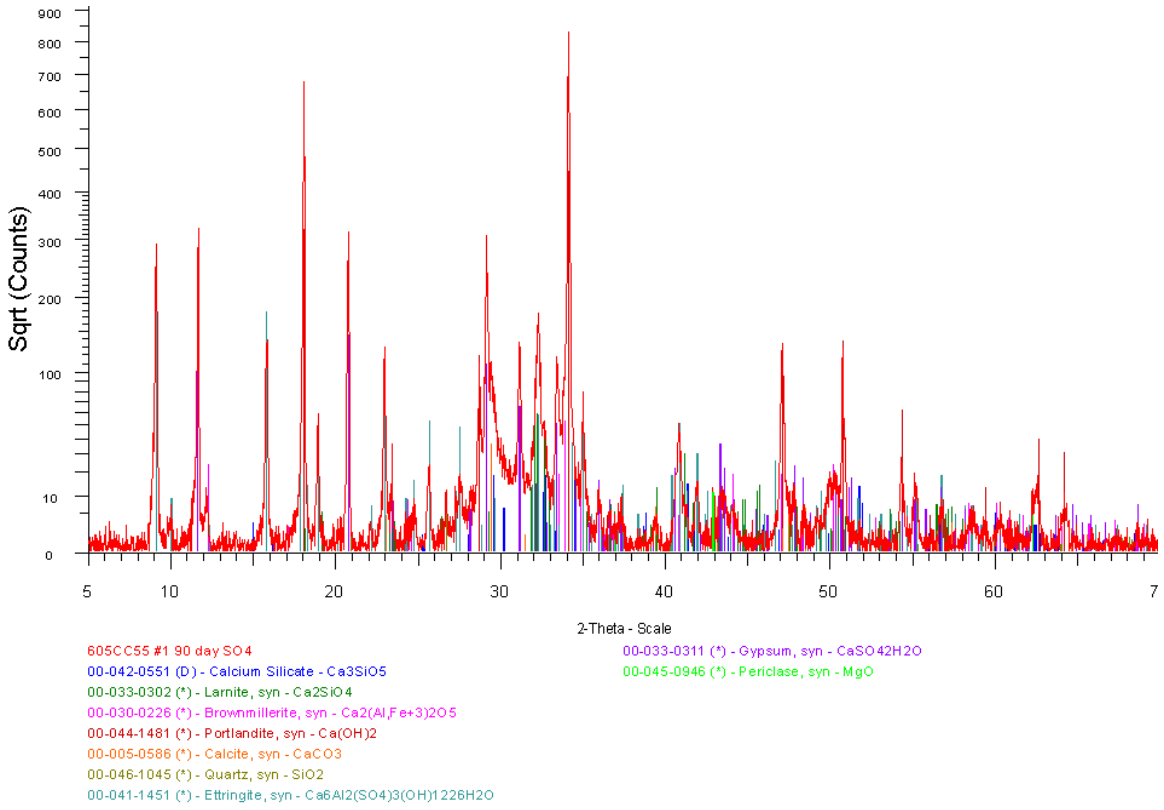

Figure E.19: T2 90-day Sulfate Exposure XRD Pattern

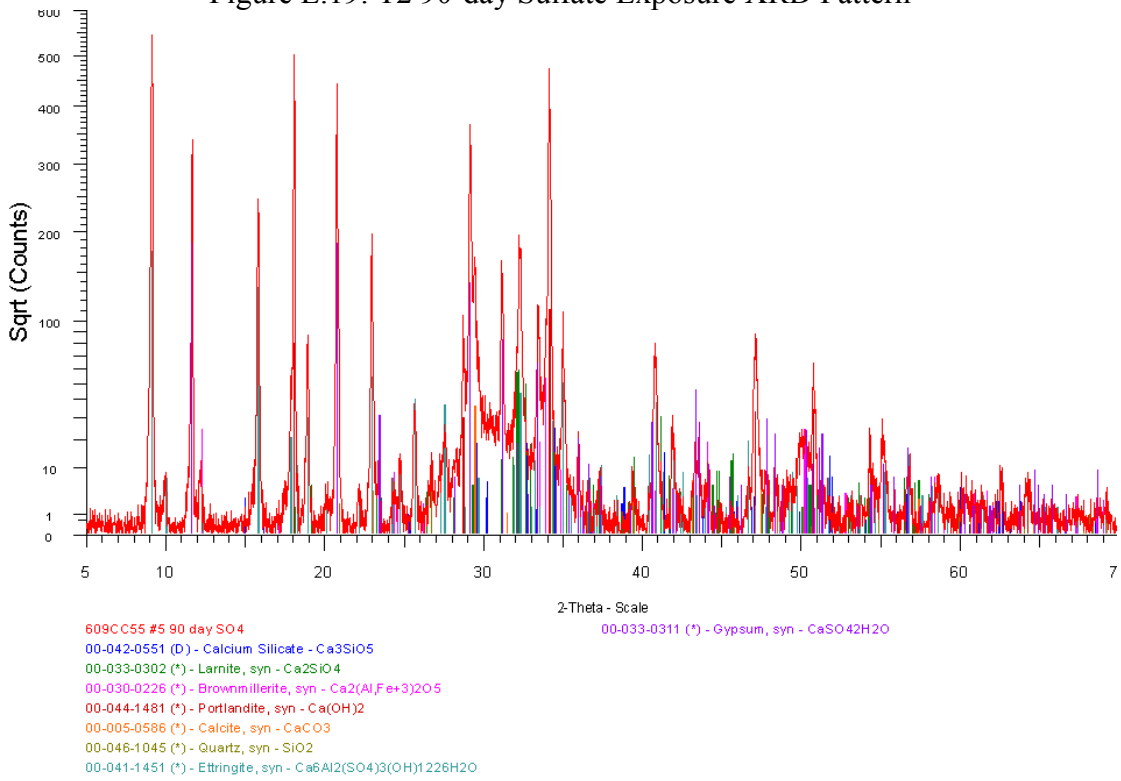

Figure E.20: T3 90-day Sulfate Exposure XRD Pattern

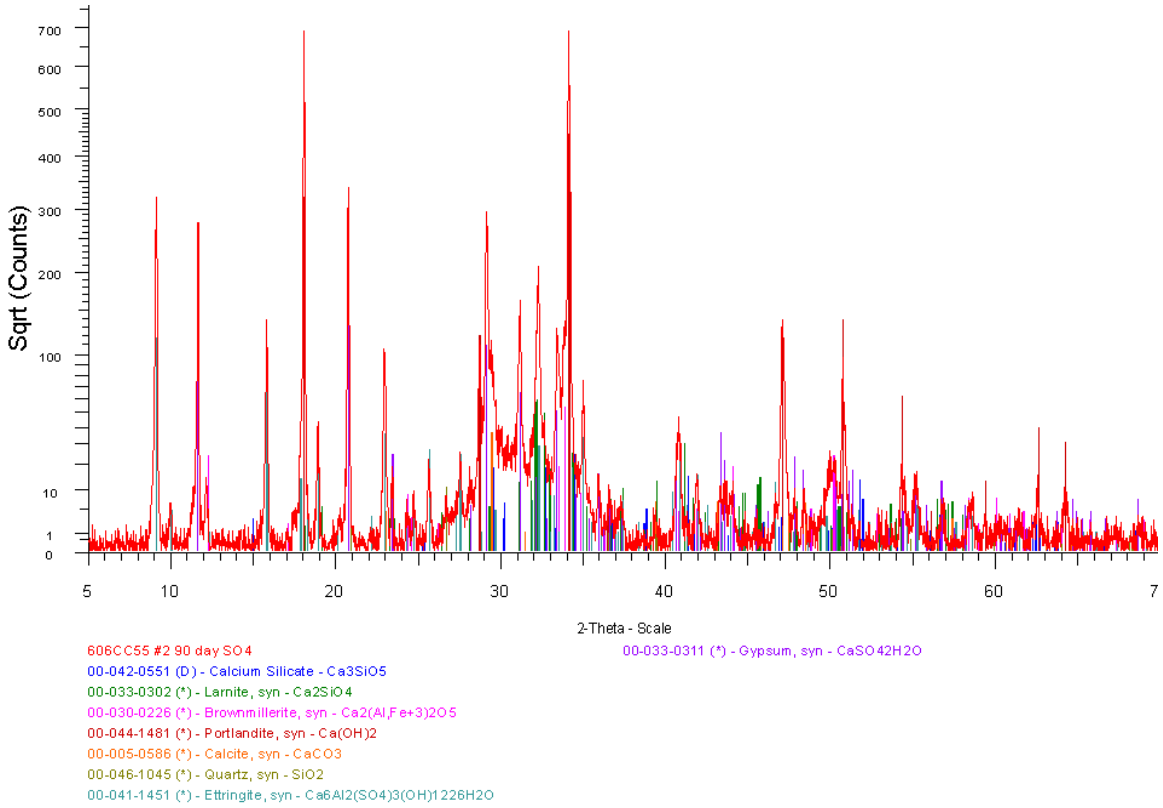

Figure E.21: T5 90-day Sulfate Exposure XRD Pattern

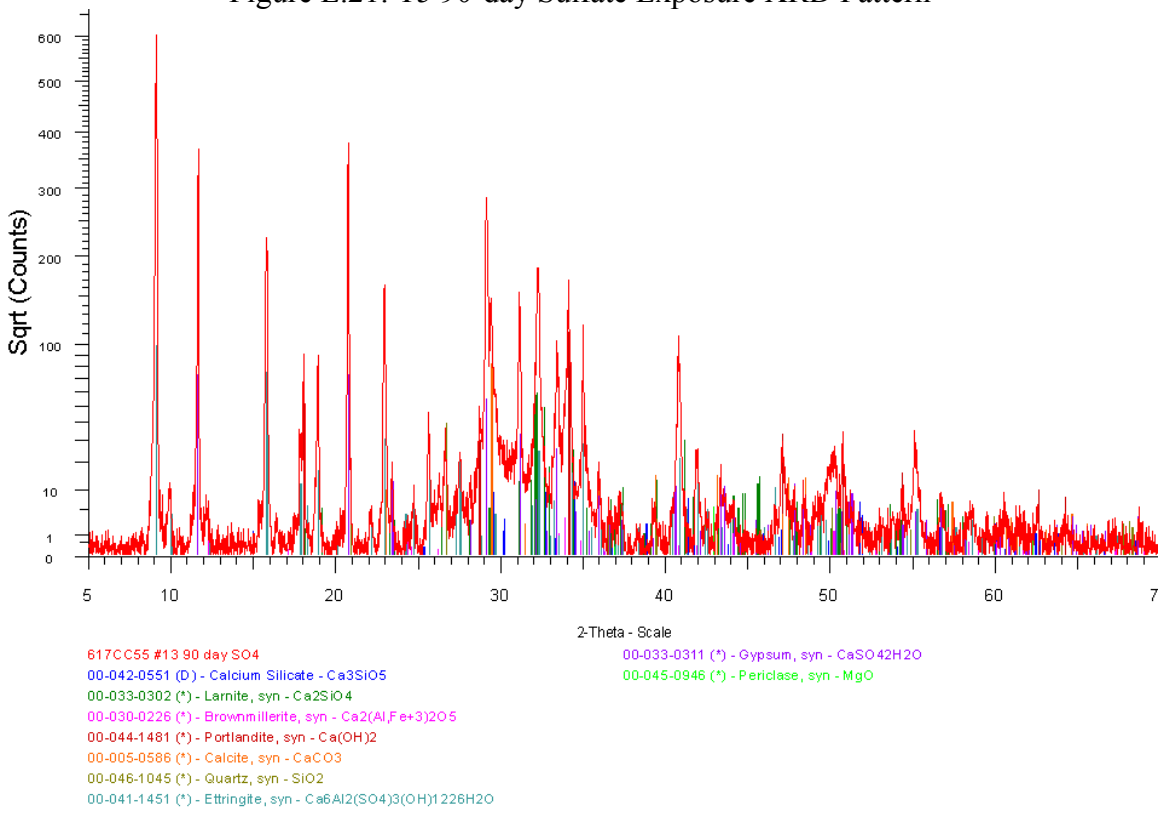

Figure E.22: T3-F15 90-day Sulfate Exposure XRD Pattern

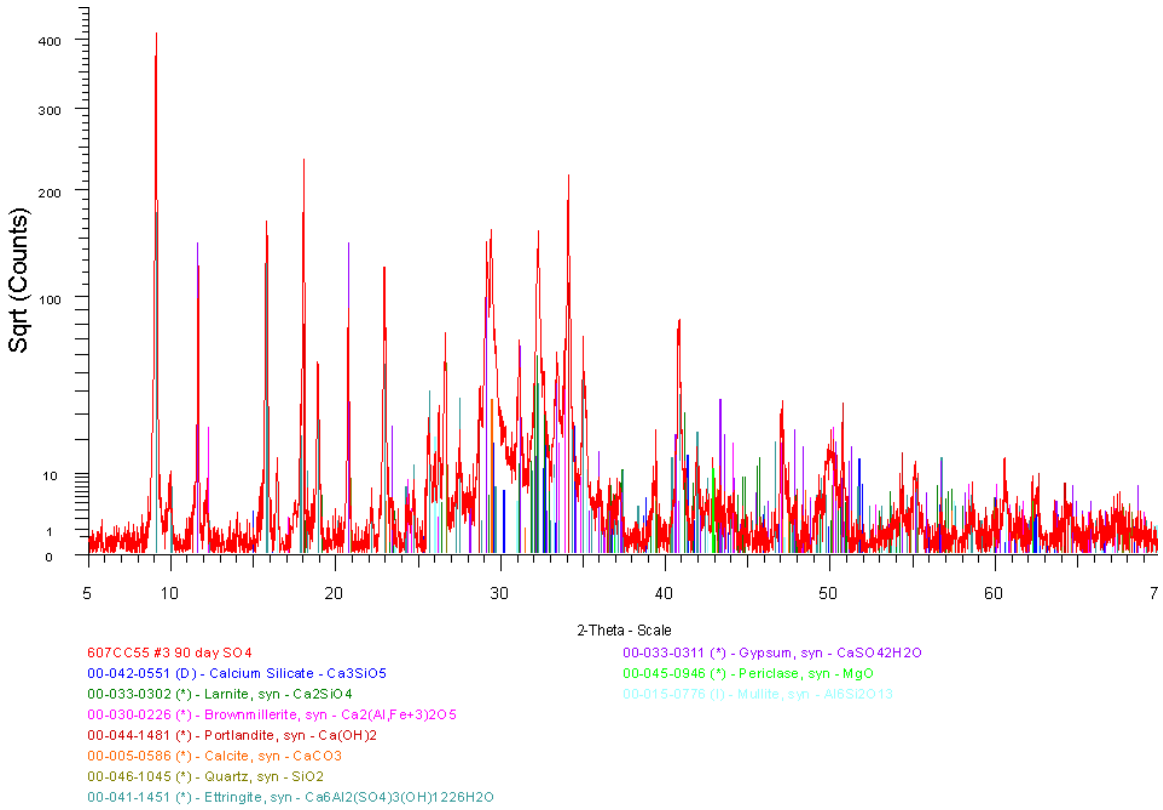

Figure E.23: F25 90-day Sulfate Exposure XRD Pattern

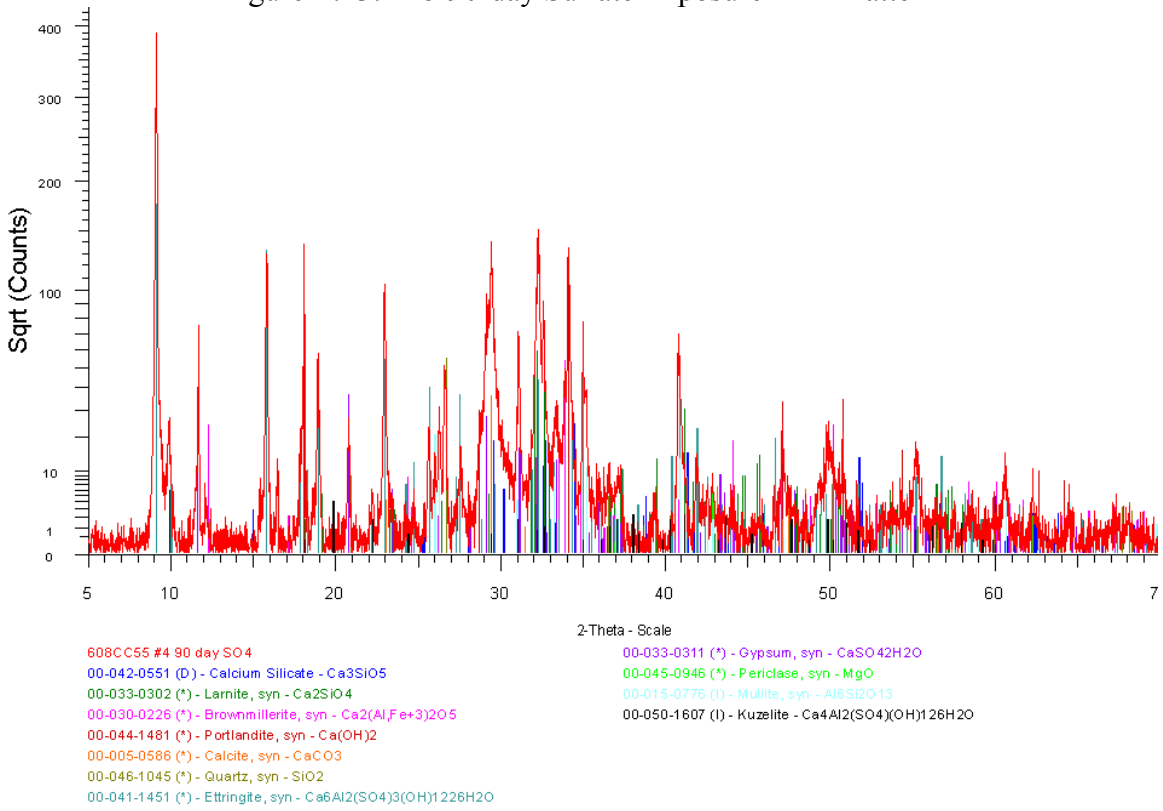

Figure E.24: F25-MK5 90-day Sulfate Exposure XRD Pattern

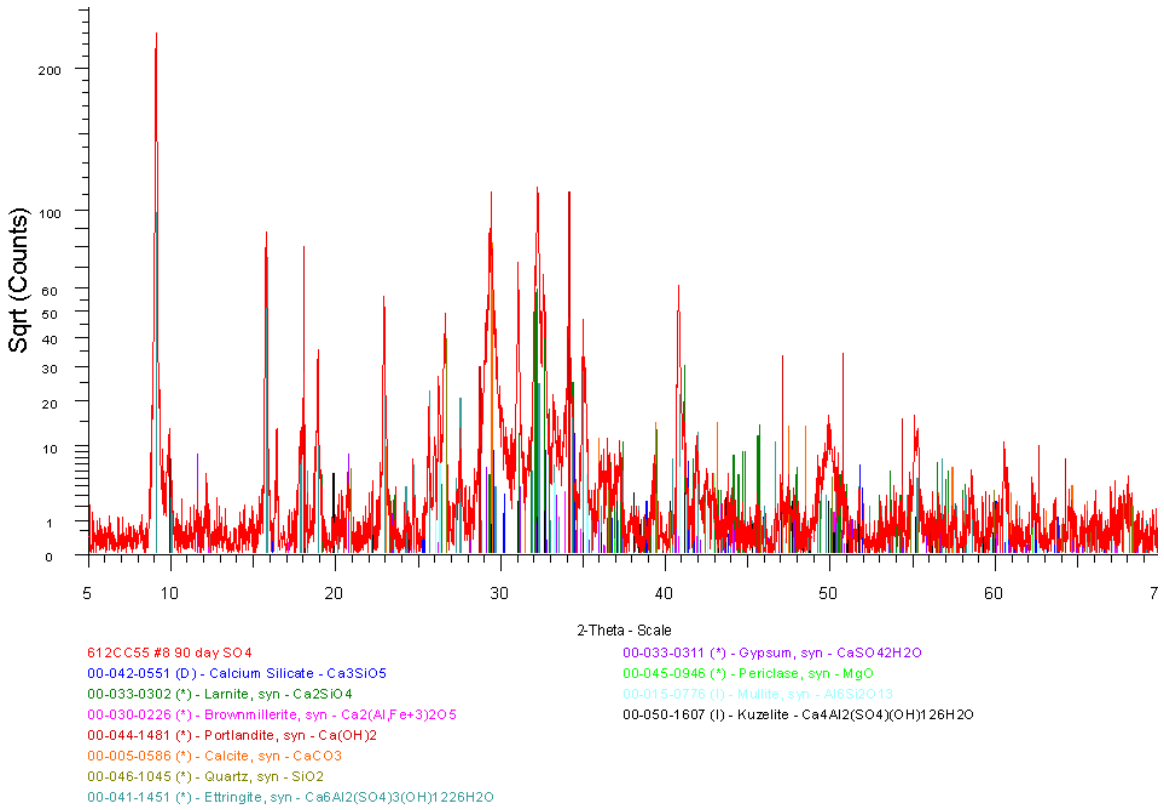

Figure E.25: F25-MK10 90-day Sulfate Exposure XRD Pattern

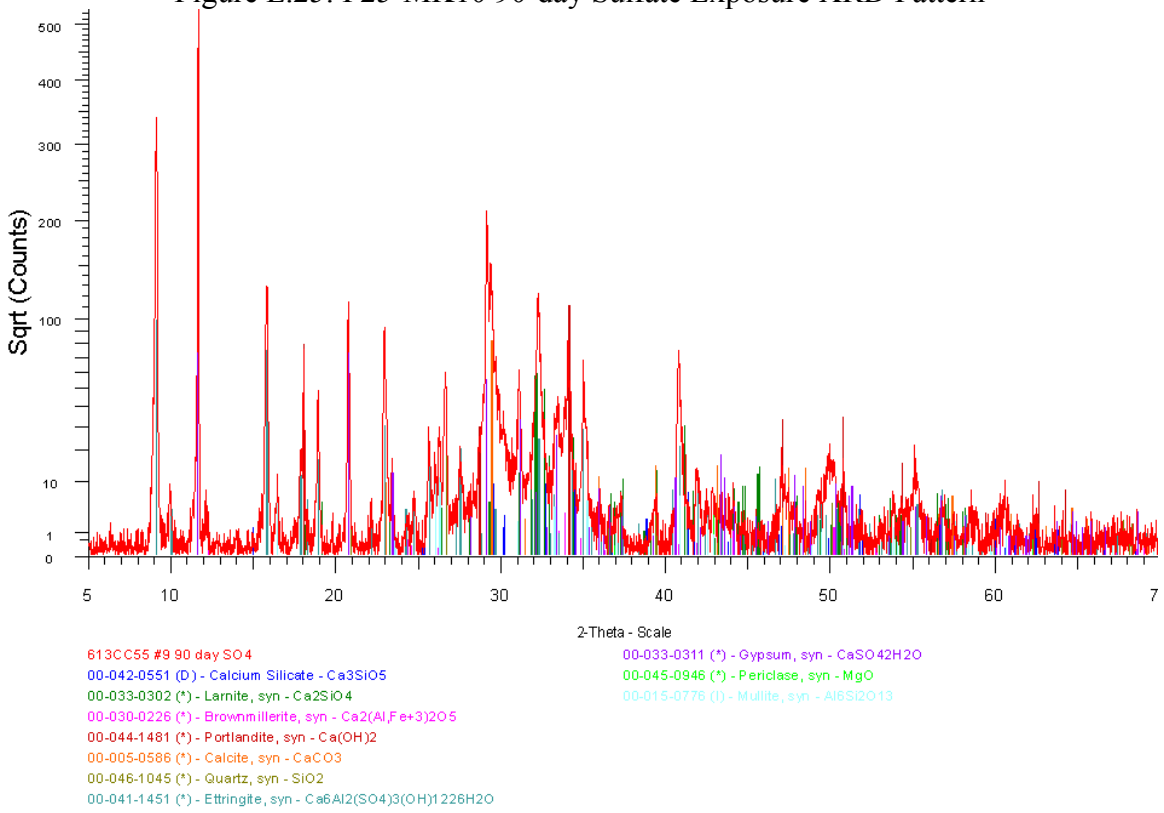

Figure E.26: F25-SF5 90-day Sulfate Exposure XRD Pattern

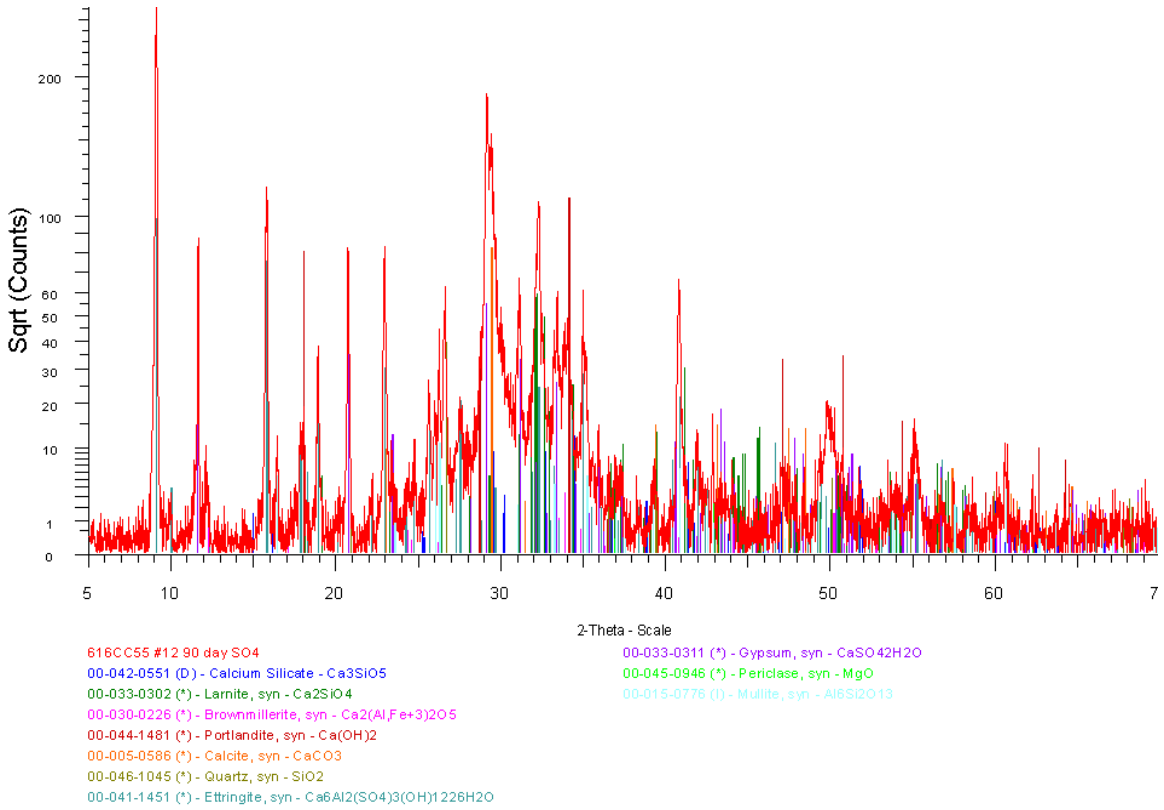

Figure E.27: F25-SF10 90-day Sulfate Exposure XRD Pattern

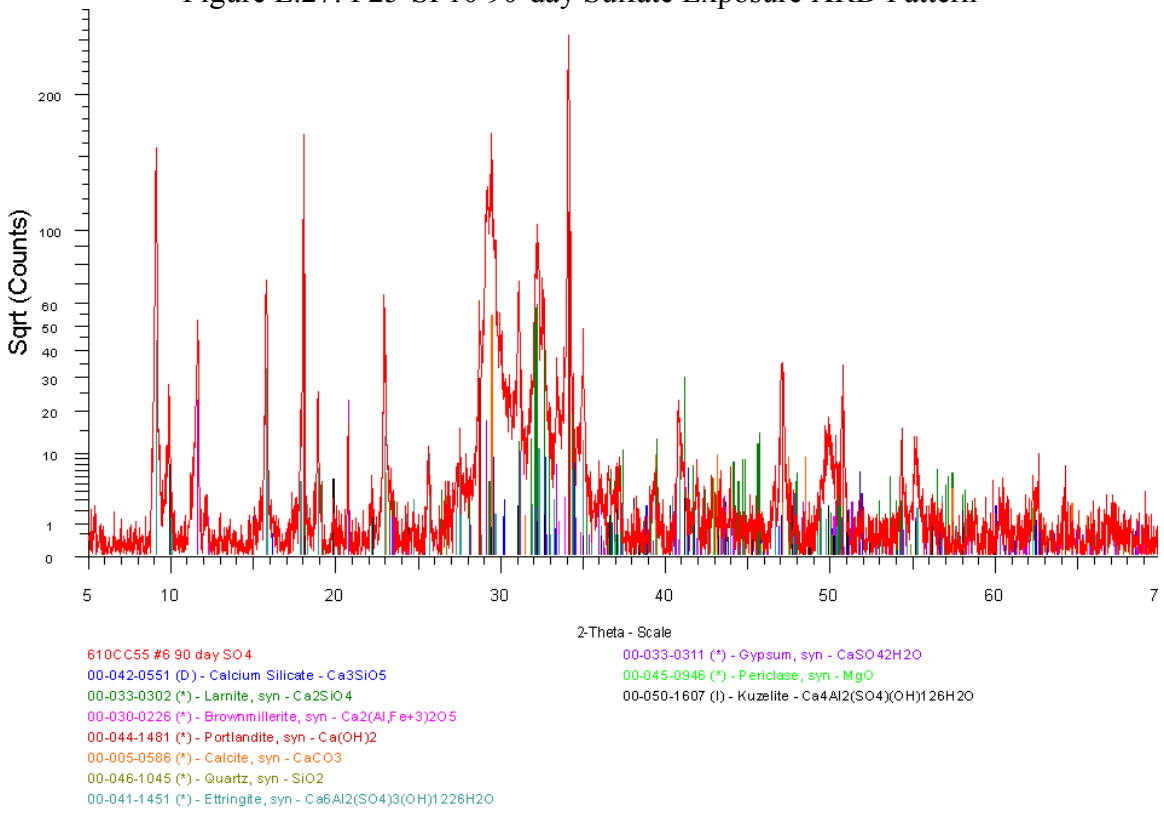

Figure E.28: S35-MK5 90-day Sulfate Exposure XRD Pattern

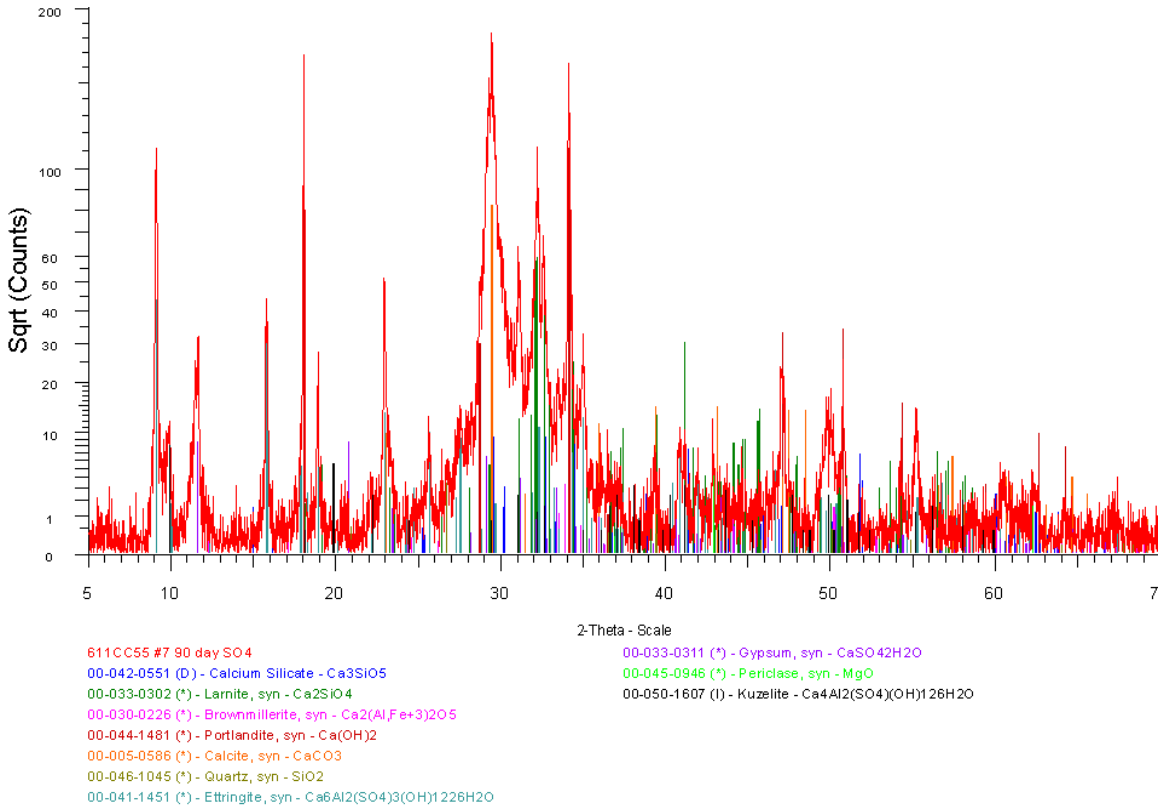

Figure E.29: S50-MK5 90-day Sulfate Exposure XRD Pattern

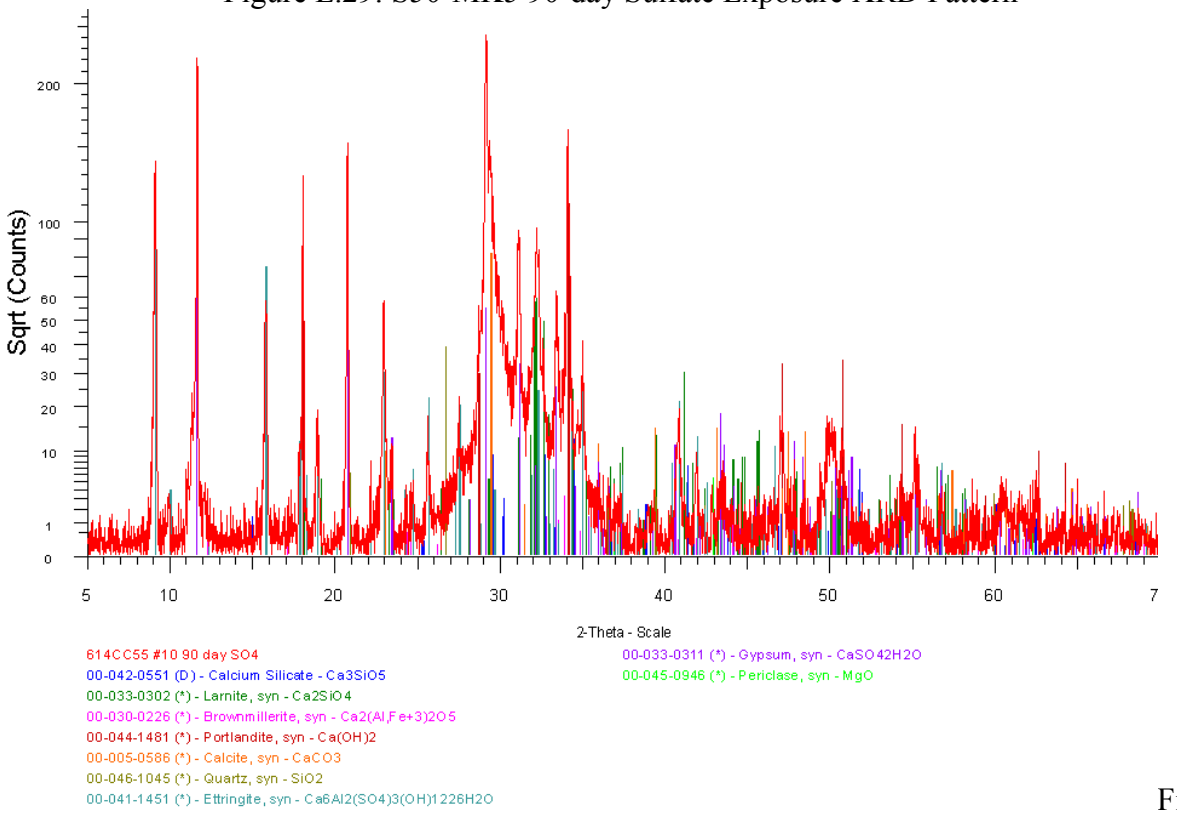

Figure E.30: S35-SF5 90-day Sulfate Exposure XRD Pattern

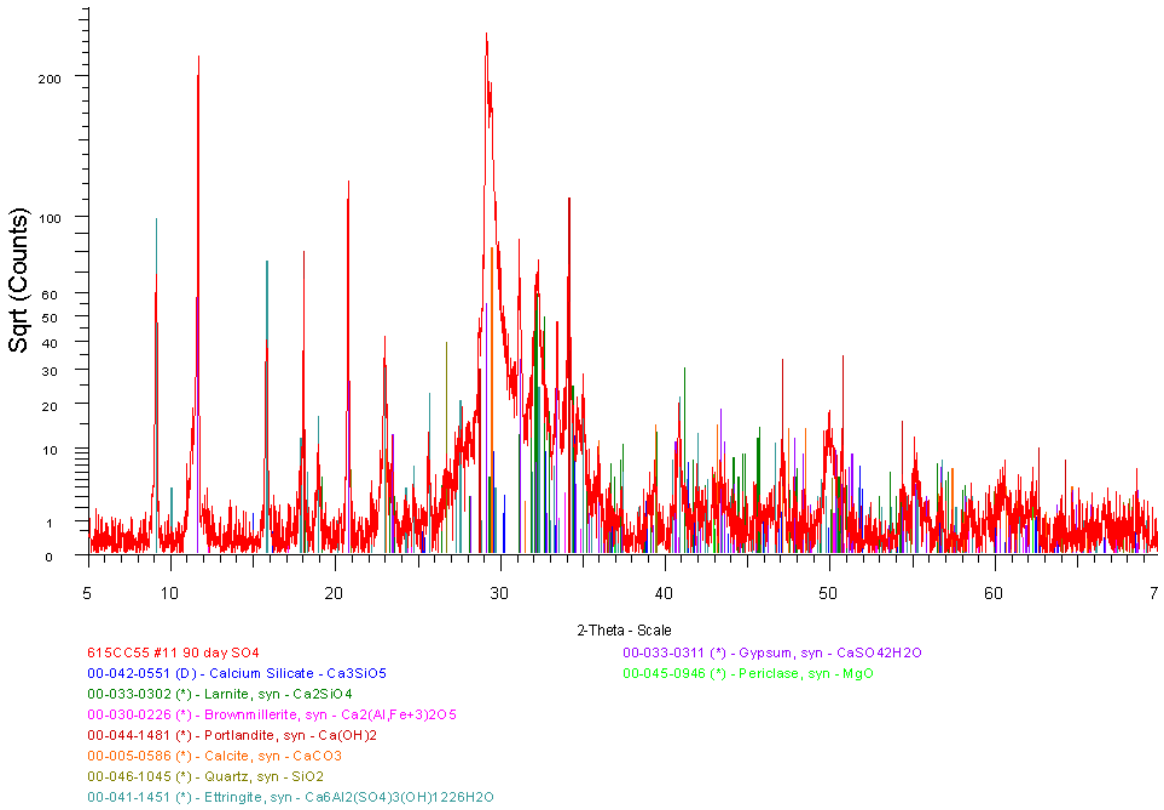

Figure E.31: S50-SF5 90-day Sulfate Exposure XRD Pattern

E.3.1.3 180-day Sulfate Exposure Specimens

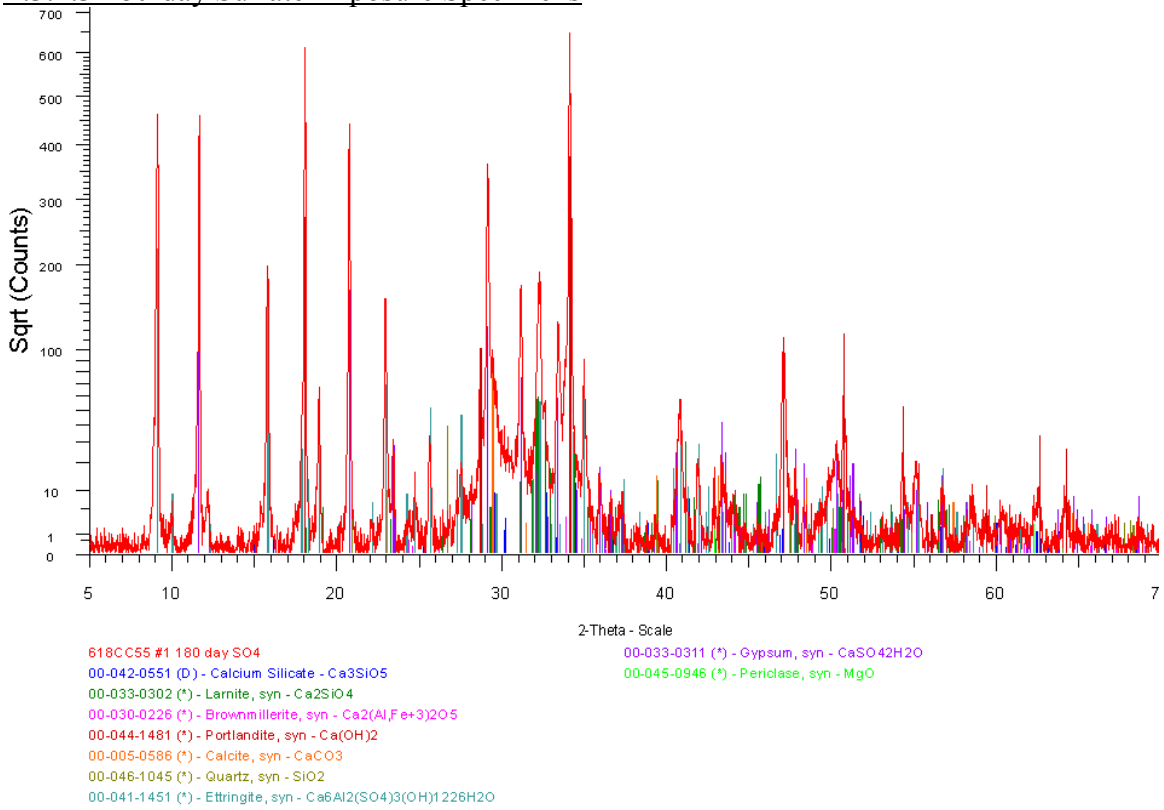

Figure E.32: T2 180-day Sulfate Exposure XRD Pattern

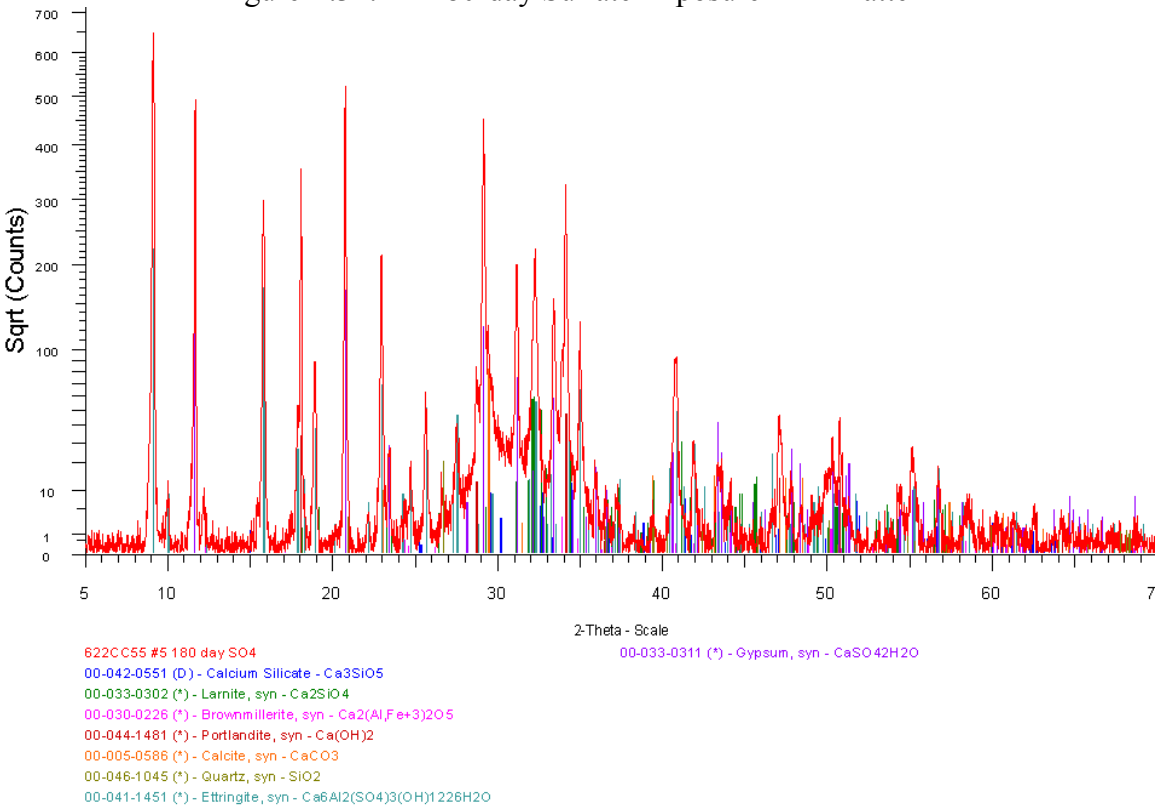

Figure E.33: T3 180-day Sulfate Exposure XRD Pattern

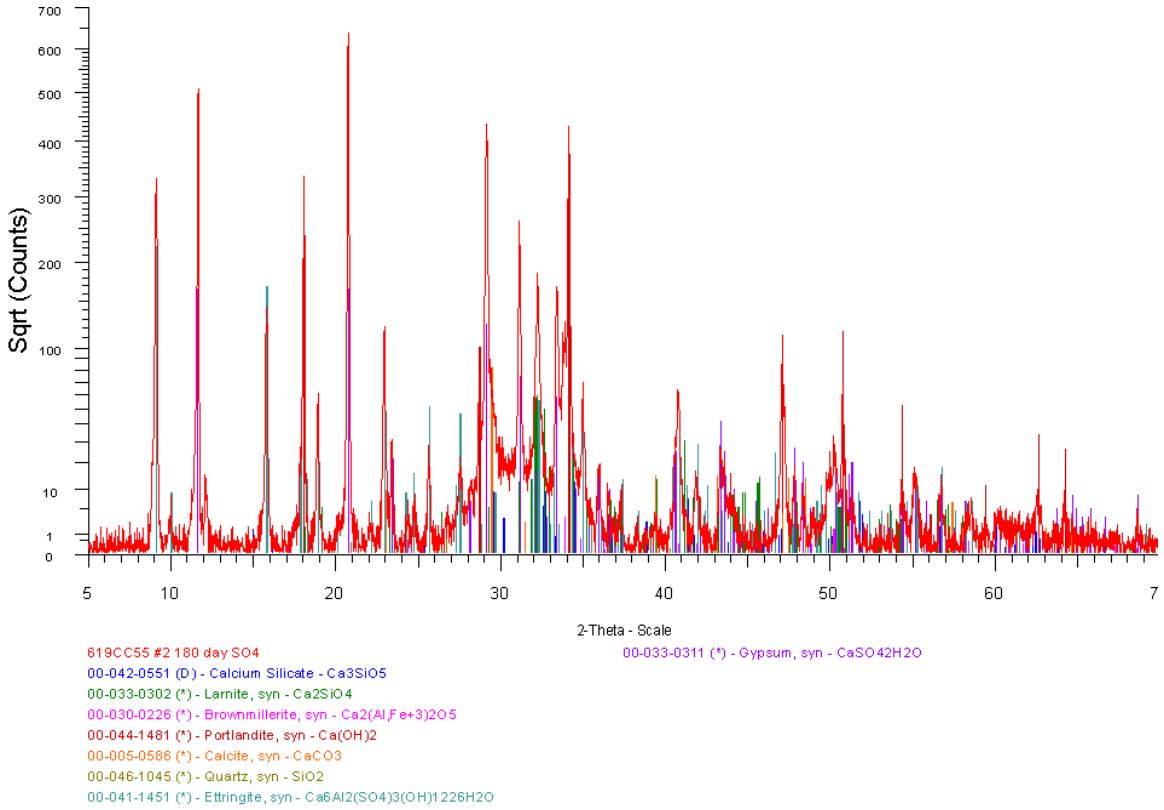

Figure E.34: T5 180-day Sulfate Exposure XRD Pattern

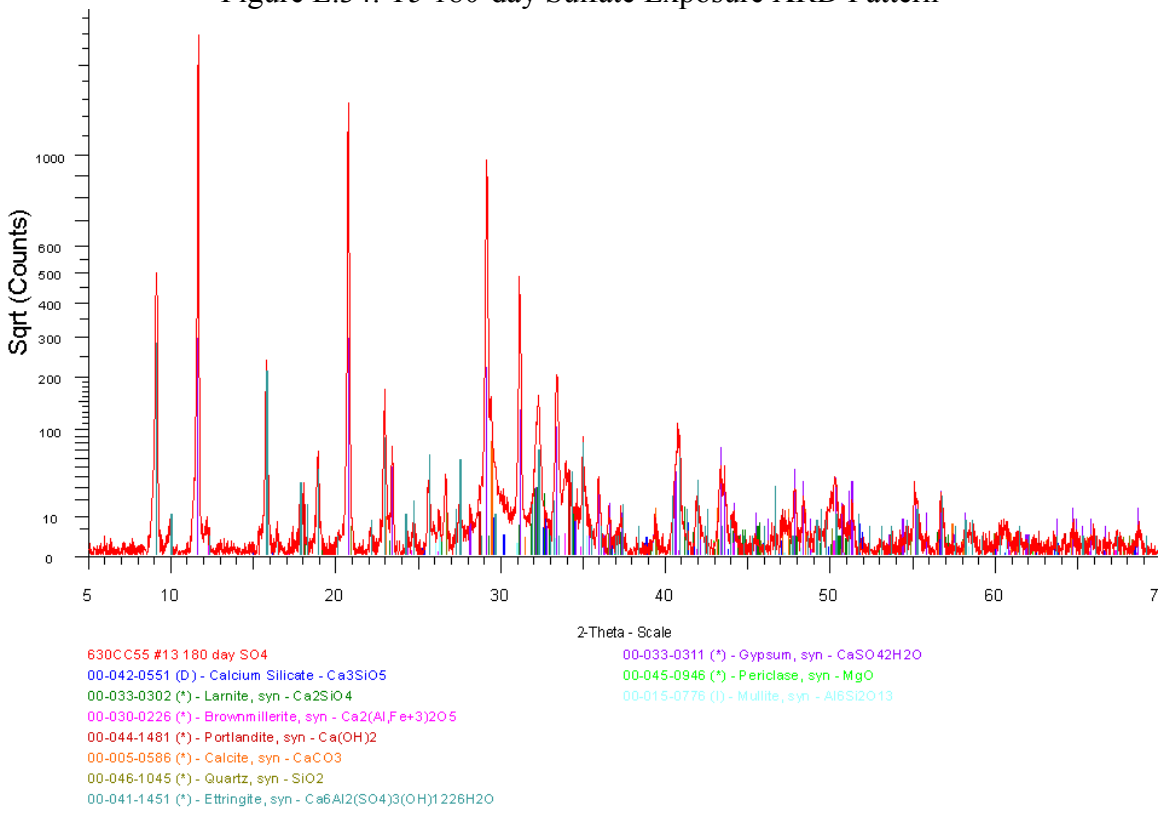

Figure E.35: T3-F15 180-day Sulfate Exposure XRD Pattern

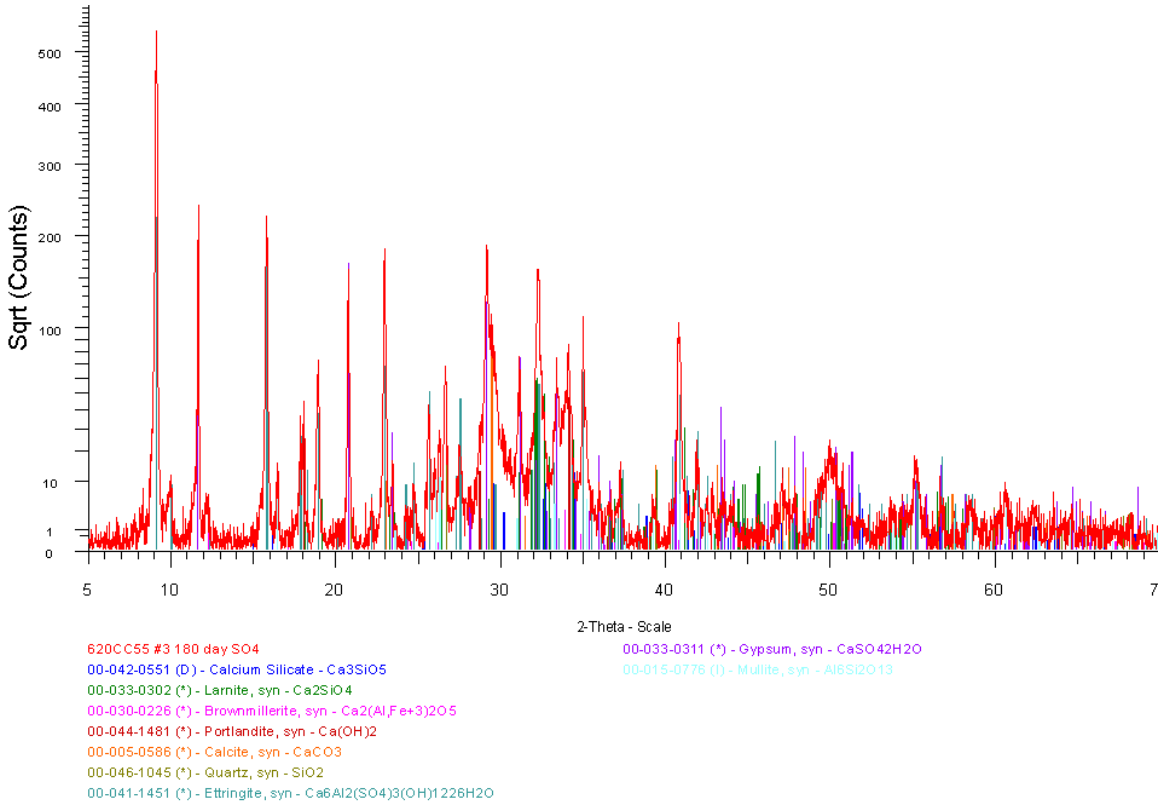

Figure E.36: F25 180-day Sulfate Exposure XRD Pattern

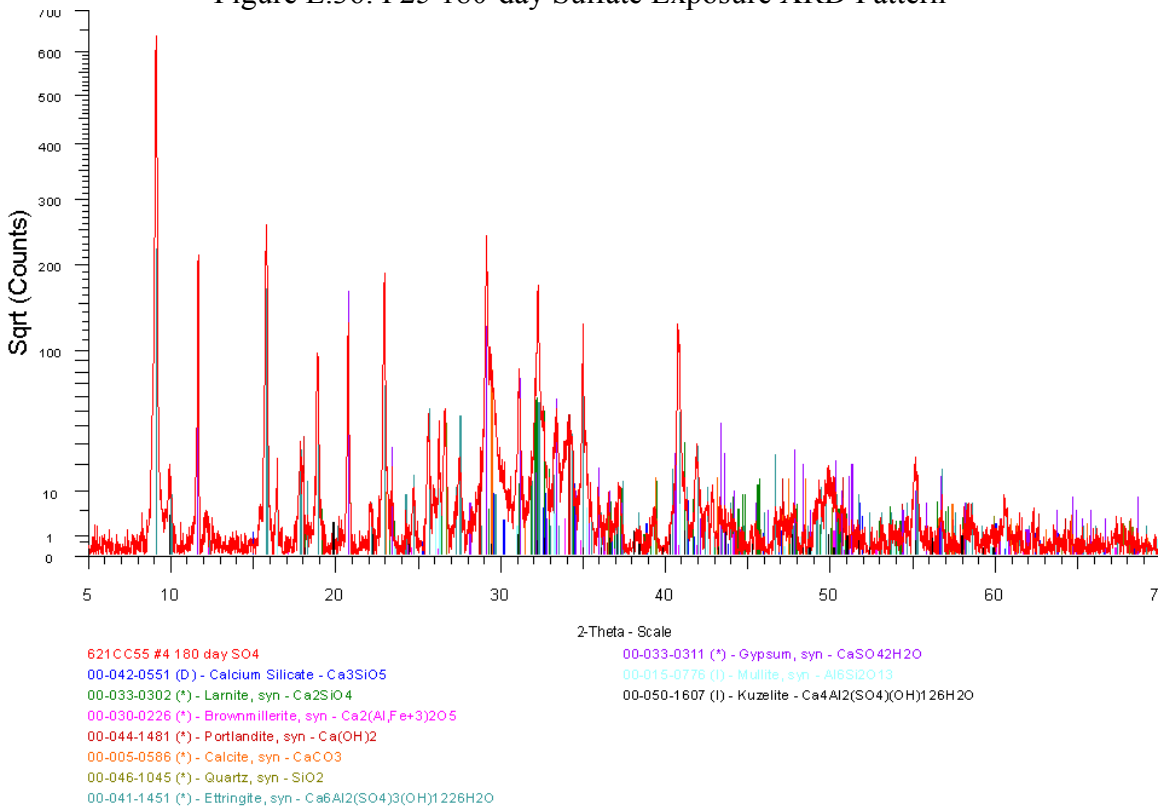

Figure E.37: F25-MK5 180-day Sulfate Exposure XRD Pattern

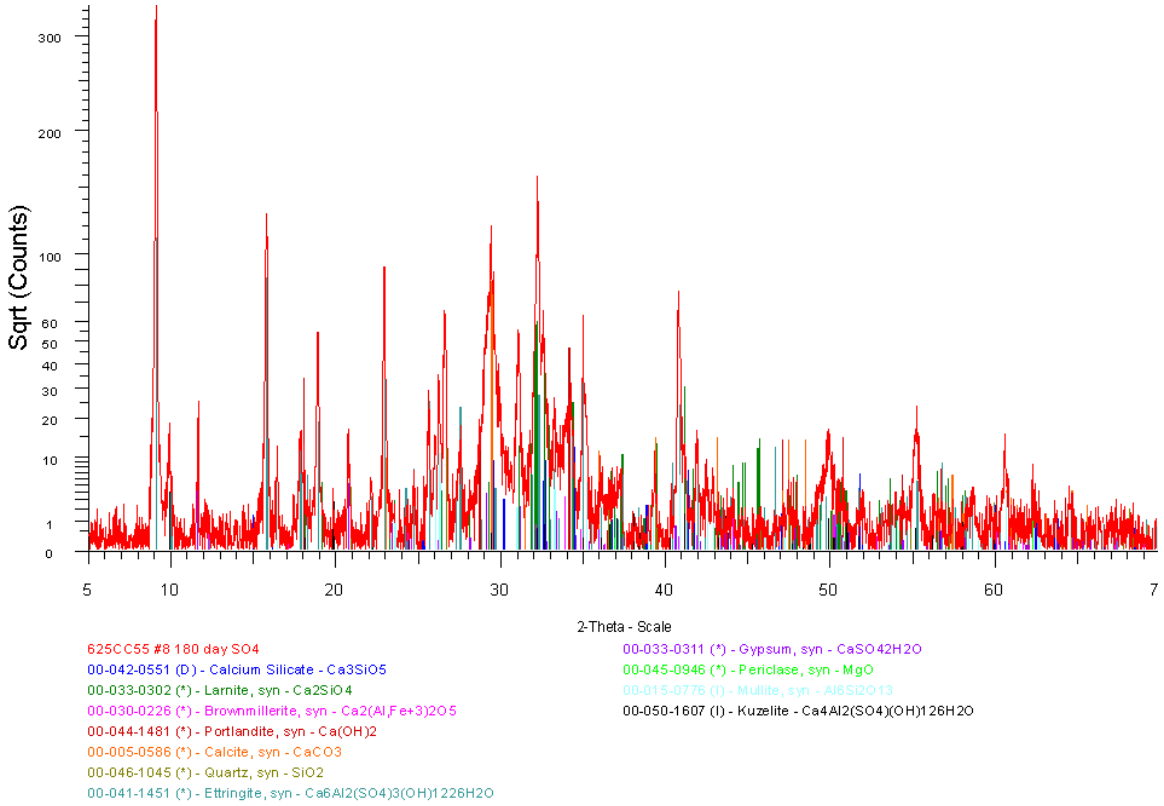

Figure E.38: F25-MK10 180-day Sulfate Exposure XRD Pattern

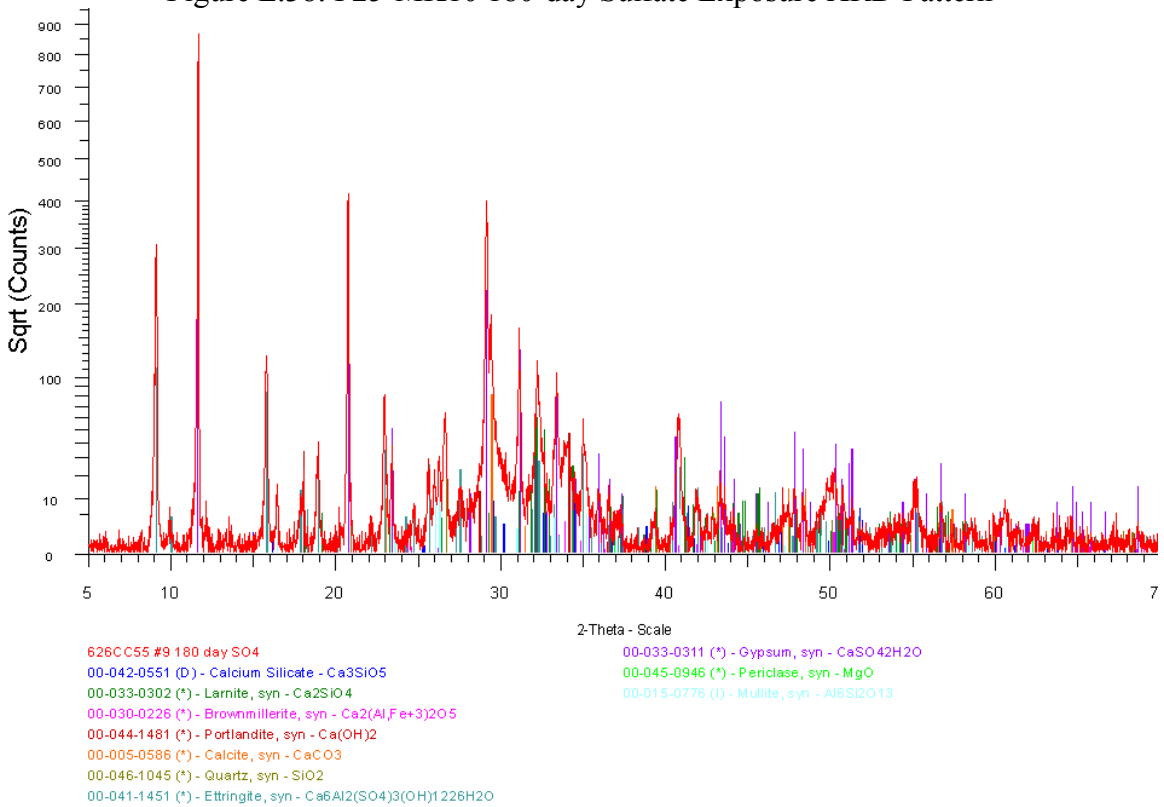

Figure E.39: F25-SF5 180-day Sulfate Exposure XRD Pattern

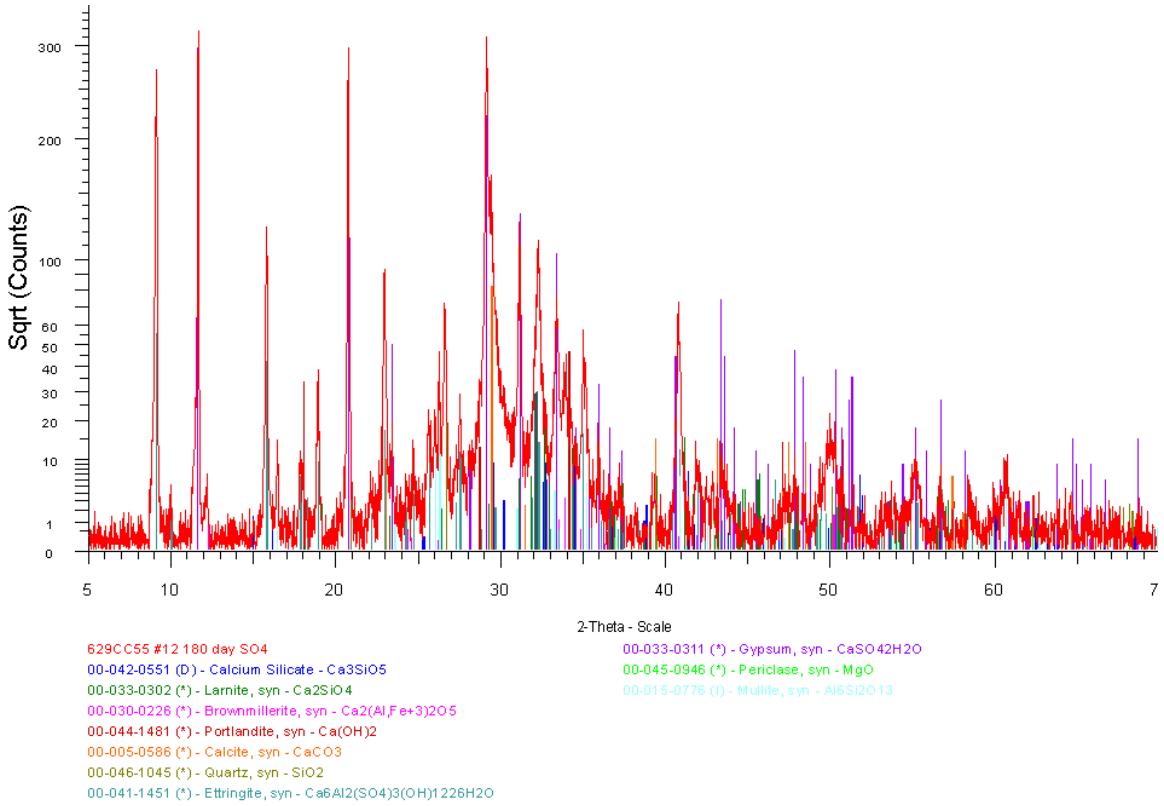

Figure E.40: F25-SF10 180-day Sulfate Exposure XRD Pattern

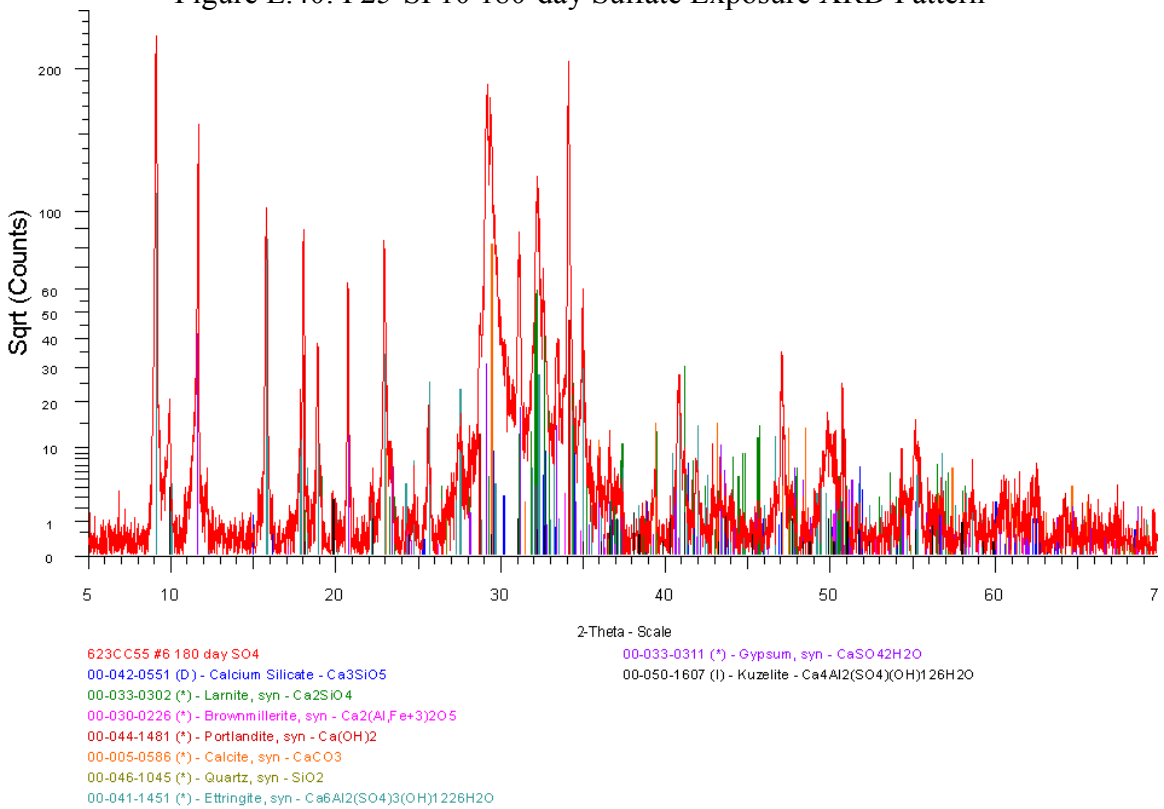

Figure E.41: S35-MK5 180-day Sulfate Exposure XRD Pattern

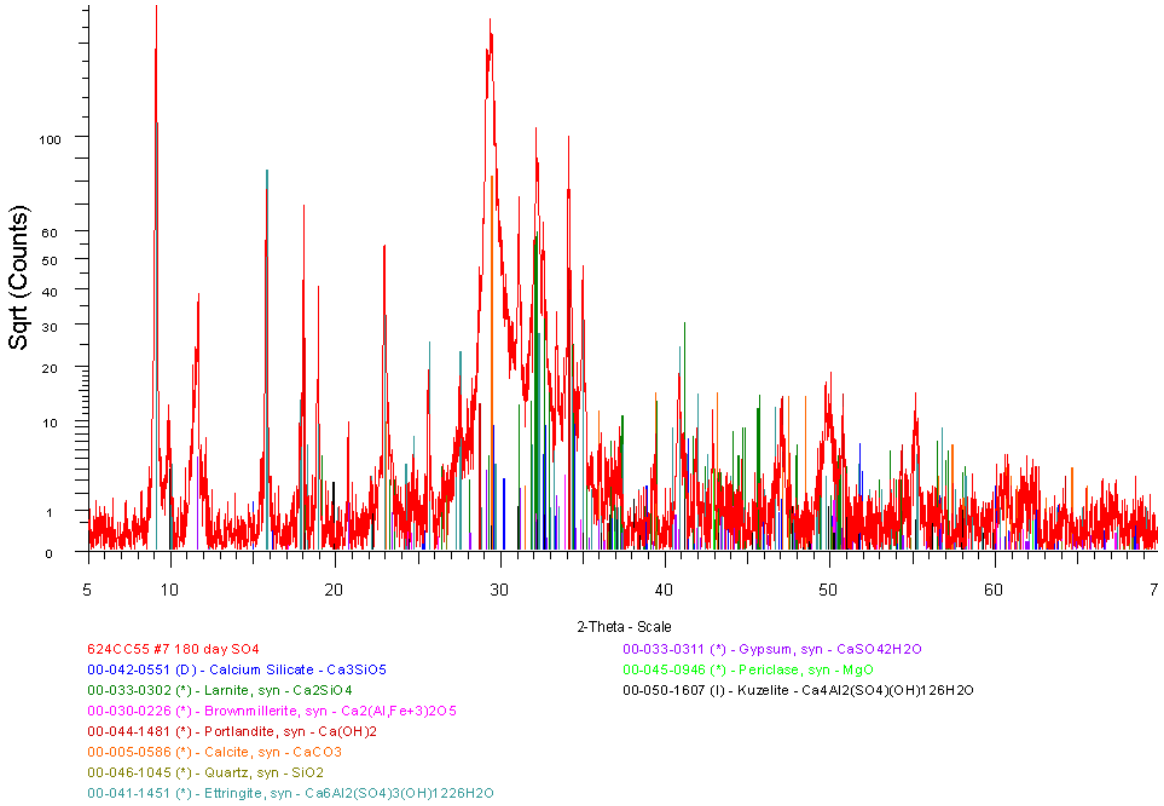

Figure E.42: S50-MK5 180-day Sulfate Exposure XRD Pattern

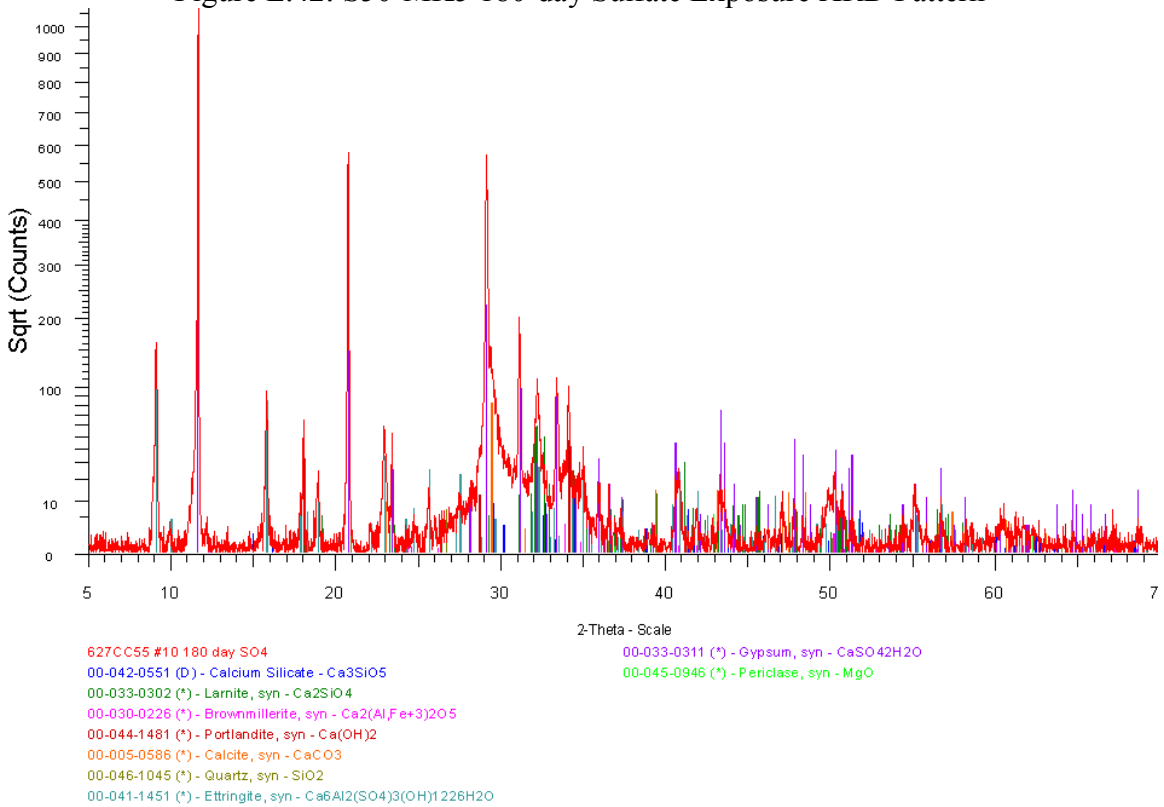

Figure E.43: S35-SF5 180-day Sulfate Exposure XRD Pattern

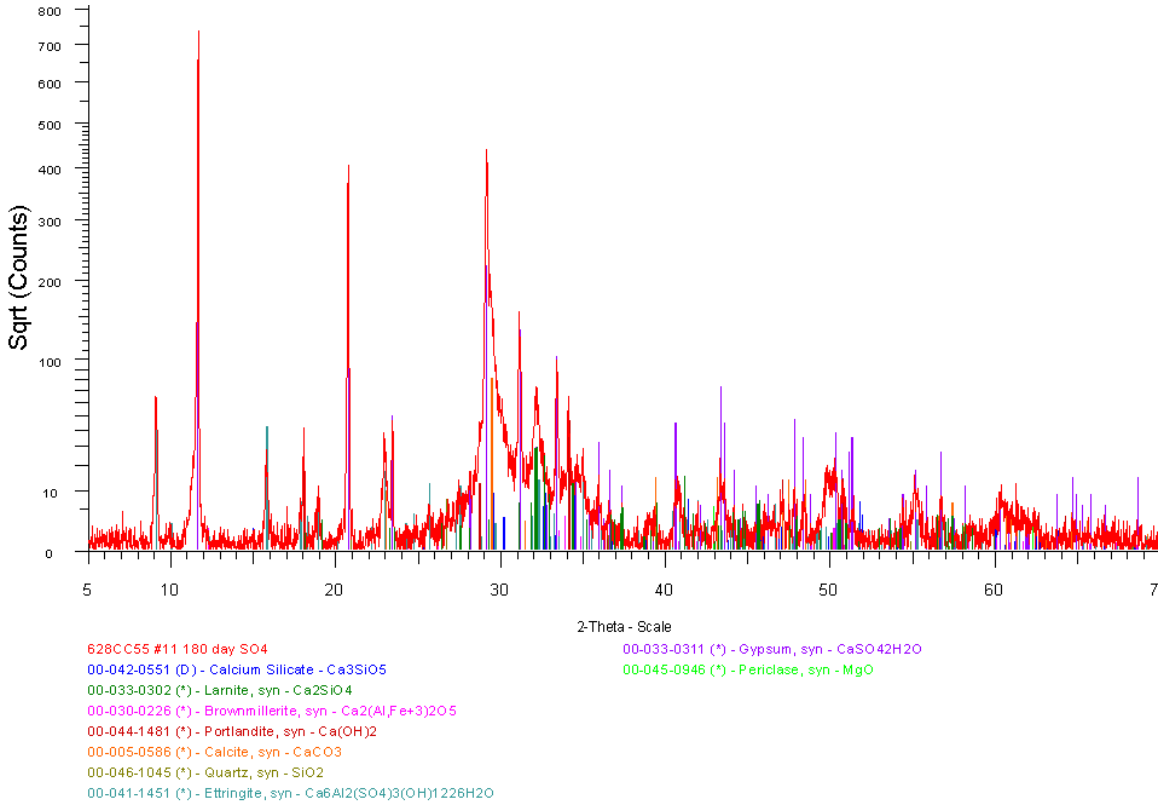

Figure E.44: S50-SF5 180-day Sulfate Exposure XRD Pattern

E.3.2 Quantitative X-Ray Diffraction Analysis Results

Table E.9: C_3S and C_2S contents of mix designs after sulfate exposure

	C_3S			C_2S		
Mix Design	180 days Control	90 days Sulfate	180 days Sulfate	180 days Control	90 days Sulfate	180 days Sulfate
T2	3.64	3.38	2.91	1.34	7.69	5.08
T3	0.86	1.49	2.07	1.16	3.12	4.93
T5	2.43	2.58	2.31	0.35	2.94	1.64
T3-F15	2.849	2.35	1.48	1.449	6.29	4.89
F25	5.39	1.70	3.35	11.55	11.34	9.23
F25-MK5	6.04	2.23	3.17	12.93	13.23	9.93
F25-MK10	4.90	2.06	2.35	17.29	17.00	14.36
F25-SF5	1.89	1.91	2.06	11.80	8.95	5.47
F25-SF10	2.886	2.01	1.99	15.619	10.68	7.93
S35-MK5	9.81	10.48	9.35	9.81	9.19	9.75
S50-MK5	12.75	9.94	11.56	9.63	15.61	12.25
S35-SF5	9.87	9.18	7.42	5.85	8.56	4.75
S50-SF5	10.06	11.75	10.59	9.38	10.24	2.66

Table E.10: C_3A and C_4AF contents of mix designs after sulfate exposure

	C_3A			C_4AF		
Mix Design	180 days Control	90 days Sulfate	180 days Sulfate	180 days Control	90 days Sulfate	180 days Sulfate
T2	0.161	0.09	0.00	16.554	14.78	13.59
T3	0.235	0.10	0.39	9.722	9.56	9.13
T5	0	0.15	0.01	16.068	13.11	12.65
T3-F15	0.425	0.21	0.47	9.036	9.88	6.91
F25	0.579	0.00	0.11	13.179	11.42	11.02
F25-MK5	0.658	0.00	0.01	8.781	8.87	7.60
F25-MK10	1.157	0.00	0.00	7.612	7.17	6.74
F25-SF5	0.687	0.00	0.24	10.398	11.32	11.96
F25-SF10	0.703	0.07	0.09	14.51	11.59	10.50
S35-MK5	0	0.00	0.00	10.777	11.33	9.45
S50-MK5	0.626	0.00	0.00	16.091	13.03	10.88
S35-SF5	0.124	0.00	0.00	18.26	14.85	11.64
S50-SF5	0.331	0.00	0.00	18.703	14.62	12.96

Table E.11: Portlandite and quartz contents of mix designs after sulfate exposure

	Portlandite			Quartz		
Mix Design	180 days Control	90 days Sulfate	180 days Sulfate	180 days Control	90 days Sulfate	180 days Sulfate
T2	34.88	16.61	12.77	0.787	0.73	0.61
T3	43.226	11.68	7.81	1.573	1.44	0.86
T5	44.353	18.57	11.52	1.347	1.31	0.65
T3-F15	30.532	4.85	1.16	4.998	3.18	2.71
F25	14.124	5.62	2.13	6.501	5.18	4.86
F25-MK5	9.834	3.44	0.85	7.119	4.84	4.55
F25-MK10	5.524	1.66	0.46	10.674	6.02	6.40
F25-SF5	8.869	2.72	0.84	7.259	6.06	5.87
F25-SF10	6.309	1.14	0.29	7.66	6.12	6.00
S35-MK5	20.471	9.94	7.51	0.717	0.73	0.68
S50-MK5	12.259	7.02	4.16	0.881	0.89	0.56
S35-SF5	16.522	6.61	3.85	1.216	1.07	1.21
S50-SF5	9.885	3.90	2.75	1.129	1.92	1.52

Table E.12: Calcite and ettringite contents of mix designs after sulfate exposure

	Calcite			Ettringite		
Mix Design	180 days Control	90 days Sulfate	180 days Sulfate	180 days Control	90 days Sulfate	180 days Sulfate
T2	6.01	2.86	2.76	29.347	33.25	38.41
T3	6.015	5.20	2.42	28.424	44.44	47.83
T5	5.373	3.81	2.56	24.912	35.68	37.08
T3-F15	9.15	3.77	3.68	21.288	44.66	36.68
F25	6.598	5.06	1.72	17.926	39.91	44.74
F25-MK5	13.971	4.56	2.01	7.226	41.18	49.64
F25-MK10	14.984	4.58	4.46	13.182	41.10	43.04
F25-SF5	17.336	5.15	5.01	18.358	41.31	35.55
F25-SF10	8.479	3.94	4.32	22.001	40.50	36.77
S35-MK5	15.196	6.99	6.28	8.815	34.26	38.24
S50-MK5	17.028	8.59	7.19	5.252	29.81	37.73
S35-SF5	12.702	4.42	4.38	12.655	32.77	32.79
S50-SF5	14.225	7.65	8.35	10.105	28.63	27.24

Table E.13: Monocarbonate and gypsum contents of mix designs after sulfate exposure

	Mono Carbonate			Gypsum		
Mix Design	180 days Control	90 days Sulfate	180 days Sulfate	180 days Control	90 days Sulfate	180 days Sulfate
T2	6.037	0.00	0.00	0	19.31	22.78
T3	8.782	0.00	0.00	0	22.40	24.33
T5	4.966	0.00	0.00	0	21.86	31.57
T3-F15	12.198	0.00	0.00	0	18.63	36.05
F25	12.414	0.00	0.00	0	9.13	11.89
F25-MK5	16.397	0.00	0.00	0	6.83	10.67
F25-MK10	11.098	0.00	0.00	0	5.03	7.05
F25-SF5	9.216	0.00	0.00	0	10.31	21.53
F25-SF10	7.37	0.00	0.00	0	11.68	19.59
S35-MK5	19.694	0.00	0.00	0	9.77	13.21
S50-MK5	22.495	0.00	0.00	0	8.50	10.79
S35-SF5	20.391	0.00	0.00	0	21.18	32.97
S50-SF5	23.07	0.00	0.00	0	20.47	32.83

Table E.14: Periclase and mullite contents of mix designs after sulfate exposure

	Periclase			Mullite		
Mix Design	180 days Control	90 days Sulfate	180 days Sulfate	180 days Control	90 days Sulfate	180 days Sulfate
T2	1.017	1.24	0.97	0	0.00	0.00
T3	0	0.06	0.00	0	0.00	0.00
T5	0.138	0.00	0.00	0	0.00	0.00
T3-F15	0	0.19	0.07	5.243	5.22	5.39
F25	0.316	0.92	0.75	9.702	8.99	9.77
F25-MK5	1.473	0.89	0.71	13.695	9.44	9.31
F25-MK10	1.294	0.35	0.77	8.304	10.53	10.48
F25-SF5	1.026	1.00	0.66	12.354	10.72	10.22
F25-SF10	1.295	0.89	0.54	13.005	11.01	11.94
S35-MK5	0.973	1.00	0.88	0	0.00	0.00
S50-MK5	1.031	1.07	1.08	0	0.00	0.00
S35-SF5	1.464	0.63	0.53	0	0.00	0.00
S50-SF5	1.215	0.80	0.25	0	0.00	0.00

Table E.15: Kuzelite content of mix designs after sulfate exposure

	Kuzelite		
Mix Design	180 days Control	90 days Sulfate	180 days Sulfate
T2	0.224	0.06	0.13
T3	0.011	0.52	0.23
T5	0.063	0.00	0.00
T3-F15	2.833	0.78	0.52
F25	1.719	0.74	0.45
F25-MK5	1.881	4.51	1.54
F25-MK10	3.979	4.50	3.90
F25-SF5	0.805	0.55	0.60
F25-SF10	0.164	0.37	0.04
S35-MK5	3.739	6.32	4.64
S50-MK5	1.952	5.55	3.80
S35-SF5	0.942	0.72	0.45
S50-SF5	1.895	0.02	0.85

(This page intentionally left blank.)

APPENDIX F

SELF-HEALING INVESTIGATION RESULTS

F.1 Photographs of Samples Preparation and Cracking

Figure F.1: Post-tensioning of specimens

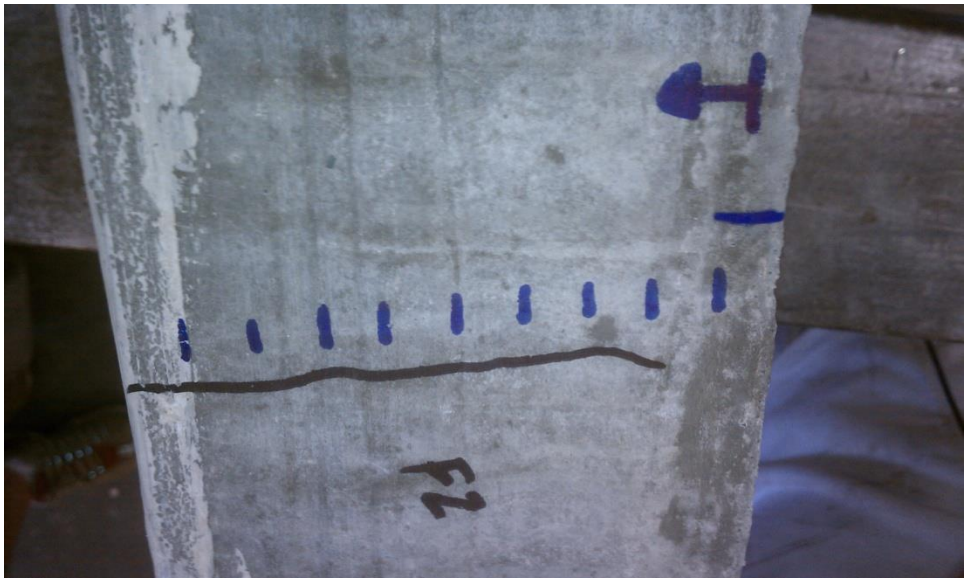

Figure F.2: Crack width measurement marks every ½ in. on flexure specimen

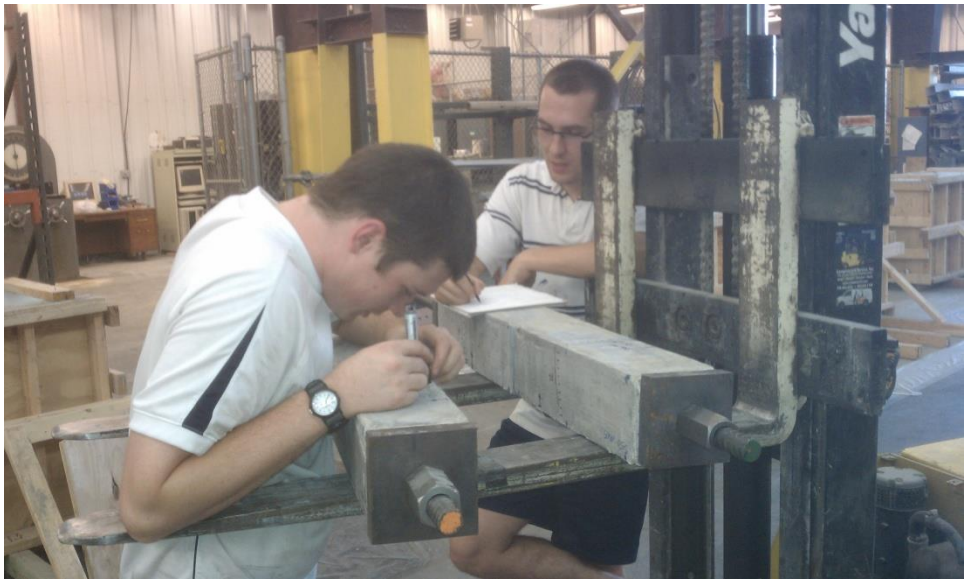

Figure F.3: Graduate students taking crack width measurements before sealing and exposure

Figure F.4: Graduate student sealing the sides of specimens with aluminum tape

Figure F.5: Sealed specimens with aluminum tape and epoxy with exposure container attached

Figure F.6: Exposure surface inside of ponding container with simulated seawater solution

F.2 Self-Healing Crack Images

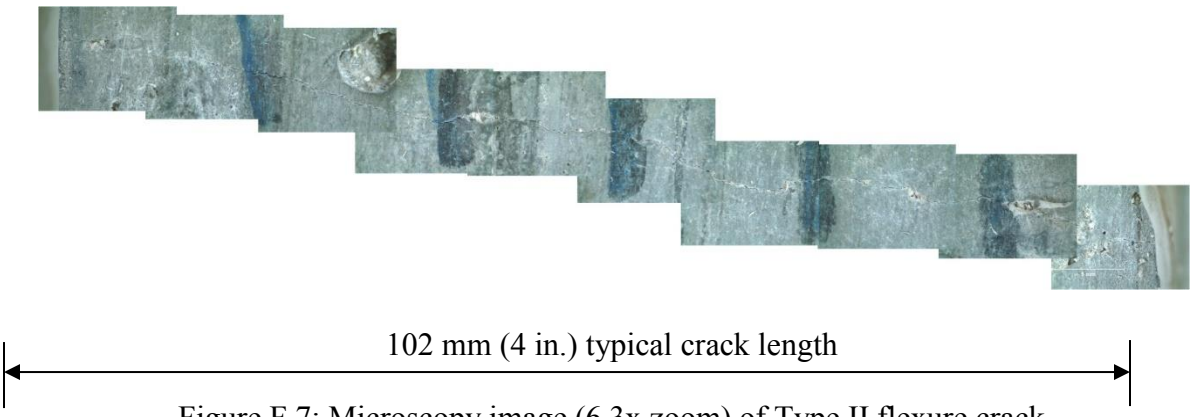

Figure F.7: Microscopy image (6.3x zoom) of Type II flexure crack

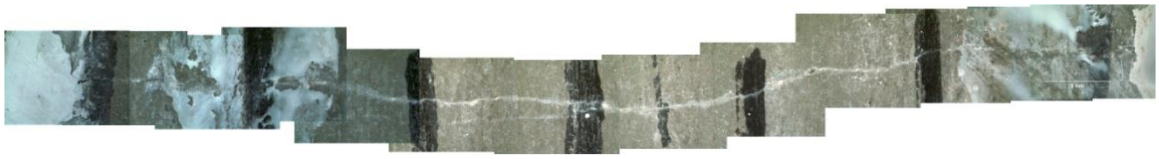

Figure F.8: Microscopy image (6.3x zoom) of Type II tension crack

Figure F.9: Microscopy image (6.3x zoom) of T3-F15 flexure crack

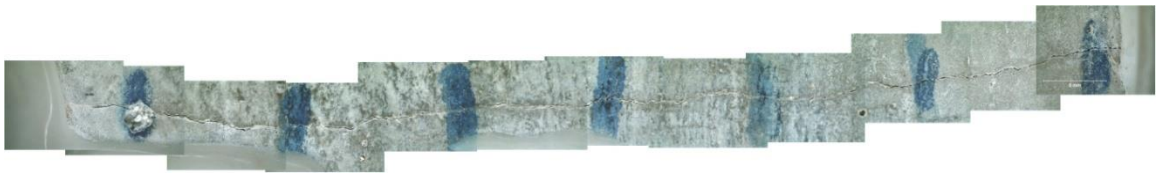

Figure F.10: Microscopy image (6.3x zoom) of T3-F15 tension crack

Figure F.11: Microscopy image (6.3x zoom) of F25 flexure crack

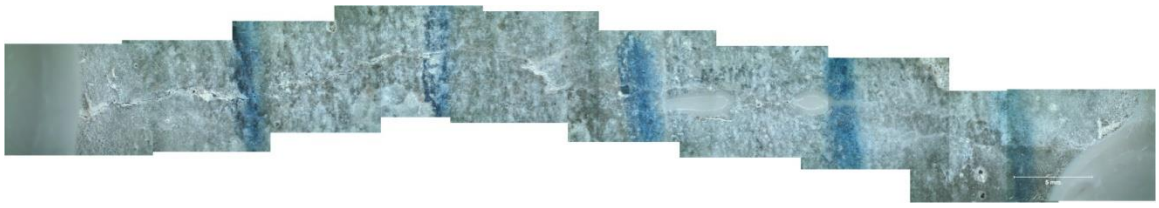

Figure F.12: Microscopy image (6.3x zoom) of F25 tension crack

Figure F.13: Microscopy image (6.3x zoom) of S35-MK5 flexure crack

Figure F.14: Microscopy image (6.3x zoom) of S35-MK5 tension crack

Figure F.15: Microscopy image (6.3x zoom) of S50-MK5 flexure crack

Figure F.16: Microscopy image (6.3x zoom) of S50-MK5 tension crack

F.3 Self-Healing Chloride Ingress Titration Data

Tables F.1 through F.15 provide the titration results for control, tension, and flexure specimens to the center of the grinding increment in mm (1 in. = 25.4 mm).

Table F.1: Type II control sample titration data

	Concentration (% Mass)			
Depth (mm)	**C1**	**C2**	**Average**	**Std. Dev.**
0.5	0.484	0.440	0.462	0.031
1.5	0.263	0.458	0.360	0.138
2.5	0.304	0.508	0.406	0.144
3.5	0.203	0.400	0.302	0.139
4.5	0.170	0.350	0.260	0.128
5.5	0.207	0.290	0.249	0.058
7	0.137	0.248	0.193	0.079
9	0.080	0.143	0.111	0.044
11	0.059	0.059	0.059	0.000
13	0.037	0.036	0.036	0.001

Table F.2: Type II tension sample titration data

	Concentration (% Mass)			
Depth (mm)	**T1**	**T2**	**Average**	**Std. Dev.**
1	0.502	0.544	0.523	0.030
3	0.468	0.402	0.435	0.046
5	0.373	0.276	0.325	0.069
7	0.276	0.204	0.240	0.051
9	0.249	0.142	0.195	0.075
11	0.192	0.073	0.132	0.084
13	0.175	0.133	0.154	0.030
15	0.189	0.079	0.134	0.077
17	0.168	0.044	0.106	0.087
19	0.141	0.044	0.093	0.069
76.2	0.048	0.053	0.051	0.004

Table F.3: Type II flexure sample titration data

	Concentration (% Mass)			
Depth (mm)	**F1**	**F2**	**Average**	**Std. Dev.**
1	0.389	0.332	0.360	0.040
3	0.313	0.280	0.297	0.023
5	0.237	0.244	0.240	0.005
7	0.151	0.196	0.174	0.032
9	0.163	0.139	0.151	0.016
11	0.117	0.090	0.104	0.019
13	0.103	0.060	0.081	0.031
15	0.092	0.042	0.067	0.035
17	0.059	0.050	0.054	0.007
19	0.059	0.047	0.053	0.008
76.2	0.014	0.011	0.012	0.002

Table F.4: T3-F15 control sample titration data

	Concentration (% Mass)			
Depth (mm)	**C1**	**C2**	**Average**	**Std. Dev.**
0.5	0.317	0.441	0.379	0.088
1.5	0.315	0.412	0.364	0.069
2.5	0.216	0.364	0.290	0.105
3.5	0.234	0.359	0.297	0.089
4.5	0.151	0.296	0.224	0.102
5.5	0.129	0.216	0.172	0.062
7	0.061	0.213	0.137	0.107
9	0.060	0.156	0.108	0.068
11	0.000	0.105	0.052	0.074
13	0.000	0.025	0.013	0.018

Table F.5: T3-F15 tension sample titration data

	Concentration (% Mass)			
Depth (mm)	**T1**	**T2**	**Average**	**Std. Dev.**
1	0.530	0.535	0.532	0.003
3	0.494	0.440	0.467	0.038
5	0.406	0.332	0.369	0.053
7	0.322	0.226	0.274	0.068
9	0.244	0.234	0.239	0.007
11	0.208	0.223	0.216	0.010
13	0.186	0.167	0.177	0.013
15	0.143	0.130	0.137	0.010
17	0.128	0.118	0.123	0.007
19	0.127	0.105	0.116	0.015
76.2	0.030	0.085	0.057	0.039

Table F.6: T3-F15 flexure sample titration data

	Concentration (% Mass)			
Depth (mm)	**F1**	**F2**	**Average**	**Std. Dev.**
1	0.520	0.501	0.510	0.013
3	0.454	0.425	0.439	0.020
5	0.368	0.262	0.315	0.074
7	0.332	0.279	0.306	0.037
9	0.249	0.173	0.211	0.054
11	0.195	0.146	0.171	0.034
13	0.166	0.061	0.114	0.074
15	0.139	0.073	0.106	0.047
17	0.100	0.053	0.076	0.033
19	0.077	0.039	0.058	0.027
76.2	0.009	0.014	0.011	0.004

Table F.7: F25 control sample titration data

	Concentration (% Mass)			
Depth (mm)	**C1**	**C2**	**Average**	**Std. Dev.**
0.5	0.578	-	0.578	-
1.5	0.477	0.355	0.416	0.086
2.5	0.332	0.364	0.348	0.023
3.5	0.262	0.348	0.305	0.061
4.5	0.262	0.241	0.251	0.014
5.5	0.221	0.149	0.185	0.051
7	0.154	0.079	0.117	0.053
9	0.087	0.038	0.063	0.035
11	0.047	0.000	0.024	0.033
13	0.018	0.000	0.009	0.013

Table F.8: F25 tension sample titration data

	Concentration (% Mass)			
Depth (mm)	**T1**	**T2**	**Average**	**Std. Dev.**
1	0.494	0.454	0.474	0.028
3	0.405	0.481	0.443	0.054
5	0.376	0.439	0.407	0.045
7	0.292	0.289	0.290	0.002
9	0.235	0.206	0.221	0.020
11	0.220	0.158	0.189	0.044
13	0.200	0.093	0.147	0.076
15	0.154	0.099	0.127	0.039
17	0.132	0.114	0.123	0.012
19	0.132	0.113	0.122	0.013
76.2	0.034	0.038	0.036	0.003

Table F.9: F25 flexure sample titration data

	Concentration (% Mass)			
Depth (mm)	**F1**	**F2**	**Average**	**Std. Dev.**
1	0.404	0.577	0.490	0.122
3	0.344	0.515	0.430	0.121
5	0.281	0.383	0.332	0.072
7	0.253	0.287	0.270	0.024
9	0.146	0.194	0.170	0.034
11	0.100	0.147	0.123	0.033
13	0.076	0.119	0.098	0.030
15	0.056	0.076	0.066	0.014
17	0.034	0.068	0.051	0.024
19	0.035	0.064	0.050	0.021
76.2	0.007	0.007	0.007	0.000

Table F.10: S35-MK5 control sample titration data

	Concentration (% Mass)			
Depth (mm)	**C1**	**C2**	**Average**	**Std. Dev.**
0.5	0.656	0.545	0.601	0.079
1.5	0.630	0.532	0.581	0.069
2.5	0.550	0.465	0.508	0.060
3.5	0.562	0.491	0.527	0.050
4.5	0.445	0.327	0.386	0.083
5.5	0.255	0.206	0.230	0.034
7	0.131	0.148	0.140	0.012
9	0.053	0.029	0.041	0.017
11	0.027	0.000	0.013	0.019
13	0.019	0.000	0.009	0.013

Table F.11: S35-MK5 tension sample titration data

	Concentration (% Mass)			
Depth (mm)	**T1**	**T2**	**Average**	**Std. Dev.**
1	0.493	0.524	0.508	0.022
3	0.472	0.407	0.440	0.046
5	0.333	0.144	0.239	0.133
7	0.207	0.118	0.163	0.063
9	0.107	0.081	0.094	0.018
11	0.097	0.080	0.089	0.012
13	0.098	0.063	0.081	0.025
15	0.093	0.079	0.086	0.010
17	0.064	0.039	0.052	0.017
19	0.057	0.000	0.029	0.041
76.2	0.036	0.024	0.030	0.008

Table F.12: S35-MK5 flexure sample titration data

	Concentration (% Mass)			
Depth (mm)	**F1**	**F2**	**Average**	**Std. Dev.**
1	0.561	0.597	0.579	0.026
3	0.476	0.465	0.470	0.008
5	0.344	0.340	0.342	0.003
7	0.241	0.171	0.206	0.050
9	-	0.139	0.139	-
11	0.144	0.160	0.152	0.012
13	0.110	0.146	0.128	0.025
15	0.101	0.100	0.100	0.001
17	0.040	0.099	0.069	0.041
19	0.000	0.060	0.030	0.042
76.2	0.000	0.000	0.000	0.000

Table F.13: S50-MK5 control sample titration data

	Concentration (% Mass)			
Depth (mm)	**C1**	**C2**	**Average**	**Std. Dev.**
0.5	0.465	0.444	0.455	0.015
1.5	0.547	0.471	0.509	0.053
2.5	0.463	0.403	0.433	0.042
3.5	0.385	0.357	0.371	0.020
4.5	0.284	0.197	0.240	0.061
5.5	0.201	0.115	0.158	0.061
7	0.108	0.038	0.073	0.049
9	0.043	0.000	0.022	0.031
11	0.000	0.000	0.000	0.000
13	0.000	0.000	0.000	0.000

Table F.14: S50-MK5 tension sample titration data

	Concentration (% Mass)			
Depth (mm)	**T1**	**T2**	**Average**	**Std. Dev.**
1	0.591	0.575	0.583	0.012
3	0.440	0.419	0.429	0.015
5	0.330	0.304	0.317	0.018
7	0.221	0.207	0.214	0.010
9	0.220	0.197	0.208	0.016
11	0.176	0.193	0.184	0.012
13	0.153	0.205	0.179	0.037
15	0.138	0.219	0.179	0.057
17	0.144	0.164	0.154	0.014
19	0.167	0.185	0.176	0.013
76.2	0.021	0.107	0.064	0.061

Table F.15: S50-MK5 flexure sample titration data

	Concentration (% Mass)			
Depth (mm)	**F1**	**F2**	**Average**	**Std. Dev.**
1	0.588	0.562	0.575	0.018
3	0.585	0.441	0.513	0.102
5	0.437	0.345	0.391	0.065
7	0.248	0.235	0.242	0.009
9	0.144	0.187	0.166	0.031
11	0.136	0.122	0.129	0.011
13	0.101	0.114	0.107	0.010
15	0.062	0.113	0.087	0.036
17	0.062	0.142	0.102	0.057
19	0.056	-	0.056	-
76.2	0.000	0.014	0.007	0.010

(This page intentionally left blank.)

APPENDIX G

HIGH PERFORMANCE MARINE CONCRETE FOR COASTAL GEORGIA: USAGE CONDITIONS

G.1 Introduction

The deterioration of precast prestressed concrete piles in marine environments has become an area of concern based on several structures having shown extensive deterioration after only 30 years of service. Recent research has shown that concrete piling can experience damage due to multiple deterioration mechanisms, including chemical, physical, and biological attack. This deterioration leads to reductions in mechanical properties, serviceability, and aesthetics of the structure.

As part of the ongoing research to develop concrete mix designs capable of providing service lives of 100+ years, a study was performed to identify where high-performance marine concretes (HPMC) are needed to attain the desired service life through the monitoring of the chloride and sulfate concentrations present in surface water.

G.2 Methodology and Results

The chloride and sulfate concentrations in coastal Georgia (Brantley, Bryan, Camden, Charlton, Chatham, Effingham, Glynn, Liberty, Long, McIntosh, and Wayne Counties) were analyzed to determine where high-performance marine concrete (HPMC) is necessary. This was performed by utilizing data available from the United States Geological Survey (USGS) monitoring stations (USGS, 2010). Only sites for surface water with more than 3 data points were considered. A skew normal distribution was fit to the data for use in statistical analyses of

the sites. The skew normal distribution was selected for its ability to fit data with a positive or negative skew that was present in the data collected (Azzalini, 2005). Then for each site, the 75th percentile of the concentration for chloride and sulfates was determined. The results for both chloride and sulfate concentration were compared versus their distance inland from Atlantic Ocean coast and site elevation (mean sea level is reference).

Figure G.1 presents the chloride concentration relative to distance inland, and Figure G.2 shows the chloride concentration compared to the site elevation. Figure G.3 presents the sulfate concentration relative to distance inland, and Figure G.4 shows the sulfate concentration compared to the site elevation.

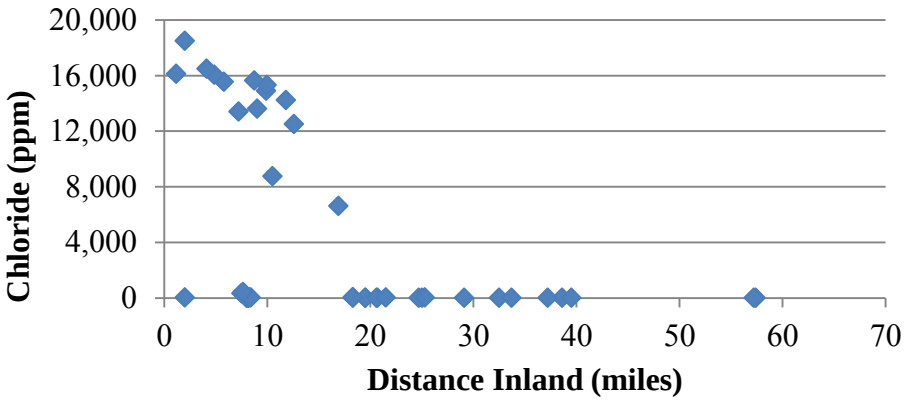

Figure G.1: Chloride concentration versus distance inland (1 mile = 1.6 km)

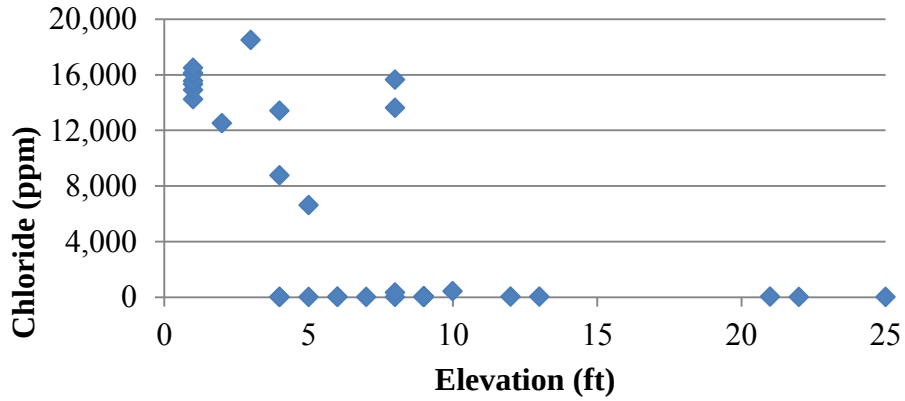

Figure G.2: Chloride concentration versus site elevation (1 ft = 0.3 m)

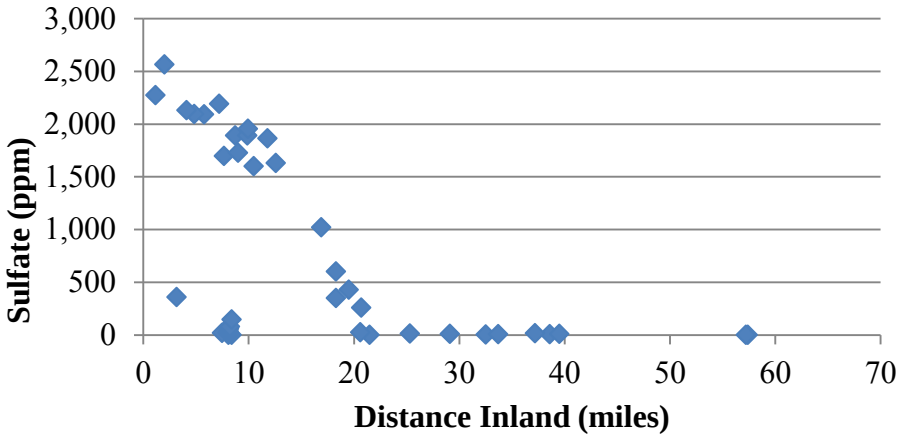

Figure G.3: Sulfate concentration versus distance inland (1 mile = 1.6 km)

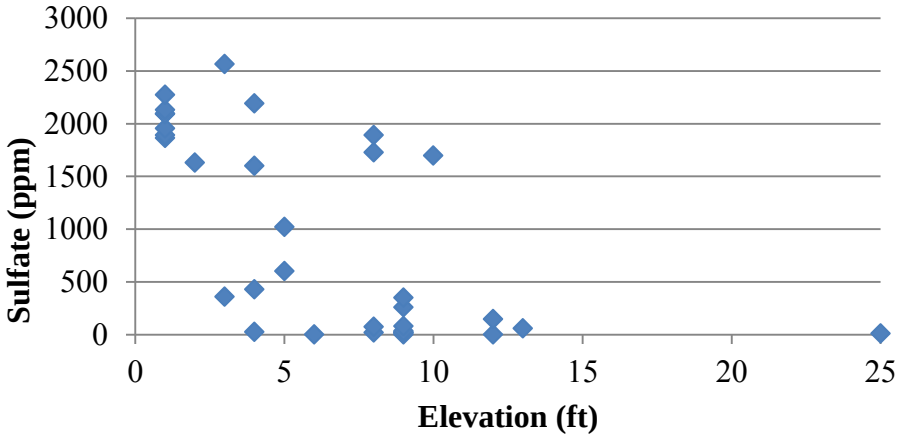

Figure G.4: Sulfate concentration versus site elevation (1 ft = 0.3 m)

Figures G.1 through G.4 demonstrate that both the chloride and sulfate concentration decrease with increasing distance inland, as well as with increases in elevation. Next, the data were compared with exposure limits that would necessitate the use of a HPMC. For sulfate concentration, the limit of 150 ppm given by ACI 201 (2010) was used, and for chlorides a threshold of 500 ppm was chosen to match the value used by the USGS (2010) for differentiating between brackish and fresh water. Table G.1 presents the maximum values of distance inland and elevation for sites with concentrations in excess of the limits chosen.

Table G.1: Maximum inland distance and elevation of sites requiring use of HPMC
(1 mile = 1.6 km, 1 ft = 0.3 m)

	Inland Distance (miles)	**Site Elevation (ft)**
Chloride	16.9	8
Sulfate	20.7	12

Figure G.5 presents a map of the sites monitored for chloride concentrations. Red icons represent a concentration above 500 ppm where HPMC is needed, blue icons represent sites where chloride levels are negligible.

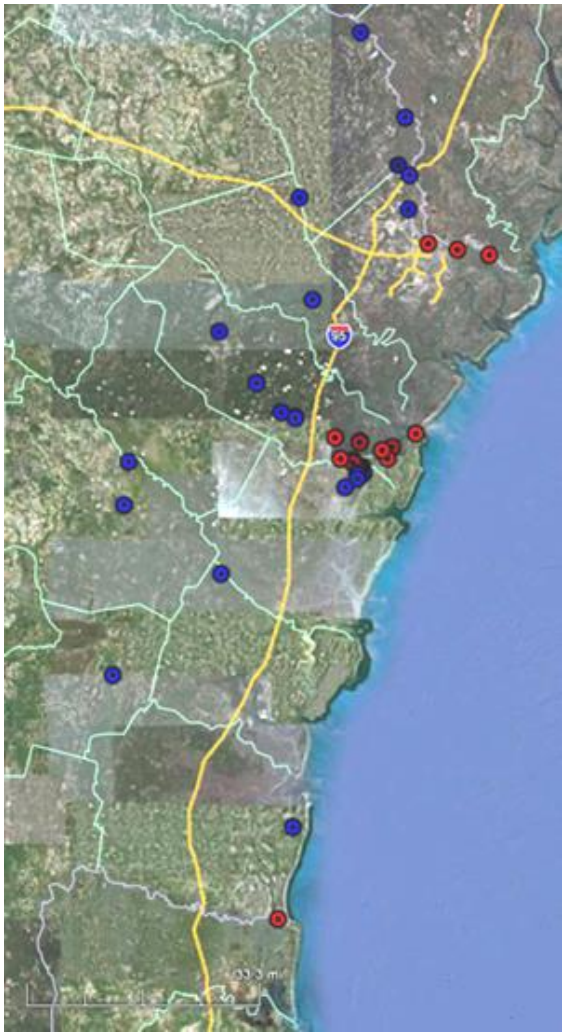

Figure G.5: Map of chloride sampling sites (Google, 2011)

Figure G.6 presents a map of the sites monitored for sulfate concentrations. Red icons represent a sulfate concentration above 1,500 ppm where HPMC with an ASTM C 150 (2009) Type V cement or equivalent is required by ACI 201.2R-10 (2010) is needed, yellow icons represent a concentration between 150 ppm and 1,500 ppm HPMC with an ASTM C 150 (2009) Type II cement or equivalent is required by ACI 201.2R-10 (2010) is needed, and blue dots represent sites where sulfate levels are negligible.

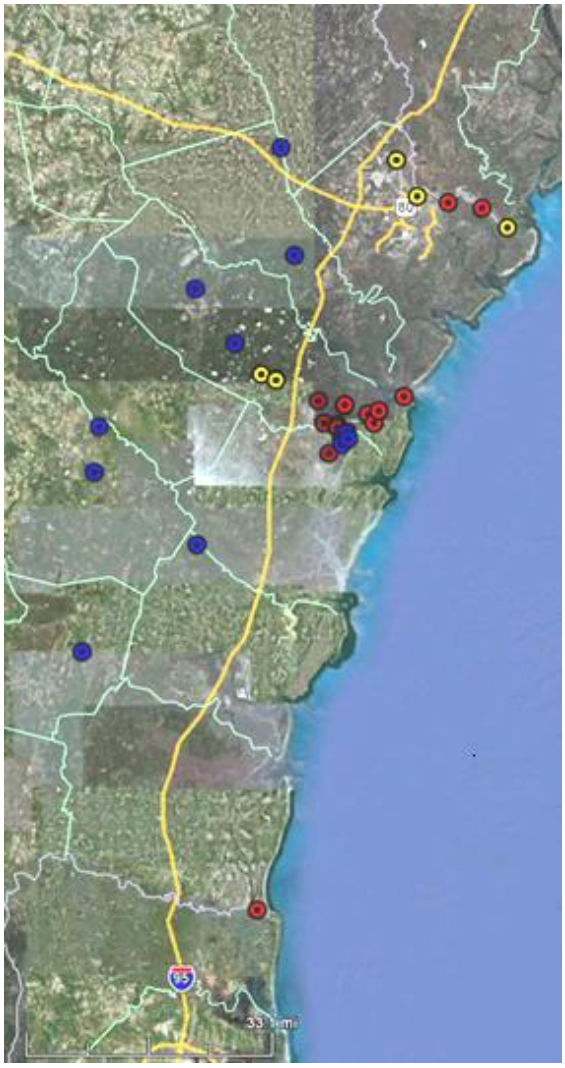

Figure G.6: Map of sulfate sampling sites (Google, 2011)

G.3 Conclusions and Recommendations

The analysis of USGS monitoring sites along the coast of Georgia suggests that HPMC is necessary for service lives of 100+ years. The data suggest that HPMC is not necessary at sites over 33.8 km (21 miles) inland from the coast. Alternatively, site elevation may be used as a criterion for usage, and a recommended value of 3.9 m (13 ft) is suggested. Figure G.7 shows a map of coastal Georgia with the 33.7 km (21 mile) suggested distance present marked with a

blue line. Any site to the east of the blue line requires the use of HPMC.

Figure G.7: Proposed HPMC use map for submerged piles, original map from GDOT (2011)

(This page intentionally left blank.)

REFERENCES

AASHTO LRFD Bridge Design Specifications, 4th ed. (2007), American Association of Highway and Transportation Officials, Washington D.C.

ACI Committee 201 (2010). "ACI 201.2R-10 Guide to Durable Concrete," *ACI Manual of Concrete Practice*, ACI 201.2R-10, American Concrete Institute, Farmington Hills, MI.

ACI Committee 211, (1991). "ACI 211.1R-91 Standard Practice for Selecting Proportions for Normal, Heavyweight, and Mass Concrete," *ACI Manual of Concrete* Practice, ACI 211.1R-91, American Concrete Institute, Farmington Hills, MI, pp. 38.

ACI Committee 211, (2008). "ACI 211.4R-08 Guide for Selecting Proportions for High-Strength Concrete Using Portland Cement and Other Cementitious Materials," *ACI Manual of Concrete* Practice, ACI 211.4R-08, American Concrete Institute, Farmington Hills, MI, pp. 25.

ACI Committee 214 (2010). "Guide for Obtaining Cores and Interpreting Compressive Strength Results," *ACI Manual of Concrete Practice*, ACI 214.4R-10, American Concrete Institute, Farmington Hills, MI, pp. 17.

ACI Committee 222 (2001), "ACI 222R-01 Protection of Metals in Concrete against Corrosion," *ACI Manual of Concrete Practice*, ACI 222R-01, American Concrete Institute, Farmington Hills, MI.

ACI Committee 222 (2001). "Corrosion of Prestressing Steels," *ACI Manual of Concrete Practice*, ACI 222.2R-01, American Concrete Institute, Farmington Hills, MI, pp. 43.

ACI Committee 224R-90 (1998). "ACI 224R-90 Control of Cracking in Concrete Structures," *ACI Manual of Concrete Practice*, ACI 224R-90, American Concrete Institute, Farmington Hills, MI.

ACI Committee 318 (2008). "Building Code Requirements for Structural Concrete (ACI 318-08) and Commentary," American Concrete Institute. Farmington Hills, Michigan.

ACI Committee 363 (1997). "Report on High-Strength Concrete," *ACI Manual of Concrete Practice,* ACI 363R-92, American Concrete Institute. Farmington Hills, Michigan.

Akoz, F.; Koral, S.; Yuzer, N.; Turker, F. (1995). "Effects of Sodium Sulfate Concentration on the Sulfate Resistance of Mortars with and without Silica Fume," *Cement and Concrete Research*, V. 25, pp. 1360-1368.

Al-Amoudi, O.S.B. (2002). "Attack on Plain and Blended Cements Exposed to Aggressive Sulfate Environments," *Cement and Concrete Composites,* V. 24, pp. 305-316.

American Association of State Highway and Transportation Officials (1980) "T259-80: Standard Method of Test for Resistance of Concrete to Chloride Ion Penetration," Washington, D.C., U.S.A.

Andrade, C. (1993). "Calculation of Chloride Diffusion Coefficients in Concrete From Ionic Migration Measurements," *Cement and Concrete Research*, V. 23, pp. 724-742.

Andrade, C. and Sanjuan, M.A. (1994), "Experimental Procedure for the Calculation of Chloride Diffusion Coefficients in Concrete from Migration Tests," *Advances in Cement Research*, V. 6, pp. 127-134.

Angst, U.; Elsener, B.; Larsen, C.; Vennesland, O. (2009). "Critical Chloride Content in Reinforced Concrete – A Review," *Cement and Concrete Research*, V. 39, pp. 1122-1138.

ASTM C 39 (2005). "Standard Test Method for Compressive Strength of Cylindrical Concrete Specimens," American Society for Testing and Materials, West Conshohocken, PA, pp. 7.

ASTM C 150 (2009). "Standard Specification for Portland Cement," American Society for Testing and Materials, West Conshohocken, PA, pp. 10.

ASTM C 469 (2002). "Standard Test Method for Static Modulus of Elasticity and Poisson's Ratio of Concrete in Compression," American Society for Testing and Materials, West Conshohocken, PA, pp. 5.

ASTM C 805 (2008). "Standard Test Method for Rebound Number of Hardened Concrete," American Society for Testing and Materials, West Conshohocken, PA, pp. 3.

ASTM C 876 (2009). "Standard Test Method for Corrosion Potentials of Uncoated Reinforcing Steel in Concrete," American Society for Testing and Materials, West Conshohocken, PA, pp. 7.

ASTM C 1012 (2009). "Standard Test Method for Length Change of Hydraulic-Cement Mortar Bars Exposed to a Sulfate Solution," American Society for Testing and Materials, West Conshohocken, PA, pp. 6.

ASTM C 1152 (2004). "Standard Test Method for Acid-Soluble Chloride in Mortar and Concrete," American Society for Testing and Materials, West Conshohocken, PA, pp. 4.

ASTM C 1157 (2004). "Standard Performance Specification for Hydraulic Cement," American Society for Testing and Materials, West Conshohocken, PA, pp. 5.

ASTM C 1202 (2007). "Standard Test Method for Electrical Indication of Concrete's Ability to Resist Chloride Ion Penetration," American Society for Testing and Materials, West Conshohocken, PA, pp. 6.

ASTM C 1218 (1999). "Standard Test Method for Water-Soluble Chloride in Mortar and Concrete," American Society for Testing and Materials, West Conshohocken, PA, pp. 3.

ASTM C 1327 (2008). "Standard Test Method for Vickers Indentation Hardness of Advanced Ceramics," American Society for Testing and Materials, West Conshohocken, PA, pp. 8.

ASTM C 1556 (2004). "Standard Test Method for Determining the Apparent Chloride Diffusion Coefficient of Cementitious Mixtures by Bulk Diffusion," American Society for Testing and Materials, West Conshohocken, PA, pp. 7.

ASTM C 1580 (2009). "Standard Test Method for Water-Soluble Sulfate in Soil," American Society for Testing and Materials, West Conshohocken, PA, pp. 3.

ASTM E 1131 (2008). "Standard Test Method for Compositional Analysis by Thermogravimetry," American Society for Testing and Materials, West Conshohocken, PA, pp. 5.

Atis, C.D. (2003). "Accelerated Carbonation and Testing of Concrete Made With Fly Ash." *Construction and Building Materials,* V. 17, pp. 147-152.

Azzalini, A. (2005). "The Skew-normal Distribution and Related Multivariate Families," *Scandinavian Journal of Statistics,* Vol. 32, No. 2, pp. 159-188.

Bamforth, P. (1993). "Concrete Classification for R.C. Structures Exposed to Marine and Other Salt-Laden Environments," *Structural Faults and Repair Conference*, Edinburgh, UK.

Bang, S. S.; Galinat, J. K.; Ramakrishnan, V. (2001). "Calcite Precipitation Induced by Polyurethane-immobilized *Bacillus pasteurii*," *Enzyme and Microbial Technology*, V. 28, pp. 404-409.

Bard, V.; Radlinska, A.; Cohen, M.; Weiss, W.J. (2009). *Relating Material Properties to Exposure Conditions for Predicting Serice Life in Concrete Bridge Decks in Indiana.* Publication FHWA/IN/JTRP-2007/27., Indiana Department of Transportation and Purdue University, West Lafayette, Indiana.

Basheer, L.; Kropp, J.; Cleland, D. (2002). "Assessment of the Durability of Concrete from Its Permeation Properties: A Review." *Construction and Building Materials.* V. 15, pp. 93-103.

Batis, G.; Pantazopoulou, P.; Tsivilis, S.; Badogiannis, E. (2005). "The Effect of Metakaolin on the Corrosion Behavior of Cement Mortars." *Cement and Concrete Composties.* V. 27, pp. 125-130.

Bentur, A; Diamond, S.; Berke, N. (1997). *Steel Corrosion in Concrete*, E&FN, Spon, London.

Bentz, D.P. (2000). "Influence of Silica Fume on Diffusivity in Cement-Based Materials II. Multi-Scale Modeling of Concrete Diffusivity," *Cement and Concrete Research*, V. 30, pp. 1121-1129.

Berke, N. S., and Hicks, M.C. (1992). "Estimating the Life Cycle of Reinforced Concrete Decks and Marine Piles Using Laboratory Diffusion and Corrosion Data," *Corrosion Forms and Control for Infrastructure, ASTM STP 1137*, American Society for Testing and Materials, Philadelphia.

Bertolini, L; Elsener. B.; Pedeferri, P.; Polder, R. (2004). *Corrosion of Steel in Concrete: Prevention Diagnosis, Repair*, Wiley-VCH, pp. 392.

Biswas, M., et al. (2010). "Bioremediase a Unique Protein from a Novel Bacterium BKH1, Ushering a New Hope in Concrete Technology," *Enzyme and Microbial Technology*, V. 46, pp. 581-587.

Bleszynski, R.; Hooten, R.; Thomas, M.; Rogers, C. (2002). "Durability of Ternary Blend Concrete with Silica Fume and Blast-Furnace Slag: Laboratory and Outdoor Exposure Site Studies." *ACI Materials Journal.* V. 99, pp. 499-508.

Böhni, H. (2005), Corrosion in Reinforced Concrete Structures, Woodhead Publishing Ltd., Cambridge, UK.

Bonakdar, A. and Mobasher, B. (2010). "Multi-parameter Study of External Sulfate Attack in Blended Cement Materials," *Construction and Building Materials*, V. 24, pp. 61-70.

Bonen, D. (1993). "A Microstructural Study of the Effect Produced by Magnesium Sulfate on Plain and Silica Fume-bearing Portland Cement Mortars," *Cement and Concrete Research*, V. 23, pp. 541-553.

Borgard, B., Ramirez, C.; Somayaji, S.; Jones, D.; Keeling, D.; Heidersbach, R. (1991). "Failure Analysis in Concrete Structures: A Cornparison of Field Data with Results from Laboratory Exposures," *Corrosion*, V. 47, pp.758-769.

Broomfield, J. P. (2007), *Corrosion of Steel in Concrete*, Taylor and Francis Group, New York, NY.

Brown, P. (1981). "An Evaluation of the Sulfate Resistance of Cements in a Controlled Environment," *Cement and Concrete Research,* V. 11, pp. 719-727.

Chang, C. F., and Chen, J. W. (2006), "The Experimental Investigation of Concrete Carbonation Depth," *Cement and Concrete Research*, V. 36 (9), pp. 1760-1767.

Cobanoglu A.; Lampros T.; Hershberger R.; Norman D.; Murata K.; Kawakami K.; Matsunaga Y.; Yamashita S. (1997), "Determination of Sulfate in Brackish Waters by Laser Raman Spectroscopy," *Analytica Chimica Acta*, 344, pp 153-157.

Cohen, M. D. and Mather, B. (1991). ''Sulfate attack on concrete— Research needs.'' ACI Materials Journal, V. 88, pp. 62– 69.

Collepardi, M.; Marcialis, A.; Turriziani, R. (1972). "Penetration of Chloride Ions into Cement Pastes and Concrete," *Journal of the American Ceramic Society*, V. 55, pp.534-535.

Concrete Durability Center (2005). *Concrete Works Version 2.0 Users Manuel*.

Concrete Durability Center (2007). *Concrete Works* (Version 2.1.3) [Software]. Available from http://www.texasconcreteworks.com

Courard, L.; Darimont, A.; Schouterden, M.; Ferauche, F.; Willem, X.; Degeimbre, R. (2003). "Durability of Mortars Modified with Metakaolin," *Cement and Concrete Research*, V. 33, pp. 1473-1479.

Crossett, K.; Culliton, T.; Wiley, P.; Goodspeed, T. (2004). "Population Trends Along the Coastal United States: 1980 to 2008," *Coastal Trends Report Series*, National Oceanic and Atmospheric Administration. Available from: oceanservice.noaa.gov/programs/mb/pdfs/coastal_pop_trends_complete.pdf.

De Muynck, W.; Debrouwer, D.; Debelie, N.; Verstraete, W. (2008). "Bacterial Carbonate Precipitation Improves the Durability of Cementitious Materials," *Cement and Concrete Research*, V. 38, pp. 1005-1014.

Dhir, R.K.; Jones, M.; Ahmed, H.; Seneviratne, A. (1990). "Rapid Estimation of Chloride Diffusion Coefficient in Concrete," *Magazine of Concrete Research*, V. 42, pp. 177-185.

Diab, H.; Bentur, A.; Heitner-Wirguin, C.; Ben-Dor, L. (1988). "The Diffusion of Cl-Ions through Portland Cement and Portland Cement-Polymer Pastes," *Cement and Concrete Research*, V. 18, pp. 715-722.

Edvardsen, C. (1995). “Chloride Penetration into Cracked Concrete,” Proceedings of the RILEM International Workshop on Chloride Penetration into Concrete, St-Remy-les-Chevreuse, France, Oct. l5-l8, pp. 243-249.

Edvardsen, C. (1996). “Water Penetrability and Autogenous Healing of Separation Cracks in Concrete,” *Betonwerk and Fertigteil Technik-Concrete Precasting Plant and Technology*, V. 62, pp. 77-85.

Edvardsen, C. (1999). “Water Permeability and Autogenous Healing of Cracks in Concrete.” *ACI Materials Journal.* V. 96, pp. 448-454.

Ehlen, M.A. (2009). *Life 365* (Version 2.1) [Software]. Available from http://www.life-365.org

Ehlen, M.A.; Thomas, M.; Bentz, E. (2009). “Life 365 Service Life Prediction Model Version 2.0,” *Concrete International*, V. 31.

Francois, R. and Arliguie, G. (1999). “Effect of Microcracking and Cracking on The Development of Corrosion in Reinforced Concrete Mernbers,” *Magazine of Concrete Research*, V. 51, pp. 143- 150.

Francois, R. and Maso, J. (1988). “Effect of Damage in Reinforced Concrete on Carbonation or Chloride Penetration,” *Cement and Concrete Research,* V. 18, pp. 961-970.

Geiker, M.; Thaulow, N.; Anderson, P. (1990). “Assessment of Rapid Chloride Ion Permeability Test of Concrete With and Without Mineral Admixtures”, *Durability of Building Materials*, (ed. J.M Baker, P.J. Nixon, A.J. Majumdar, H. Davis) E&FN Spon, London, pp. 493-502.

Georgia Department of Transportation (2004). “Section 500- Concrete Structures,” *Georgia Department of Transportation Standard Specifications*, Available from www.dot.ga.gov/doingbusiness/theSource/Pages/specifications.aspx.

Google Earth (2011). *Map of Coastal Georgia*, created December 5th, 2011.

Gowripalan, N.; Sirivivatnanon, V.; Lim, C. (2000). “Chloride Diffusivity of Concrete Cracked in Flexure,” *Cement and Concrete Research*, V. 30, pp. 725-730.

Gruber, K.A.; Ramlochan, T.; Boddy, A.; Hooton, R.; Thomas, M. (2001). “Increasing Concrete Durability with High-reactivity Metakaolin.” *Cement and Concrete Composites.* V. 23, pp. 479-484.

Guneyisi, E.; Gesoglu, E.; Mermerdas, K. (2010). “Strength Deterioration of Plain and Metakaolin Concretes in Aggressive Sulfate Environments,” *Journal of Materials in Civil Engineering*, V. 22, pp. 403-407.

Heide, N. (2005). *Crack Healing in Hydrating Concrete.* Masters thesis. Delft University of Technology. pp.128.

Hooton, R. and Emery, J. (1990). "Sulfate Resistance of a Canadian Slag Cement," *ACI Materials Journal*, V. 87, pp. 547-555.

Hopkins, S.E. (1962). "Distribution of the Species of *Cliona* (boring sponge) on the Eastern Shore of Virginia in Relation to Salinity," *Chesapeake Science*, V. 3, pp. 121-125.

Ismail, M.; Toumi, A.; Francois, R.; Gagne, R. (2008). "Effect of Crack Opening on the Local Diffusion of Chloride in Cracked Mortar Samples," *Cement and Concrete Research*, V. 38, pp. 1106-1111.

Jacobsen, S.; Marchand, J.; Boisvert, L. (1996). "Effect of Cracking and Healing on Chloride Transport in OPC Concrete." *Cement and Concrete Research.* V. 26, pp. 869-881.

Jacobsen, S.; Marchand, J.; Gerard, B. (1998). "Concrete Cracks 1: Durability and Self Healing – A Review," Proceedings of the Second International Conférence on Concrete under Severe Conditions, Tromso, Norway, Jun. 21-24, pp.217-231.

Jia, Y.; Aruhan, B.; Yan, P. (2012). "Natural and Accelerated Carbonation of Concrete Containing Fly Ash and GGBS after Different Initial Curing Period," *Magazine of Concrete Research*, V. 64, pp. 143-150.

Johnson, D.; Miltenberger, M.; Almy, S. (1996). "Determining Chloride Diffusion Coefficients for Concrete using Accelerated Test Methods," *Proceedings on Performance of Concrete in a Marine Environment,* New Brunswick, Canada, pp. 95-114.

Jonkers, H. M.; Thijssen, A.; Muyzer, G.; Copuroglu, O.; Schlangen, E. (2008). "Application of Bacteria as Self-healing Agent for the Development of Sustainable Concrete," *Ecological Engineering*, V. 36, pp. 230-235.

Kanaya, M.; Masuda, Y.; Abe, M.; Nishiyama, N. (1998). "Diffusion of Chloride Ions in Concrete Exposed in the Coastal Area," *Concrete Under Severe Conditions 2: Environment and Loading*, E & FN Spon, pp. 242-249.

Khatib, J. M. and Wild, S. (1998). "Sulphate Resistance of Metakaolin Mortar." *Cement and Concrete Research*, V. 28, pp. 83-92.

Koch, G. H.; Brongers, M.; Thompson, N.; Virmani, Y.; Payer, J. (2008), "Corrosion Costs and Preventive Strategies in the United States," National Association of Corrosion Engineers, Houston, TX.

Konin, A.; Francois, R.; Arliguie, G. (1998). "Penetration of Chlorides in Relation to the Microcracking State into Reinforced Ordinary and High Strength Concrete," *Materials and Structures*, V. 31, pp. 310-316.

Kurth, J.C. (2008). *Mitigating Biofilm Growth through the Modification of Concrete Design and Practice*. Master's Thesis. Georgia Institute of Technology. pp. 234.

Kurtis, K.E.; Monteiro, P.; Madanat, S. (2000). "Empirical Models to Predict Concrete Expansion Caused by Sulfate Attack," *ACI Materials Journal,* V. 97, pp. 156-162.

Kurtis, K.E.; Shomglin, K.; Monteiro, P.; Harvey, J.; Roesler, J. (2001). "Accelerated Test for Measuring Sulfate Resistance of Calcium Sulfoaluminate, Calcium Aluminate, and Portland Cements," *Journal of Materials in Civil Engineering*, V. 13, pp. 216-221.

Lauer, K. and Slate, F.O. (1955). "Autogenous Healing of Cement Paste." *Journal of the American Concrete Institute.* V. 41, June, pp. 1083-1097.

Lea, F.M. (1971). *The Chemistry of Cement and Concrete*, 3rd Edition, Chemical Publishing Co., New York, pp. 627.

Lee, S.; Moon, H.; Swamy, R. (2005). "Sulfate Attack and Role of Silica Fume in Resisting Strength Loss," *Cement and Concrete Composites*, V. 27, pp. 65-76.

Li, X., and Zhang, D. (2011) " Effect of Binary Admixture of Fly Ash and Slag on the Carbonation of Concrete for Hydraulic Structure," *Advanced Materials Research,* V. 150, pp. 1673-1676.

Luo, R.; Cai, Y.; Wang, C.; Huang, X. (2003). "Study of Chloride Binding and Diffusion in GGBS Concrete." *Cement and Concrete Research.* V. 33, pp. 1-7.

Luping, T. (1995). "On Chloride Diffusion Coefficients Obtained by Using the Electrically Accelerated Methods," *RILEM International Conference*, Paris, France.

Luping, T., and Nilsson, L.O. (1992). "Chloride Diffusivity in High Strength Concrete at Different Ages," *Nordic Concrete Research*, V. 11, pp. 162-171.

Mangat, P.S. and Gunisamy**,** K. (1987). "Chloride Diffision in Steel Fibre Reinforced Marine Concrete," *Cement and Concrete Research*, V. 17, pp. 385-396.

Mangat, P.S. and Khatib, J. M. (1995). "Influence of Fly Ash, Silica Fume, and Slag on Sulfate Resistance of Concrete," ACI Materials Journal, V. 92, pp. 542-552.

Mangat, P.S., and Molloy, B.T. (1994). "Prediction of Long Term Chloride Concentration in Concrete," *Materials and Structures*, V. 27, pp. 338-346.

Maslehuddin, M.; Page, C.; Rasheeduzzafar (1996). "Effect of Temperature and Salt Contamination on Carbonation of Cements." *Journal of Materials in Civil Engineering,* V. 63, pp. 63-69.

McGrath., P. and Hooton, R.D. (1996). "Influence of Voltage on Chloride Diffusion Coefficients From Chloride Migration Tests," *Cement and Concrete Research*, V. 26, pp. 1239-1244.

Mehta, P.K. (1975). ''Evaluation of Sulfate-resisting Cements by a New Test Method,'' *Journal of ACI,* V. 72, pp. 573–575.

Mehta, P.K. (1991). *Concrete in the Marine Environment*, Elsevier Science Pulishers, New York, NY, pp. 214.

Mehta, P. K., and Gjorv, O. E. (1974). ''A New Test for Sulfate Resistance of Cements,*''Journal of Testing and Evaluation*, V. 2, pp. 510–515.

Miller, A.N.; Strychar, K.; Shirley, T.; Rutzler, K. (2010). "Effects of Heat and Salinity Stress on the Sponge *Cliona celata*," *International Journal of Biology*, V. 2, pp. 3-16.

Mindess, S.; Young, J.; Darwin, D. (2003). *Concrete*, 2nd Edition, Prentice Hall Publishers, Upper Saddle River, NJ.

Mobasher, B. and Mitchell, T.M. (1988). "Laboratory Experience with the Rapid Chloride Permeability Test," *ACI SP-108: Permeability of Concrete*, (ed. D. Whiting, A. Walitt), American Concrete Institute.

Mohammed, T.U. and Hamada, H. (2003). "Corrosion of Steel Bars in Concrete at Joints under Tidal Environment." *ACI Materials Journal.* V. 100, pp. 265-273.

Mohammed, T.U., and Hamada, H. (2003). "Relationship Between Free Chloride and Total Chloride Contents in Concrete," *Cement and Concrete Research*, V. 33, pp. 1487-1490.

Monteiro, P. and Kurtis, K. (2003). "Time to Failure for Concrete Exposed to Severe Sulfate Attack," *Cement and Concrete Research*, V. 33, pp. 987-993.

Murata, K.; Cobanoglu, A.; Lampros, T.; Hershberger, R.; Norman, D.; Kawakami, K.; Matsunaga, Y.; Yamashita, S. (1997). "Determination of Sulfate in Brackish Waters by Laser Raman Spectroscopy," *Analytica Chimica Acta*, V. 344, pp 153-157.

National Cooperative Highway Research Program (2007), *Report 595: Application of the LRFD Bridge Design Specifications to High-Strength Structural Concrete: Flexure and Compression Provisions*, Transportation Research Board, Washington D.C.

Neumann, A.C. (1966). "Observations on Coastal Erosion in Bermuda and Measurements of the Boring Rate of the Sponge, *Cliona lampa*," *Limnology and Oceanography*, V. 11, pp. 92-108.

Neville, A.M. (1997). *Properties of Concrete*, 4 ed., John Wiley and Sons, New York, NY, pp. 844.

Nicol, W.L. and Reisman, H.M. (1976). "Ecology of the Boring Sponge (*Cliona celata*) at Gardiner's Island, New York," *Chesapeake Science*, V. 17, pp. 1-7.
Odler, I. (1997). "Expansive Reactions in Concrete," Materials Science of Concrete II, John Wiley & Sons Inc., New Jersey, pp. 221-247.

Otsuki, N.; Miyazato, S.; Diola, N.; Suzuki, H. (2000). "Influences of Bending Crack and Water-Cement Ratio on Chloride-Induced Corrosion of Main Reinforcing Bars and Stirrups," *AC1 Materials Journal*, V. 97, pp. 454-464.

Papadakis, V.G. (2000). "Effect of Supplementary Cementing Materials on Concrete Resistance against Carbonation and Chloride Ingress." *Cement and Concrete Research*, V. 30, pp. 291-299.

Papadakis, V.G.; Vayenas, C.; Fardis, M. (1991). "Fundamental Modeling and Experimental Investigation of Concrete Carbonation." *ACI Materials Journal,* V. 88, pp. 363-373.

Parks, J.; Edwards, M.; Vikesland, P.; Dudi, A. (2010). "Effects of Bulk Water Chemistry on Autogenous Healing of Concrete," *Journal of Materials in Civil Engineering*, V. 22, pp. 515-524.

Patil, H. S.; Raijiwala, D.; Prashant, H.; Vijay, B. (2008). "Bacterial Concrete – A Self Healing Concrete," *International Journal of Applied Engineering Research*, V. 3, pp. 1719-1725.

Pease, B., Couch, J., Geiker, M., Stang, H., and Weiss, J. (2009). "Assessing the Portion of the Crack Length Contributing to Water Sorption in Concrete Using X-Ray Absorption," *Proceedings of ConcreteLife'09: Second International RILEM Workshop on Concrete Durability and Service Life Planning*, Haifa, Israel.

Pedersen, V. and Arntsen, B. (1998). "Effect of Early-Age Curing on Penetration of Chloride Ions into Concrete in the Tidal Zone," *Concrete Under Severe Conditions 2: Environment and Loading*, E & FN Spon, pp. 468-477.

Polder, R.B. (1995) "Chloride Diffusion and Resistivity Testing of Five Concrete Mixes for Marine Environment," *RILEM International Conference*, Paris, France.

Raharinaivo, A.; Brevet, P.; Grimaldi, G.; Pannier, G. (1986). "Relationship between Concrete Deterioration and Reinforcing-Steel Corrosion," *Durability of Building Materials*, V. 4, pp**.** 97-112.

Rodriguez, O.G. (2001). *Influence of Cracks on Chloride Ingress into Concrete.* Masters thesis. University of Toronto. pp.273.

Roy, D.M. (1989). "Hydration, Microstructure and Chloride Diffusion of Chloride Ions in Hardened Cement Pastes," *ACI SP-114,* V. 2, American Concrete Institute, Detroit, pp. 1265-1281.

Roziere, E.; Loukili, A.; El Hachem, R.; Grondin, F. (2009). "Durability of Concrete Exposed to Leaching and External Sulfate Attacks," *Cement and Concrete Research*, V. 39, pp. 1188-1198.

Sahmaran, M. (2007). "Effect of Flexure Induced Transverse Crack and Self-healing on Chloride Diffusivity of Reinforced Mortar," *Journal of Material Science,* V. 42, pp. 9131-9136.

Sahmaran, M.; Keskin, S.; Ozerkan, G.; Yaman, I. (2008). "Self-healing of Mechanically-loaded Self Consolidating Concretes with High Volumes of Fly Ash," *Cement and Concrete Composites,* V. 30, pp. 872-879.

Saleem, H., et al. (2010). "Durability and Strength Evaluation of High-performance Concrete in Marine Structures," *Construction and Building Materials,* V. 24, pp. 878-884.

Scott, P.J.B.; Moser, K.; Risk, M. (1988). "Bioerosion of Concrete and Limestone by Marine Organisms," *Marine Pollution Bulletin*, V. 19, pp. 219-222.

Sideris, K.K.; Savva, A.; Papayianni, J. (2006). "Sulfate Resistance and Carbonation of Plain and Blended Cements," *Cement and Concrete Composites*, V. 28, pp. 47-56.

Skalny, J.; Marchand, J.; Odler, I. (2002). *Sulfate Attack on Concrete*, Spon Press, New York, NY, pp. 217.

Smith, B.G. (2001). "Durability of Silica Fume Concrete Exposed to Chloride in Hot Climates." *Journal of Materials in Civil Engineering.* V. 13, pp. 41-48.

Stanish, K.D. and Thomas, M. (2003). "The Use of Bulk Diffusion Tests to Establish Time-dependent Concrete Chloride Diffusion Coefficients." *Cement and Concrete Research.* V. 33, pp. 55-62.

Stanish, K.D.; Hooton, R.; Thomas, M. (1997). *Testing the Chloride Penetration Resistance of Concrete: A Literature Review*, FHWA contract report, pp. 33.

Streicher, P.E. and Alexander, M.G. (1995). "A Chloride Conduction Test for Concrete," *Cement and Concrete Research*, V. 25, pp. 1284-1294.

Sulapha, P.; Wong, S.; Wee, T.; Swaddiwudhipong, S. (2003). "Carbonation of Concrete Containing Mineral Admixtures." *Journal of Materials in Civil Engineering.*V. 15, pp. 134-143.

Suryavanshi, A.; Swamy, R.; Cardew, G. (2002). "Estimation of Diffusion Coefficients for Chloride Ion Penetration into Structural Concrete," *ACI Materials Journal,* V. 99, pp. 441-449.

Suzuki, K.; Ohno, Y.; Praparntanatorn, S.; Ninomiya, H.; Tamura, H. (1989)**. "**Influence of Flexural Crack on Corrosion of Steel in Concrete," *Technology Reports of the Osaka University*, V.39, pp. 49-57.

Suzuki, K.; Ohno, Y.; Praparntanatorn, S.; Tamura, H. (1990)**. "**Mechanism of Steel Corrosion in Cracked Concrete," Corrosion of Reinforcement in Concrete Construction, Third International Symposium, Wishaw, UK**;** Elsevier Applied Science, pp. 19-28.

Termkhajornkit, P.; Nawa, T., Yamashiro, Y.; Saito, T. (2009). "Self-healing Ability of Fly Ash - Cement Systems," *Cement and Concrete Composites,* V. 31, pp. 195-203.

Thomas, M. and Bamforth, P. (1999). "Modelling Chloride Diffusion in Concrete: Effect of Fly Ash and Slag." *Cement and Concrete Research.* V. 29, pp. 487-495.

Thomas, M.D.A. and Matthews, J.D. (2004). "Performance of PFA Concrete in a Marine Environment – 10 Year Results." *Cement and Concrete Composites.* V. 26, pp. 5-20.

Thomas, M.D.A., and Jones, M.R. (1996). "A Critical Review of Service Life Modeling of Concretes Exposed to Chlorides," *Concrete in the Service of Mankind: Radical Concrete Technology*, (eds. R.K. Dhir and P.C. Hewlett), E.&F.N. Spon, London, pp. 723-736.

Thomas, M.D.A.; Shehata, M.; Shashiprakash, S.; Hopkins, D.; Cail, K. (1999). "Use of Ternary Cementitious Systems Containing Silica Fume and Fly Ash in Concrete." *Cement and Concrete Research.* V. 29, pp. 1207-1214.

Thomas, M.D.A.; Scott, A.; Bremner, T.; Bilodeau, A.; Day, D. (2008). "Performance of Slag Concrete in Marine Environment." *ACI Materials Journal.* V. 105, pp. 628-634.

Thuresson, T.; Hansson, C.; Seabrook, P.; Tullmin, M. (1997). "Effect of Cracking and Accelerated Curing on the Corrosion of Steel Embedded in High Performance Concretes Exposed to an Industrial Effluent," Fourth international Conference, Sydney, Australia, CANMET/ACI SP-170, Farmington Hills, Michigan, pp. 965-986.

Tikalsky, P. and Carrasquillo, R. (1992). "Influence of Fly Ash on the Sulfate Resistance of Concrete," *ACI Materials Journal*, V. 89, pp. 69-75.

Torii, K. and Kawamura, M. (1994). "Effects of Fly Ash and Silica Fume on the Resistance of Mortar to Sulfuric Acid and Sulfate Attack." *Cement and Concrete Research*, V. 24, pp. 361-370.

UNEP/GRID-Arendal (2005). "Trends in Natural Disasters," UNEP/GRID-Arendal Maps and Graphics Library, Available at:http://maps.grida.no/go/graphic/trends-in-natural-disasters.

USGS Surface Water Information Pages, United States Geological Survey, June 3rd, 2010, from http://water.usgs.gov/osw/.

Van Tittelboom, K.; Belie, N.; Mynck, W.; Verstraete, W. (2010). "Use of Bacteria to Repair Cracks in Concrete," *Cement and Concrete Research*, V. 40, pp. 157-166.

Winitzki, S. (2006). "A Handy Approximation for the Error Function and Its Inverse," Lecture note, Ludwig-Maximilians University, Munich, Germany.

Yang, Y.; Lepech, M.; Yang, E.; Li, V. (2009). "Autogenous Healing of Engineered Cementitious Composites under Wet–Dry Cycles." *Cement and Concrete Research.* V. 39, pp. 382-390.

Zea, S. and Weil, E. (2003). "Taxonomy of the Caribbean Excavating Sponge Species Complex *Cliona carribaea – C. Aprica – C. langae* (Porifera, Hadromerida, Clionaidae)," *Caribbean Journal of Science*, V. 39, pp. 348-370.

Zhang, M.H., and Gjorv, O.E. (1991). "Permeability of High Strength Lightweight Concrete," *ACI Materials Journal,* V. 88, pp. 463-469.

(This page intentionally left blank.)